

UCLA

UCLA Electronic Theses and Dissertations

Title

Metal Oxide Nanofiber Catalysis

Permalink

<https://escholarship.org/uc/item/08z226bp>

Author

Noon, Daniel Patrick

Publication Date

2015

Peer reviewed|Thesis/dissertation

UNIVERSITY OF CALIFORNIA
Los Angeles

Metal Oxide Nanofiber Catalysis

A dissertation submitted in partial satisfaction of the requirements for the degree of
Doctor of Philosophy in Chemical Engineering

by

Daniel Patrick Noon

2015

ABSTRACT OF THE DISSERTATION

Metal Oxide Nanofiber Catalysis

by

Daniel Patrick Noon

Doctor of Philosophy in Chemical Engineering

University of California, Los Angeles, 2015

Professor Selim M. Senkan, Chair

The synthesis of solids with finely turned nanostructures that offer superior catalytic performance is a major challenge in heterogeneous catalysis for gas phase reactions. Industrial catalysts are almost universally composed of quasi-spherical nanoparticles, or powders plagued with particle agglomeration, migration and sintering problems that lead to deactivation. In this work, quasi-cylindrical nanofibers are electrospun and extensively utilized for the oxidative coupling of methane (OCM), as well as for propylene epoxidation and the catalytic partial oxidation (CPO) of methane.

Electrospun nanofibers of metal oxides may be tuned to have high surface areas but typically possess no internal porosity, reducing diffusion limitations that would lengthen the exposure of target intermediate oxidation products to unselective catalysis. Additionally, experiments and density functional theory (DFT) studies have previously shown that pentagonal Ag nanowires exhibit higher selectivity than conventional particles

in ethylene epoxidation since their surfaces are terminated mainly by the (100) surface facet rather than the lowest energy (111) facet that dominates particles. Hence, nanofibers may elevate catalytic performance in broad range of partial oxidation reaction schemes.

Research into the oxidative coupling of methane, or, the catalytic conversion of methane to ethane and ethylene by molecular oxygen, almost exclusively utilized powders and failed to result in viable catalyst despite four decades of intense, global efforts. Accordingly, the use of catalytic nanofibers provides a potentially fruitful path towards a solution. Here, nanofiber fabrics of $\text{La}_2\text{O}_3\text{-CeO}_2$ were electrospun and used in fixed bed OCM reactors to achieve 70% selectivity and 16% yield for C_{2+} hydrocarbons at a CH_4/O_2 feed ratio of 7 and remarkably low feed temperature of 470 °C. Powders of $\text{La}_2\text{O}_3\text{-CeO}_2$ documented in the literature exhibit similar selectivity and yield, but with the feed at 715 °C. The electrospun fabrics used in this research were found to have dense nanofibers of diameters typically within the 20 – 200 nm range and, accordingly, surface areas of 10 – 20 m^2/g as well as thinner fibers tending towards both higher C_{2+} selectivity and CH_4 conversion.

While performing reaction engineering studies using the aforementioned fabrics, it was found that designing reactors comprising *dual* catalytic $\text{La}_2\text{O}_3\text{-CeO}_2$ fabric beds with inter-stage O_2 injection and cooling pushes yields to 21%. Moreover, a novel *in-situ* microprobe sampling technique for acquiring spatial temperature and concentration profiles within these OCM reactors was developed, providing a means to formulate and validate detailed chemical kinetic mechanisms. This has led to the discovery of prompt H_2 formation in OCM, a feature previously unidentified that may break ground in mechanism

refinement. Additionally, spatial concentration and temperature profiles were acquired in fixed bed reactors comprising $\text{La}_2\text{O}_3\text{-CeO}_2$ fabrics doped with varying levels of Ir and fed CH_4/O_2 mixtures to gain insight into the transition from OCM to the catalytic partial oxidation of methane. It was found that, in general, OCM and CPO appear to occur both in parallel and sequentially in a fixed bed, evidenced by the temporary rise and subsequent destruction of C_{2+} hydrocarbons when the catalyst is doped with 0.05 wt% Ir. Clearly, this sampling technique has broad applicability in catalysis research over a limitless number of reactions for the acquisition of comprehensive data sets potentially useful for formulating and refining detailed chemical kinetic mechanisms (DCKM), thus furthering a fundamental understanding of the catalysis and advancing faster towards the development of higher performing materials.

The dissertation of Daniel Patrick Noon is approved.

Yunfeng Lu

Robert F. Hicks

Richard B. Kaner

Selim M. Senkan, Committee Chair

University of California, Los Angeles

2015

TABLE OF CONTENTS

Chapter 1. Introduction.....	1
Chapter 2. Background.....	4
2.1. Research in Heterogeneous Catalysis.	4
2.2. Tuning the Architecture of Heterogeneous Catalysts.	6
2.3. Electrospinning and Catalytic Nanofiber Fabrics.	9
2.4. Propylene Epoxidation.	14
2.4.1. Propylene Oxide (PO) and its Established Means of Production.....	14
2.4.2. Direct Catalytic Epoxidation of Propylene Using Molecular Oxygen.....	16
2.5. Oxidative Coupling of Methane (OCM).	19
2.5.1. Motivation Behind Utilizing the Methane in Natural Gas.	19
2.5.2. Naphtha Steam Cracking for Ethylene Production.	20
2.5.3. Indirect Routes for Natural Gas Utilization.....	22
2.5.4. Oxidative Coupling of Methane for Direct Ethylene Synthesis from Natural Gas.....	23
2.6. Catalytic Partial Oxidation (CPO) of Methane.	27
Chapter 3. Propylene Epoxidation by Co-Impregnated $\text{Sb}_2\text{O}_3\text{-CuO-NaCl/SiO}_2$ Catalysts.	29
3.1. High-Throughput Catalytic Performance Screening System.	29
3.2. Preparation of Silica-Supported Catalysts Composed of Sb_2O_3 , CuO, NaCl and combinations thereof.	33

3.3. Catalytic Performance Evaluation and Characterization.	34
3.4. Catalyst Composition Optimization.	35
3.5. Calcination Temperature Optimization.	41
3.6. Active Site Analysis by H ₂ -Temperature Programmed Reduction (H ₂ -TPR).	45
3.7. Time on Stream Analysis.	46
3.8. Summary.	50
Chapter 4. Electrospinning, Electrospun Silica Supported and Metal Oxide Nanofibers and Their Application to Propylene Epoxidation.	51
4.1. Electrospinning Process Parameter Investigation on Protein/Synthetic Polymer Composite Nanofibers.	51
4.1.1. Mixing and Viscosity Experimental Approach.	51
4.1.2. Electrospinning and Imaging Procedures.	53
4.1.3. Mechanical Tensile and Permeability Properties Acquisition Methodology. .	55
4.1.4. Mixing and Viscosity Results.	56
4.1.5. Electrospun Protein/Synthetic Polymer Nanofibers and Images.	58
4.1.6. Strength Assessments of Nanofibers.	71
4.1.7. Permeability Assessments of Fabric Mats.	73
4.2. Nanofiber Catalysts and Propylene Epoxidation.	76
4.2.1. Preparation of Silica Supported Nanofiber Catalysts.	76
4.2.2. Preparation of Unsupported Metal Oxide Nanofiber Catalysts.	78
4.2.3. Performance Evaluation and Characterization Procedures.	79
4.2.4. Nanofiber Fabric Imaging.	80

4.2.5. Catalytic Performance Results.	86
4.3. Summary.	91
Chapter 5. Oxidative Coupling of Methane (OCM) by Metal Oxide Nanofiber Catalysts.	93
5.1. Catalyst Preparation.	93
5.2. Performance Evaluation Using Tubular Packed Bed Reactors and Characterization.	94
5.3. Performance of Catalytic La ₂ O ₃ -CeO ₂ Nanofiber Fabrics.	95
5.4. Effects of Catalyst Composition and Nanofiber Diameter.....	101
5.5. Characterization Studies.....	104
5.6. Summary.	107
Chapter 6. OCM Using La₂O₃-CeO₂ Fabrics: Reaction Engineering Aspects.....	109
6.1. Nanofiber Catalyst Synthesis by Electrospinning.....	109
6.2. Catalytic Performance Evaluation and Temperature Profiling.	110
6.3. Nanofiber Fabric Imaging.	111
6.4. Feed temperature hysteresis.	112
6.5. Effect of feed flow rate and CH ₄ /O ₂ ratio.	114
6.6. Effect of bed depth and space velocity.....	119
6.7. Time on stream.....	121
6.8. Summary.	126
Chapter 7. Direct In-Situ Spatial Concentration and Temperature Profiling and OCM Reactors of Multiple Fixed Beds.	127

7.1. Reactor Setup.	127
7.2. Acquisition of Spatial Profiles.	128
7.3. Spatial Profiles on a Single Fixed Bed Catalytic Reactor.....	131
7.4. Spatial Profiles on a Dual Fixed Bed Catalytic Reactor.	139
7.5. Summary.	148
Chapter 8. Examining the Transition from OCM to the Catalytic Partial Oxidation of Methane Using Spatial Profiles.	150
8.1. Electrospun Fabric Synthesis and Reactor Setup.	150
8.2. Acquisition of Spatial Profiles.	151
8.3. Characterization Studies.....	152
8.4. Reaction Studies.....	155
8.5. Summary.	162
Chapter 9. Spatial Profiles in RuO₂-CuO-NaCl/SiO₂ Packed-Bed Propylene Epoxidation Reactors.....	164
9.1. Reactor System and Powder Catalyst Used.	164
9.2. Acquisition of Spatial Profiles.	165
9.3. Spatial Profiling Results in Nanoparticle-Based Propylene Epoxidation Catalytic Reactors.....	167
9.4. Summary.	176
Chapter 10. Simulation of Oxygen Vacancies on La₂O₃-based Surfaces Using Quantum Espresso.	178
10.1. Motivation Behind Simulating Oxygen Vacancies.....	178

10.2. Quantum ESPRESSO Simulation Procedure.....	181
10.3. Simulated Oxygen Vacancies and Structural Changes.....	182
10.4. Summary.....	190
Chapter 11. Conclusions.....	191

ACKNOWLEDGEMENTS

I would like to thank my advisor, Professor Selim Senkan, for his guidance, support and respect; without him, this work would not have been possible. I can similarly say the same for my current coworker Bahman Zohour, whose contributions to the group's projects were critical in all aspects. I acknowledge past students in our group, Professor Anusorn "Nu" Seubsai, Aaron Miller and Dr. Michael Kahn for their help, all of whom especially helped in my initial training in catalysis research. I also thank Anthony Plauck and Daniel Goodman for their assistance in the electrospinning process.

Additionally, I acknowledge collaborators from outside of the Senkan laboratory. Our colleagues from the group of Professor Yunfeng Lu, especially Xiaolei Wang, Fang Liu, Huihui Zhou and Li Shen, assisted us in both BET surface area and x-ray diffraction characterizations. I also thank Hang Yu from the group of Professor Robert Hicks for his help, especially in XPS analysis and Michael Yeung of Professor Richard Kaner's group for his assistance in materials chemistry aspects of the work. I thank Walter Liao of Professor Andrea Kasko's group for being my colleague during the biomaterials electrospinning project that aided our nanofiber pursuits. I also thank Dr. Raffaella D'Auria for her assistance with density functional theory studies.

Lastly, I acknowledge NSF IGERT Materials Creation Training Program (MCTP – DGE-0654431, the California NanoSystems Institute (CNSI) and UCLA for support.

VITA

B. Sc. Chemical Engineering 2010

Department of Chemical and Biomolecular Engineering, University of California, Los Angeles (UCLA)

Henry Samueli School of Engineering and Applied Science (HSSEAS)

Materials Creation Training Program (MCTP) Fellowship 2011 – 2013

National Science Foundation Integrative Graduate Education and Research Traineeship (NSF-IGERT)

Teaching Associate and Fellow 2013 – 2015

Fall 2013, Winter 2014, Spring 2014, Fall 2014, Spring 2015

UCLA Department of Chemical and Biomolecular Engineering

PUBLICATIONS

A. Seubsai, D. Noon, T. Chuksaw, B. Zohour, M. Charoenpanich, S. Senkan. Epoxidation of Propylene to Propylene Oxide with Molecular Oxygen over $\text{Sb}_2\text{O}_3\text{-CuO-NaCl/SiO}_2$ Catalysts. In press, *Journal of Industrial and Engineering Chemistry*.

D. Noon, B. Zohour, S. Senkan. Oxidative Coupling of Methane with $\text{La}_2\text{O}_3\text{-CeO}_2$ Nanofiber Fabrics: A Reaction Engineering Study. *Journal of Natural Gas Science & Engineering* 18, 406-411 (2014).

B. Zohour, D. Noon, S. Senkan. Spatial Concentration and Temperature Profiles in Dual-Packed-Bed Catalytic Reactors: Oxidative Coupling of Methane. *ChemCatChem* 6, 2815-2820 (2014).

B. Zohour, D. Noon, A. Seubsai, S. Senkan. Spatial Concentration Profiles in Packed Bed Propylene Epoxidation Reactors. *Industrial & Engineering Chemistry Research* 53, 6243-6248 (2014).

B. Zohour, D. Noon, S. Senkan. New Insights on the Oxidative Coupling of Methane from Spatially Resolved Concentration and Temperature Profiles. *ChemCatChem* 5, 2809-2812 (2013).

D. Noon, A. Seubsai, S. Senkan. Oxidative Coupling of Methane by Nanofiber Catalysts. *ChemCatChem* 5, 146-149 (2013).

PRESENTATIONS

D. Noon, B. Zohour, S. Senkan. *Oxidative Coupling of Methane by Nanofiber Fabrics. Oral Presentation*, at 24th North American Catalysis Society Meeting (NAM 24). Pittsburgh, PA. Richard J. Kokes Travel Awardee.

D. Noon, B. Zohour, S. Senkan. *Oxidative Coupling of Methane by La₂O₃-CeO₂ Nanofiber Catalysts. Oral Presentation*, 2013 American Institute of Chemical Engineers (AIChE) Annual Meeting. San Francisco, CA.

D. Noon. *Metal Oxide Nanofiber Catalysts. Oral Presentation*, 2013 UCLA Materials Creation Training Program (MCTP) Symposium. California NanoSystems Institute (CNSI), Los Angeles, CA.

Chapter 1. Introduction.

The discovery of materials that function as high performing heterogeneous catalysts is the subject perpetual academic and industrial research. Most commercialized catalysts are composed of nanoparticles, or quasi-spherically shaped structures of diameters ranging approximately from 1 – 20 nm [1, 2]. At the macroscopic scale, such materials take on the appearance of powders and are synthesized by well-established and scalable techniques like impregnation and co-precipitation. The ease of production of these materials is what principally makes them attractive and the success of industrial heterogeneous catalysis can largely be attributed to the existence of powder catalysts. However, nanoparticles do not necessarily confer the ideal nanostructure for optimizing catalytic performance for all reactions of industrial interest [1, 3, 4]. In many cases, they may in fact be the least attractive option. The route this work focuses on in creating superior performing catalysts is through the fine tuning of a catalyst's nanostructure. Specifically, catalysts in this work are primarily fabrics of long, quasi-cylindrically shaped nanofibers composed of metal oxides and synthesized by electrospinning. These fabrics are utilized in reactions in which hydrocarbon based reactants are transformed into products of higher oxidation states but without full oxidation (i.e. partial oxidation reactions): namely, the oxidative coupling of methane (OCM), propylene epoxidation and the catalytic partial oxidation (CPO) of methane. Their catalytic performance assessments are compared to that of powder catalysts to assess their viability for future use on an industrial platform.

Reactions in which a hydrocarbon is partially oxidized by molecular oxygen pose extraordinary challenges in industrial catalysis because the most thermodynamically favorable product of an entire reaction scheme is carbon dioxide, which provides little economic value. Partially oxidized hydrocarbons also often have exceptional economic utility because they can be utilized in a wide variety of subsequent reactions that lead to consumer products. In other words, they are valuable chemical intermediates. The key role of a catalyst here is to both *produce* the economically valuable partially oxidized hydrocarbon and isolate it from being *further oxidized*. The problem is that the catalysis responsible for the chemical intermediate's production also tends to lead to its destruction, a near catch-22. Hence, the creation of catalysts of alternate morphologies, with precisely tuned features, and used for such applications is an attractive route for both furthering the performance of existing industrial catalysts and, more importantly, discovering catalysts that are capable of bringing novel processes from laboratory scale to the commercial marketplace.

This dissertation, a summary of the author's search for electrospun nanofiber fabrics that establish new levels for what is considered state of the art performance in the aforementioned reactions, consists of eleven chapters. This first chapter constitutes an overview of the research problem. The second covers prior relevant research in heterogeneous catalysis, with emphasis on synthesizing catalysts of various architectures and background information on the three reaction schemes targeted in the research. The third chapter covers the author's initial research into propylene epoxidation using classical co-impregnated powder catalysts. The fourth focuses on the research's transition toward

using electrospinning in fabricating nanofiber catalysts and their initial use in propylene epoxidation. The fifth documents the research's transition to pioneering the use of electrospun nanofibers for OCM and constitutes the most substantial milestone of this work. The material most commonly used in the OCM research as the catalyst is a La_2O_3 - CeO_2 nanofiber fabric. The sixth highlights reaction engineering follow-up studies done on this fabric. The seventh chapter documents the research's in-situ concentration and temperature spatial profiling technique discovery and its application towards OCM in both single and dual bed catalytic reactors loosely packed with nanofiber fabric catalysts. The eighth discusses utilizing the profiling method to analyze the transition from OCM to methane CPO by incrementally doping the La_2O_3 - CeO_2 fabric with Ir. The ninth documents spatial profiling work done in propylene epoxidation reactors with powder catalysts. The tenth discusses density functional theory studies on various dopants used on La_2O_3 surfaces and their effects on the tendency for neighboring oxygen atom vacancies to form. Lastly, the eleventh chapter summarizes the findings of this work.

Chapter 2. Background.

This chapter comprises a literature survey of topics relevant to the research. The motivation behind using nanofiber fabrics as novel catalytic materials is covered as well as all the reaction schemes investigated. The electrospinning process is also a critical focus of this section.

2.1. Research in Heterogeneous Catalysis.

Much of the modern day standard of living in first and second world civilizations can be attributed to the development of high performing industrial catalytic processes that function as key elements in the production lines of various consumer products. Internationally, about 80% of chemical processes depend on catalysts, most of which are of the heterogeneous type; consequently, catalysts contribute at least indirectly towards 35% of the international gross domestic product [5]. It has been estimated that 60% of the production of chemicals involves the use of catalysts and that catalyst manufacture is an industry of about \$10 billion per year in revenues, mostly serving the market segments of refining, polymerization and environmental processes [6]. Clearly, economies across the globe have become strongly dependent on catalytic processes and advancements in the standard of living in many parts of the world can be attributed to catalysis [6-8]. Additionally, since catalytic processes are typically more environmentally friendly than non-catalytic analogues, there is a strong driving force for the continuous research and development of new catalytic processes and improvements of old ones, especially in a

context where pollution is a concern of scientists, political leaders and the general public [9].

In the U.S., catalysis research has a strong history, along with other fundamental subareas of chemical engineering, such as transport phenomena, separations and reactor design [10]. However, a 2007 study by the National Research Council, analyzing measures such as journal publications, citations, patents, awards and funding, suggests that these areas, especially heterogeneous catalysis, are weakening academically in the U.S. relative to other countries due to a shift in federal funding to other research areas and a decrease in relevant academia-industry partnerships [10]. Despite these shortcomings, there have nevertheless been significant advances in heterogeneous catalysis in the past 10-15 years, including the development of efficient hydrodesulfurization catalysts for industrial fuels and the creation of combinatorial and high-throughput methodologies to facilitate the rapid discovery of promising materials [10].

This work focuses on gas phases reactions that utilize catalysts of solid materials, the most prominent subset of *heterogeneous* catalysts in which the material's state of aggregation is different than that of the compounds participating in the overall reaction. Partial oxidation reactions are of particular interest because they create chemical intermediates of high economic value to the processing industries. They also pose challenges because compounds that are intermediate partial oxidation products of a sequence of reactions are difficult to isolate. The presence of an oxidant in the feed mixture leaves the chemical intermediate exposed to potential further oxidation, ultimately to CO₂.

Effective catalytic materials need to have high activity but shut off deep oxidation routes, posing one of the greatest tasks in heterogeneous catalysis research.

2.2. Tuning the Architecture of Heterogeneous Catalysts.

The size, morphology and spatial composition of a heterogeneous catalyst all may have dramatic influences on activity and selectivity; hence, they are critical factors to consider when choosing a synthesis method for preparing a material. Shown in Figure 2.1 are sketches of the same general type of metal cluster but with varying sizes, from 13 atoms up to 561 atoms [11, 12]. In the smallest case, the 13 atom cluster has 92% of its structure externally exposed while the 561 atom cluster has 45%. Suppose these metal clusters have some catalytic value and every atom in all of the clusters is of the same element. Reacting gases or chemical intermediates may adsorb onto the surface of a given cluster as part of a catalytic reaction. Since each cluster has a different surface morphology, the degree and nature of the catalysis that occurs may differ substantially from cluster-to-cluster, despite the fact that they all have identical elemental compositions, by altering adsorbate-adsorbent interactions both geometrically and electronically.

Figure 2.2 shows turnover frequencies for reactions relevant to the epoxidation of propylene by molecular oxygen using two silver based catalytic materials [13]. In the left plot, the catalyst used has active sites each comprising merely three atoms of silver deposited on an aluminum substrate by size filtering laser fired metal clusters using quadrupole mass spectrometry. In the right, the catalytically active sites are 3.5 nm nanorod (2 nm height, 4 nm diameter) aggregates of silver trimers synthesized by intentionally

sintering the original catalyst at 200 °C. Over most temperatures, the total turnover rate to product, and thus the propylene conversion per catalyst weight, is higher for the silver trimer. This is typical because the silver trimer has a much higher surface area-to-volume ratio than the silver nanoparticle; hence, a larger percentage of silver atoms are able to directly participate in catalysis. However, the selectivity and yield to propylene oxide, the target compound, is the best with the silver nanoparticle-based catalyst, especially at ~100 °C. Nanoparticle silver-based catalysts synthesized by traditional methods (e.g. impregnation) are substantially lower performing than both the trimer and aggregates [14-16]. Density functional theory (DFT) simulations suggest that this is due to the dominant presence of the Ag(111) crystal plane on nanoparticles versus an open-shell electronic structure for silver trimers that is highly reactive with the propylene double bond, causing the epoxidation mechanisms for the two structures to have significant intrinsic differences [13].

Shown in Figure 2.3 is a comparison of the catalytic performance of various silver-based structures for the epoxidation of ethylene by O₂ [3, 4]. Silver nanowires are almost uniformly superior to silver spheres, synthesized by incipient wetness impregnation on an α -Al₂O₃ support, for ethylene oxide selectivity over the range of feed O₂ concentrations and conditions examined. However, in particular, the larger silver nanowires of 125 nm are the best catalysts. In a manner similar to the previous study on propylene epoxidation catalysts with silver-based materials, a concurrent DFT study found the Ag(100) crystal plane was more selective for epoxidation than Ag(111) by enhancing the conversion of the oxametallacycle intermediate to ethylene oxide [3]. The exterior surfaces of nanowires are

enriched in Ag(100), offering some explanation to their superior performance [1]. On a more qualitative level, nanowires or nanofibers are cylindrically shaped structures, which, by nature, have less steep curvature than spheres of the same diameter due to the linear extension of the circular cross-section. This type of “softer” structure is shown to be effective at isolating epoxide intermediates that are susceptible to further combustion in both ethylene and propylene epoxidation. Also, as shown in Figure 2.3, larger sizes likewise have “softer” curvatures and are also more effective for epoxidation, whether using quasi-spherical nanoparticles or quasi-cylindrical nanofibers. Hence, it follows that the use of nanofibers or similarly structured materials may be a plausible route for the catalysis of a broad range of partial oxidation reactions.






Full-Shell "Magic Number" Clusters					
Number of shells	1	2	3	4	5
Number of atoms in cluster	M ₁₃	M ₅₅	M ₁₄₇	M ₃₀₉	M ₅₆₁
Percentage surface atoms	92%	76%	63%	52%	45%

Figure 2.1. Illustration of the structural surface changes that occur as a nanoparticle’s size is increased [11, 12].

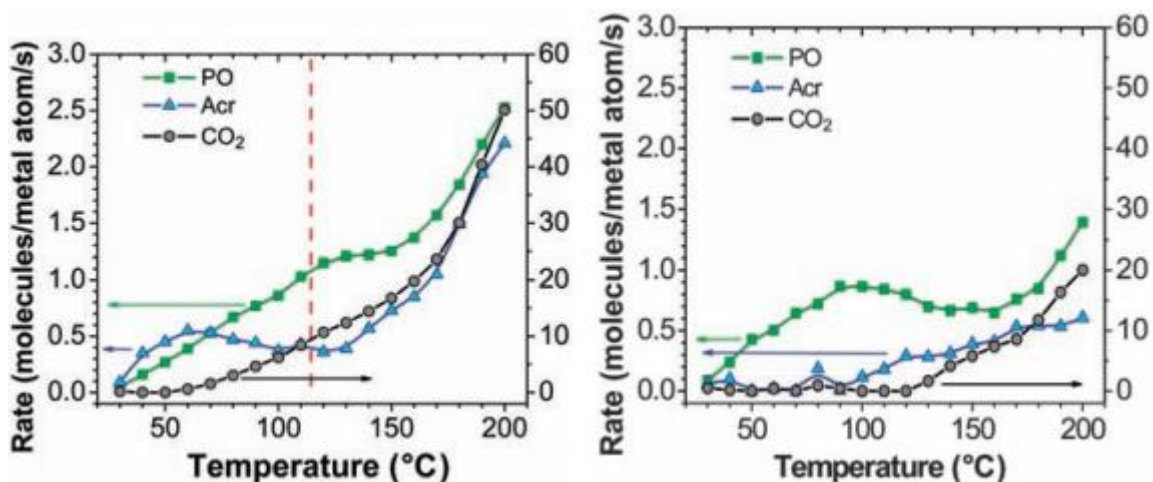


Figure 2.2. Turnover rates to propylene oxide (PO), acrolein (Acr) and CO₂ for the direct epoxidation of propylene by molecular oxygen utilizing a silver trimer catalyst (left) and a 3.5 nm silver nanoparticle catalyst (right) [13].

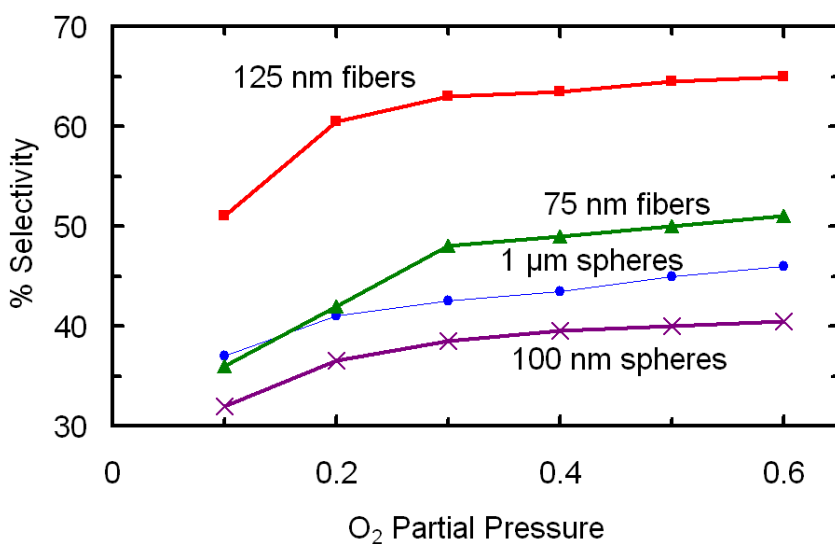


Figure 2.3. Performance comparison of silver ethylene epoxidation catalysts composed of nanofibers and nanoparticles of varying diameters [4].

2.3. Electrospinning and Catalytic Nanofiber Fabrics.

Electrospinning is a nanofiber fabrication technique studied and implemented by researchers in many fields, including separations, biotechnology and semiconductors. The

experimental process involves drawing out a solid polymeric fiber from a viscous liquid by applying an electric field. Electrospun fibers have an immensely wide range of applications. For example, polymeric fibers produced by electrospinning have been used to increase the strength of composite materials [17]. The mechanical strengths of rubber films have been enhanced by incorporating electrospun poly(benzimidazole) into the film while electrospun Nylon has been shown to increase the stiffness and mechanical strength of epoxy resins [17-19]. Nanofibers made by electrospinning have also been used successfully in filtration systems due to a high resistance to air convection, low resistance to water vapor transport and an excellent ability to capture aerosols [17, 20]. For tissue engineering and more specifically for tissue growth, it is necessary to make synthetic scaffolds similar to natural ones in terms of composition, morphology and surface groups [17, 21]. Electrospinning has been used previously to construct biopolymers for use as scaffolds successfully due to the experimental technique's ability to yield interconnected porous structures with large and controllable surface areas [17, 22-25]. Due to their high specific surface areas, electrospun polymeric nanofibers have also been used for delivery of therapeutics [17, 26, 27]. Other applications exist, such as electronics, optoelectronics and sacrificial templates for the production of nanofluidic channels and mechanical oscillators, clearly illustrating the versatility of electrospinning [17].

Needless to say, the critical electrospinning application of concern here is catalysis. Electrospun polymeric nanofibers have favorable sizes and surface areas shown in many cases to yield improvements in catalytic activity as support materials for both traditional catalysts and enzymes compared to materials synthesized by traditional methods [17].

Enzymes have previously been attached to electrospun nanofibers made of materials such as polystyrene, polyethylene oxide and polyvinyl alcohol, to yield manifold increases in reactivity [17, 28, 29]. It has been shown that catalysts for the selective hydrogenation of dehydrolinalool made by incorporating palladium onto electrospun nanofibers were 4.5 times more active than the standard palladium on Al₂O₃ powder catalyst [17, 30]. These facts in conjunction with the advantages nanowire structures have displayed in ethylene epoxidation, electrospun nanofibers may thus accordingly offer advantages as catalysts in a broad range of reactions.

The use of fibers in heterogeneous catalysis dates back to as early as 1980, when methane combustion was investigated over platinum-alumina fibers, of 2-5 μm diameters, synthesized using a solution-based method [31-33]. Catalysts of nanometer diameter fibers were first proposed in 2005 but were not commercializable because the electron beam lithography technique used to fabricate them was expensive [34]. In addition to different exposed crystal facets, nanofibers can effectively ameliorate metal dispersion problems associated with impregnated and co-precipitated powders, giving reactant gases easier access to larger numbers of active sites. Additionally, sintering should be less of an issue with fibers than nanoparticles since they are lower surface energy structures, thus giving more durable catalysts of reliable and predictable performance characteristics.

In electrospinning, a viscoelastic polymeric liquid is pumped continuously through a fine needle that is under high voltage and is facing an electrically grounded collector nearby [17, 35-37]. As shown in Figure 2.4, in order to produce long, straight fibers, this voltage, along with the viscoelasticity of the solution, must be high enough to overcome

the competing force provided by the liquid-air surface tension, which is a driving force for the formation of spherical droplets, i.e. electrospray [38]. The solution's viscoelasticity essentially serves as evidence of polymer chains being entangled with each other in solution [39]. This entanglement, coupled with the stretching motion caused by the voltage gradient, may allow for straight, cylindrically shaped fibers to be formed. The high voltage applied at the needle creates charges that stimulate the jetting of the liquid towards the grounded collector. During the flight of this liquid jet, the solvent evaporates due to convection. With a sufficiently large distance between the needle and collector, the jet evaporates completely and the fiber lands on the grounded collector as a solid and gets neutralized.

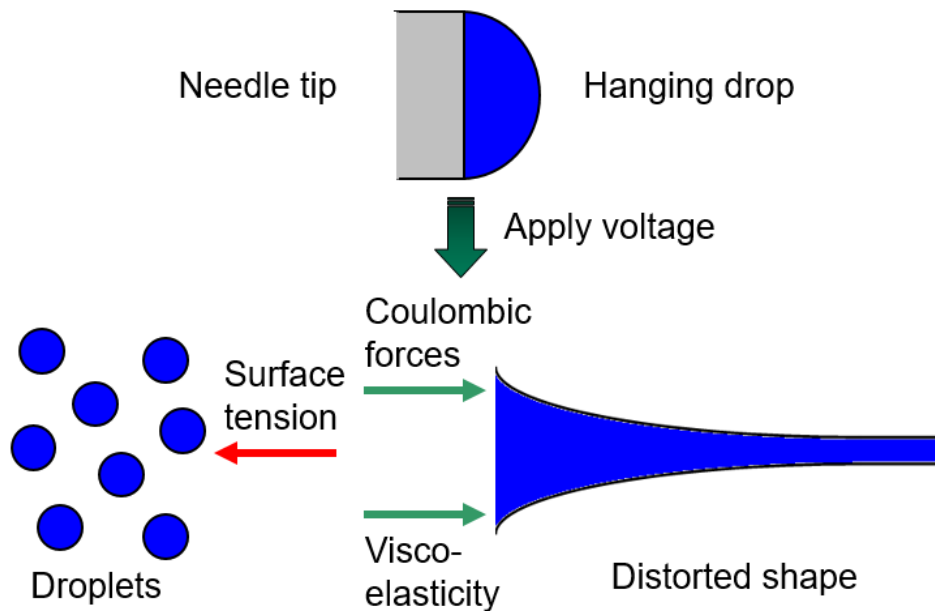


Figure 2.4. Application of a sufficiently high voltage to the needle in electrospinning creates a conical shape (Taylor cone; right) as opposed to electrospray droplets (left) for solutions of adequate viscoelasticity.

In the production of metal oxide fibers, the aforementioned polymeric liquid is also loaded with soluble metal salts [40]. This part of the spinning process probably is the most challenging because of the need to fulfill several competing requirements for spinnability. Also, the presence of a metal salt within the polymeric liquid causes a dramatic increase in the solution's conductivity which can complicate the spinning procedure.

The nanofiber fabric collected during electrospinning is transferred to an oven and calcined at temperatures high enough to burn off the polymer template and create metal oxides. As shown in Figure 2.5, the fibers formed when electrospinning a solution of metal salt and polymer template (i.e. prior to calcination) have previously been suggested to be of core-shell morphology, with the metal salt in the core and the polymer as the shell [41].

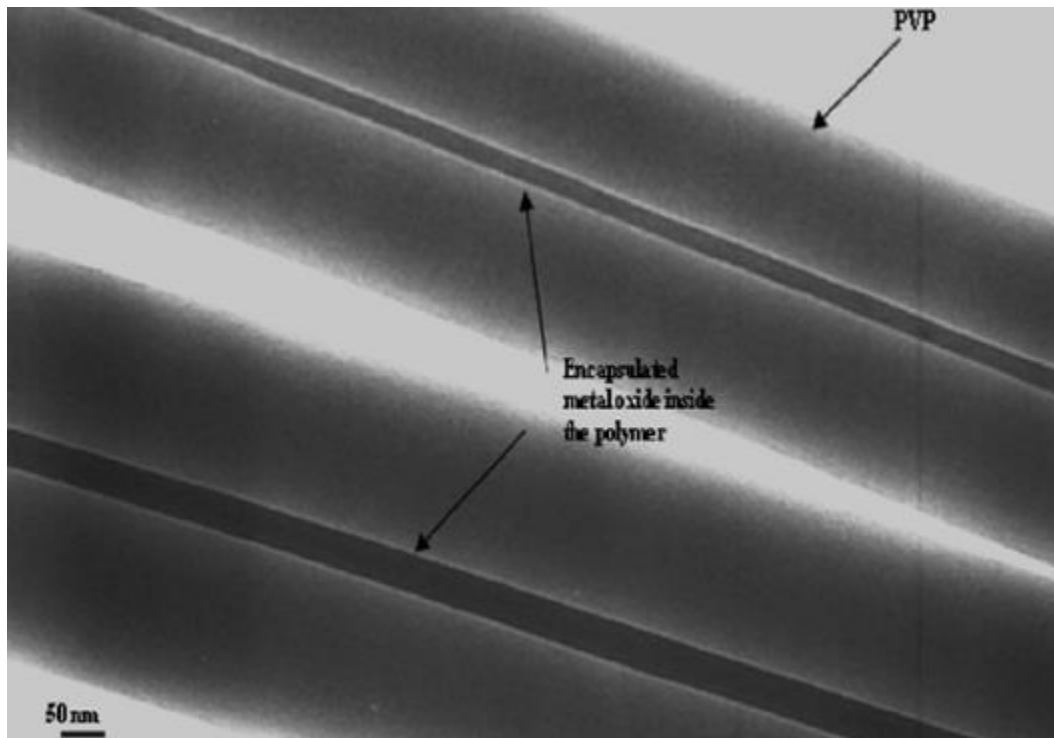


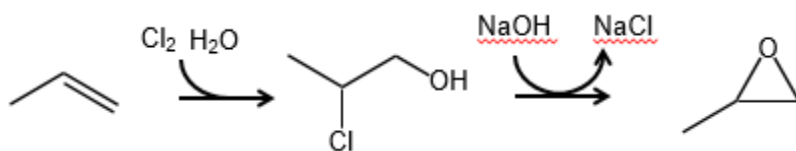
Figure 2.5. Co-spun nanofiber of polyvinylpyrrolidone (PVP) and molybdenum metal salt [41].

2.4. Propylene Epoxidation.

2.4.1. Propylene Oxide (PO) and its Established Means of Production.

Propylene oxide (PO) is a critical intermediate used in the chemical process industry and, accordingly, whose derivatives have utility in a wide range of consumer products [42-44]. A majority of PO (60-70%) is converted to polyether polyols and subsequently utilized as polyurethane foams and plastics. PO can also be hydrolyzed into propylene glycol, which has applications in antifreeze products and as a moisturizer foundation. PO is industrially produced by methods that can be divided into three classes: the chlorohydrin, hydroperoxide and co-product processes. Each of these has major caveats that drive research into developing alternative routes.

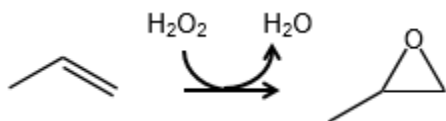
The chlorohydrin process involves reacting propylene with hypochlorous acid to create 1-chloro-2-propanol and 2-chloro-1-propanol, which are subsequently dehydrochlorinated using a basic aqueous solution of $\text{Ca}(\text{OH})_2$ to produce PO with an impressive 88-96% selectivity:



The key drawback of the process is that environmentally hazardous byproducts are produced, namely chlorinated hydrocarbons that function as major greenhouse gases and CaCl_2 waste. The latter is produced in massive quantities, about forty times that of PO, and

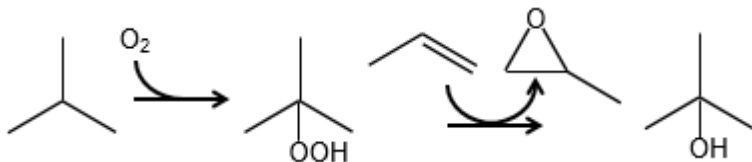
contains hydrocarbon side products that are challenging to separate. While commercialized, the environmental disadvantages of the chlorohydrin process have eliminated its consideration in the construction of new plants [43].

The catalytic transformation of propylene to propylene oxide can be accomplished via indirect oxidation, in which the oxidant is a hydroperoxide-type compound. The premier example of this is the proprietary Hydrogen Peroxide-Propylene Oxide (HPPO) technology developed by Dow Chemical and BASF [43, 45]:

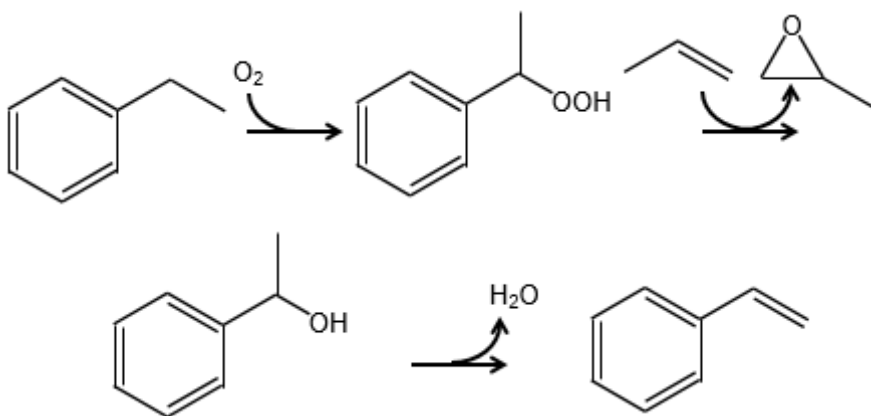


The environmental hazards associated with the chlorohydrin process are effectively eliminated here. However, the largest drawback of HPPO is the costly need for a separate plant that produces highly concentrated H₂O₂ solutions [46]. Another variation of this method of PO production, employed by Sumitomo Chemical, uses cumyl hydroperoxide as the oxidant and similarly avoids the pitfalls of the chlorohydrin route [43]. However, this process suffers from poor conversion and accordingly requires the separation and recycle of large amounts of unreacted propylene.

The co-product class for PO production consists of two specific commercialized routes. The first involves oxidizing ethylbenzene with molecular oxygen, with the end products being PO and styrene as a co-product [46]:



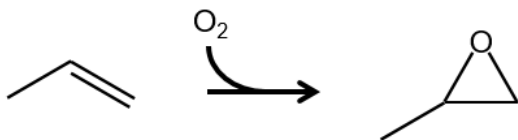
The second likewise entails oxidizing isopropane, with tert-butyl alcohol instead as the co-product [42]:



The epoxidation step in either process needs a homogeneous molybdenum, tungsten or vanadium catalyst or titanium-based heterogeneous catalyst [46]. Both processes have the advantage of >95% propylene conversion but suffer from the creation of large amounts of co-products whose levels of demand are not comparable with that of PO.

2.4.2. Direct Catalytic Epoxidation of Propylene Using Molecular Oxygen.

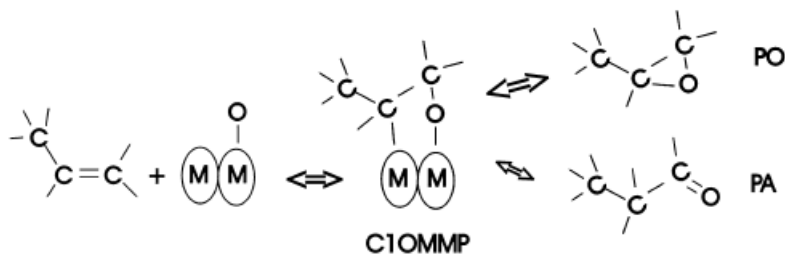
Caveats with the previous established methods of PO production trigger research into the direct catalytic epoxidation of propylene by molecular oxygen:

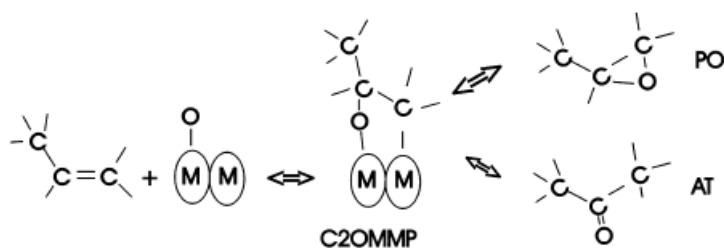


Superficially, this is the simplest route but suffers from its own problem that research has failed to solve: poor catalytic performance. The epoxidation of *ethylene* is done industrially by this direct route using a $Ag/\alpha-Al_2O_3$ -based catalytic system in which ethylene yields in

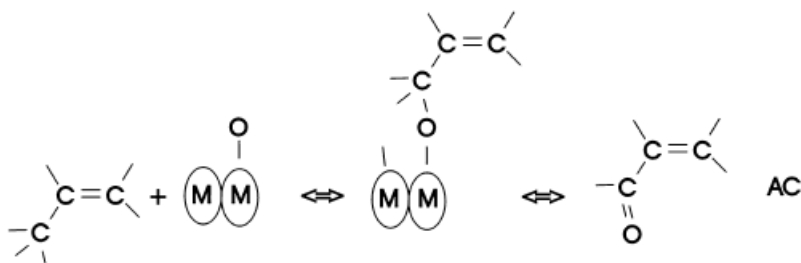
optimized reactors can reach 80% [44, 47-49]. Similar catalysts utilized in *propylene* epoxidation reactors vastly underperform, and it is generally understood that the epoxidation of propylene is far more challenging than that of ethylene due to the formation of an unstable allyl radical that readily undergoes combustion [44, 50-52]. Hence, arguably the greatest task in catalysis research here is the discovery of an active catalyst that selectively shuts off the allyl radical's formation.

Besides PO, the partial oxidation of propylene can also form acetone (AT), acrolein (AC), propionaldehyde (propanal, PA), acetaldehyde (AA) and formaldehyde (FA), together with the deep oxidation products CO and CO₂. PO is believed to occur via the formation of an oxametallacycle propylene intermediate (OMMP, where M represents a general surface metal atom) similar to that proposed for ethylene epoxidation [53-55]. However, the presence of the methyl group in propylene results in the formation of two distinct OMMP structures, which lead to different products. For example, C1-OMMP formation (i.e., surface O is bonded to the =CH₂) can directly form PO by cyclization and, via C1 to C2 H atom transfer, PA. Similarly, C2-OMMP formation (i.e., surface O is bonded to the =CHCH₃) can also produce PO and, via C2 to C1 H atom transfer, AT. These OMMP structures and plausible subsequent reactions are:

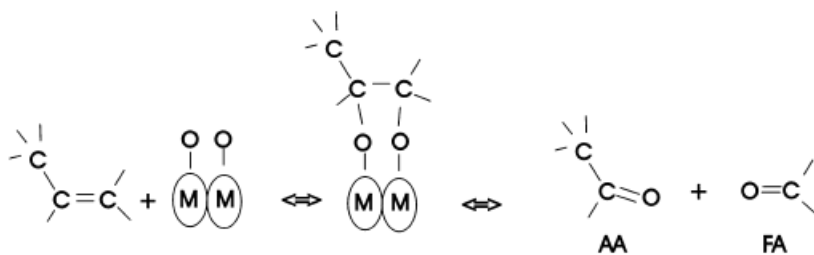




Based on this representation, the relative amounts of PA and AT produced can indicate the dominant OMMP structure expected to be present in a given catalytic system. On the other hand, the formation of AC requires O insertion into the methyl group (C3) of propylene, which is an entirely different pathway, and, as such, could involve a different surface metal atom M:



It should be recognized that the products PO, AT and PA can also undergo subsequent isomerizations and related reactions [56]. Similarly, the formation of CH₃CHO and HCHO could be taken into account by the formation of a C1OMMOC2 structure:



Propylene, as well as all partial oxidation products, can undergo further oxidation reactions, ultimately forming CO₂ and H₂O.

2.5. Oxidative Coupling of Methane (OCM).

2.5.1. Motivation Behind Utilizing the Methane in Natural Gas.

The direct utilization of methane, the main component of natural gas (NG), as an alternate chemical feedstock to petroleum, has been a highly desirable but difficult goal in industrial catalysis [57]. Many direct and indirect methods have been proposed and studied to convert CH_4 into more useful products, including olefins (e.g. C_2H_4 , C_3H_6), higher molecular weight hydrocarbons and transportable liquids (e.g. benzene and gasoline), as discussed in a recent review [57]. The production of ethylene (C_2H_4) from NG represents a particularly significant opportunity, because of its massive worldwide use as an intermediate in the production of plastics, such as polyethylene and polyvinyl chloride (PVC). In addition, ethylene can be oligomerized into liquid hydrocarbons, such as alpha olefins, thereby enabling the efficient utilization of natural gas in remote parts of the world. The global production rate for ethylene is over 130 million tons per year, representing an annual business in excess of \$150 billion (2013).

The economic feasibility of using natural gas instead of crude oil for this purpose depends on the relative prices of the two feedstocks and the efficiency of the available refining processes. Discoveries of new natural gas reserves at the turn of the decade, especially domestically, triggered a heightened global focus towards commercializing methods that transform methane into ethylene. The production of ethylene using natural gas is favored by low prices of natural gas relative to oil and the high sale prices of ethylene's refined consumer products. Although the more recent precipitous fall in the

price of oil has made this route less attractive for the time being, the development and availability of technologies that allow for the transformation of natural gas into value added products nevertheless adds a novel dimension to the capabilities of the chemical processing industry.

2.5.2. Naphtha Steam Cracking for Ethylene Production.

At present, ethylene is primarily produced by the steam cracking of naphtha, a petroleum product typically composed of C₅-C₁₂ hydrocarbons [58]. In this technique, naphtha is put through a high-temperature (~850 °C), non-catalytic process that breaks these high-order hydrocarbons into smaller ones (e.g. C₂-C₅). This step is extremely energy intensive, produces large quantities of CO₂ and consumes chemicals that have value in other applications (e.g. jet fuel). A process diagram of cracking and separation of the various hydrocarbons involved is shown in Figure 2.6 while that of the cracking furnace alone is in Figure 2.7 [59, 60].

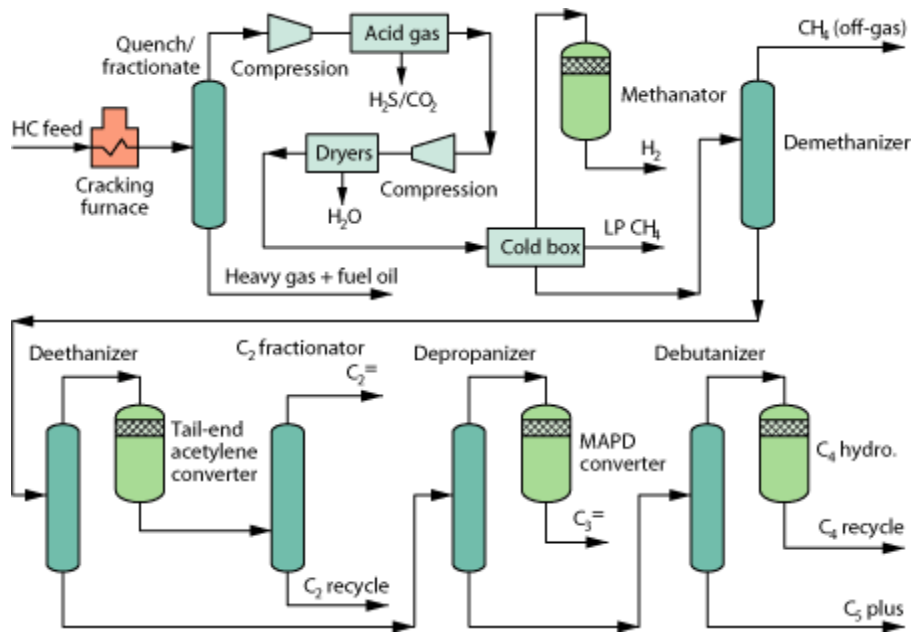


Figure 2.6. Typical cracking process, including downstream separation steps, for ethylene production [59].

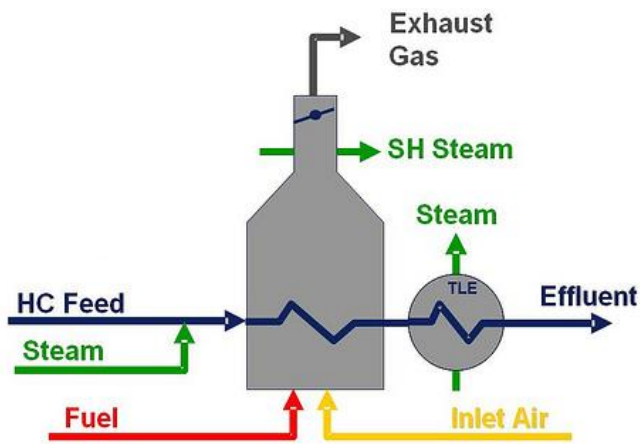
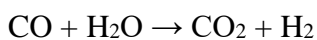
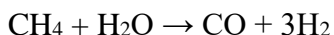


Figure 2.7. Schematic of a cracking furnace [60].

2.5.3. Indirect Routes for Natural Gas Utilization.

All indirect NG conversion routes utilize the high temperature, endothermic and costly steam reforming as a first step, in which the target product is synthesis gas (H₂/CO mixtures) [57, 61]. Methane steam reforming generally involves two reactions, the second of which is water gas shift:



The creation of H₂/CO is followed by the synthesis of useful liquid products via various catalytic processes, two of which have been developed into full commercial scale operations: methanol-to-gasoline (MTG) and Fischer-Tropsch (FT) [57, 61].

In the MTG route, developed by Mobil, CO/H₂ mixtures are first converted to methanol using a catalyst comprising copper, zinc and alumina. Using zeolite-based catalysts, the methanol is then dehydrated to dimethyl ether and then ethylene, which is polymerized to produce gasoline. Typical catalysts used for NG conversion to higher order hydrocarbons with Fischer-Tropsch are zeolite-supported cobalt-based materials. This has been employed in Qatar by Shell and also in Sasol and PetroSA in South Africa. Also, in addition to its utility in NG conversion, Fischer-Tropsch is used on syngas produced by the gasification of solid carbon-based materials (e.g. coal); however, in this case, iron-based catalysts are used. MTG has also more recently been employed utilizing coal feedstocks by ExxonMobil in China.

Although direct methods for methane upgrading avoid use of costly syngas steps, they remain uneconomical due in part to low C₂₊ yields, high temperatures and low throughputs. High temperatures are particularly detrimental since they result in catalyst deactivation and create materials problems for reactors.

2.5.4. Oxidative Coupling of Methane for Direct Ethylene Synthesis from Natural Gas.

The oxidative coupling of methane (OCM) scheme is shown in Figure 2.8 [62]. The reactions involving stable chemical species, along with reaction enthalpies and Gibbs-free energy changes, both calculated at approximately 500 °C, are [63]:

	ΔH_{rx} (kJ/mol)	ΔG_{rx} (kJ/mol)
$2\text{CH}_4 + 4\text{O}_2 \rightarrow 2\text{CO}_2 + 4\text{H}_2\text{O}$	-1600	-1600
$2\text{CH}_4 + 0.5\text{O}_2 \rightarrow \text{C}_2\text{H}_6 + \text{H}_2\text{O}$	-175	-135
$2\text{CH}_4 + 3\text{O}_2 \rightarrow 2\text{CO} + 4\text{H}_2\text{O}$	-1035	-1175
$2\text{CO} + \text{O}_2 \rightarrow 2\text{CO}_2$	-565	-425
$\text{C}_2\text{H}_6 + 0.5\text{O}_2 \rightarrow \text{C}_2\text{H}_4 + \text{H}_2\text{O}$	-40	-165
$\text{C}_2\text{H}_4 + 2\text{O}_2 \rightarrow 2\text{CO} + 2\text{H}_2\text{O}$	-820	-875
$\text{C}_2\text{H}_4 + 2\text{H}_2\text{O} \rightarrow 2\text{CO} + 4\text{H}_2$	170	-60
$\text{C}_2\text{H}_6 \rightarrow \text{C}_2\text{H}_4 + \text{H}_2$	205	35
$2\text{CO} + 2\text{H}_2\text{O} \leftrightarrow 2\text{CO}_2 + 2\text{H}_2$	-75	-20

The selective route involves CH₄ being *directly* converted to C₂H₆, C₂H₄ and H₂O in the presence of O₂ and a suitable catalyst [57]. The first step involves the abstraction of H from

CH₄ by the catalyst to form methyl radicals (CH₃•) [64, 65]. The coupling of two CH₃• then creates C₂H₆, followed by its dehydrogenation to C₂H₄. Some C₃ hydrocarbons also form by addition of CH₃• to C₂H₄ [66]. However, undesirable surface and gas phase combustion reactions also lead to CO and CO₂ (CO_x). Since high temperatures promote homogeneous gas phase free radical reactions detrimental for C₂₊ products, the development of new catalysts that can operate at low temperatures is crucial for the economic viability of OCM [57, 64].

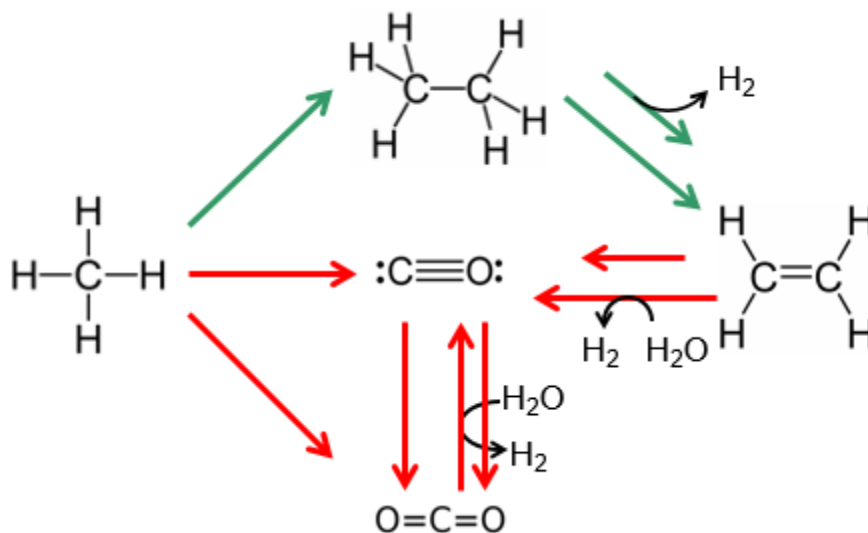


Figure 2.8. The oxidative coupling of methane (OCM) reaction scheme, with both target (C₂H₆ and C₂H₄) and side product (CO, CO₂) traditional synthesis routes [62].

Since the pioneering works of Keller and Bhasin, Hinsen and Baerns and Ito and Lunsford, OCM has received immense global attention, as evidenced by the large number of catalysts investigated [64, 67-69]. OCM catalysts comprising the oxides of virtually all metals on the periodic table, individually or their combinations, have been considered and analyzed recently [64]. Even the best catalysts are reported to require *feed gas temperatures*

(T_f) of 700-850 °C and reaction times of 0.2-5.5 s, with C_{2+} yields less than 25% [64]. Prior research on OCM catalysis essentially involved *quasi-spherically shaped nanoparticles*, concomitant with problems of particle migration, agglomeration and sintering, all of which lead to deactivation [57]. Therefore, the development of scalable methods capable of enabling the production of catalytic nanostructures that maintain their high performance in reactive environments is highly desirable. Nanofiber fabrics synthesized by electrospinning offer the promise to ameliorate these problems, and a represents a new direction in heterogeneous catalysis.

Heterogeneous catalysts typically are prepared by well-established techniques such as impregnation and co-precipitation, which normally lead to the production of quasi-spherical particles terminated by low-energy surface facets, such as the (111) surface for fcc crystals and the (0001) surface for hcp crystals [1, 2]. These particles generally have diameters of 1 to 20 nm and are referred to as nanoparticles. As previously discussed, it has been demonstrated that the shapes of particles significantly affect the selectivity and conversion of reactions, such as in the case of ethylene epoxidation by silver [3, 4]. In these works, the cubic and pentagonal nanowire shapes exhibited higher selectivity than conventional spherical particles, due to fact that their surfaces were terminated mainly by the (100) surface facets, rather than the lowest energy (111) facet that dominates spherical particles.

However, in spite of these findings, the syntheses of shape- and size-selected metal and metal oxide particles are inherently complex and do not lend themselves to convenient scale-up. Furthermore, controlled synthesis of particles of specific shapes and sizes directly

on high surface area supports and anchoring them on surfaces has been a difficult task [4]. In addition, the improved chemical reactivities exhibited by certain nanoparticles could be related to their unique geometric and electronic features, which may be metastable. Thus, under high temperature reaction conditions, e.g. partial oxidation reactions, particles may transform into the lowest energy structures, i.e. small clusters will migrate and agglomerate into larger structures to minimize surface energy. It should be noted that nanoparticle agglomeration also creates local (nano-scale) diffusion limitations, which can adversely affect the reaction selectivity. It is therefore necessary to develop scalable methods that both produce and preserve the desired optimal shape and size of catalytic nanostructures in reactive environments.

Here, we propose to investigate a fundamentally different approach to oxidative coupling of methane, partial oxidation reactions and, more broadly, nanocatalysis overall: the synthesis and use of *nanofibers* as catalytic materials. We refer to nanofibers as one-dimensional structures with diameters in the 10-300 nm range and high aspect ratios (e.g. length/diameter greater than approximately 100). Specifically, ***electrospinning*** can be exploited to create nanofibers of single and mixed metal oxides and subsequently evaluate their catalytic properties using partial oxidation reactions, e.g. oxidative coupling of methane (OCM).

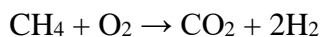
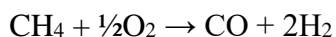
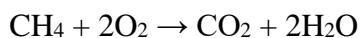
Related research efforts have suggested that this general approach towards the commercialization of OCM is promising. Siluria Technologies of San Francisco, CA are also pursuing OCM catalysts, but instead using “nanowires” synthesized by viral templating [70-73]. These structures are similar to nanofibers synthesized by

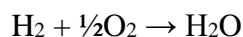
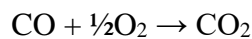
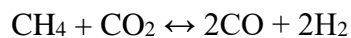
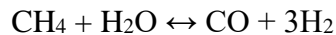
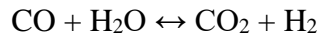
electrospinning, but typically with substantially smaller length-to-diameter aspect ratios. Additionally, electrospinning represents a more versatile, scalable and simpler alternative to viral templating.

2.6. Catalytic Partial Oxidation (CPO) of Methane.

The catalytic partial oxidation (CPO) of methane utilizes the same reactants as OCM, O_2 and CH_4 ; however, the target products are CO and H_2 , synthesis gas or syngas, which is traditionally produced by methane steam reforming [74-77]. Like OCM, the products of CPO are key chemical intermediates that can be further processed into consumables traditionally derived from crude oil. Consequently, both CPO and OCM are widely studied routes for the utilization of natural gas as an alternate chemical feedstock. Methane CPO has been studied as an alternative to steam reforming due to the latter being highly endothermic and thus expensive [78, 79]. Since the CPO and OCM schemes share the same reactants and the target products of CPO are OCM side-products, and vice versa, a substantial mechanistic overlap between them is anticipated. Hence, insights or discoveries regarding one process may further the understanding of the other.

The relevant reactions involving reactants (CH_4 , O_2), target products (CO, H_2), side products and stable chemical intermediates in methane CPO are [76]:





This process could, in theory, be accomplished exclusively and directly by dry partial combustion when achieving 100% selectivity. However, there are number of indirect ways through which CO/H₂ mixtures could be produced. For example, methane may undergo complete wet combustion, producing CO₂ and H₂O. The energy released by combustion could then be used to fuel the conversion of H₂O to H₂ via the methane steam reforming reaction. Likewise, the carbon dioxide reforming of methane would then create CO as well as H₂. The specific route and mechanism taken accordingly is dependent on the catalytic material and reaction conditions. Combustion-reforming mechanisms have been reported for Ir-based catalysts, including those in which La₂O₃ and MgO are support materials [76]. This is particularly interesting since rare earth and alkaline earth metal-based catalysts are traditional state-of-the-art materials for methane coupling. Incrementally doping an OCM catalyst with Ir therefore may help realize a transition from OCM to methane CPO, allowing for an analysis of the mechanisms of both reaction schemes synergistically.

Chapter 3. Propylene Epoxidation by Co-Impregnated Sb₂O₃-CuO-NaCl/SiO₂ Catalysts.

This chapter details some of my initial training in heterogeneous catalysis research. Specifically, this chapter involves using quasi-spherical nanoparticle-based catalysts for the direct epoxidation of propylene by molecular oxygen and evaluating the catalytic materials using high throughput screening technology. This chapter is largely representative of a recent work published in the *Journal of Industrial and Engineering Chemistry* (In press, available online currently).

3.1. High-Throughput Catalytic Performance Screening System.

The catalysts synthesized in this work that are used for propylene epoxidation are examined for performance using the high-throughput screening system shown in Figure 3.1 [80, 81]. This apparatus is subdivided into: a flow system comprising MKS electronic mass flow controllers, a pressure controller a mixing port; a reactor system whose positioning is adjusted by a computer-controlled x-y-z motion system (Newmark Systems, Irvine, CA); and an analysis system composed of a gas chromatography (GC) unit, mass spectrometer (MS) and heated sampling capillary that the delivers product gas into either the GC or MS. The reactant gases and inert diluent, or carrier (e.g. helium, molecular nitrogen) if needed, are delivered from high pressure gas cylinders into an initial set of mass flow controllers, subsequently mixed, then divided by a second set of flow controllers into as many as four reactors, each comprising 20 cells. Hence, the performance of up to

80 catalytic materials may be evaluated in a single set of screenings, which would typically take a few hours [82]. The positioning of the reactor system is adjusted such that the sampling capillary is inserted precisely to analyze the effluent gas of a single cell, with an insertion depth of 1-5 mm.

The GC uses a vacuum pump to withdraw the effluent gas and deliver it through adsorption chromatography columns that separate the various components of the gas, allowing for its composition to be estimated and thus the effectiveness of the catalyst. After a single sample is ascertained, the motion control system may then be adjusted so that the capillary is inserted into the next catalyst containing cell. The evaluation process is repeated until the effluent from all the relevant cells are evaluated for their compositions. In each reactor, at least one cell is left without any catalytic material yet still sampled to establish background effects (e.g. homogeneous gas phase reactions, unintended catalysis by otherwise inert materials), if any.

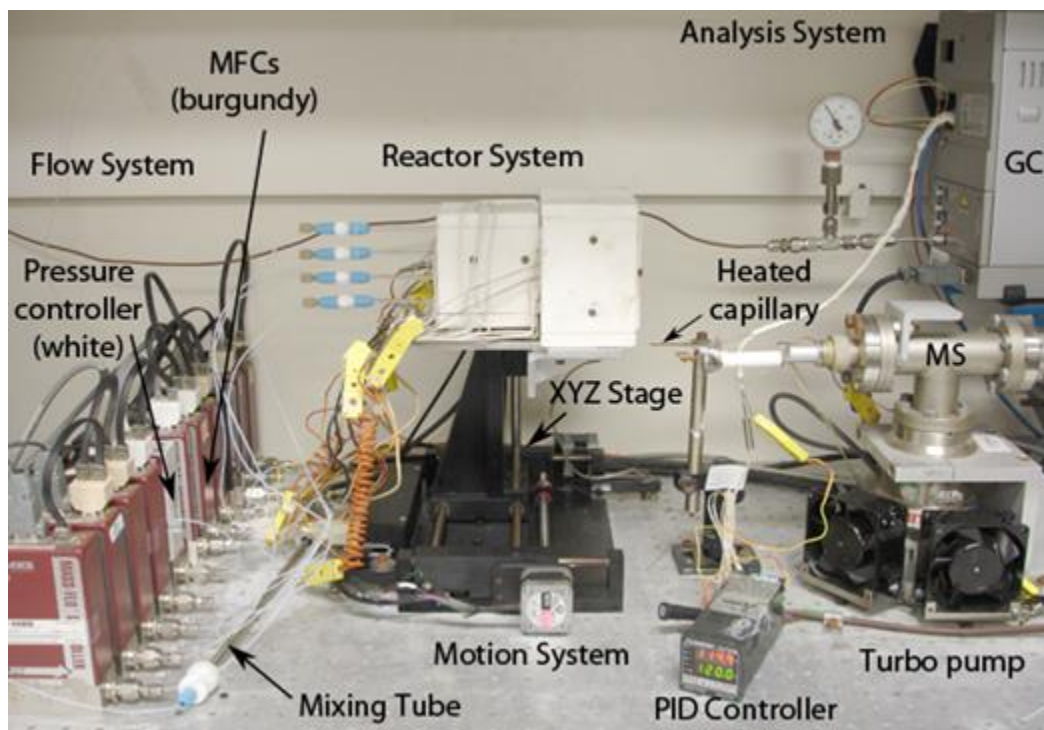


Figure 3.1. The high-throughput catalytic performance screening system used in this work.

Shown in the left of Figure 3.2 is a typical silica ceramic twenty-celled array channel microreactor ($7.5 \text{ cm} \times 3.75 \text{ cm} \times 0.63 \text{ cm}$) used in the screening system. The reactant gases (e.g. propylene, molecular oxygen and helium carrier) are fed through the glass tube and distributed evenly to each cell using baffles. Each cell is shaped as a cylindrical well with a diameter and depth of 4 and 1 millimeters respectively. When a cell is filled with catalyst, it typically contains 1 – 10 milligrams depending on the materials density and texture, such that the flowing gas is sufficiently contacted but that no catalytic material is ejected. Each reactor's contents are sealed using a ceramic block such that the gases can only exit through the end of the array channels. Overall, gas flow in this system

is precisely directed through each channel, unobstructed and resisted solely by wall skin friction [83, 84].

The reactor block is shown in the right of Figure 3.2 with two inserted microreactors, one partially inserted and the final, fourth space left empty. A side view of the reactor block is shown in Figure 3.3, illustrating the insertion of gas feeding tubes and insertion of the thermocouples near the reactor heaters to allow for proper temperature sampling and control. The reactor block is composed of insulating ceramic material to keep the temperature uniform.

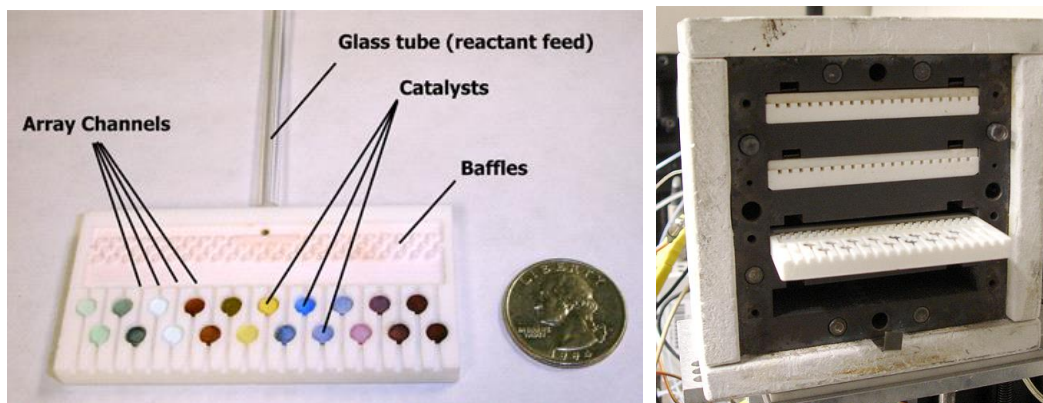


Figure 3.2. Array channel microreactor (left) and its insertion into the reactor system (right) of Figure 3.1.

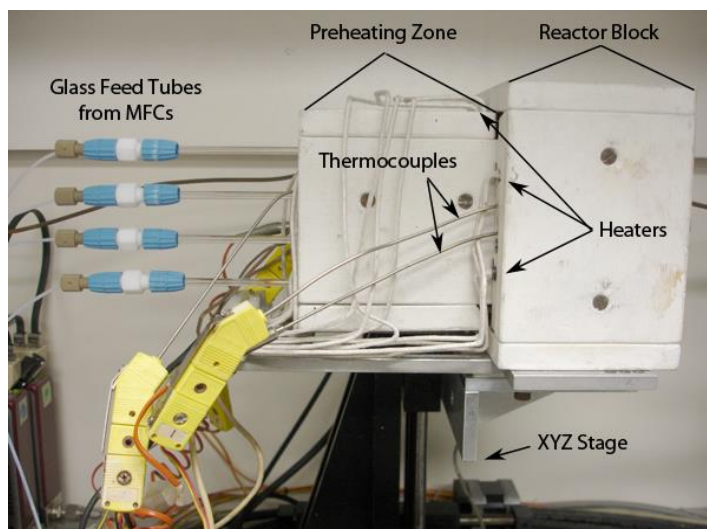


Figure 3.3. Reactor system and its critical parts.

3.2. Preparation of Silica-Supported Catalysts Composed of Sb_2O_3 , CuO , NaCl and combinations thereof.

All catalysts discussed in this chapter are nanoparticle-based materials that were prepared by co-impregnation [85, 86]. The unimetallic (Sb/SiO_2 , Cu/SiO_2 and NaCl/SiO_2), bi-metallic ($\text{Sb-Cu}/\text{SiO}_2$, $\text{Sb-NaCl}/\text{SiO}_2$, $\text{Cu-NaCl}/\text{SiO}_2$) and tri-metallic ($\text{Sb-Cu-NaCl}/\text{SiO}_2$) catalysts were prepared in parallel by mixing appropriate aqueous metal salt precursor solutions [$\text{Cu}(\text{NO}_3)_2 \cdot 2.5\text{H}_2\text{O}$, SbCl_3 , NaCl ; Alfa Aesar] with the SiO_2 support (surface area of $\sim 100 \text{ m}^2/\text{g}$; Alfa Aesar). The solution volumes and support weights were varied to achieve catalysts comprising a comprehensive set of metal loadings. The mixtures were stirred at $20 \text{ }^\circ\text{C}$ for 24 hours, allowing for the metal salts to diffuse into the support material. This was followed by drying at $120 \text{ }^\circ\text{C}$ while mixing. The materials were subsequently air calcined at $460\text{-}540 \text{ }^\circ\text{C}$ for 6 hours.

3.3. Catalytic Performance Evaluation and Characterization.

Each catalyst (5 milligrams) was evaluated for performance at atmospheric pressure using the previously described computer-controlled high-throughput array channel microreactor system [81]. The gas hourly space velocity (GHSV) was fixed at 20,000 h⁻¹ using mass flow controllers (MKS, Andover, MA). The feed gas consisted of 1 vol% propylene (C₃H₆), 5 vol% O₂ and balance He at 250 °C for all experiments. Data analysis was conducted at a pseudo-steady condition (i.e. 2-4 hours after the reactor reached 250 °C) by an on-line Micro-Gas Chromatograph (GC, Varian, CP-4900) equipped with a thermal conductivity detector (TCD) and Porapak U (10 m) and Molecular sieve 5 Å (10 m) columns [85, 86]. The products propylene oxide (PO), acrolein (AC) and CO₂ were consistently detected in substantial amounts, along with traces (<1%) of acetone (AT) and acetaldehyde (AD). The product selectivities and propylene conversions for each catalyst were calculated on the basis of carbon balance. The repeatability of all experiments was within ±10%. In general, a variety of catalysts in the same set were prepared in parallel to minimize uncertainty. GC calibrations for gaseous species (propylene, O₂, CO₂) were conducted with He as the carrier gas and calibrations for liquid species (PO, AC, AT, AD) were performed by vaporizing the injected liquids of these species in a heated, evacuated 2,250 cm³ stainless steel tank (He as carrier gas). Using peak area as the basis of GC calculations, all calibrations yielded linear five-point curves with $R^2 \geq 0.995$.

N₂ physisorption, conducted with a Quantachrome Autosorp-1C instrument with BET and BJH methods at -196 °C, was used to measure the catalysts' specific surface area. Powder X-ray diffraction (XRD) patterns were obtained on an X-ray power diffractometer (XRD: JEOL JDX-3530 and Philips X-Pert) using Cu K α radiation, 45 kV and 40 mA to identify the active catalyst phase and average crystallite sizes. A scanning electron microscope and an energy dispersive X-ray spectrometer (SEM/EDS, SEM: JEOL, JSM-5410LV) operated at 20 keV were used to image the catalysts' morphology and elemental composition. Continuous H₂-temperature programmed reduction (H₂-TPR) measurements were carried out in a continuous-flow Inconel tube reactor held at 25-900 °C with a heating rate of 5 °C/min. The H₂/Ar mixture gas (9.6% H₂) was introduced into the catalyst bed at a total flow rate of 30 cm³/min. The H₂ consumption was continuously monitored using a TCD-equipped GC (Shimadzu GC-2014). A Simultaneous TGA-DTA Analyzer (TA instrument, SDT2960 Simultaneous TGA-DTA Universal 2000) in air at a temperature range of 30-1,000 °C was used to examine types of carbon on fresh and used catalysts.

3.4. Catalyst Composition Optimization.

Figure 3.4 and Figure 3.5 show an optimization of the Sb:Cu:Na metal ratio of the trimetallic system with the total metal loading fixed at 18 wt% for all catalysts. The results are plotted in the triangular diagrams in terms of PO selectivity (Figure 3.4) and propylene conversion (Figure 3.5). Each corner of the triangle represents the corresponding unimetallic Sb₂O₃/SiO₂, CuO/SiO₂ and NaCl/SiO₂ catalyst at 18 wt% loading. The

bimetallic catalysts of $\text{Sb}_2\text{O}_3\text{-CuO/SiO}_2$, $\text{Sb}_2\text{O}_3\text{-NaCl/SiO}_2$ and CuO-NaCl/SiO_2 are on the rear, left and right perimeters of the triangle respectively. Each step traversed on the perimeter entails a 3.0 wt% change in the loading of each metal on the bimetallic. All trimetallic $\text{Sb}_2\text{O}_3\text{-CuO-NaCl/SiO}_2$ catalysts are within the triangle's interior blocks. From Figure 3.4, the trimetallic $\text{Sb}_2\text{O}_3\text{-CuO-NaCl/SiO}_2$ and bimetallic $\text{Sb}_2\text{O}_3\text{-CuO/SiO}_2$ catalysts exhibit remarkably superior PO selectivities (up to 43%) and propylene conversions (up to 1.15%) compared to the unimetallic $\text{Sb}_2\text{O}_3/\text{SiO}_2$ and NaCl/SiO_2 and bimetallic catalysts $\text{Sb}_2\text{O}_3\text{-NaCl/SiO}_2$ and most of the CuO-NaCl/SiO_2 combinations (Cu:Na = 12:6, 9:9, 6:12 and 3:15 by weight), which exhibit virtually 0% PO selectivity. The unimetallic CuO/SiO_2 catalyst achieves 10.2% PO selectivity with 0.23% propylene conversion. Doping CuO/SiO_2 with a small amount of NaCl (Cu:Na = 15:3 by weight) has a promotional effect, giving 11.8% PO selectivity at 0.27% propylene conversion, consistent with earlier works done by Lambert et al [52]. Clearly, the combined presence of Sb_2O_3 , CuO and NaCl enables the synergistic effects for propylene epoxidation catalysis.

The catalyst comprising a weight (molar) ratio for Sb:Cu:Na of 2:3:1 (1.0:2.9:2.6) was the most productive for epoxidation, with selectivities for PO, AC and CO_2 at 43%, 6% and 51% respectively at a propylene conversion of 0.66%. Interestingly, when comparing the optimum ratio to the proximate bimetallic $\text{Sb}_2\text{O}_3\text{-CuO}$ ratios (e.g. Sb:Cu = 12:6 and 9:9), the PO selectivity of the trimetallic catalyst was about twice that of the bimetallics, but the propylene conversion was about half. This indicates that the coexistence of Sb_2O_3 and CuO in the catalyst plays an important role in propylene epoxidation and that NaCl acts as a promotor for the reaction [15, 87]. It is important to

note that highly active sites of other catalysts for propylene epoxidation (e.g. Ag-based catalysts [16], RuO₂/SiO₂ [86]) generally create a route for combustion [55]. The addition of NaCl can, therefore, reduce the reactivity of the catalyst surface for propylene combustion and thereby improve the PO selectivity but reduce propylene conversion [55, 88]. This is because NaCl crystals are incorporated into the catalyst's solid structure and so primarily occupy the highly active sites on the catalyst surface responsible for combustion of propylene or intermediates. After NaCl captures the highly active sites for propylene combustion, the route for PO generation becomes more pronounced and the PO selectivity is increased. Since the total combustion route (i.e. CO₂ formation) is partially inhibited by NaCl addition, the propylene conversion is expected to be reduced as confirmed here [89].

In an attempt to further optimize the performance of the Sb₂O₃-CuO-NaCl/SiO₂ catalysts for PO synthesis, an investigation of the effects of total metal loading from 3 to 20 wt% on the SiO₂ support was undertaken. The results of the catalyst performance are shown in Figure 3.6 and the XRD spectra of the selected catalysts (5, 9, 13, 18 and 20 wt%) are presented in Figure 3.7. Note that the selectivities of other byproducts (such as AT and AD) are insignificant compared to CO₂, PO and AC. At low total metal loadings (5, 7 and 9 wt%), only CO₂ was detected. The XRD spectrum at 9 wt% suggests CuO is the only crystalline species, i.e. Sb₂O₃ and NaCl are either amorphous or constituted crystals too small to be detected (less than about 2.0 nm). When further increasing the loading from 9 to 15 wt%, the PO selectivity rapidly increased from 0 to a maximum of 43%, while the propylene conversion increased from 0.10 to 0.40%. At 13 wt%, XRD suggests the

presence of Sb_2O_3 and NaCl crystals, in addition to the previously detected CuO , potentially accounting for the sudden rise in PO production. Also, at higher loadings, crystals of Sb_2O_3 and CuO are more likely to be adjacent, allowing for synergistic catalysis towards PO. Below 13 wt%, CuO and Sb_2O_3 crystals may be more isolated from each other for this to occur; therefore, these materials function in the manner of the unimetallic CuO/SiO_2 catalyst, which generally produces significant amounts of AC [86].

In between 15 and 18 wt%, the PO selectivity is fixed at 43% as well as the AC selectivity at 5%, whereas the propylene conversion rises sharply from 0.40 to 0.66%. Beyond this loading, the aforementioned synergistic catalysis deteriorates, leading to a rise in CO_2 selectivity. The propylene conversion, however, continues to increase, simply because the number of active Sb_2O_3 - CuO - NaCl phases (i.e. the proximity of Sb_2O_3 and CuO crystals) increased. Figure 3.7 indicates that the average Sb_2O_3 crystallite size according to the Sherrer equation at 20 wt% (23 nm) is larger than that of 18 wt% (21 nm), implying that the sintering of active Sb_2O_3 reduces the PO selectivity and propylene conversion for loading above the optimal PO yield at 18 wt% (43% PO selectivity, 0.66% propylene conversion). This implies that when the crystallite size becomes larger, the agglomerates of crystallites also tend to become large such that the overall contact area between Sb_2O_3 and CuO crystals, responsible for the synergistic catalysis, lessens.

The metal distributions (Sb, Cu and Na) of the catalysts prepared at different total metal loadings were also investigated by SEM/EDS. The images are shown in Figure 3.8. Each metal was uniformly dispersed on the SiO_2 support.

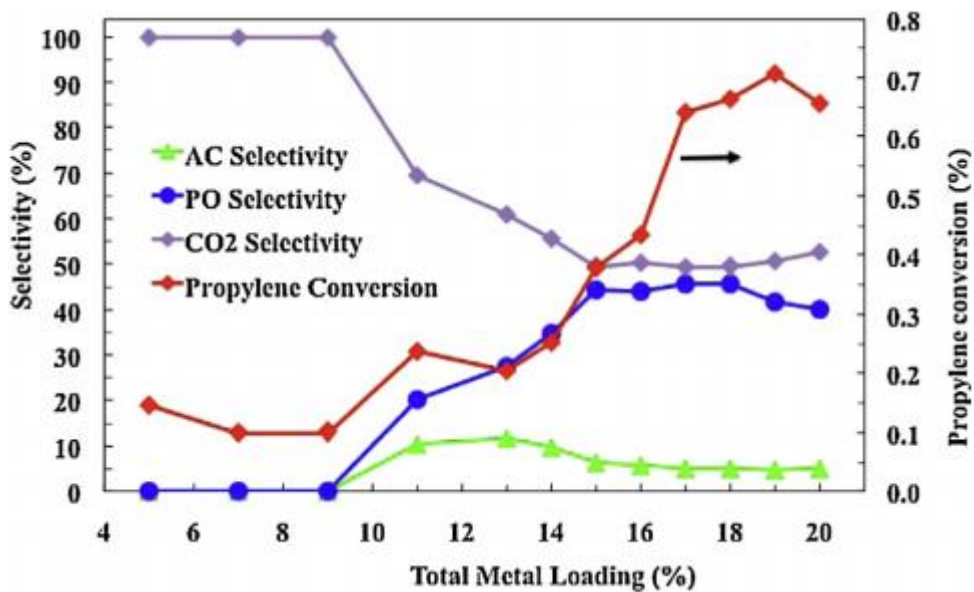


Figure 3.6. Effect of total metal loading on SiO₂ from 3 to 20 wt%, Sb:Cu:Na = 2:3:1. The catalysts were calcined at 500 °C.

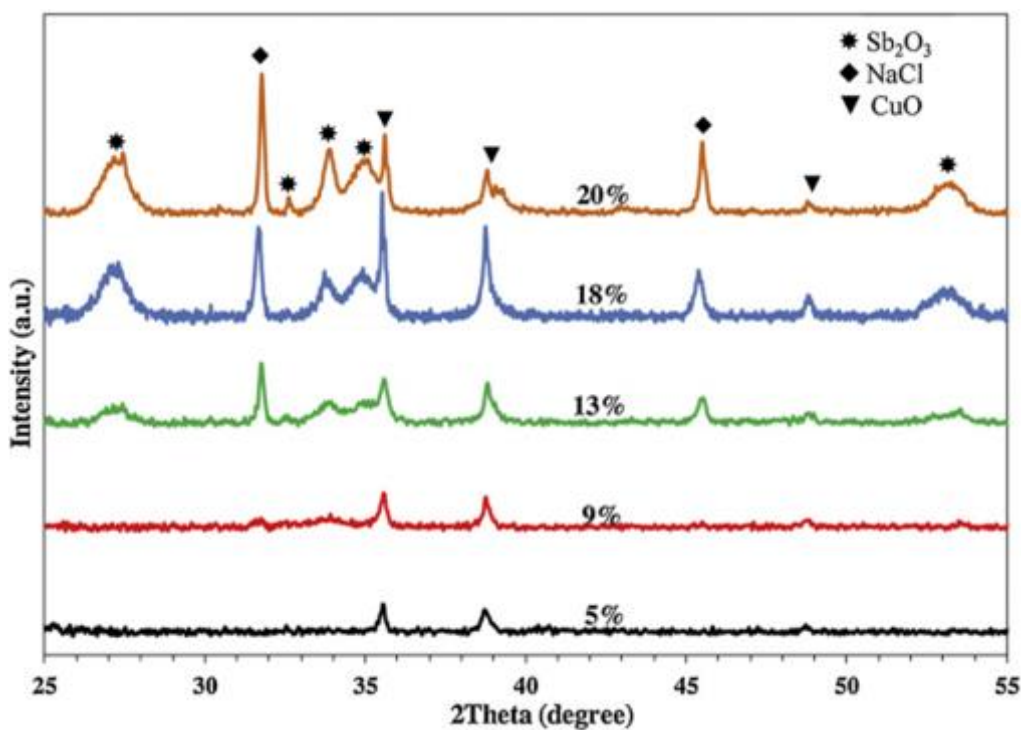


Figure 3.7. XRD spectra of 5, 9, 13, 18 and 20 wt% total metal loading on SiO₂, Sb:Cu:Na = 2:3:1. The catalysts were calcined at 500 °C.

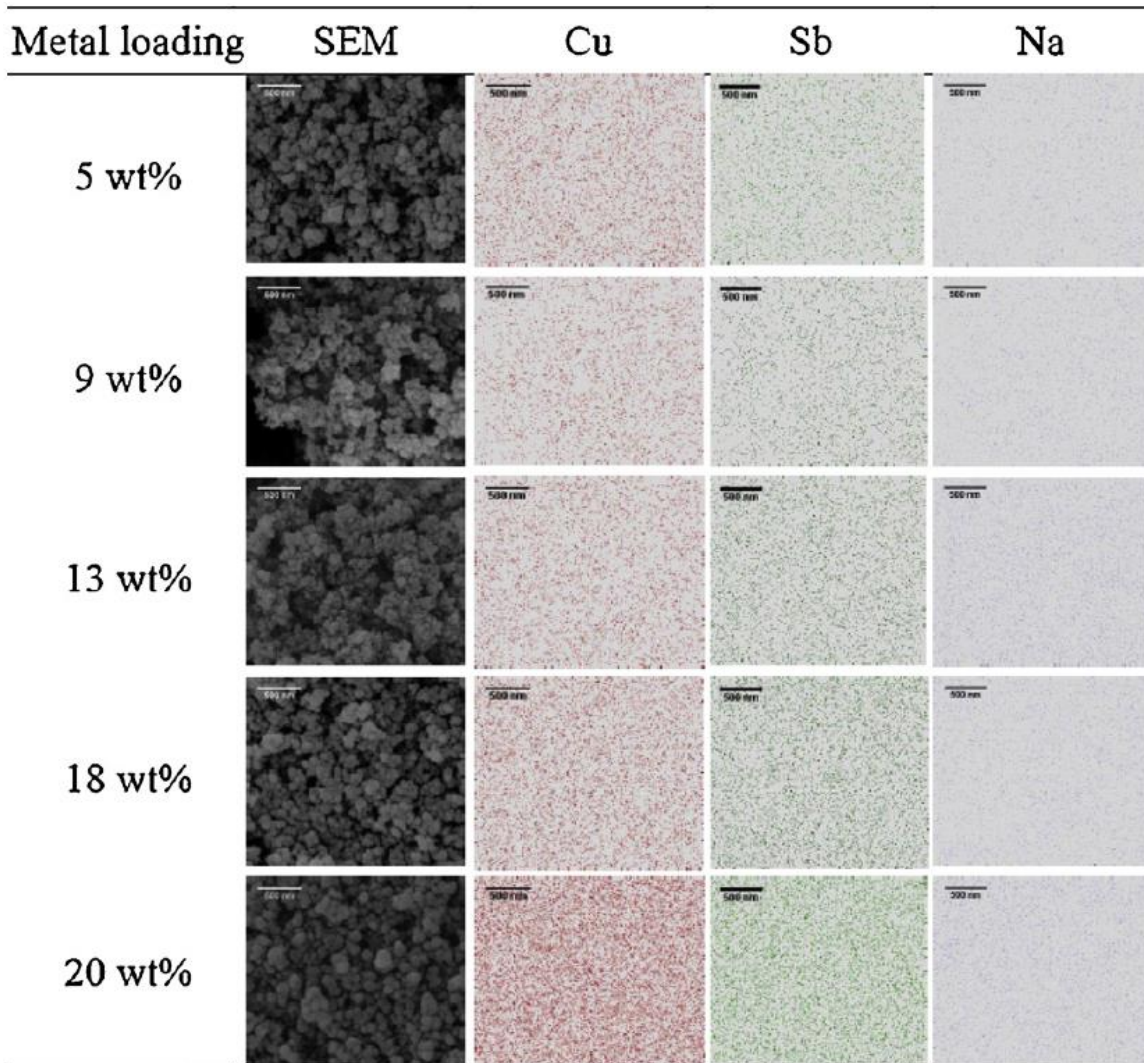


Figure 3.8. SEM/EDS of catalysts at 5, 9, 13, 18 and 20 wt% total metal loading on SiO₂, Sb:Cu:Na = 2:3:1. The catalysts were calcined at 500 °C. Each scale bar is 500 nm.

3.5. Calcination Temperature Optimization.

Figure 3.9 shows the relationship between PO formation and calcination temperature. The catalysts were calcined at 460, 480, 500, 520 and 540 °C for 6 h. The propylene conversion was the highest for the catalyst calcined at 460 °C, but CO₂ was the

main product. The propylene conversion decreased with increasing PO selectivity until achieving the optimum selectivity at 500 °C, the same temperature used for preparing the catalysts in Figure 3.4 and Figure 3.5. Calcination temperatures >500 °C decreased PO formation. The AC selectivity was virtually fixed at about 5% until dropped precipitously at 540 °C.

The XRD spectra of catalysts examined in Figure 3.9 are presented in Figure 3.10, and the BET surface area and crystallite sizes of Sb₂O₃, CuO and NaCl are shown in Figure 3.11 as a function of calcination temperature. The analyses of the XRD spectra reveal the characteristic diffraction patterns of Sb₂O₃ ($2\theta = 27.3, 32.5, 33.8, 34.8, 53.2^\circ$), CuO ($2\theta = 35.6, 38.7, 48.9^\circ$) and NaCl ($2\theta = 31.7, 45.5^\circ$). At all calcination temperatures, the crystallinity and the crystallite size of NaCl were virtually unchanged at ~100 nm according to the Sherrer equation. Above 480 °C, the crystallite sizes of CuO remain about the same (at 76-79 nm) but the intensity of the characteristic CuO peaks slightly increased, indicating the quantity of CuO crystals slightly increased with rising calcination temperatures.

The most significant influence on PO formation is the crystallite Sb₂O₃ size. The XRD spectra of Sb₂O₃ are broader at lower calcination temperatures, indicating smaller crystallite sizes. The crystallite Sb₂O₃ size is 14, 19, 21, 23 and 24 nm at 460, 480, 500, 520 and 540 °C respectively. Considering that the propylene conversion decreases with increasing calcination temperature (see Figure 3.9), the increase in crystallite size with increasing calcination temperature is consistent with a reduction of active surface area as indicated in Figure 3.11. The optimum PO selectivity occurs at 500 °C. Below 500 °C, the decrease in PO production rate with increasing calcination temperature is smaller than the

decrease in CO₂ production rate. Above 500 °C however, the larger crystallite Sb₂O₃ sizes (i.e. the fewer active sites) apparently have a stronger influence on the reduction of PO formation than on the reduction of CO₂ formation. These results suggest that both the presence and sizes of Sb₂O₃, CuO and NaCl crystals play a significant role in PO formation.

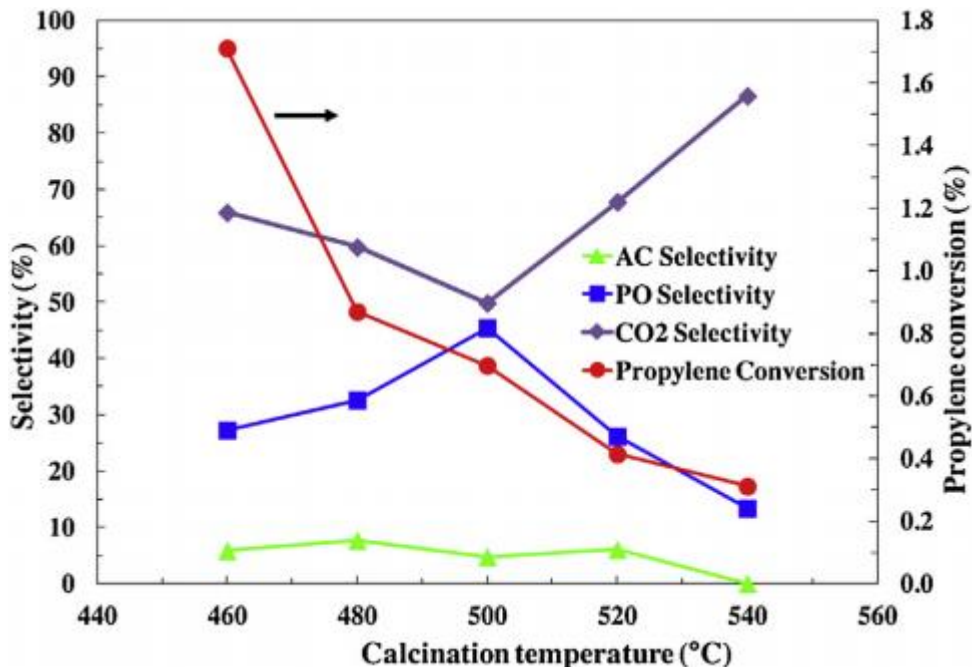


Figure 3.9. Performance of Sb₂O₃-CuO-NaCl/SiO₂ (Sb:Cu:Na = 2:3:1, 18 wt%) catalysts calcined at different temperatures.

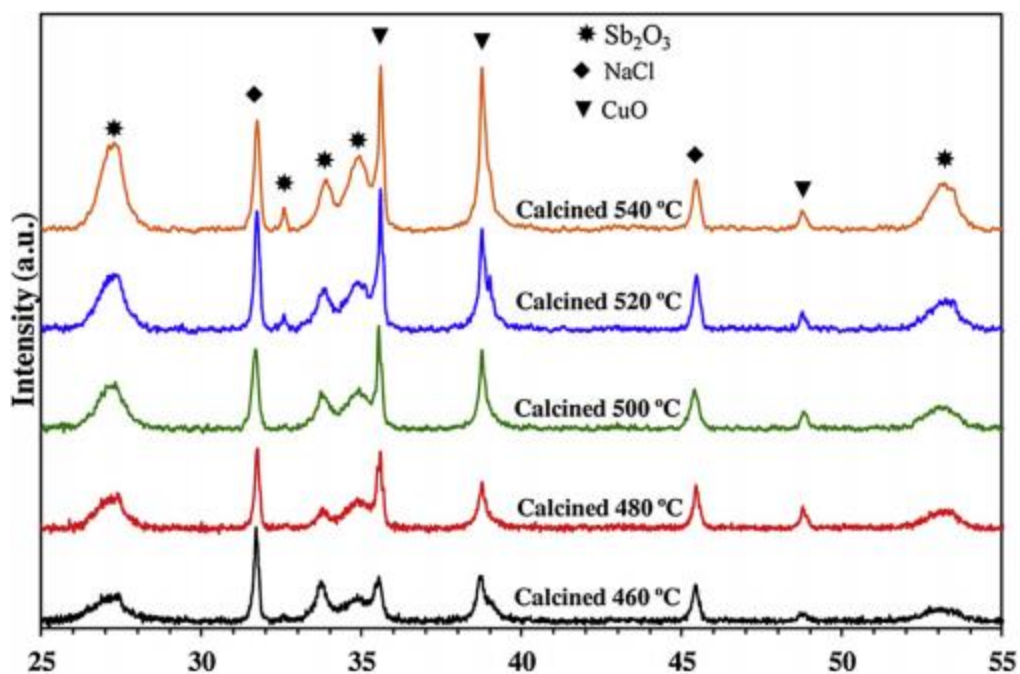


Figure 3.10. XRD spectra of $\text{Sb}_2\text{O}_3\text{-CuO-NaCl/SiO}_2$ catalysts calcined at 460-540 °C.

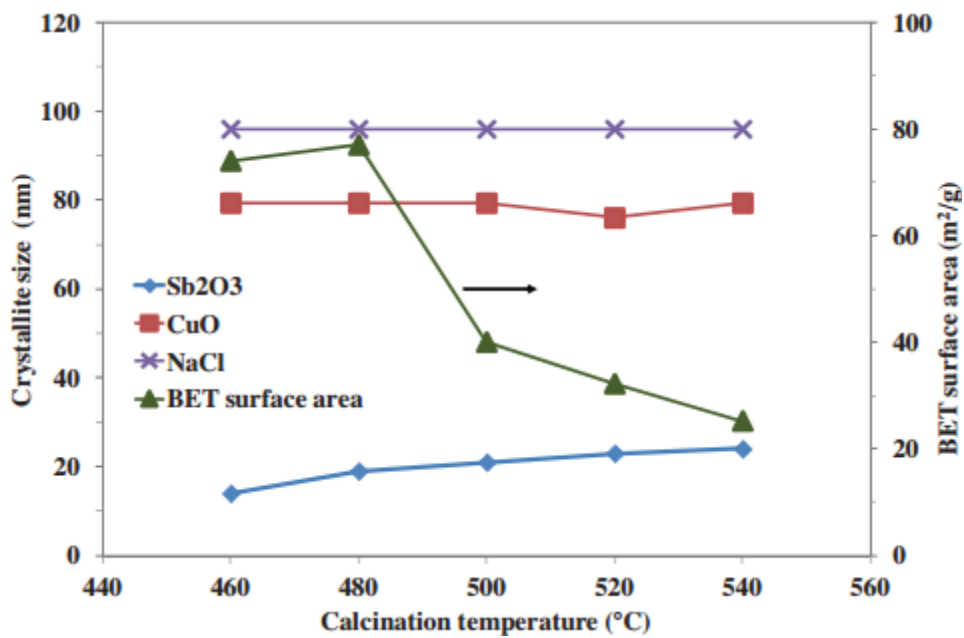


Figure 3.11. Crystallite sizes of Sb_2O_3 , CuO and NaCl ; and BET surface area of the $\text{Sb}_2\text{O}_3\text{-CuO-NaCl/SiO}_2$ ($\text{Sb:Cu:Na} = 2:3:1$, 18 wt%) catalyst calcined at 460-540 °C.

3.6. Active Site Analysis by H₂-Temperature Programmed Reduction (H₂-TPR).

H₂-TPR measurements, shown in Figure 3.12, were conducted to examine the interaction between the distinct Sb₂O₃ and CuO phases in the Sb₂O₃-CuO-NaCl/SiO₂ catalyst at 18 wt% total metal loading and calcined at 500 °C. The unimetallic CuO/SiO₂ and Sb₂O₃/SiO₂ catalysts showed single peaks around 300 and 570 °C, attributed to the reduction of bulk CuO [90] and Sb₂O₃ [91] respectively. The bimetallic Sb₂O₃-CuO/SiO₂ catalyst showed two peaks: a main peak at 300 °C and a shoulder around 390 °C. The peak at the lower temperature is attributed to the reduction of CuO and the shoulder at higher temperature is ascribed to the reduction of Sb₂O₃. The presence of CuO, presumably in close proximity or completely in contact with Sb₂O₃, appears to shift the Sb₂O₃ peak to lower temperatures. Therefore, in the bimetallic of Figure 3.12, Sb₂O₃ and CuO are reduced almost simultaneously because of a spillover induced by the reduction of CuO [92]. Similarly, the trimetallic of Sb₂O₃-CuO-NaCl/SiO₂ catalyst shows the main reduction peak of CuO around 300 °C and two shoulders around 370 and 460 °C. The 370 °C shoulder is attributed to the Sb₂O₃ phases that are in close proximity to CuO phases while that at 460 °C is assigned to Sb₂O₃ phases displaced from CuO phases. The addition of NaCl may separate some of the Sb₂O₃ phases by blocking the contact of the two metal oxides [93]. These H₂-TRP results corroborate the notion that the Sb₂O₃ and CuO phases are in close proximity, and thus may enhance the synergistic effects of the catalysts for the title reaction.

Since the addition of NaCl induces both the apparent phase separation of Sb_2O_3 from CuO while improving the catalyst's performance, the active sites of the Sb_2O_3 -CuO/ SiO_2 bimetallic essentially have a surplus of Sb_2O_3 that attenuates PO formation and enhances combustion. Hence, NaCl may favorably assist in finely tuning the localized spatial metal oxide composition on the surface of the catalyst support.

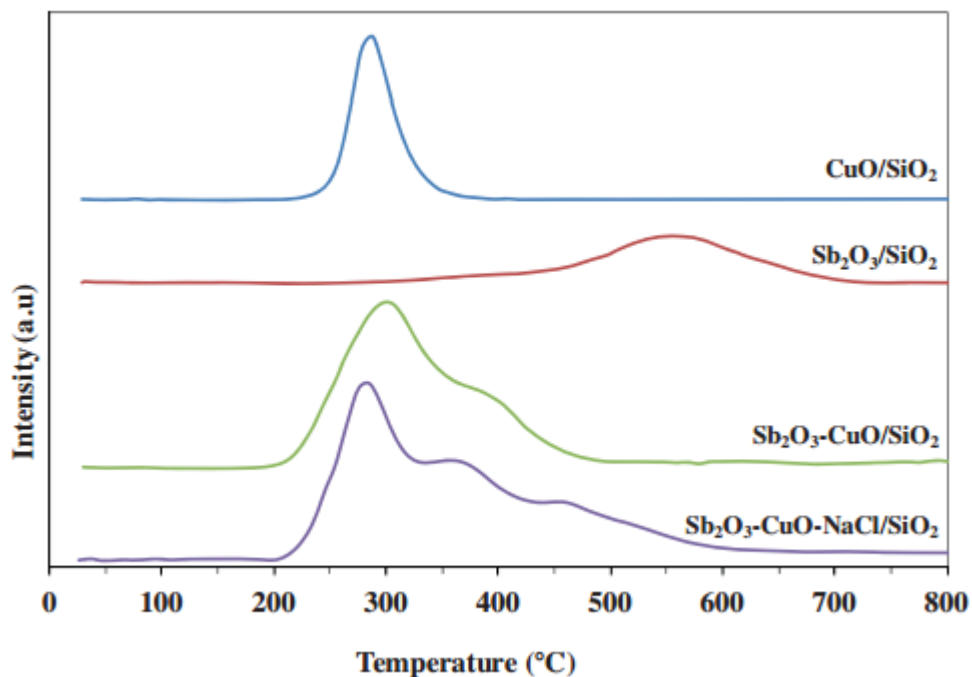


Figure 3.12. H_2 -TPR profiles of Sb_2O_3 , CuO, CuO- Sb_2O_3 and CuO- Sb_2O_3 -NaCl on SiO_2 . For each metal indicated, the loading is 6, 9 and 3 wt% for Sb, Cu and Na, respectively.

3.7. Time on Stream Analysis.

Since catalyst durability is essential, a time-on-stream test of the Sb_2O_3 -CuO-NaCl/ SiO_2 catalyst with the optimal composition (i.e. Sb:Cu:Na = 2:3:1 at 18 wt% total metal loading on SiO_2 and calcined at 500 °C) for propylene epoxidation using oxygen was

performed. Figure 3.13 charts PO and AC selectivities together with propylene conversions over 10 h of continuous operation at 250 °C. The XRD (Figure 3.14), TGA-DTA (Figure 3.15) and BET surface area measurements of the fresh and used catalyst were carried out to investigate its deactivation. As indicated in Figure 3.13, PO selectivity gradually increased during the first 3 h, reaching a maximum of about 42%. During hours 3-10, PO selectivity minimally decreased to 41%, while propylene conversion continuously decreased from 0.95% at the first hour to 0.65% at 10 h. Evidently, this is due to the coalescence of crystals (i.e. catalyst sintering). As is indicated in Figure 3.14, the crystallite size of Sb_2O_3 particles increased during the experiment – 21 nm on the fresh catalyst compared to 23 nm on the used catalyst. This increase in crystallite size is consistent with the BET surface area analysis; the surface area of the catalyst after 10 h of reaction was found to be 35 m^2/g compared to 40 m^2/g of the fresh catalyst. The reduction in the Sb_2O_3 crystallite surface area accordingly weakens the synergy between Sb_2O_3 and CuO responsible for PO formation. TGA-DTA analyses (shown in Figure 3.15) showed no coke formation. The TGA and TDA curves of the fresh and used catalysts were virtually unchanged, suggesting no carbonaceous compounds were generated and then deposited on the catalyst. Both the fresh and used catalysts exhibited weight loss around 600-800 °C; this could be due to the changing oxide states of CuO or Sb_2O_3 .

After the 10 h of performance testing, the catalyst was stirred in 1.0 M HCl for 24 h in an effort to regenerate it. The material was then dried at 120 °C and calcined at 500 °C for 6 h. This procedure was found to elevate the PO selectivity to 40% (53% CO_2 selectivity and 7% AC selectivity at 0.84% propylene conversion) at 1.5 h of a time-on-stream

evaluation, similar to the results of the fresh catalyst shown in Figure 3.13. Also, the XRD spectrum of this material was identical to that of the fresh catalyst (in Figure 3.14). The dilute solution of HCl dissolves CuO and Sb₂O₃, enabling the re-calcination step to recover the original crystallite morphology and thus catalytic performance characteristics.

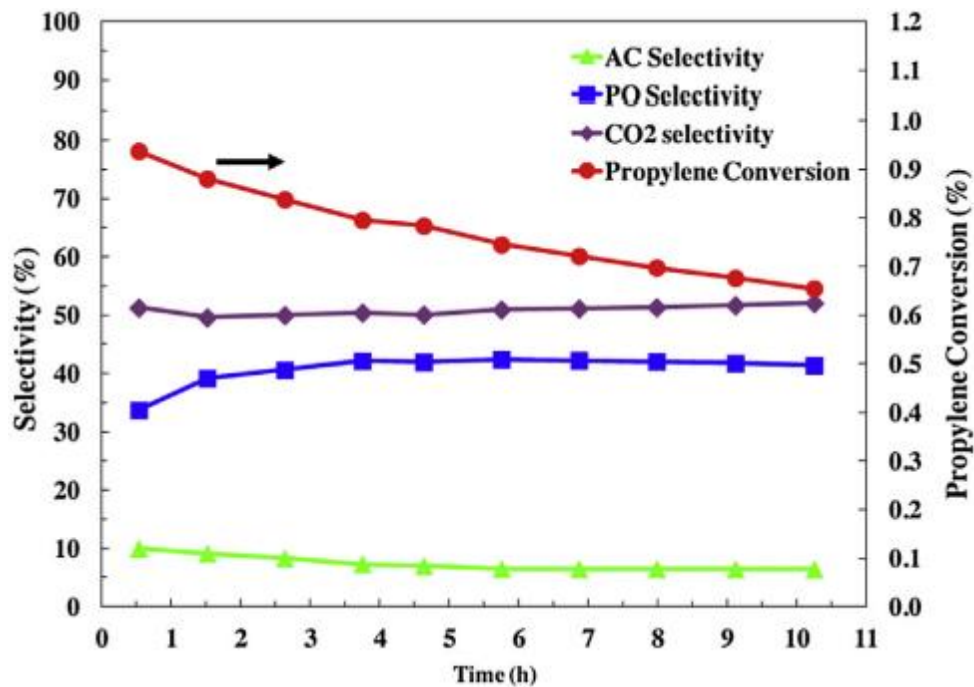


Figure 3.13. Time-on-stream testing results of Sb₂O₃-CuO-NaCl/SiO₂ catalysts; Sb:Cu:Na = 2:3:1 at 18 wt% total metal loading and calcined at 500 °C.

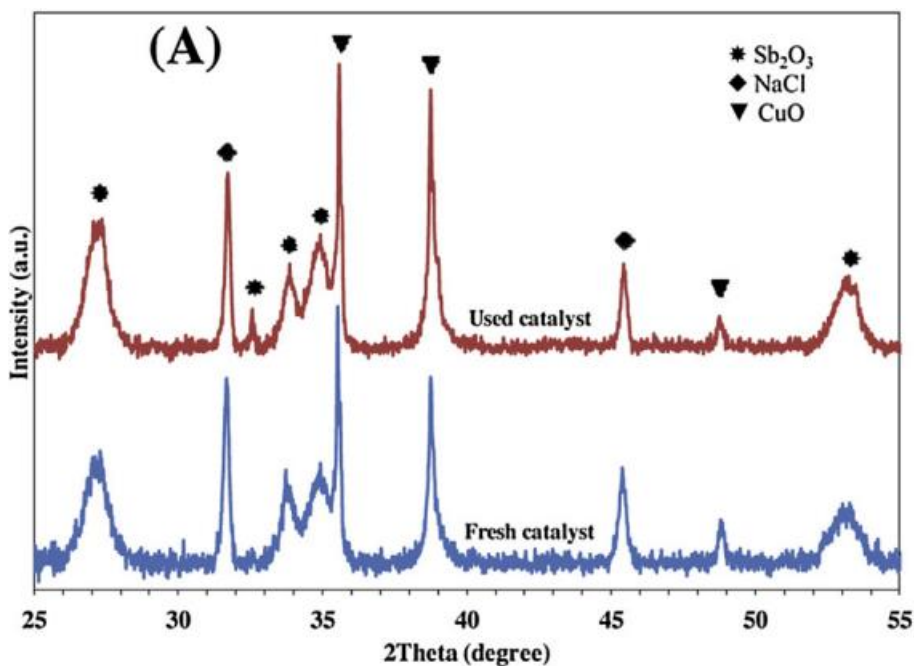


Figure 3.14. XRD patterns of fresh and used $\text{Sb}_2\text{O}_3\text{-CuO-NaCl/SiO}_2$ catalysts (Sb:Cu:Na = 2:3:1 at 18 wt% total metal loading and calcined at 500 °C).

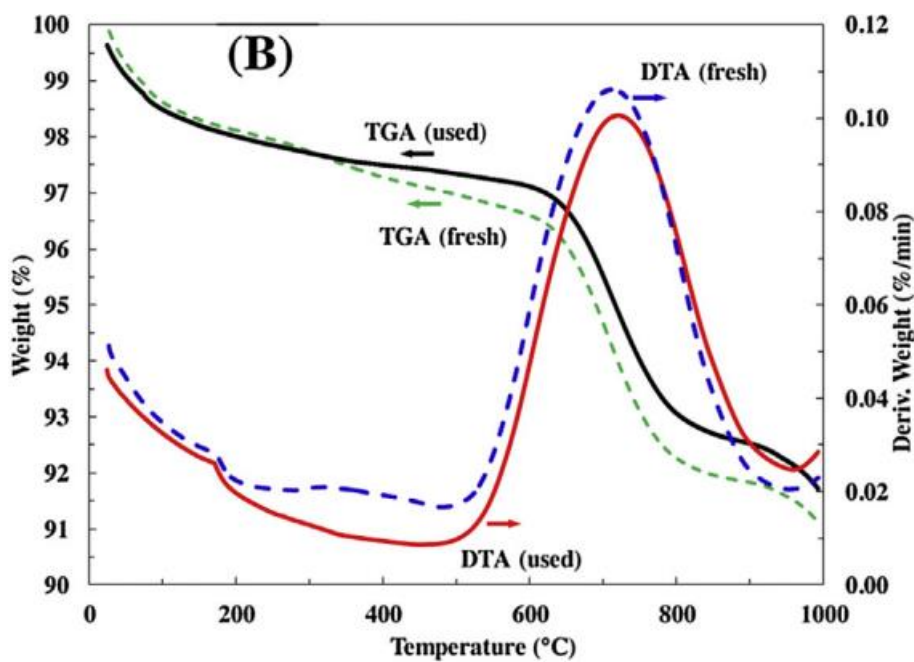


Figure 3.15. TGA-DTA curves of fresh and used $\text{Sb}_2\text{O}_3\text{-CuO-NaCl/SiO}_2$ catalysts (Sb:Cu:Na = 2:3:1 at 18 wt% total metal loading and calcined at 500 °C).

3.8. Summary.

Co-impregnated catalysts of $\text{Sb}_2\text{O}_3\text{-CuO-NaCl/SiO}_2$ were studied by first maximizing the catalytic performance for propylene epoxidation with respect to the metal ratios of Sb:Cu:Na with the total metal loading and calcination temperature fixed at 18 wt% and 500 °C. Peak performance (43% with 0.66% propylene conversion) occurred at Sb:Cu:Na = 2:3:1 by weight. Since the 18 wt% total metal loading maximized PO yield, it was chosen to explore the effects of calcination temperature between 480 and 540 °C. The coexistence of the crystallinity of Sb_2O_3 and CuO was found to be essential in the epoxidation, and NaCl acted as a promotor, enhancing PO selectivity by reducing combustion. The stability of the trimetallic catalyst was tested continuously over a 10-h period; the catalyst exhibited a slow deactivation due to sintering. However, it can be regenerated by dissolving in dilute HCl and re-calcining.

Chapter 4. Electrospinning, Electrospun Silica Supported and Metal Oxide Nanofibers and Their Application to Propylene Epoxidation.

While the electrospun catalysts in this dissertation are metal oxide-based materials, the most thoroughly documented study performed in this work on the electrospinning process was done on protein/synthetic fiber nanofiber composites. The trends ascertained in this study are presented here and offer great insight for tuning the electrospinning process for the creation of fabric catalysts. This chapter also covers attempts at synthesizing metal oxide-based catalysts, silica supported and unsupported, for use in the direct epoxidation of propylene by molecular oxygen. It was found that electrospun nanofibers were uniformly poor epoxidation catalysts compared to powders of similar materials. An explanation of why is presented that utilizes a proposed mechanism for propylene epoxidation on $\text{RuO}_2\text{-CuO-NaCl/SiO}_2$ catalytic materials.

4.1. Electrospinning Process Parameter Investigation on Protein/Synthetic Polymer Composite Nanofibers.

4.1.1. Mixing and Viscosity Experimental Approach.

In order to electrospin, our biopolymer mixtures need to be stable suspensions or solutions such that the material did not sediment. In addition, the solvents need to be non-toxic and maintain our biopolymers' biofunctionality. Hence, we first performed a screening

of different solvent systems to see which were suitable for each of our three proteins: bovine casein, bovine hemoglobin, and bovine serum albumin (BSA). We examined the following solvents: water, acetic acid, ethyl acetate, and dimethylformamide [94]. We also examined combining each protein with the synthetic polymers to improve spinning parameters. Polyethylene oxide (PEO) and polyvinylpyrrolidone (PVP) were selected due to their previous use in biomedical applications.

Each protein was first dissolved in water at as high of concentration as possible. 0.667g/mL solutions of BSA and hemoglobin were created. Casein, being not very water soluble, was eventually seen to create a stable suspension using ethanolamine. Upon attempts to electrospin these protein solutions, we found that none of these solutions could produce fibers, even upon dilution. By gradually adding 100 kDa polyethylene oxide (PEO) or 1.3 MDa polyvinylpyrrolidone (PVP), to each protein solution, we were able to obtain solutions that sprayed droplets. Through a series of trials, solutions were eventually obtained that produced fibrous webs. Upon further tuning, solutions were eventually obtained from which fibrous material could be spun.

The viscosity was measured using an Ubbelohde viscometer by filling the viscometer up to the filling marks. Using a pipet bulb, fluid was drawn up past both graduation marks. After removing the bulb, the fluid flowed towards the graduation marks. Using a stopwatch, the time that it takes the fluid to flow from the first graduation mark to the second was collected. Using this time, we calculated the viscosities of our solutions using water as a standard. These viscosities are under the assumption of a Newtonian fluid, which is not

precisely the case for polymer solutions; however, the utility of these calculations is to help achieve a rudimentary relationship between viscosity, spinnability and nanofiber morphology.

4.1.2. Electrospinning and Imaging Procedures.

For any of the mixtures that were found to be either a clear, homogeneous solution or a stable suspension, electrospinning was attempted. As shown in Figure 4.1, a syringe pump was used to slowly deliver the solution through Teflon tubing to a 25 gauge needle. A conductive collector plate, covered with aluminum foil, was positioned a distance of 15 cm from the needle tip and was electrically grounded. Depending on the experiment, the needle and collector were positioned such that spinning commenced either at a 45 degree angle downwards, or vertically upwards (Figure 4.2). The flow rate was 1.0 mL/hr when spinning downwards and 3.0 mL/hr when spinning upwards. The needle was connected to a high-voltage power supply. The applied DC voltage was 25 kV in all experiments. We also attempted to electrospin fibers with the voltage applied to the plate and the needle grounded.

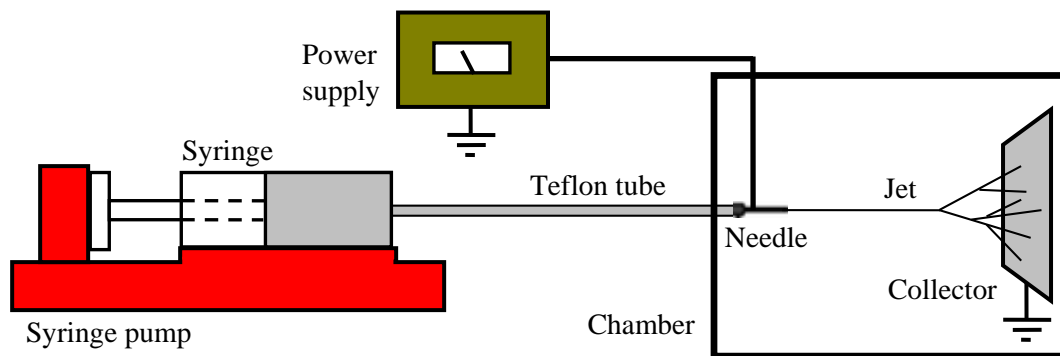


Figure 4.1. Electrospinning setup used in the synthesis of nanofibers.

If a mixture fired droplets at the collector plate when the voltage was applied, the process was stopped. For mixtures that created solid material, spinning commenced for about one hour. Once the process was finished, the power supply and syringe pump were turned off, and the aluminum foil, containing the collected material, was removed from the plate and stored in a petri dish. Sections of aluminum foil with collected material were cut for scanning electron microscope (SEM) imaging on a JEOL JSM-67 Field-Emission Scanning Electron Microscope. Energy-dispersive x-ray spectroscopy (EDS) was also performed using the previous JEOL SEM on one sample to study compositional uniformity for proteins that were co-spun with PVP.

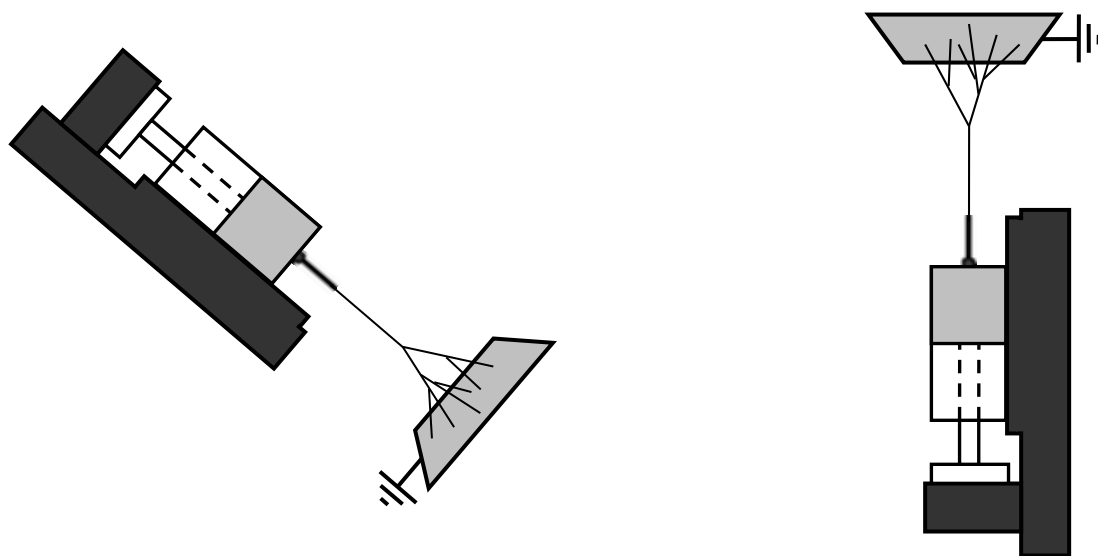


Figure 4.2. Electrospinning vertically downwards (left), at a 45 degree tilt downwards (middle) and vertically upwards (right).

Since all our samples are composed of non-conductive polymer, it is necessary to coat the fibers with a conductive metal for imaging with SEM. Samples were all cut to 1 cm²

squares and sputter-coated with gold at 15 mA and 70 mtorr for 90 seconds prior to imaging. Samples appear dark green in color after sputtering. Images were taken at different magnifications and fiber thickness was measured.

4.1.3. Mechanical Tensile and Permeability Properties Acquisition Methodology.

Initially, mechanical tensile properties were to be investigated using a system in which the material is suspended from a binder clip and various masses are suspended from the sample. As larger masses are suspended, the change in strain was to be measured. When this method was attempted, it was found that the samples were too fragile for repeated attachment of different masses and would fail at the clamp boundary. In addition, the materials were too weak to suspend anything except the smallest mass, resulting in only one data point. Alternatively, a TA Instruments DMA Q800 was used to apply a constant strain rate, while measuring the stress applied to obtain that strain. Even using the DMA Q800, many of the samples were too fragile to load onto the machine.

Samples were loaded onto the DMA Q800 equipped with thin film clamps using a torque wrench set to 3 lbs/inch². The width and thickness were measured using calipers and the initial length is measured using the displacement displayed by the DMA. These values were inputted into the computer. The machine is set to pull at a constant displacement rate of 100 $\mu\text{m}/\text{min}$ to 10% the initial length. Since our samples are viscoelastic materials, a fast strain rate is desired to minimize viscous effects, but the strain rate must be slow enough to collect sufficient data points prior to destroying the sample. The data collected was plotted as

stress versus strain and the Young's modulus and maximum tensile strength was read off the graph.

For permeability tests, vials were filled with 2 mL of methanol, chosen since it is hydrophilic like water and thus may somewhat simulate moisture evaporation through a wound covered with a bandage, but has a much higher vapor pressure at ambient temperature. One vial was left open to atmosphere while the others were covered with portions of electrospun fiber mats. The portion of the mat that was cut out was weighed on an analytical balance beforehand. The rate of mass change was observed on an analytical balance over a ten-minute time frame to estimate evaporation rates. Since the evaporation is endothermic, during the experiments, the vials were placed on a stainless steel block, functioning as an energy reservoir to help fix the temperature, which was held at approximately 20 °C.

4.1.4. Mixing and Viscosity Results.

Initially, protein solutions of the three proteins were attempted using water, ethyl acetate, and acetic acid as co-solvents, as has been used with gelatin, denatured collagen [94, 95]. The solvent system, however, failed to produce homogenous suspensions of protein in solution. Since each protein has unique properties due to either unique amino acid sequence resulting in unique intramolecular and intermolecular interactions, we decided to evaluate each protein individually for solubility, viscosity, and eventually electrospinnability.

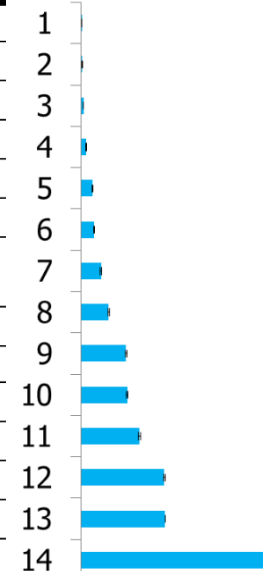
None of the proteins dissolved well in dimethylformamide, a common peptide synthesis solvent. Water was able to dissolve both BSA and hemoglobin up to a concentration

of 0.67g/mL with gentle heating, but neither of these solutions was spinnable. These solutions were tuned for spinnability by addition of synthetic polymers (PEO and PVP) to the solution. Casein, however, would not dissolve in only DI water. Casein solubility was reported to increase in basic solutions [96]. Adding sodium hydroxide to the solution created a stable suspension, but was not spinnable. Due to the harsh pH (pKa of 13), the protein denatured after a short period of time evolving a smell similar to spoiled milk. Using ethanolamine (pKa of 9.5) instead of sodium hydroxide yielded a similar stable suspension, but did not denature casein over the appreciable time required for electrospinning. Just like BSA and hemoglobin, the addition of synthetic polymer was necessary to obtain a spinnable solution.

For solutions that were electrospun, viscosity was measured (Table 4.1). As expected, the higher concentration of protein and polymer within the solution, the higher the viscosity of the solution. In the casein solution, the addition of ethanolamine (1.9×10^{-2} Pa·s) significantly increased the viscosity of the solution.

Table 4.1. Measured viscosities of electrospun solutions.

Sample #	Solution	viscosity (Pa x s)	percent uncertainty
1	water	$1.0 \cdot 10^{-3}$	
2	1g BSA, 0.11g PEO, 12mL H ₂ O	$1.4 \cdot 10^{-3}$	0.66%
3	1g BSA, 0.2g PEO, 9mL H ₂ O	$2.8 \cdot 10^{-3}$	2.29%
4	1g BSA, 0.3g PEO, 7mL H ₂ O	$5.5 \cdot 10^{-3}$	0.94%
5	1g BSA, 0.3g PEO, 5mL H ₂ O	$1.3 \cdot 10^{-2}$	4.10%
6	1g BSA, 0.5g PEO, 7mL H ₂ O	$1.5 \cdot 10^{-2}$	4.14%
7	0.5g casein, 0.225g PVP, 6.275mL H ₂ O, 1mL ethanolamine	$2.2 \cdot 10^{-2}$	3.15%
8	BSA 1g/mL H ₂ O	$3.1 \cdot 10^{-2}$	6.46%
9	1g BSA, 0.5g PVP, 5.83mL H ₂ O	$5.0 \cdot 10^{-2}$	3.65%
10	1g BSA, 0.5g PVP 5.33mL H ₂ O	$5.2 \cdot 10^{-2}$	2.36%
11	1g BSA, 0.5g PVP, 4.83mL H ₂ O	$6.4 \cdot 10^{-2}$	2.64%
12	1g hemoglobin, 0.5g PVP, 4.33mL H ₂ O	$9.2 \cdot 10^{-2}$	2.82%
13	1g BSA, 0.5g PVP, 4.33mL H ₂ O	$9.3 \cdot 10^{-2}$	1.70%
14	1.5g PVP, 8.5mL H ₂ O	$2.0 \cdot 10^{-1}$	0.24%



4.1.5. Electrospun Protein/Synthetic Polymer Nanofibers and Images.

Fourteen unique samples were electrospun. The specifications and diameter data, including relative standard deviation (RSD), are compiled into Table 4.2. Also shown in Table 4.2 is a summary of the figures in this section that reference each sample. Diameter data were collected by selecting about 10 fibers in each sample and measuring the sizes on the SEM software. It is important to note that we found none of the proteins would electrospin in aqueous solution without an accompanying synthetic polymer such as PEO or PVP, even at very high protein concentrations (~ 40 wt%). We suppose that globular proteins alone do not entangle substantially. When protein and PEO (or PVP) are present in solution, the globular proteins may become “caged in” by PEO polymers due to interactions of the outer hydrophilic

shell of the protein with the hydrophilic synthetic polymer. With this effect, the globular protein would be carried along while the PEO is electrospun, giving a composite nanofiber of fairly uniform composition.

Table 4.2. Compilation of solutions that were electrospun, their compositions, their key spinning conditions, and resulting fiber diameters.

Sample #	Composition (wt %)	Key Conditions	Spinning	Diameter (nm) & RSD	Appears in Figure(s)
1	8% BSA, 0.8% PEO	45° down, grounded collector	-	-	Figure 4.3(a)
2	10% BSA, 2% PEO	45° down, grounded collector	-	-	Figure 4.3(b)
3	12% BSA, 4% PEO	45° down, grounded collector	-	-	Figure 4.3(c), Figure 4.4(a)
4	16% BSA, 5% PEO	45° down, grounded collector	-	79 ± 12%	Figure 4.3(d)
5	12% BSA, 6% PEO	45° down, grounded collector	-	80 ± 20%	Figure 4.4(b)

6	16% BSA, 8% PVP	45° down, grounded collector	499 ± 34%	Figure 4.5, Figure 4.7(a)
7	13.6% BSA, 6.8% PVP	Up, grounded collector	120 ± 45%	Figure 4.6(a,b)
8	14.6% BSA, 7.3% PVP	Up, grounded collector	171 ± 36%	Figure 4.6(c,d)
9	17.2% BSA, 8.6% PVP	Up, grounded collector	236 ± 27%	Figure 4.6(e,f), Figure 4.7(b)
10	17.2% Hb, 8.6% PVP	Up, grounded collector	109 ± 33%	Figure 4.8(a,b)
11	17.2% Hb, 8.6% PVP	45° down, grounded collector	171 ± 41%	Figure 4.8(c,d)
12	7% casein, 3% PVP, 13% ethanolamine	45° down, grounded collector	118 ± 40%	Figure 4.9(a,b)
13	7% casein, 3% PVP, 13% ethanolamine	45° down, grounded needle	64 ± 33%	Figure 4.9(c,d)
14	15% PVP	Up, grounded collector	199 ± 27%	Figure 4.10

Shown in Figure 4.3 are samples electrospun from aqueous solutions containing BSA and PVP. The total polymer concentration of the spinning solution is increasing from (a) through (d). The sample in Figure 4.3(a) is electrospay spheres of ~100 nm diameter, indicating the viscoelastic property of the solution was insufficient to create a stable, straight jet that would form nanofibers. In Figure 4.3(b), both the total polymer concentration and PEO:BSA ratio are increased relative to Figure 4.3(a), resulting in what appears to be electrospay spheres connected to form outlines of fibers. The PEO:BSA ratio and total polymer content are both increased again in Figure 4.3(c), giving fibers that appear as beads on a string along with some electrospay. In Figure 4.3(d), the total polymer concentration is increased with the PEO:BSA ratio fixed relative to Figure 4.3(c), giving nanofibers with occasional beads. Clearly, the total polymer content is critical for achieving straight fibers. The pictures in Figure 4.3 show an increasing progressive dominance of the viscoelasticity over the liquid-air surface tension to form straight fibers as the polymer concentration is increased.

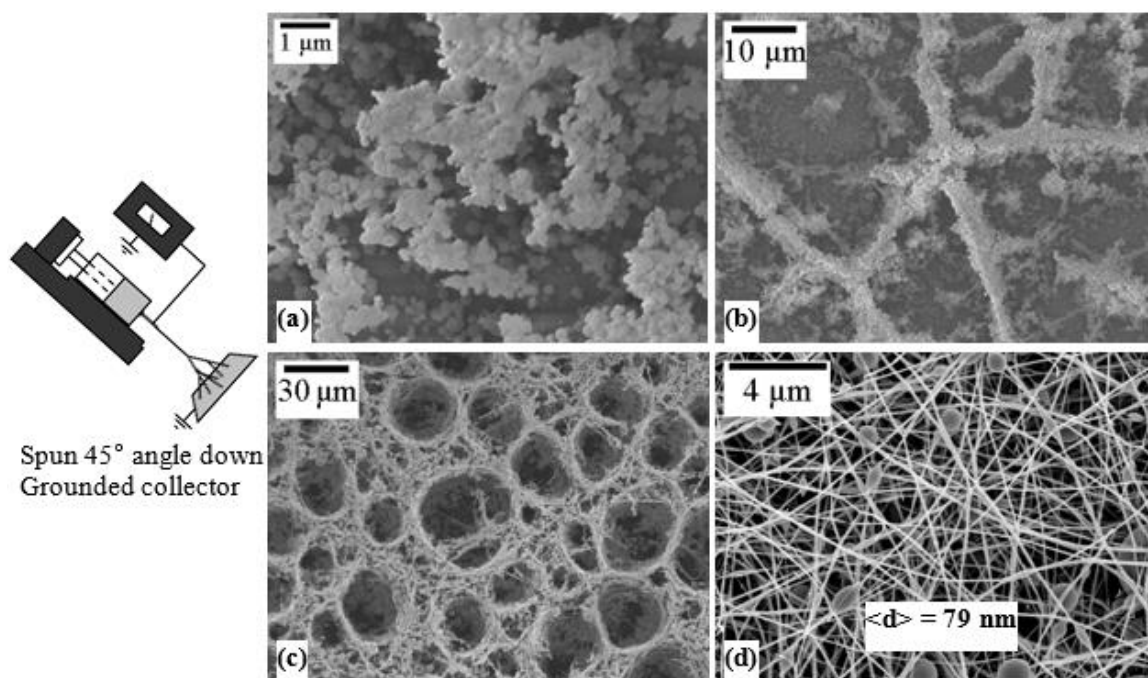


Figure 4.3. Illustration of progressive tendency to stabilize straight fibrous structure as total polymer content of the aqueous spinning solution, containing BSA and PEO, increases.

Figure 4.4 shows that when the PEO:BSA ratio is increased with the BSA concentration fixed, fibrous structures are stabilized. Figure 4.4(a) is the same sample shown in Figure 4.3(c), containing mostly beaded fibers. A 50% increase in the PEO:BSA ratio is sufficient to stabilize the fibers shown in Figure 4.4(b), suggesting that PEO has a critical function of facilitating entanglement of all polymeric components within the spinning solution as we stated previously. To reiterate, the trend from Figure 4.3 shows stabilization of fiber structure as both PEO and BSA are increased whereas the trend from Figure 4.4 shows this occurs when PEO only is increased. These facts combined with the fact that we were unable to produce nanofibers with PEO:BSA ratios much lower than what we used in Figure 4.3(d) and Figure 4.4(b) support the idea that the synthetic polymer is being electrospun while it encases globular proteins by attractive hydrophilic actions. Thus, it is entirely possible that

the proteins, which have diameters in the single nanometer range, are still globular in form when incorporated into the nanofiber. A study with transmission electron microscopy (TEM) may be able to see fine enough features on the fiber to investigate this.

Shown in Figure 4.5 are nanofibers electrospun from an aqueous BSA/PVP solution. These fibers have an average diameter of 499 nm, much larger than the BSA/PEO electrospun fibers of ~80 nm. Note that the weight percent of BSA and synthetic polymer is not identical in this comparison as the fiber with PVP has a ~33% higher concentration of synthetic polymer and protein. However, we would not expect a 6-7 fold increase in diameter from a concentration increase of that degree. We attribute the large size of the BSA/PVP nanofibers principally due to the fact that the PVP we use has a molecular weight of 1.3 MDa whereas the PEO we use has a molecular weight of 100 kDa. To substantiate this hypothesis, PVP has fewer hydrogen bonding sites than PEO, per mole, which may result in decreased molecular cohesion and a decreased diameter, which is what we do not see.

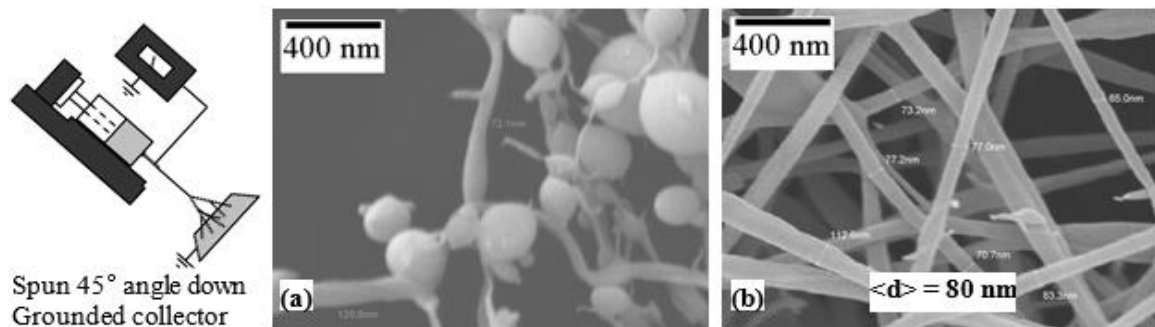


Figure 4.4. Straight fibrous structure is stabilized as PEO/BSA ratio is increased with BSA concentration fixed.

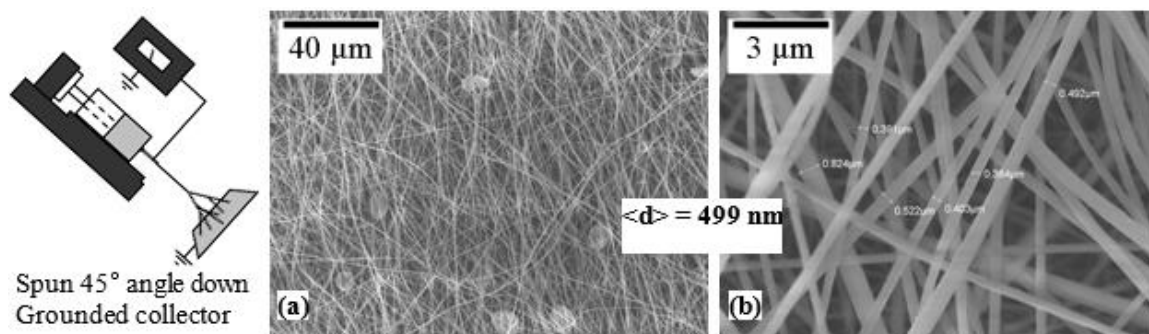


Figure 4.5. Electrospun BSA/PVP composite nanofibers exhibit much larger diameters than BSA/PEO fibers of Figure 4.3(d) and Figure 4.4(b).

Figure 4.6 compiles SEM images of BSA/PVP nanofibers electrospun in the vertical arrangement with a grounded collector. Figure 4.6(a,b) are from the same sample of 120 nm average diameter. Figure 4.6(c,d) are from the same sample of 171 nm average diameter while Figure 4.6(e,f) are from a sample of 236 nm average diameter. The PVP:BSA ratio is fixed in all these samples. We find that as the total polymer concentration increases, the fiber diameter increases as expected due to more entanglement.

Shown in Figure 4.7 is a comparison of BSA/PVP fibers produced from different spinning orientations. The sample spun downward at a 45° angle downward has a larger diameter than the sample spun upward by nearly twofold. Note that while these samples did not have identical composition, the fiber of smaller diameter actually had a higher concentration of both BSA and PVP, which, as an isolated factor, would result in an increase in diameter. This contradicts the result of Yang *et. al.*, who found an increase in fiber diameter when electrospinning poly(vinylidene fluoride) in dimethylformamide upwards relative to downwards [97]. We suppose that this contradiction may be due to the fact that fiber length has not been accounted for. When a long fiber is being electrospun upwards, long enough

such that it is nearly connected from needle to ground, the gravitational body force will resist the upward electrical force and cause a decrease in the degree of jet extension. However, when fibers are short, such that we can visualize short cylinders being ejected at the collector, the electrical force would pull at the front of the fibers while the gravitational force would be able to pull at the back of the fibers because they are midair, resulting in a net increase in the degree of extension and thus giving thinner fibers. Since the nature of our SEM images did not allow us to account for fiber length, a future study could work to investigate this hypothesis. A supporting factor in our reasoning is that dimethylformamide has a surface tension of 37 mN/m while water has a surface tension of 73 mN/m at 20 °C. Surface tension may be a limiting factor in fiber length, with higher values impeding the formation of a long jet.

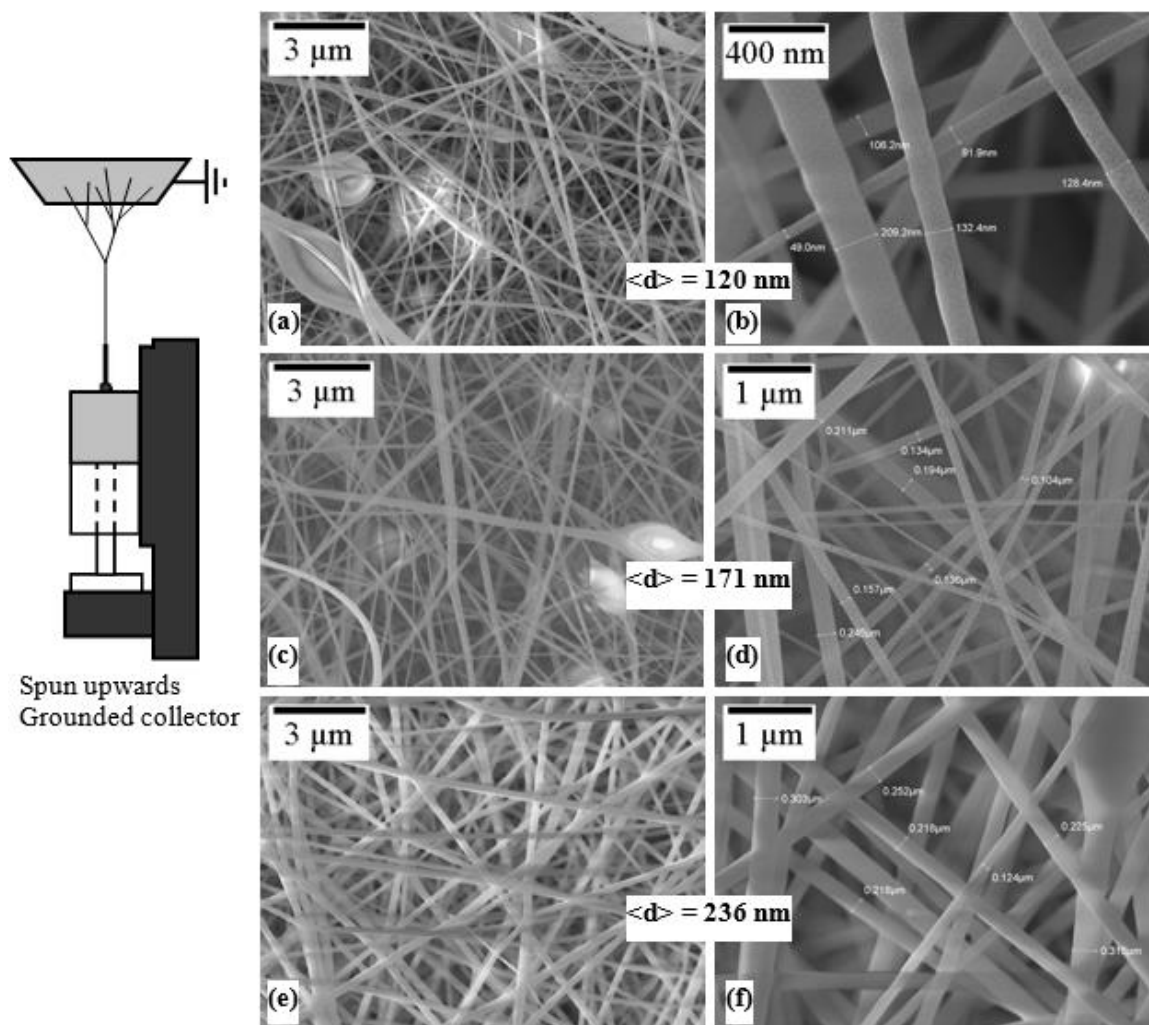


Figure 4.6. Illustration of progressively increasing average fiber diameter as total polymer content increases for BSA/PVP composite nanofibers spun vertically upwards with grounded collector.

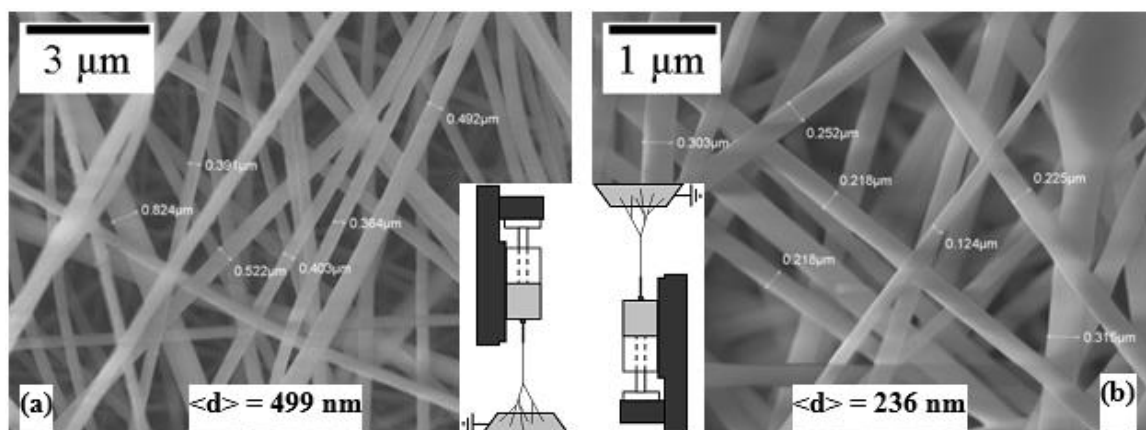


Figure 4.7. BSA/PVP composite nanofibers shown to have larger diameter when electrospun downward at 45° angle compared to when spun vertically upwards.

Figure 4.8 shows a Hb/PVP sample electrospun upwards (a,b) and downwards at a 45° angle (c,d). Both samples had identical compositions. We see that electrospinning upwards results in smaller diameter fibers, consistent with our results with BSA/PVP and in conflict with the conclusions of Yang *et. al* [97]. Furthermore, these solutions had identical weight percents of protein and PVP compared to the BSA/PVP solution used to electrospin the sample of Figure 4.6(e,f). The hemoglobin samples have average diameters smaller than the BSA/PVP sample. Both proteins are hydrophilic and have similar molecular weights. One significant difference in structure could be the presence of an iron atom in hemoglobin, which could increase the conductivity of the spinning solution and potentially result in faster charge migration to the fluid surface at the needle tip, giving thinner fibers due to faster ejection.

Shown in Figure 4.9 are a casein sample electrospun with a grounded collector (a,b) and a sample electrospun from an identical solution with a grounded needle (c,d). When the needle is grounded instead of the collector, the resulting fibers have a smaller average diameter and are beaded. It is important to note that when measuring diameter of a beaded fiber, we typically avoided the bead portion. Thus, the discrepancy in diameter is at least partly due to the fact that a beaded fiber has a non-uniform diameter and we selected the smaller parts. When the collector is grounded and positive voltage applied to the needle, electrons are stripped from the liquid at the needle tip, creating positive charges that can distort the hanging droplet into the Taylor cone shape. After the evaporated jet hits the collector, the ground serves as an infinite reservoir of electrons that neutralizes the positive charges that were on

the jet. When the needle is grounded and voltage applied to the collector, electrons flow from the grounded needle to the fluid and then to the collector. The electric field is no longer as focused at the tip. Also, the positively charged collector may interact with and draw electrons from the surrounding environment. This would essentially make the 25 kV voltage less effective at creating jet motion for the case of the grounded needle compared to the case of the grounded collector, consistent with the results we get in Figure 4.9.

Figure 4.10 shows a sample spun from an aqueous solution containing only PVP and no protein. A large percentage of the sample appeared wet and it was observed during spinning that the collector plate was moist. PVP is hygroscopic and thus may be unwilling to surrender water solvent molecules to the surrounding environment during the travel of the jet to the collector.

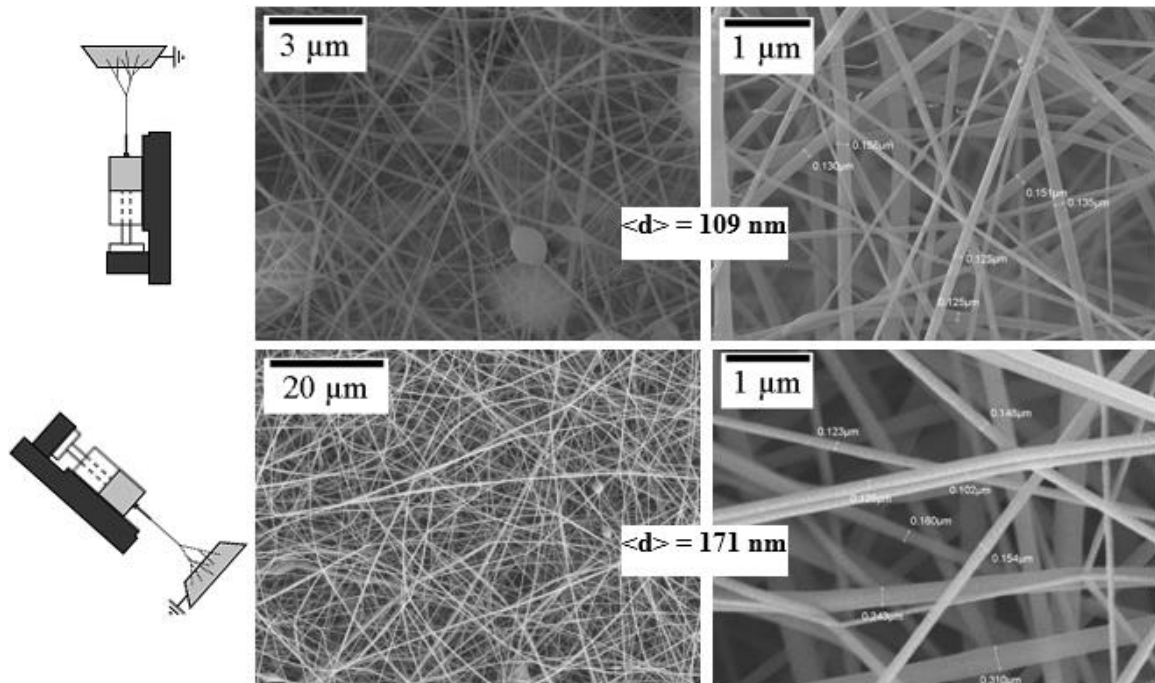


Figure 4.8. Hb/PVP composite nanofibers shown to have larger diameter when electrospun downward at 45° angle compared to when spun vertically upwards.

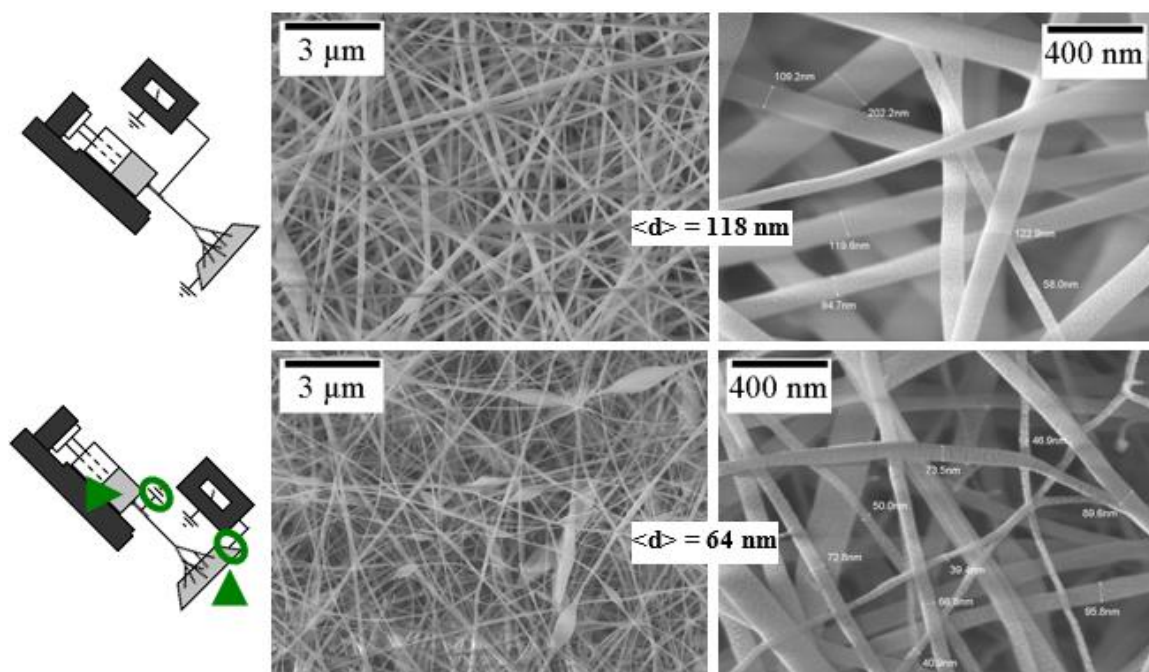


Figure 4.9. Casein/PVP nanofibers electrospun with a grounded needle shown to have smaller diameters and frequent beads compared to those electrospun with a grounded collector plate.

Shown in Figure 4.11 is a plot of solution viscosities as a function of the fiber diameter that results after electrospinning for the three BSA solutions spun upwards from Figure 4.6 and the two hemoglobin solutions spun upwards and down at a 45° angle from Figure 4.8. Note that the two hemoglobin fiber samples electrospun at the two different orientations were from the same solution, hence the identical values for the viscosity. For BSA, there clearly is a positive correlation between viscosity and fiber diameter as expected. Additionally, the third BSA solution and Hb solutions were electrospun into fibers with similar solution viscosities had vastly different diameters despite significantly different viscosities. Hence, the viscosity may not be a good predictor of diameter across different chemical species. One must consider, among other things, cohesiveness, which involves attractive and repulsive molecular

interactions, and conductivity in addition to the viscosity when rationalizing the size of an electrospun fiber.

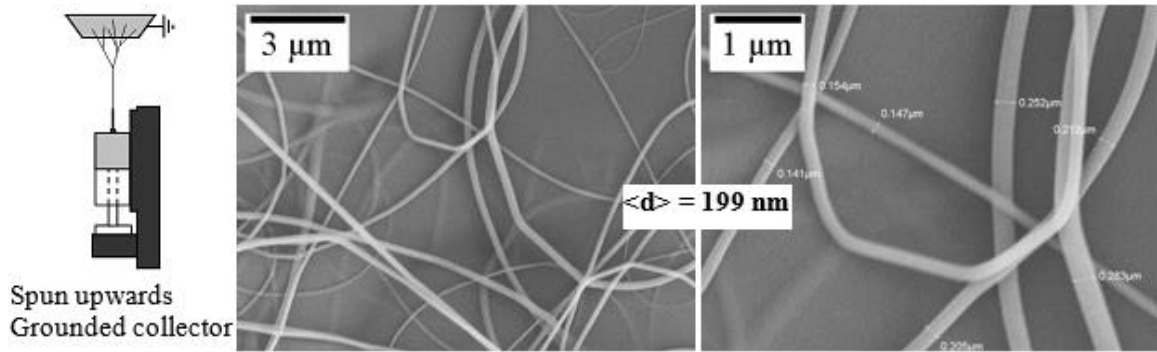


Figure 4.10. PVP electrospun alone in aqueous solution at conditions similar to previous samples shown to arrive wet at the collector plate.

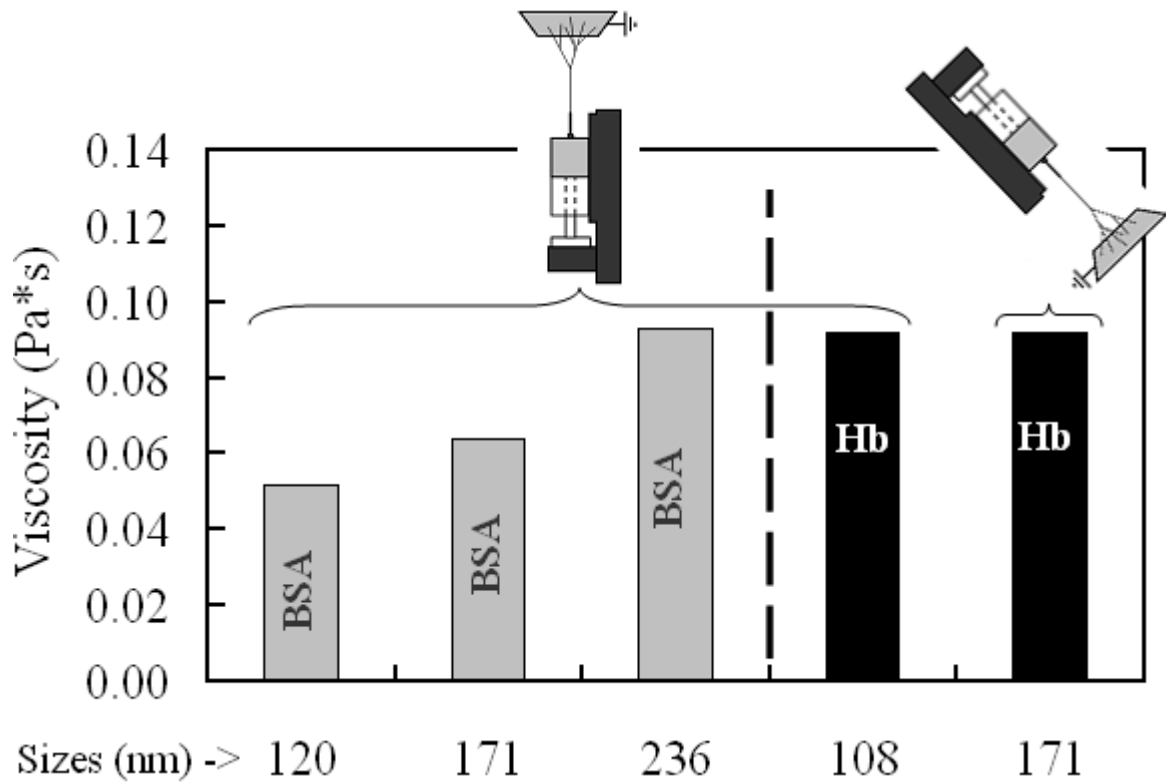


Figure 4.11. Bar plot illustrating a correlation between viscosity and resulting fiber diameter for a given chemical species.

4.1.6. Strength Assessments of Nanofibers.

In order to assess the strength of our electrospun materials, they must be peeled off the aluminum backing and be strong enough to survive handling and loading. Initially, the yield modulus was to be assessed by hanging a series of weights to the material and measuring the change in strain. Of the three samples that survived the peeling, handling, and loading process, none of them were strong enough to handle the masses that were readily available. In addition, they tend to rip at the sample-mass interface from repeated attachment and detachment of the mass.

Alternatively, we used a TA Instrument DMA Q800 to evaluate the material properties of our testable materials. Samples used in the DMA Q800 could be as small as 5 mm in width and 1 cm in length, much smaller than required by the crude method previously employed, due to the machine's sensitivity. The DMA Q800 was set to pull at a constant rate as the force cell measured the amount of force required to maintain that constant displacement rate. This force cell emits a voltage proportional to the force it measures, and the voltage is monitored and translated back into a force by the acquisition computer, which also divides the force by the cross-sectional area measured to produce a stress-strain curve. Representative stress-strain curves are plotted in Figure 4.12 and the results of the test are summarized in Table 4.3.

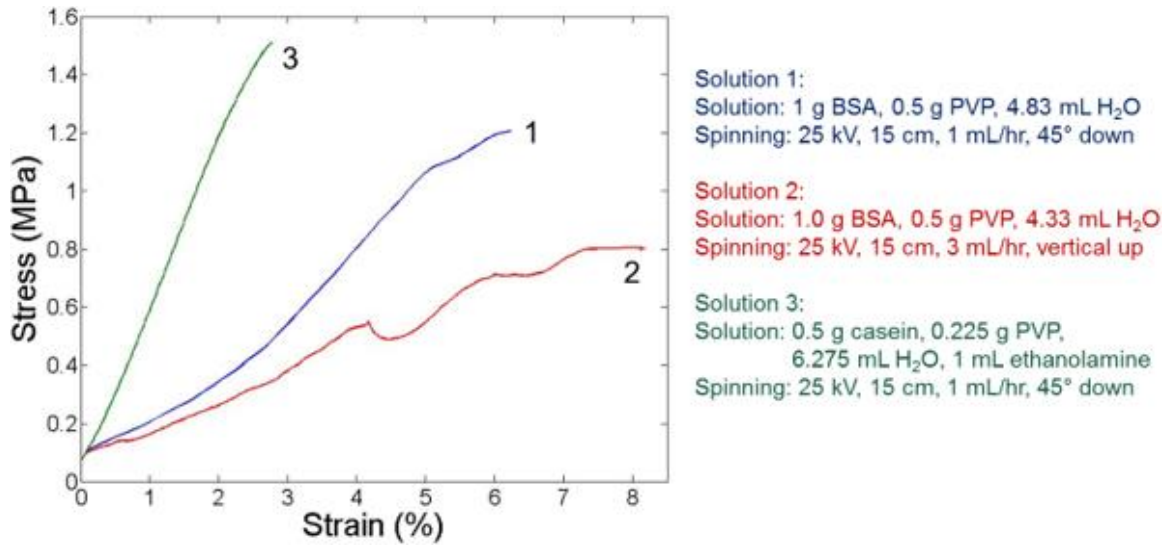


Figure 4.12. Representative stress-strain curves for the samples tested for strength assessment.

Table 4.3. Young's Moduli and Ultimate Tensile Strength of Tested Electrospun Materials.

Sample	Young's Modulus (MPa)	% error	Ultimate Strength (MPa)	% error	Fiber diameter (nm)
Solution: 1.0 g BSA, 0.5 g PVP, 4.83 mL H ₂ O Spinning: 25 kV, 15 cm, 1 mL/hr, 45° down	24.2	2%	1.1	16%	499
Solution: 1.0 g BSA, 0.5 g PVP, 4.33 mL H ₂ O Spinning: 25 kV, 15 cm, 3 mL/hr, vertical up	11.7	5%	0.9	11%	236

Solution: 0.5 g casein, 0.225 g PVP, 6.275 mL H ₂ O, 1 mL ethanolamine Spinning: 25 kV, 15 cm, 1 mL/hr, 45° down	55.1	3%	1.7	56%	118
---	------	----	-----	-----	-----

With larger diameter fibers, electrospun BSA fibers are stiffer and exhibit a higher ultimate tensile strength. With larger fibers, there is a higher cross-sectional area compared to smaller fibers that take up the same overall volume. Unexpectedly, the casein sample, having the smallest fiber diameter exhibited significantly higher stiffness and ultimate tensile strength. We hypothesize that casein electrospun materials exhibit these observed properties due to its hydrophobicity causing the proteins to aggregate on a molecular level. The protein's tight intermolecular interaction creates fibers that are more densely packed, increasing the strength of the fibers.

4.1.7. Permeability Assessments of Fabric Mats.

For permeability determination, we use a simplified mass transfer model. After liquid methanol evaporates at the vapor-liquid interface, it experiences three distinct mass transfer resistances that occur in series: within the gas phase *internal* to the vial, through the fibrous *mat*, to the surrounding *external* air. The methanol vapor concentration at the vapor-liquid

interface is assumed to be equal to the vapor pressure of methanol in air c_{vap} at 20 °C. The volumetric flow rate Q of methanol is given by Eq. 4.1:

$$Q = (A/R)(c_{vap} - c_{atm}) \quad (4.1)$$

where $A = \pi d^2$ is the surface area at the top of the vial, d is the vial inner diameter, and c_{atm} is the methanol concentration of the bulk atmosphere, assumed to be zero. The total mass transfer resistance is $R = R_i + R_m + R_e$, where the internal, mat and external resistances are $R_i = 1/k_{m,i}$, $R_m = 1/P_m'$ and $R_e = 1/k_{m,e}$ respectively. The permeance $P_m' = P_m/m$ is the ratio of the permeability and the mass of the mat resting on the top of the vial. The literature often uses the thickness instead of the mass; however, we assume the thickness scales linearly with the mass, which is simpler to measure. The mass transfer coefficients are $k_{m,i}$ and $k_{m,e}$, found from:

$$Q_{ref} = [A/(R_i + R_e)](c_{vap} - c_{atm}) \quad (4.2)$$

where Q_{ref} is the methanol volumetric flow rate for the case the vial is not covered with a mat. Combining the previous relationships, an explicit expression for the permeability may be obtained:

$$P_m = (4m/\pi d^2 c_{vap})[(1/Q) - (1/Q_{ref})]^{-1} \quad (4.3)$$

where the vials have inner diameters of $d = 0.01$ m and $c_{atm} = 0$ for a methanol free external environment. The vapor pressure of methanol at 20 °C is approximately 100 mmHg, corresponding to a concentration of $c_{vap} = 5.2$ mol/m³ assuming ideal gas behavior. Since each mat may have a different thickness, m varies in addition to Q . The flow rates Q and Q_{ref} were determined from the rate of mass change on an analytical balance over a ten minute timeframe. The fiber mass m that impedes mass transfer was found by cutting out rectangular shaped

pieces of an electrospun mat, measuring the dimensions, weighing it, and scaling the weight to the ratio of the vial area $\pi d^2/4$ to the area of the cut rectangle.

The computed permeabilities for the fiber mats that were investigated are shown in Figure 4.13. The nanofibers made of casein were shown to have the lowest permeability of the six electrospun samples. Since methanol is hydrophilic, this may be due to repulsive interactions with hydrophobic casein side chains, thus impeding diffusion within the mat. BSA is more hydrophilic than casein and we see that the permeability of BSA fibers tend to be higher than the casein fibers. Also, with BSA, the permeability tends to increase with decreasing fiber size. Attractive forces between methanol and BSA may be significant enough that physisorption and surface diffusion may be significant, adding another mode of transport that may either be minor or non-existent with casein. Lastly, the band aid material, presumably made of cotton, showed the lowest permeability despite visually appearing to have large void spaces. This could be due to the presence of adhesive on these fibers that were holding it together with the rest of the bandage.

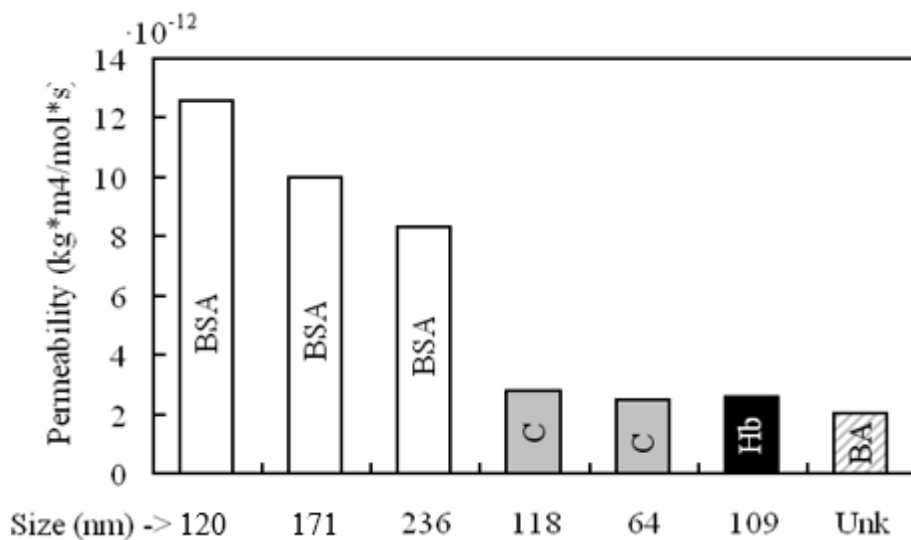


Figure 4.13. Permeability for various nanofibers of different diameter and composition, including bovine serum albumin (BSA), casein (C), hemoglobin (Hb), and band aid (BA) fiber.

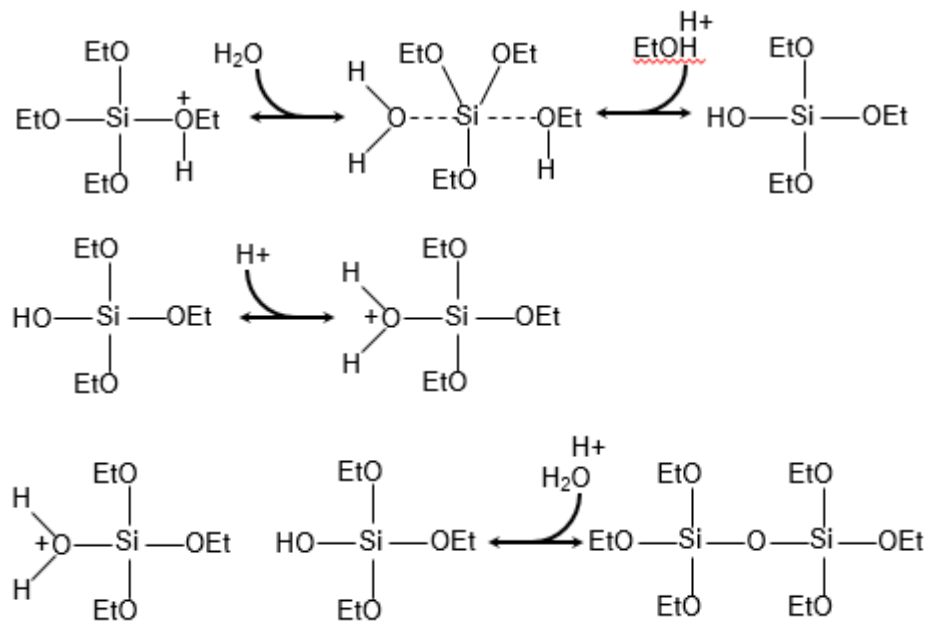
4.2. Nanofiber Catalysts and Propylene Epoxidation.

4.2.1. Preparation of Silica Supported Nanofiber Catalysts.

A typical synthesis of silica supported nanofiber fabrics was based on a previously detailed methodology [98-100]. This synthesis process involves a three-stage sequence of creating a partial sol gel comprising linear SiO₂ polymers, electrospinning this sol gel then calcining the collected fibers.

For the creation of the sol gel, tetraethyl orthosilicate (TEOS; 1.5 g), polyvinylpyrrolidone (PVP; 1.2 g; 1.3 MDa), Pluronic P-123 (0.5 g) and ethanol (10 g) were vigorously mixed in a screw cap vial at room temperature. The TEOS functioned as a precursor for the polymerization of SiO₂. The PVP and P-123 both functioned as polymer templates to allow for the formation of entangled networks of linear SiO₂ polymers into

nanofibers; the former also functioned as a means of increasing the solution viscosity, a necessary feature of solutions that can be electrospun, while the latter, as an amphiphilic template, allowed for the formation of *porous* silica fibers. The ethanol, as a co-solvent with H₂O, which is added later, allowed for the mutual solubility of all components during the following gelation process. Metal salts were also added as precursors for catalytically active sites on the materials such that the typical metal loading on the final material was 1-10 wt%. Once all components were well-mixed, the solution was heated to 80 °C, and, subsequently, 0.1 g of 2.0 M HCl was added to trigger the polymerization process, which involves hydrolysis and a set of condensation reactions. This heated solution was stirred for 30 min, after which it was cooled to room temperature. The relevant gelation reactions specifically utilize acidic conditions to promote the creation of linear silica polymers, whereas the use of a base would cause branching [101-104]:



in which the first reaction represents hydrolysis and ethanol condensation while the latter two are water condensation.

This sol gel was then subjected to electrospinning as shown in Figure 4.1. It was loaded into a syringe, which was placed onto a syringe pump. The syringe was connected to a fine steel needle held stationary inside a closed chamber via Teflon tubing. The chamber provided an enclosure which prevented fibers from exiting to the external environment and to shield the system from alternate electrical grounds. Inside the chamber, at a fixed distance horizontally away from the needle (typically 20-50 cm) was an electrically grounded steel collector covered in aluminum foil. The sol gel solution was pumped through the needle at a fixed rate (typically 0.5-2.0 mL/h) and the power supply provided 20-50 kV, causing liquid jets to be ejected towards the collector. These liquid jets would then convectively evaporate during flight, causing a solid fiber to precipitate upon landing on the foil.

Once a sufficient amount of material was collected to use as catalyst, the foil containing the co-spun material was transferred to an oven and air calcined at 550 °C to oxidize the synthetic polymers PVP and P-123, presumably to CO_x and NO_x, transform the metal salts into metal oxides and thus create fabrics of metal oxides with fibrous silica supports.

4.2.2. Preparation of Unsupported Metal Oxide Nanofiber Catalysts.

For nanofibers, composed solely of metals and/or metal oxides without and support material, the same electrospinning setup of Figure 4.1 was used. However, now, there is no initial gelation process needed. In a typical preparation, polyvinylpyrrolidone (PVP; 1.3 MDa) is mixed with a solvent containing water and ethanol (~1:1 – 1:2 weight ratio). To this solution, metal salts are added (e.g. $\text{AgCl}_3 \cdot x\text{H}_2\text{O}$, $\text{RuCl}_3 \cdot x\text{H}_2\text{O}$, $\text{Cu}(\text{NO}_3)_2 \cdot 2.5\text{H}_2\text{O}$, NaCl). The final solution may range approximately between 4-10 wt% PVP with a metal-to-polymer weight ratio of 0.10-0.30. Once these ingredients are well-mixed with a vortexer, the solution is loaded into a syringe, which is placed on a syringe pump. The solution is pumped at a fixed rate of 0.5-2.5 mL/h through a fine needle under 30-50 kV, causing streams to jet out towards the electrically grounded collector covered in aluminum foil. A typical needle-to-collector distance is 20-50 cm, adjusted long enough to allow for the liquid in the streaming jets to completely evaporate, creating composite nanofibers of PVP embedded with metal salts. After a sufficient amount of material is collected, the foil is then placed inside an oven for air calcination at 550 °C, high enough to fully combust the PVP.

4.2.3. Performance Evaluation and Characterization Procedures.

The materials (≈ 5 mg) were investigated for catalytic performance using the previously developed high-throughput heterogeneous catalytic screening system of Chapter 3. All experiments were performed under atmospheric pressure at a gas hourly space velocity of approximately $20,000 \text{ h}^{-1}$ controlled by using mass flow controllers

(MKS, Andover, MA). The feed gas consisted of 1 vol% propylene, 4 vol% O₂ and the balance He at 250 °C. Data analysis was conducted by an online Micro-Gas Chromatograph (Varian, CP-4900) equipped with a thermal conductivity detector (TCD), Porapak U (10 m) and 5 Å molecular (10 m) sieve columns. The detected products were propylene oxide, acetone, acetaldehyde, CO₂ and acrolein. The propylene conversion and selectivity of the products were determined on the basis of carbon balance. The reproducibility of the experiments was within ±10%.

Transmission electron microscopy (TEM) studies were performed by using an FEI Titan 80-300 TEM. For high-resolution TEM imaging, a field emission gun operating at 300 kV was used.

4.2.4. Nanofiber Fabric Imaging.

Shown in Figure 4.14 is an optical microscope image of electrospun silica nanofibers compared to a sample of human hair. The nanofibers are considerably thinner than the strand of hair and appear to exhibit high length-to-diameter aspect ratios, with no apparent terminal ends in the image. The fibers do, however, contain spherically shaped beads, indicative of the significance of surface tension during the spinning for this particular sample. The fibers are randomly oriented, as is typical for traditional electrospinning processes. Electrospun nanofibers are capable of being ordered; however, advanced equipment, such as a rotating collector, is necessary to accomplish this and is not implemented in this dissertation [105-108].

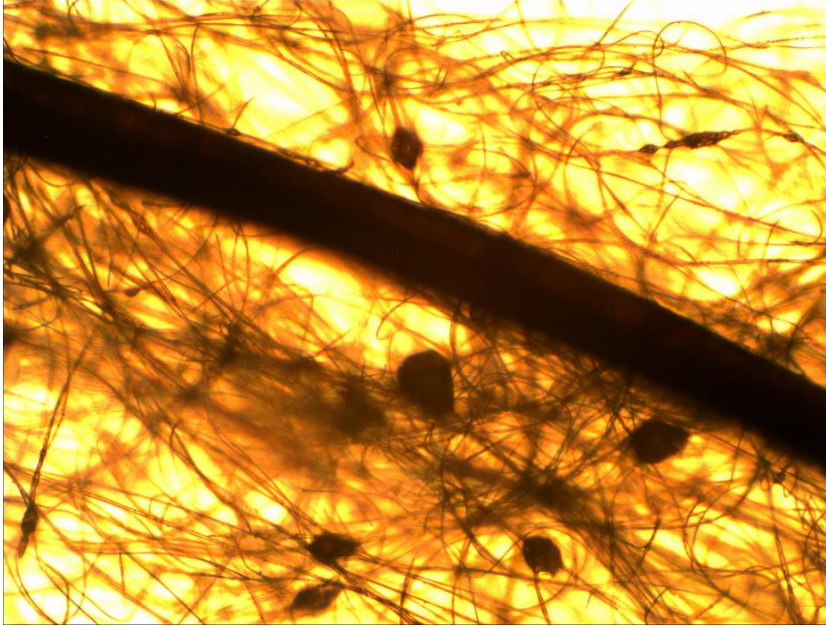


Figure 4.14. Optical microscope image of electrospun SiO₂ nanofibers compared to much thicker strand of human hair.

Shown in Figure 4.15 is a TEM image of an SiO₂-based nanofiber electrospun according to the aforementioned experimental procedure, but with Cu(NO₃)₂·2.5H₂O metal salt present in the spinning solution, resulting in composite CuO/SiO₂ nanofibers. By contrast, Figure 4.16 shows a TEM image of an Ag/SiO₂ nanofiber synthesized by electrospinning with AgNO₃. The latter image clearly shows discrete nanoparticles, presumably of Ag, dispersed on the external fibrous SiO₂ support material and is consistent with similar previously spun fibers, except the sol-gel solution was not refluxed in our work [99]. The former image does not show any clear distinct solid phases; however, its discoloration relative to Figure 4.16 would suggest that CuO exists in some form on the material, either as molecularly dispersed CuO, nanoparticles or both. The diameter of the CuO/SiO₂ nanofiber is approximately 190 nm while that of the Ag/SiO₂ nanofiber is 960

nm, the difference potentially due to the high conductivity of the $\text{Cu}(\text{NO}_3)_2 \cdot 2.5\text{H}_2\text{O}$ metal salt.

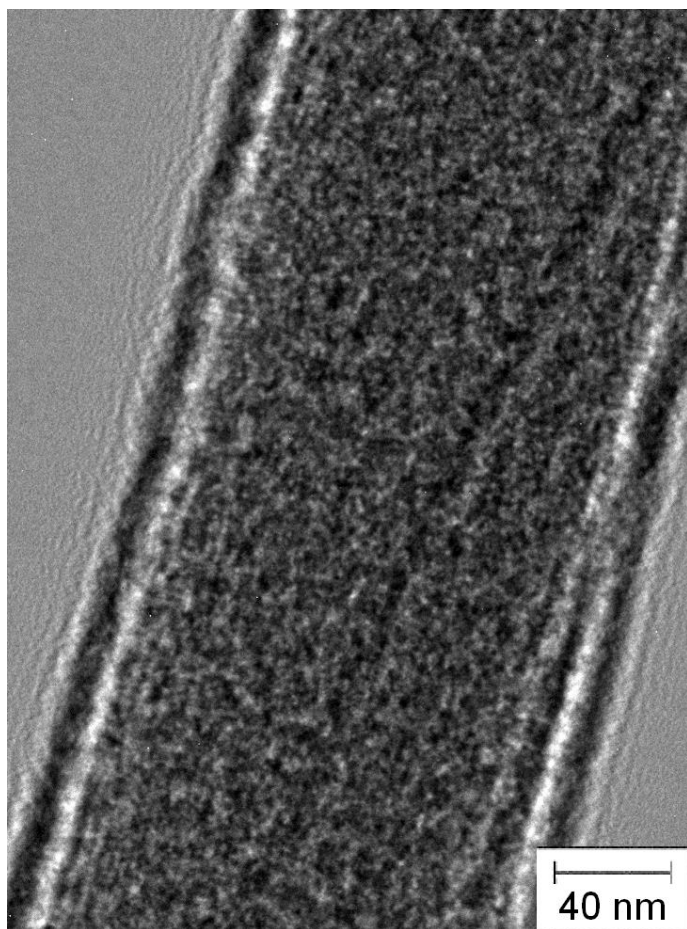


Figure 4.15. TEM image of CuO/SiO_2 nanofiber synthesized by electrospinning.

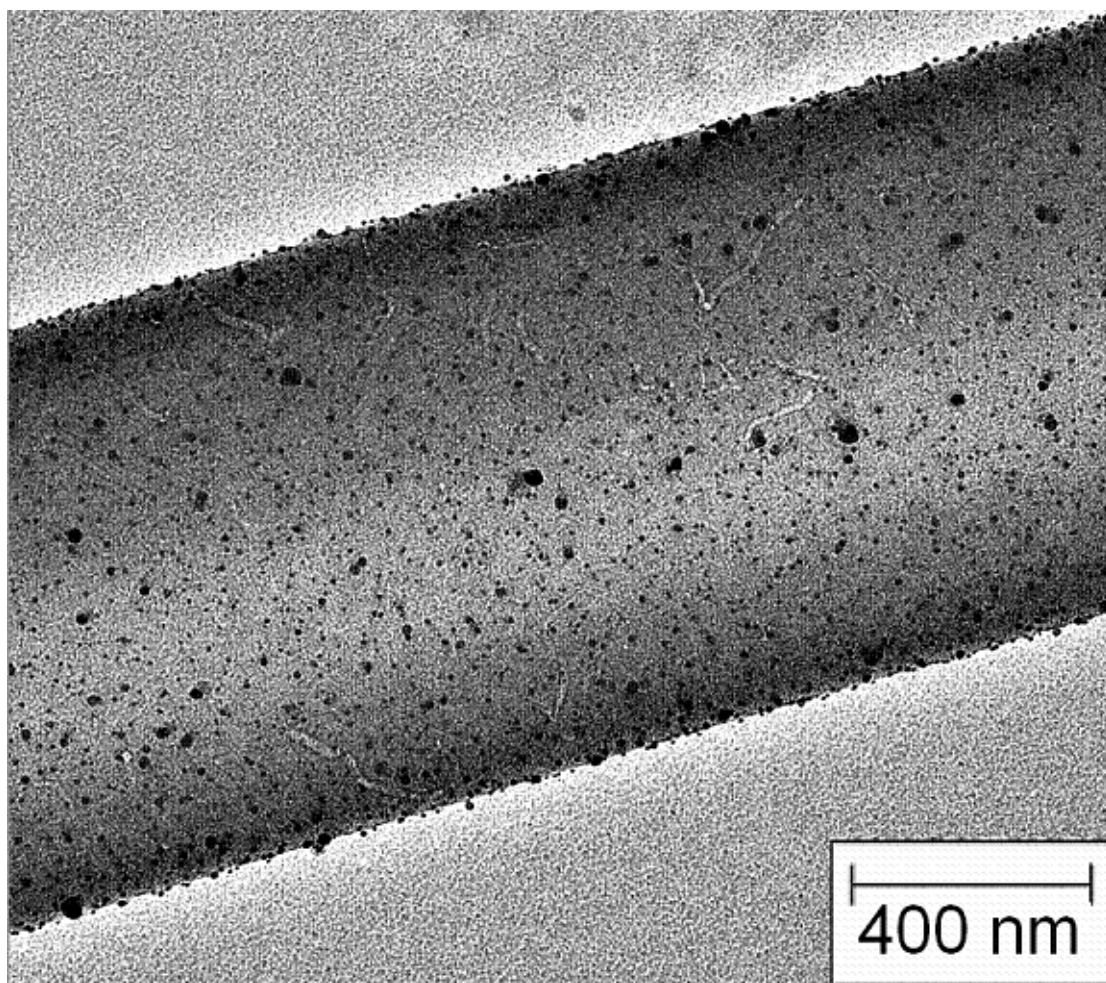


Figure 4.16. TEM image of Ag/SiO₂ nanofiber synthesized by electrospinning.

Figure 4.17 shows a TEM image of a bimetallic electrospun CuO-NaCl/nanofiber that appears to either be partly transparent, have multiple phases of solid materials or both. This nanofiber has a diameter of 1.4 μm , in stark contrast to the unimetallic CuO/SiO₂ fiber of Figure 4.15. The TEM image of Figure 4.18, showing nanofibers of unimetallic RuO₂/SiO₂ shows similar behavior, with partial transparency or multiple solid phases, the latter of which would therefore comprise of only distinct SiO₂ or RuO₂ phases. However, there may be RuO₂ nanoparticles or atomically dispersed RuO₂. The former is much more

likely because the $\text{RuCl}_3 \cdot x\text{H}_2\text{O}$ metal salt has substantial solubility limitations, especially in the multicomponent electrospinning solution. Hence, it would be unsurprising if RuO_2 exists on this nanofiber as large nanoparticles, which may account for the image's rugged appearance.

Figure 4.19 shows a TEM image of a composite $\text{PVP}/\text{Cu}(\text{NO}_3)_2 \cdot x\text{H}_2\text{O}$ electrospun nanofiber prior to calcination. A typical fiber diameter in this sample appears to be about 200 nm. A nanofiber of a calcined sample is shown in Figure 4.20.

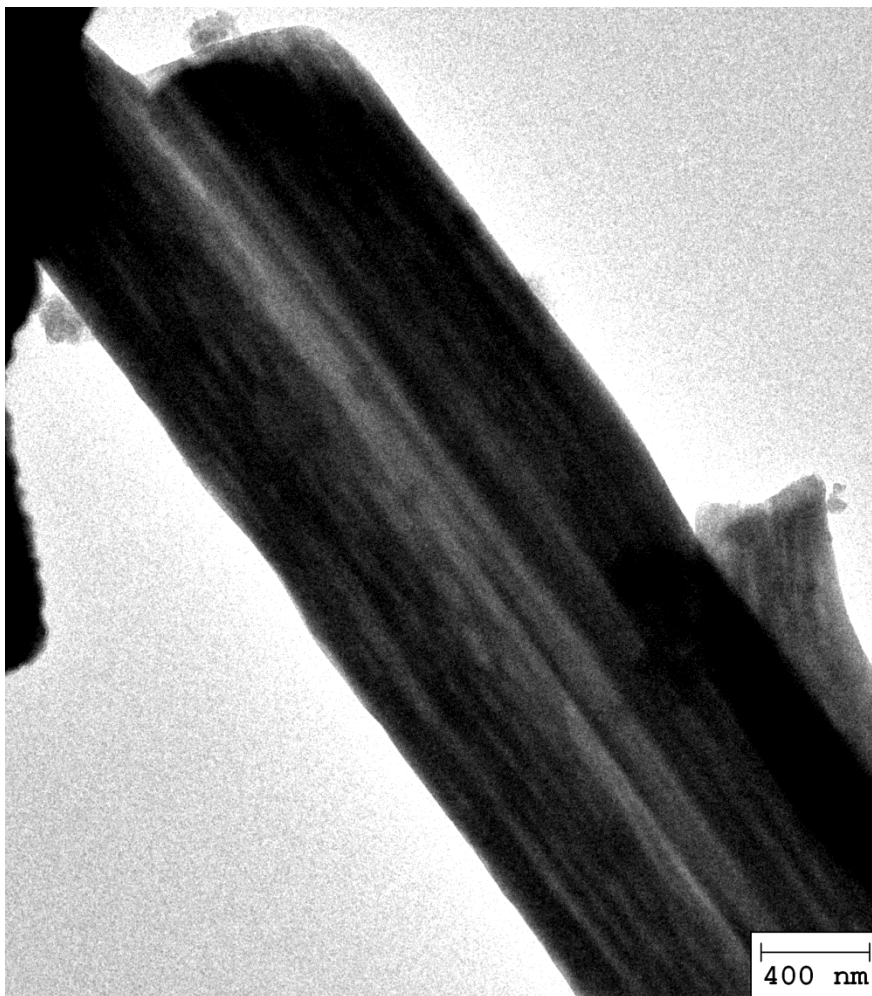


Figure 4.17. TEM image of CuO-NaCl/SiO_2 nanofiber synthesized by electrospinning.

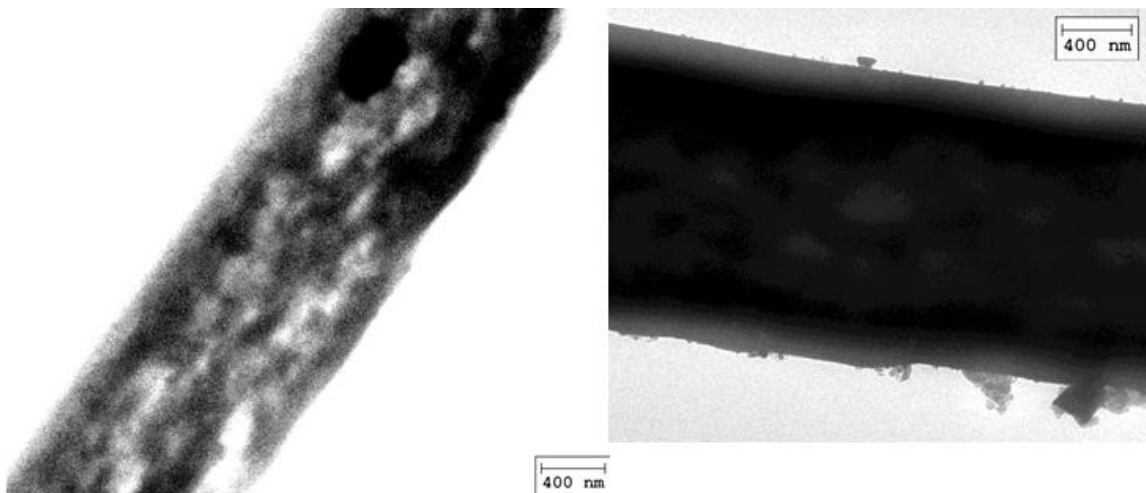


Figure 4.18. TEM image of RuO₂/SiO₂ nanofiber synthesized by electrospinning.

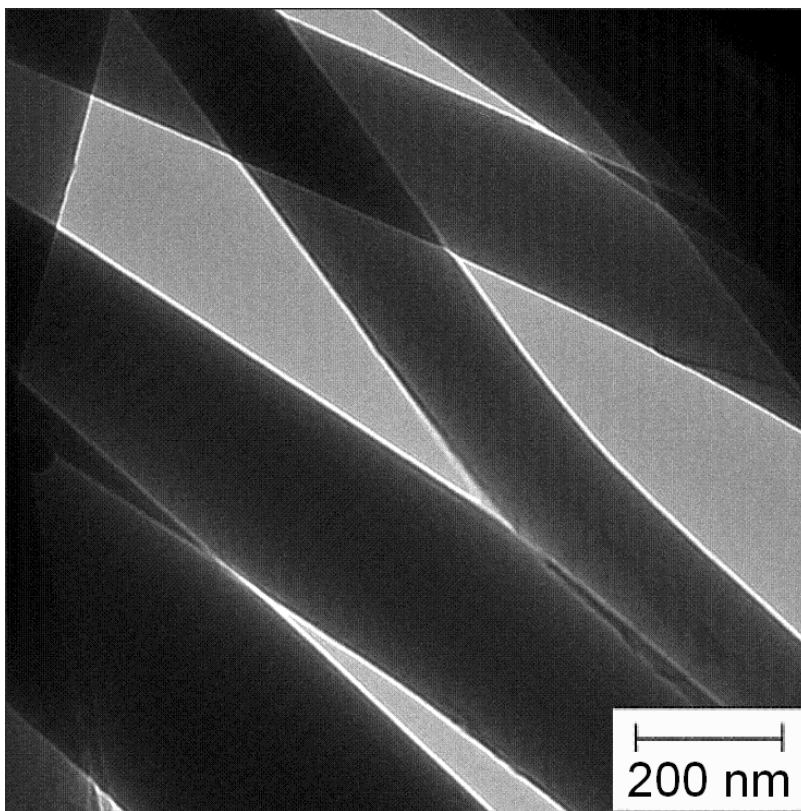


Figure 4.19. TEM image of an electrospun PVP/Cu(NO₃)₂·xH₂O composite nanofiber.

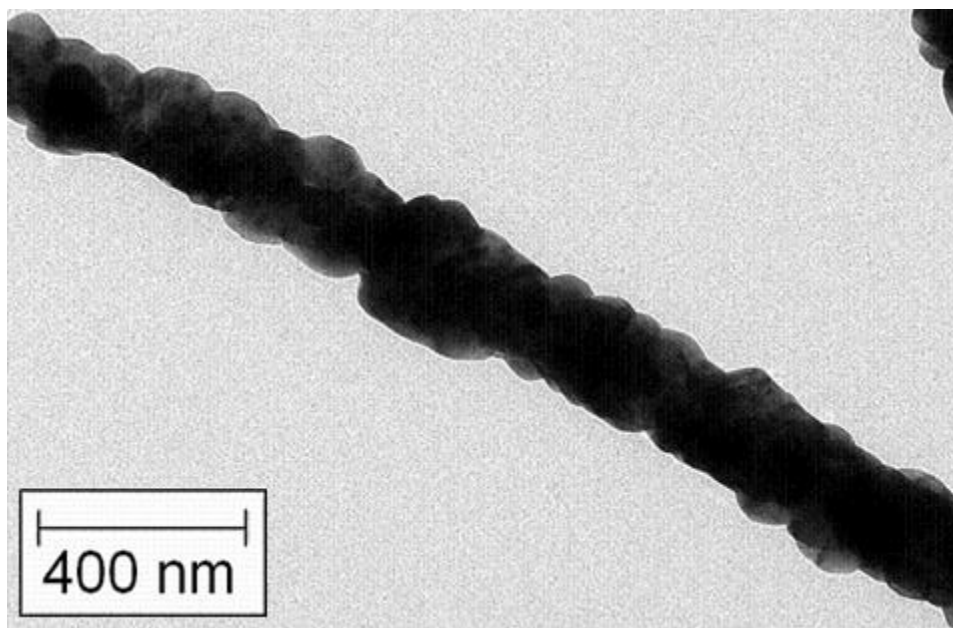


Figure 4.20. TEM image of CuO nanofiber, after calcination.

4.2.5. Catalytic Performance Results.

A summary of the catalytic performance ascertained using the high throughput catalytic screening system of Chapter 3 with silica supported nanofibers synthesized by electrospinning is shown in Table 4.4. The materials tested are CuO/SiO₂, CuO-NaCl/SiO₂, RuO₂/SiO₂ and RuO₂-CuO-NaCl/SiO₂. The unimetallic CuO/SiO₂ catalyst shows exceptional acrolein selectivity, consistent with experiments done on powders, but creates no PO [86]. The bimetallic CuO-NaCl/SiO₂ exhibits the highest PO selectivity at 15% while all other catalysts creates no PO. All propylene conversions are 1.0% or less, with the single metallic RuO₂/SiO₂ and trimetallic RuO₂-CuO-NaCl/SiO₂ materials both achieving this highest mark. Unsupported metal oxide nanofibers (e.g. Figure 4.20) gave similarly poor results.

Table 4.4. Catalytic performance analysis results for silica supported nanofibers electrospun with $\text{Cu}(\text{NO}_3)_2 \cdot 2.5\text{H}_2\text{O}$, $\text{RuCl}_3 \cdot x\text{H}_2\text{O}$, NaCl and calcined at 550 °C.

SiO₂-based Fabric	% PO selectivity	% C₃H₆ conversion
CuO/SiO ₂	0 (55 acrolein)	0.6
CuO-NaCl/SiO ₂	15	0.2
RuO ₂ /SiO ₂	0	1.0
RuO ₂ -CuO-NaCl/SiO ₂	0	1.0

All of the materials of Table 4.4 perform far below that of the impregnated powder RuO₂-CuO-NaCl/SiO₂ catalyst, which reaches 45-50% PO selectivity and 10% propylene conversion, translating to a PO yield of 4.5-5.0%.

Shown in Figure 4.21 is a high-resolution transmission electron microscope (HR-TEM) image of the RuO₂-CuO-NaCl/SiO₂ *powder* catalyst [87]. Although it is difficult to identify small CuO crystals (3-5 nm) on the surface of the RuO₂ crystals ($\approx 10 \times 30$ nm), the use of a crystal plane unique (fast Fourier transform) to RuO₂ and CuO can identify these components. The TEM images also confirmed that CuO and RuO₂ were distinct crystal structures that were in close proximity. Notably, NaCl crystals were also present as cubic structures (≈ 30 nm) but are not shown in this particular TEM image.

By taking into account the aforementioned image, along with previous catalytic performance results, XRD and H₂-TPR experiments similar to those performed for the SbO₂-CuO-NaCl/SiO₂ catalyst of Chapter 3, a model for the RuO₂-CuO-NaCl/SiO₂ catalyst and a plausible mechanism for the epoxidation of propylene over this catalytic

system may be formulated [87]. The proposed model (left) and mechanism (right) are shown in Figure 4.22. According to this mechanism, an O_2 molecule first adsorbs (chemisorption) onto an active center on the RuO_2 surface and dissociates into two surface O atoms (O_a). The O_a migrates across the surface to a neighboring CuO site, which is in close proximity, to form CuO-O. Gas phase propylene then interacts with CuO-O ultimately to form PO through the formation of relevant intermediates such as an oxametallocycle and other species [87, 109].

The previous mechanism is critical in rationalizing why the electrospun nanofibers fail to achieve even modest PO performance, especially compared to the trimetallic powder catalyst. During electrospinning, the flight time of a liquid jet from its path from needle to collector is difficult to track and depends strongly on many factors, especially the applied voltage and the needle-to-collector distance. The size of the jet and ultimate fiber size are also critical because they will strongly influence the drag forces experienced against the surrounding atmosphere. A crude estimate for the jet flight time is on the order of milliseconds [110]. Regardless, the time elapsed for a solid fiber to precipitate during electrospinning is certainly many orders of magnitude smaller than the time it takes for solids to crystallize during impregnation. Due to this quick precipitation, electrospinning does not allow for the soluble metal salts to mobilize substantially within the liquid jet. Hence, it is unexpected that discrete crystals of RuO_2 , CuO and NaCl would carefully arrange in the manner of Figure 4.21 and Figure 4.22 as they are in the impregnated powder catalyst. As a result, it is unsurprising that the silica-supported fabrics underperform and this fact is indirectly supportive of the previous proposed mechanism for PO formation.

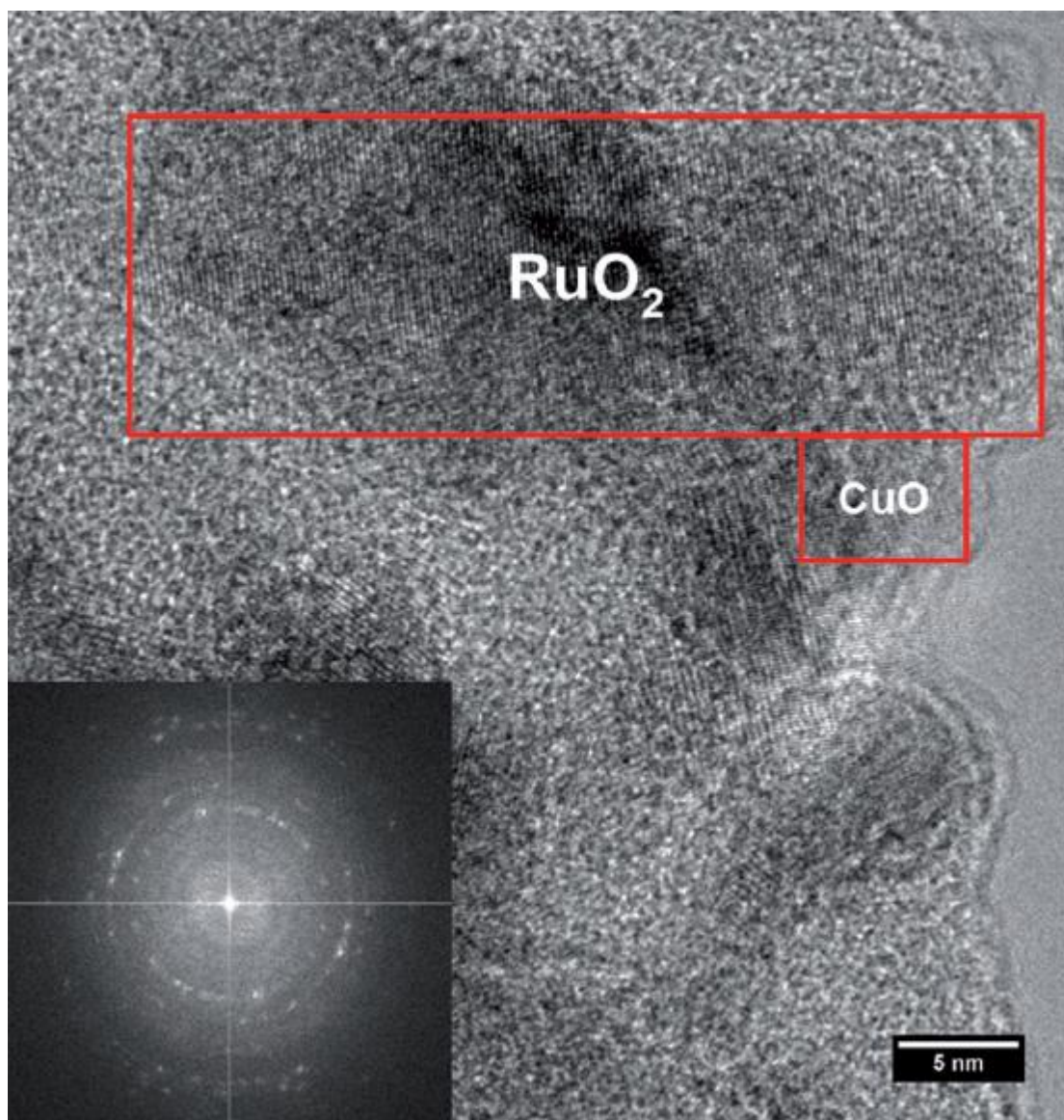


Figure 4.21. HR-TEM image of RuO₂-CuO-NaCl/SiO₂ nanoparticle catalyst synthesized by impregnation. The RuO₂ + CuO clusters are in close proximity. Fast Fourier transform of the HR-TEM image was used to identify crystal planes unique to RuO₂, CuO and NaCl [87].

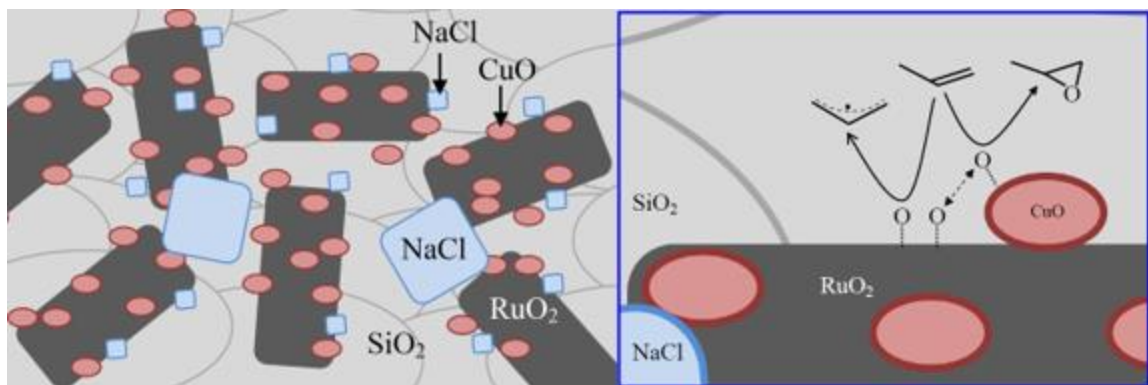


Figure 4.22. Schematic structure of the $\text{RuO}_2\text{-CuO-NaCl/SiO}_2$ nanoparticle catalyst synthesized by impregnation (left). Proposed mechanism for the epoxidation of propylene, showing the dissociative adsorption of O_2 onto the surface of RuO_2 , surface migration of adsorbed oxygen to CuO and the subsequent formation of PO (right) [87].

Further characterization of the silica supported fabrics is needed to support this notion. However, a fast check is provided in Table 4.5. Here, pure silica fabrics were electrospun *without any metal salts*. They were calcined at $550\text{ }^\circ\text{C}$, allowed to cool and then subsequently co-impregnated with $\text{RuCl}_3 \cdot x\text{H}_2\text{O}$, $\text{Cu}(\text{NO}_3)_2 \cdot 2.5\text{H}_2\text{O}$ and/or NaCl and then calcined again at $500\text{ }^\circ\text{C}$. From Table 4.5, the unimetallic $\text{RuO}_2/\text{SiO}_2$ catalyst made by this method converted 25% of the fed propylene completely to CO_2 while the trimetallic $\text{RuO}_2\text{-CuO-NaCl/SiO}_2$ material elicited 35% PO selectivity and 10% propylene conversion. By performing co-impregnation of the metal salts distinctly after electrospinning the support material, the PO performance was far higher than with co-spinning. Clearly, the impregnation process allows for the formation of a crystal structure on the support material that is much more conducive to PO formation. However, the use of silica powder instead of silica nanofibers is still favorable at this point.

Another issue with using electrospun nanofibers by the aforementioned procedure is that the co-spun fabrics need to be calcined at a temperature higher ($550\text{ }^\circ\text{C}$) than what

was found to be optimal (500 °C) for the powder RuO₂-CuO-NaCl/SiO₂ catalyst. Lower calcination temperatures, in all likelihood, would not be sufficient to fully remove the PVP. Hence, the catalytic performance of the nanofibers may have been distorted by this skewed procedure. Experiments were also conducted replacing the PVP with polyvinyl alcohol (PVA), which requires a lower calcination temperature for full removal; however, PVA posed its own problems during the electrospinning process, posing mutual solubility issues with the metal salts and solvents other than water and thus making it difficult to reduce the solutions' surface tensions.

Table 4.5. Catalytic performance analysis results of electrospun silica nanofibers impregnated with active metallic species.

Impregnated SiO₂ Fiber	% PO selectivity	% C₃H₆ conversion
RuO ₂ /SiO ₂	0	25
RuO ₂ -CuO-NaCl/SiO ₂	35	10

4.3. Summary.

Electrospinning on biologically based nanofibers fabrics was accomplished with the primary goal of gaining insight into process tuning methodologies. Increases in the viscosity resulted in expected increases in the fiber diameter for a fixed fiber composition. However, there was considerable variation in fiber morphologies between different protein species. PVP nanofibers also tended to result in larger fibers than with PEO. Spinning upwards resulted in thinner fibers as opposed to spinning downwards at a 45° angle, which

contradicts the literature when electrospinning was performed on a different system. A possible explanation is that the fibers may have been shorter, would could cause the electric field to pull at the front of the fibers while gravity pulls on the back of the fibers, creating extension and thus thinning in both directions.

Catalytic nanofibers synthesized by electrospinning were found to be uniformly inadequate for propylene epoxidation performance compared to similar catalytic powder materials made by co-impregnation. Electrospinning involves quick precipitation of solid materials while impregnation and co-precipitation involve slow crystallization that may allow for the careful arrangement of distinct solid phases for multimetallic catalysts. The mechanism for propylene epoxidation on $\text{RuO}_2\text{-CuO-NaCl/SiO}_2$ catalysts was previously rationalized to involve O_2 chemisorption on a RuO_2 tetrahedron and subsequent surface migration to an adjacent, distinct CuO sphere that functions as the active site for epoxidation. Hence, propylene epoxidation on $\text{RuO}_2\text{-CuO-NaCl/SiO}_2$ -based materials appears to require the presence of separate nanoparticles that act synergistically to lead to the formation of PO. Electrospinning, in all likelihood, does not provide enough time during precipitation to allow for the metal salts to be arranged in such a way that such a structure could be formed after calcination. Further characterization is needed to support this notion.

Chapter 5. Oxidative Coupling of Methane (OCM) by Metal Oxide Nanofiber Catalysts.

This portion of the dissertation focuses on the discovery of nanofiber fabrics as being particularly superior performing materials for the oxidative coupling of methane (OCM). Despite the previous shortcomings of utilizing fabrics as catalysts for propylene epoxidation, their use in this other partial oxidation reaction scheme was shown as promising. Nanofiber fabrics, particularly of $\text{La}_2\text{O}_3\text{-CeO}_2$, are able to perform OCM at substantially lower feed temperatures compared to analogous powders at comparable C_2+ selectivity and CH_4 conversion. Hence, these fabrics serve as the primary basis for the remainder of this dissertation. This chapter is largely based on a *ChemCatChem* publication [111].

5.1. Catalyst Preparation.

$\text{La}_2\text{O}_3\text{-CeO}_2$ nanofibers were prepared by electrospinning [37]. In a typical experiment, the metal precursor (0.15 g), as $\text{La}(\text{NO}_3)_3 \cdot 6\text{H}_2\text{O}$ and $\text{Ce}(\text{NO}_3)_3 \cdot 6\text{H}_2\text{O}$ and polyvinylpyrrolidone (PVP, 0.40 g, 1.3 MDa) were added to a water/EtOH mixture (1:1 w/w, 9.5 g). Upon completely mixing, the solution was loaded into a syringe, which was placed onto a syringe pump. The syringe was connected to a metal needle and DC voltage (30 kV) was applied that caused the nanofibers to be ejected towards a grounded collector that was 15 cm away. The electrospun material was calcined at 625 °C in a furnace to form metal-oxide nanofiber fabrics. The La/Ce weight ratio was about 15. An analogous

La₂O₃/CeO₂ powder catalyst was also prepared for comparison. This powder was synthesized by simply mixing the aforementioned metal nitrate precursors at the same ratio in water, followed by evaporation over a hot plate to precipitate out the powders and subsequent calcination at 625 °C. Notably, the OCM performance of the La₂O₃-CeO₂ nanofibers was extremely sensitive to the preparation and storage conditions.

5.2. Performance Evaluation Using Tubular Packed Bed Reactors and Characterization.

The nanofiber and powder catalysts (8 mg) were packed into a 4 mm ID quartz tube, sandwiched between two quartz wool plugs and placed inside a temperature-controlled tube furnace. The reactor pressure was 1 atm. The inlet gas flow rates were regulated at 120 cm³/min by electronic mass flow controllers (MKS). These conditions corresponded to a feed gas throughput of 900·10³ cm³/h per gram of catalyst (5-10 ms contact time). The gas compositions were maintained between 80-87.5 mol% CH₄ and 12.5-20 mol% O₂. The reaction products were sampled by using a small amount of glass-lined tubing and analyzed by on-line gas chromatography (Varian 4900 Micro-GC, with Molecular Sieve 5Å and Porapak U columns). The reactor temperature was changed incrementally and, after each temperature had settled, the outlet gas composition was determined. The temperature in the furnace was measured by a thermocouple that was placed in the upstream of the reactor. A thermocouple (diameter: 0.25 mm) was also placed immediately after the catalyst to determine the temperature of the reaction products.

Characterization of the catalysts was performed by powder X-ray diffraction (PANalytical X'Pert PRO that was fitted with a Ni filter and a Soller slit collimator). $\text{CuK}\alpha$ radiation (45 kV, 40 mA) was used to identify the active catalyst phases. BET surface areas were determined on Quantachrome Autosorb-1 units with a micropore-analysis option. SEM images were obtained on a JEOL JSM-67 Field-Emission Scanning Electron Microscope.

5.3. Performance of Catalytic $\text{La}_2\text{O}_3\text{-CeO}_2$ Nanofiber Fabrics.

OCM experiments with $\text{La}_2\text{O}_3\text{-CeO}_2$ fabrics were conducted by using a microreactor and compared to co-precipitated powders with the same La/Ce weight ratio (15:1). Feed gas compositions were kept between 80-87.5 mol% CH_4 and 12.5-20 mol% O_2 , which corresponded to CH_4/O_2 ratios of 7:1 to 4:1. The feed gas throughput (W) was typically about $900 \times 10^3 \text{ cm}^3/\text{h}$ per gram of catalyst.

The performances of various single metal oxide-based catalytic fabrics were assessed and the results are summarized in Figure 5.1. Nanofiber fabrics of the metal oxides of Mg, Ca, La, Ce and the subset of transition metals shown were readily synthesized due to the availability of metal nitrates or chlorides soluble and compatible with electrospinning solutions. The nanofibers of the alkali metals were generally not spinnable despite having high solubility, presumably due to large increases in the solution conductivity resulting in prohibitive leakage currents through the liquid jets. Regardless, the highest OCM performers were fabrics composed of alkaline earth metal oxides and the rare-earth-based

La₂O₃. Transition metal-based fabrics CeO₂ were all combustion catalysts. The La₂O₃-based fabrics were taken to be the best unimetallic material due high C₂₊ selectivity (>50%), CH₄ conversion (>20%) and low light-off temperatures (~500-600 °C feed gas).

Shown in Figure 5.2 are the effects that various dopants have on the previous La₂O₃ fabrics. Dopants were generally introduced into the spinning solution at levels of 0.1-10 wt%; however, some were also impregnated onto La₂O₃ fiber samples, especially if the dopant's metal salt has solubility issues in the spinning solution (e.g. W-based materials). We also conducted additional experiments in which La₂O₃ unimetallic fibers were mechanically mixed with other unimetallic fibers and powder materials. Alkali and alkaline earth metals were found to be the best dopants and transition metals, unsurprisingly, the worst. Doping the system with Sr led to an enhancement in C₂₊ yields but required higher light off temperatures. Fabrics of La₂O₃-CeO₂ were determined to be the best OCM performers, able to enhance OCM performance in terms of both C₂₊ yields and necessary feed conditions.

In Figure 5.3, the results of the nanofiber experiment are compared to powders at a CH₄/O₂ ratio of 7:1. The percentage selectivities for C₂₊ products are yields (C₂₊ selectivity from the conversion of CH₄) are presented as a function of the feed gas temperature (T_f). As shown in Figure 5.3Figure 5.1, the La₂O₃-CeO₂ nanofibers exhibited OCM ignition at $T_f \approx 470$ °C, concomitant with an 18% yield of C₂₊ compounds and 65% C₂₊ selectivity. Thermocouple measurements in the reactor tube, in the direction of the gas flow, indicated a sharp increase in temperature to a maximum value (T_{rx}) of about 630 °C within the catalytic zone, which represents a temperature rise of 160 °C, owing to the OCM reaction

scheme. The temperature immediately started to decrease at the downstream quartz wool plug and reached the furnace temperature within 10-15 mm. As shown in Figure 5.3, an increase in T_f increased the C_{2+} yield and selectivity to 20% and 70% respectively, peaking at 520 °C ($T_{rx} \approx 670$ °C).

Under identical conditions, the performance of our $La_2O_3-CeO_2$ powders was significantly different. The powders ignited at a higher feed temperature of 540 °C, with an initial C_{2+} yield of only 5% and a C_{2+} selectivity of 60%. However, with increasing T_f values, both the C_{2+} selectivity and yield increased steadily. At $T_f \approx 630$ °C, the C_{2+} yield and selectivity were 9% and 70%, respectively.

The yield and selectivity of C_{2+} products that were reported by Dedov et al. [112] for their $La_2O_3-CeO_2$ powder catalysts by using a similar packed-bed reactor are also shown in Figure 5.3, right, albeit at significantly lower gas throughput ($W = 45 \times 10^3$ cm³/h per gram of catalyst). As shown in Figure 5.3, substantially higher feed gas temperatures, in the range of 715-830 °C, were required to achieve C_{2+} yields and selectivities that were similar to those of our nanofiber catalysts. Also, notably, even at the lower gas throughputs used by Dedov et al., higher catalyst bed temperatures (in excess of 900 °C) would still be expected, based on the axial temperature profiles reported in OCM reactors under similar W values and CH_4/O_2 ratios at comparable CH_4 conversions and C_{2+} selectivities [113].

In all of our experiments, O_2 conversions were near or above 90% after ignition. Also, the $La_2O_3-CeO_2$ fabrics did not exhibit an apparent deactivation or change in selectivity, even after longer-term experiments (>10 h). OCM studies with pure La_2O_3 nanofibers without the CeO_2 dopant produced inferior results.

We believe that the increased OCM performance that is offered by the fabrics reported herein warrants more detailed studies to better understand the underlying physical and chemical processes that are responsible for these results. In addition to thorough characterization, an exploration of the effects of the diameter of these nanofibers, the La/Ce ratio and space time on the OCM reaction will provide important new insights into the nanofiber catalysis. Although nanofibers provide excellent metal dispersion and easy access to the catalytic sites, their high performance could also be related to different crystal facets that are exposed compared to particles, as reported previously in an entirely different system [1, 3].

The OCM results for the same $\text{La}_2\text{O}_3\text{-CeO}_2$ fabric catalyst are presented for a CH_4/O_2 feed ratio of 4 (Figure 5.4). Here, the onset of catalyst ignition was at $520\text{ }^\circ\text{C}$ on increasing the T_f value, with a C_{2+} selectivity of 55% and a yield of 22%. However, a remarkably broad hysteresis window was noted. In Figure 5.4, on decreasing the T_f value, the high performance of the $\text{La}_2\text{O}_3\text{-CeO}_2$ nanofibers was shown to extend down to a quench of $T_f \approx 230\text{ }^\circ\text{C}$, thus indicating an autothermal T_f range of $290\text{ }^\circ\text{C}$ (i.e. $520\text{-}230\text{ }^\circ\text{C}$). OCM was also shown to be possible at room temperature ($\sim 20\text{ }^\circ\text{C}$) at a CH_4/O_2 ratio of 2.7:1 as shown in Figure 5.5. However, the catalytic performance deteriorates substantially, with a C_{2+} selectivity of 45% and CH_4 conversion of 25%. The presence of OCM and its combustion side reactions is evidenced by the visible appearance of H_2O as a co-product, in the form of condensation within the quartz tube.

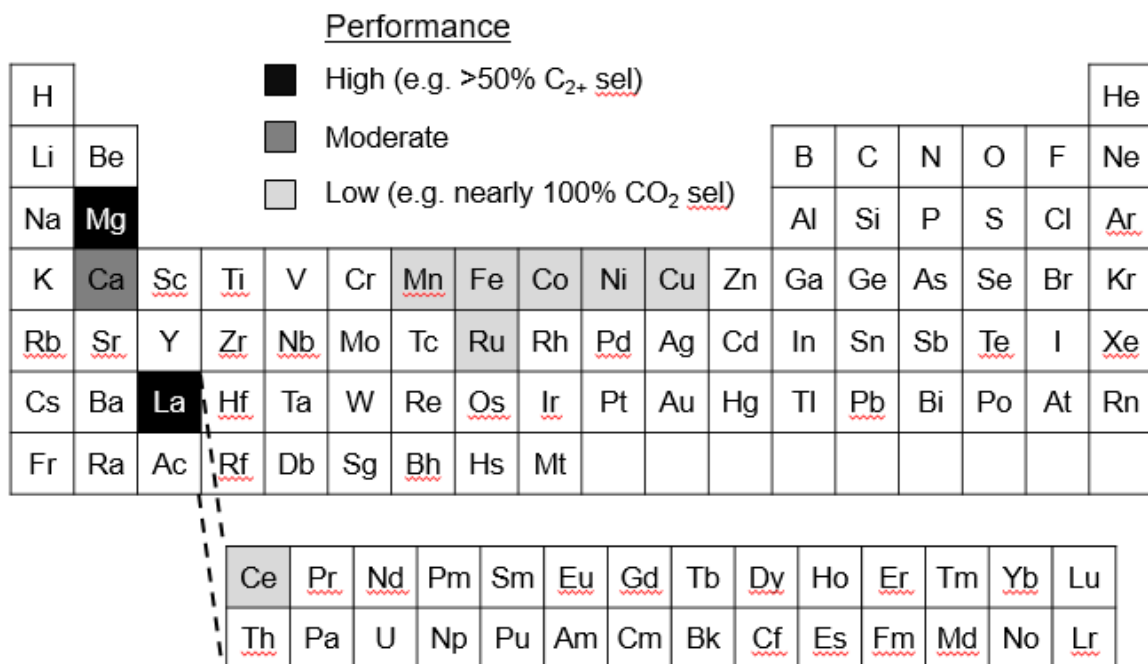


Figure 5.1. Results from nanofiber catalytic screening experiments done on unimetallic metal oxide nanofibers.

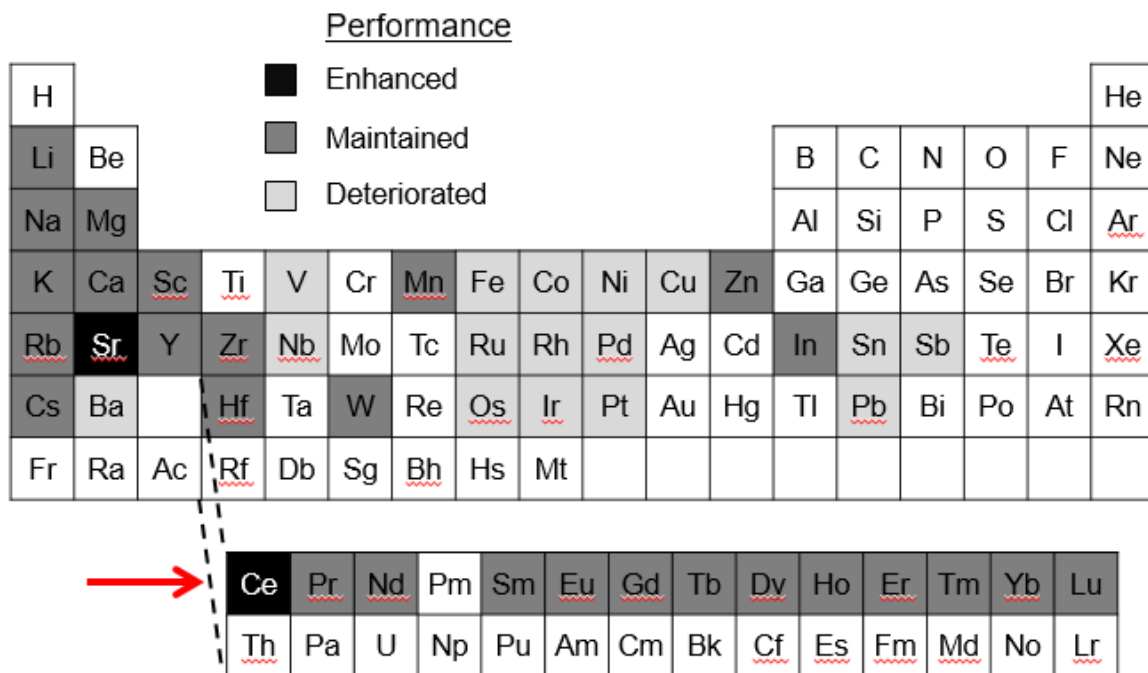


Figure 5.2. Results from nanofiber catalytic screening experiments done on La₂O₃-based fabrics doped with various elements.

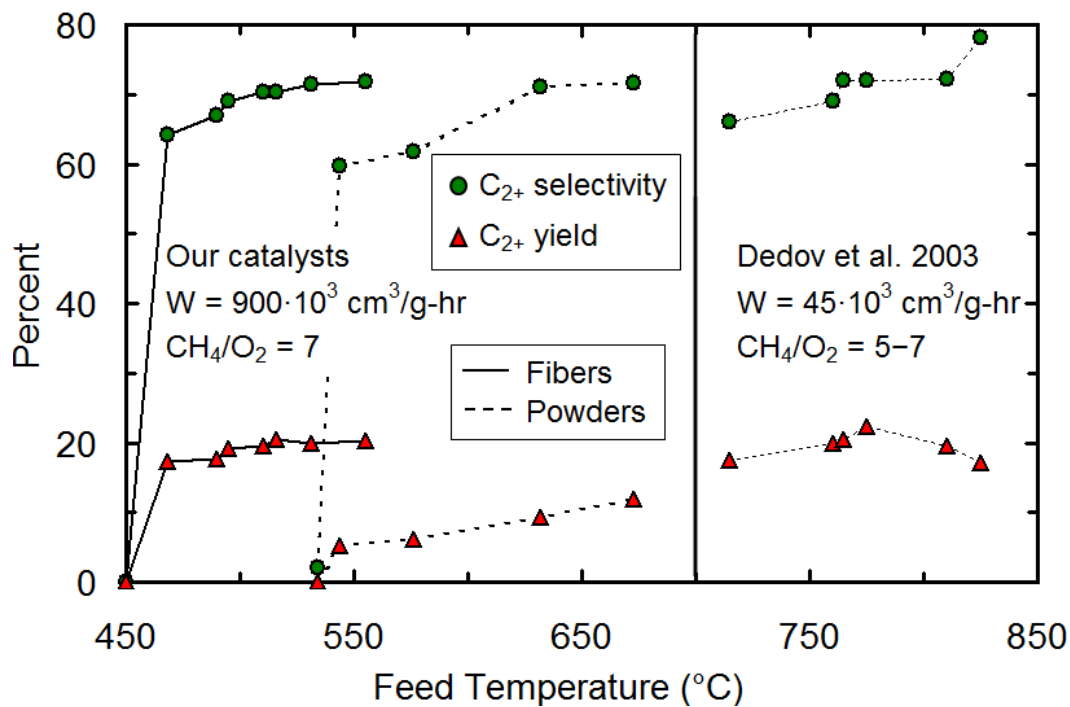


Figure 5.3. Left: comparison of the OCM results with the $\text{La}_2\text{O}_3\text{-CeO}_2$ fabric catalyst to those with co-precipitated powders at the same gas-throughput value (W). Right: previous powder studies by Dedov et al. at a 20-fold lower W value [112].

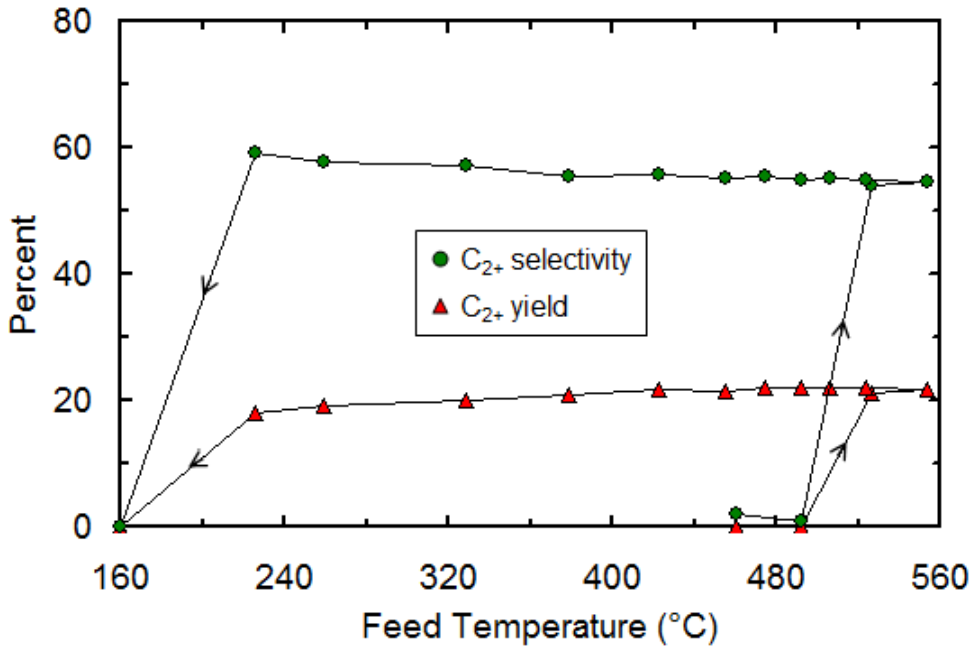


Figure 5.4. OCM results with the $\text{La}_2\text{O}_3\text{-CeO}_2$ fabric catalyst at a CH_4/O_2 feed ratio of 4 and a throughput of $W = 900 \times 10^3 \text{ cm}^3/\text{g-h}$.

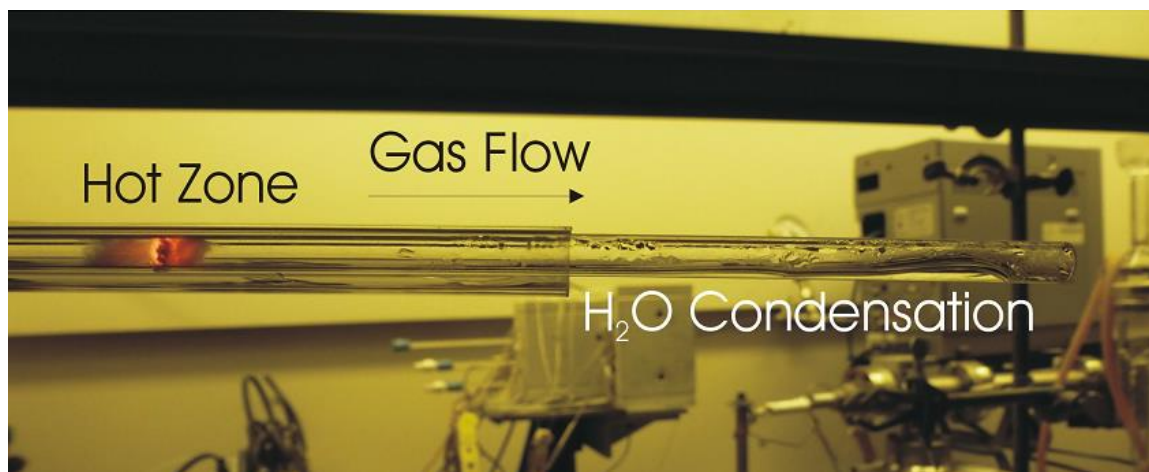


Figure 5.5. OCM performed at room temperature with a La_2O_3 catalytic nanofiber fabric, feed with CH_4/O_2 of 2.7 and achieved by utilizing the hysteresis illustrated in Figure 5.4.

5.4. Effects of Catalyst Composition and Nanofiber Diameter.

The nanofiber fabric catalysts investigated in Figure 5.3 and Figure 5.4 had a metallic composition of $\text{La}/\text{Ce} = 15/1$. The powders of Noon et al. were likewise at the same composition while the powders of Dedov et al. were at $\text{La}/\text{Ce} = 9/1$. An investigation of the catalyst composition for nanofiber fabrics is provided in Figure 5.6. Both the CH_4 conversion and C_{2+} selectivity peak at 20 wt%. Dedov et al. suggests that the performance enhancement should be greater than what is shown in Figure 5.6, largely due to conversion enhancement. Our results may be understating the CH_4 conversion because it is estimated via carbon atom balances and since the production of H_2 was not accounted for in these early experiments. The production of H_2 suggests that C_{2+} hydrocarbons may, at least indirectly, be produced via some non-oxidative coupling route in which O_2 is spared and

hence may be used for additional conversion of CH₄. Further investigations are thus warranted in this matter.

The catalytic performance of these binary nanofiber fabrics is shown as a function of fiber diameter in Figure 5.7. Decreasing the diameter of the nanofibers has a positive impact on both C₂₊ selectivity and CH₄ conversion. The rise in the latter comes as no surprise since there is a clear increase in the surface area of the catalyst at smaller diameters. However, the increase in the C₂₊ selectivity is a pleasant surprise despite the increase in catalytic activity, which would presumably result in an increase in catalytic combustion of both CH₄ and C₂₊ species. Two possible reasons could be at play here. First, increasing the total catalytic area may increase the ratio of catalytic reactions to gas phase reactions. Since CO and CO₂ are understood to be created by homogenous gas phase reactions initiated by heterogeneous catalysis, providing more solid surface area in the reactor may enhance the ratio of surface to undesired gas phase contributions, thus leading to an enhancement of C₂₊ production. Secondly, as discussed previously, a decrease or increase in the size of a structure, whether nanoparticle, nanofiber, etc., can impact the nature of the crystal facets exposed at the surface of the material, change the nature of how exposed orbitals interact with gas phase species and thus tune the catalysis [1, 3, 4, 13]. A decrease in diameter may accordingly increase the C₂₊ selectivity through these means.

Nanofibers of the smallest diameters require a depletion in the PVP concentration in the spinning solution (e.g. ~2.0-2.5 wt% for 30 nm fibers). The extra solvent in these diluted solutions are best dealt with by delivering dehumidified air over the spinning apparatus (e.g. via pressure swing adsorption) to ensure the liquid jet dries sufficiently.

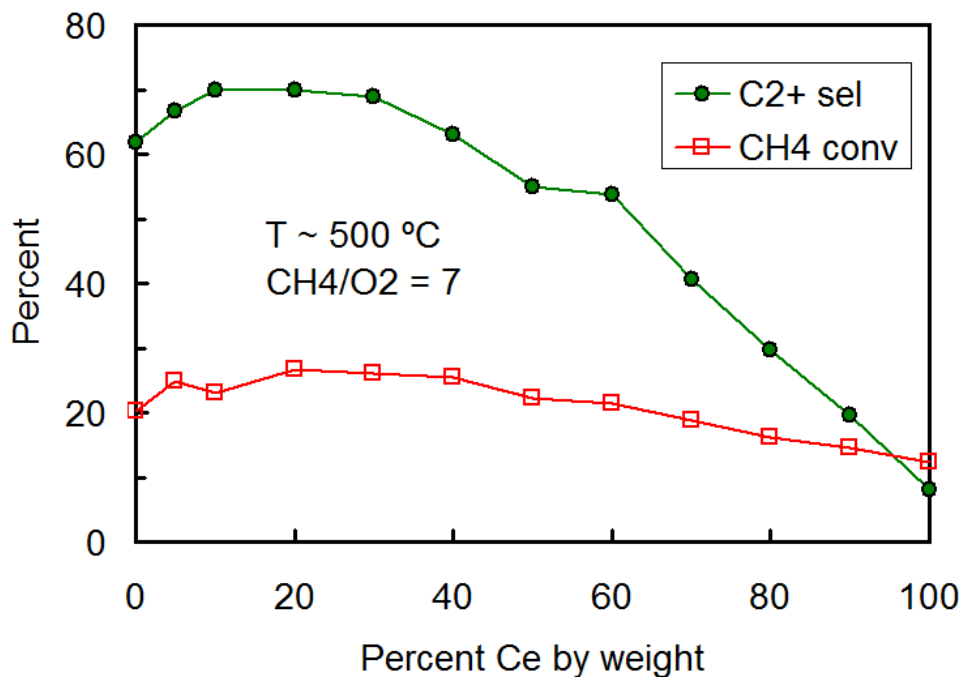


Figure 5.6. OCM catalytic performance as a function of catalyst composition on a metals basis for $\text{La}_2\text{O}_3\text{-CeO}_2$ nanofiber fabrics.

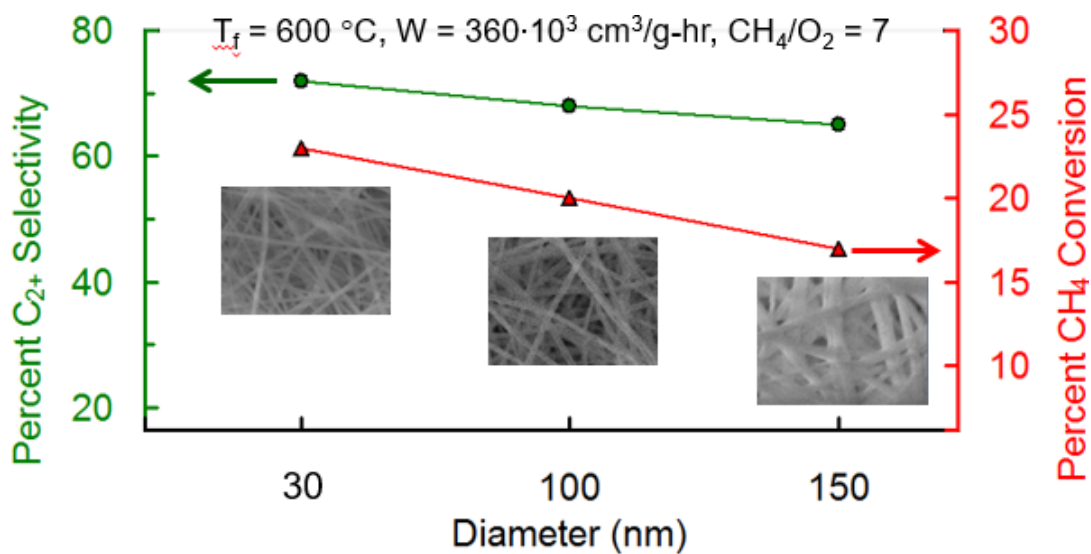


Figure 5.7. OCM catalytic performance as a function of nanofiber diameter for $\text{La}_2\text{O}_3\text{-CeO}_2$ fabrics.

5.5. Characterization Studies.

Shown in Figure 5.8 (left) is the calcined $\text{La}_2\text{O}_3\text{-CeO}_2$ nanofiber fabric (La/Ce, 15:1 w/w) that was used in Figure 5.3 and Figure 5.4. A SEM image of this fabric (Figure 5.8, right) shows the formation of highly uniform $\text{La}_2\text{O}_3\text{-CeO}_2$ nanofibers with diameters in the range of 40-70 nm. This fabric had a low BET area of about $26 \text{ m}^2/\text{g}$, which suggested that the nanofibers were dense and did not possess any internal porosity. The SEM image also shows the presence of large voids between the fibers, which enhances fabric diffusivity and decreases sintering. By comparison, co-precipitated $\text{La}_2\text{O}_3\text{-CeO}_2$ powders, shown in Figure 5.9, have much smaller BET areas at about $10 \text{ m}^2/\text{g}$, evidence of agglomeration and few voids.

The XRD data for $\text{La}_2\text{O}_3\text{-CeO}_2$ nanofibers and powders, both before and after the test conditions, are presented in Figure 5.10 (A, B and C, D) along with those for individual La_2O_3 (E) and CeO_2 (F) fibers and powders. From these data, several interesting features are revealed. First, both the La_2O_3 fibers (Figure 5.10) and powders exhibit almost identical mixed cubic (222 and 440 reflections) and hexagonal structures (100, 101 and 102 reflections) [114]. Similarly, the same cubic (111, 200 and 220 reflections) CeO_2 phases were present in both the fibers and the powder [115]. However, the XRD spectrum of binary $\text{La}_2\text{O}_3\text{-CeO}_2$ nanofibers showed that they were remarkably less crystalline than the La_2O_3 and CeO_2 fibers (Figure 5.10). This result can be attributed to the formation of solid solutions and the reactions of La_2O_3 and CeO_2 , such as the partial reduction of ceria into Ce_7O_{12} and the incorporation of La^{3+} ions into the cubic lattice of CeO_2 [112, 116].

Significant shortening and broadening of the $\text{La}_2\text{O}_3\text{-CeO}_2$ nanofiber peaks are also shown, thus indicating fewer crystallites and smaller mean crystallite dimensions compared to single metal-oxide nanofibers.

Second, the diffractograms of the $\text{La}_2\text{O}_3\text{-CeO}_2$ nanofibers were substantially different to those of the co-precipitated powders at the same La/Ce weight ratio (15:1). Most interestingly, although the $\text{La}_2\text{O}_3\text{-CeO}_2$ nanofibers were less crystalline (Figure 5.10), the powders exhibited reflections that were characteristic of crystalline phases (Figure 5.10) and remained as such, even after the OCM experiments (Figure 5.10). Third, the post-test XRD peaks for the nanofibers were slightly sharper, thus suggesting some increase in the crystallite size. Lastly, the $\text{La}_2\text{O}_3\text{-CeO}_2$ nanofibers exhibited a number of new peaks (indicated by *) that were not present in either the powders or in the single metal-oxide fibers. Clearly, further characterization is required to develop a better understanding of the active sites in the binary $\text{La}_2\text{O}_3\text{-CeO}_2$ nanofibers and to further improve their OCM performances.

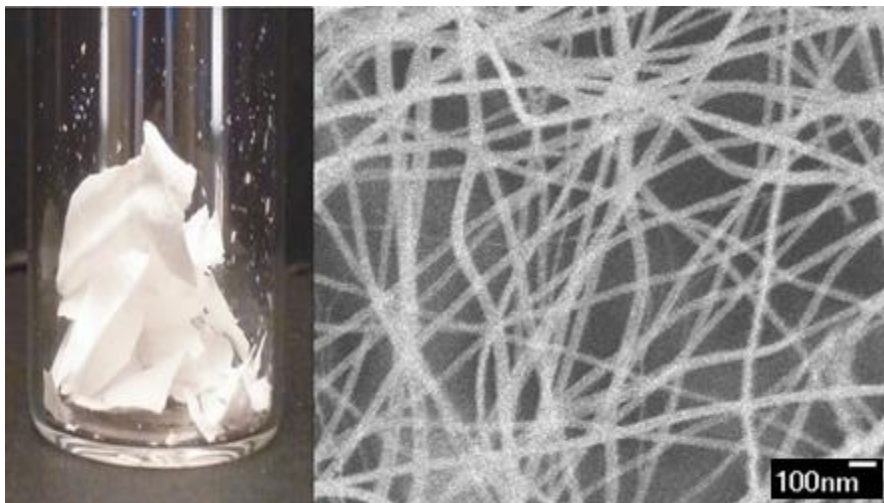


Figure 5.8. $\text{La}_2\text{O}_3\text{-CeO}_2$ fabric catalyst (left) and its SEM image (right; secondary electron imaging, 5.0 kV, $\times 30,000$ magnification, 6.9 mm working distance).

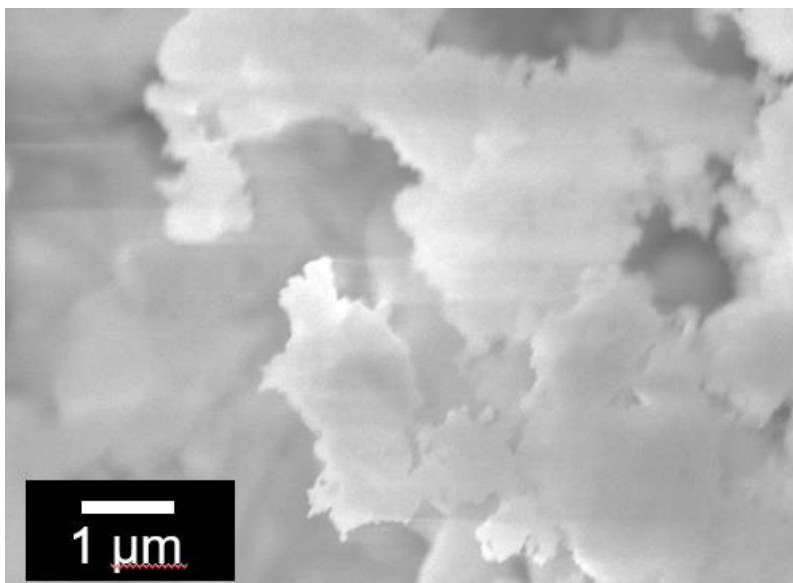


Figure 5.9. $\text{La}_2\text{O}_3\text{-CeO}_2$ powders synthesized by co-precipitation (secondary electron imaging, 15 kV, $\times 7,000$ magnification, 7.8 mm working distance).

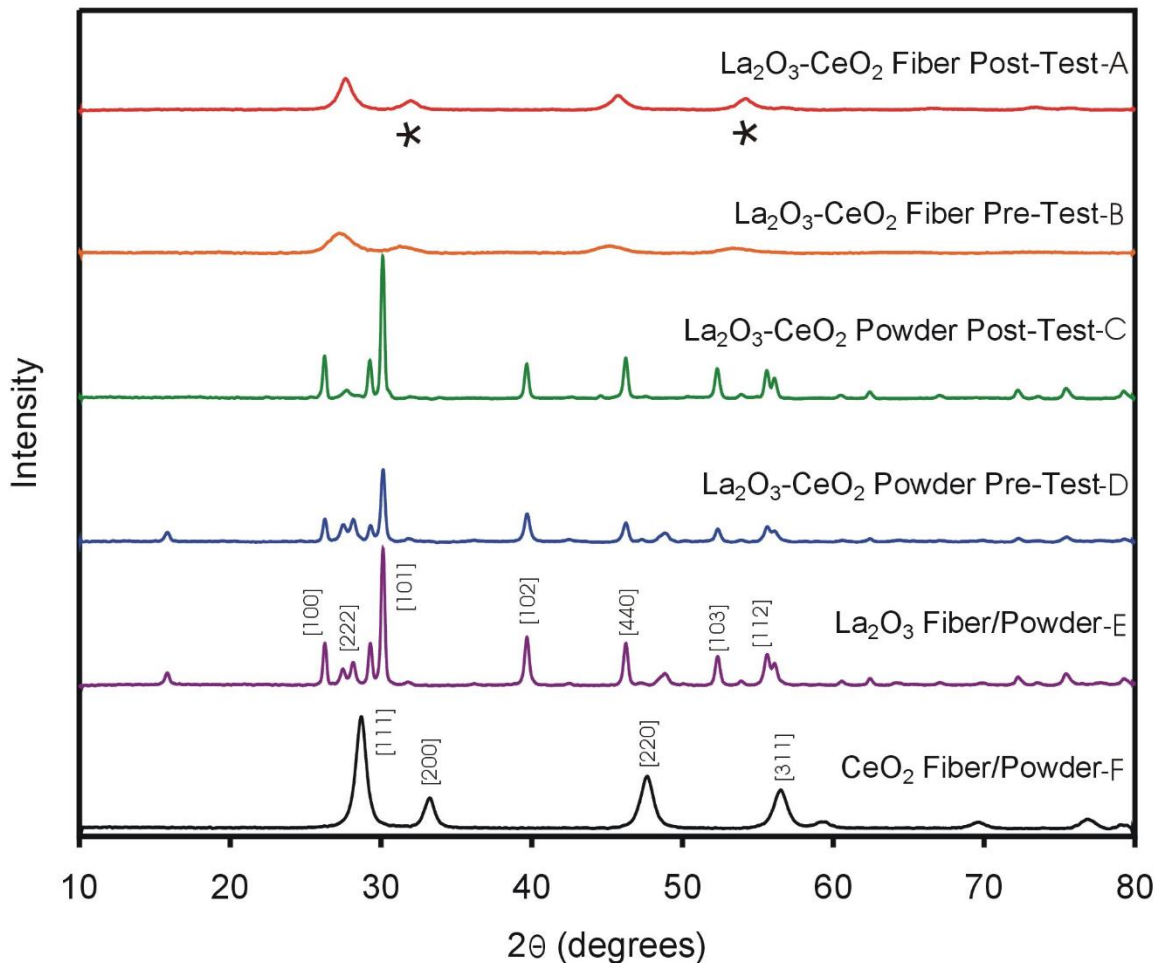


Figure 5.10. Comparison of the XRD spectra of La₂O₃-CeO₂ nanofibers with those of related materials.

5.6. Summary.

Fabrics of metal-oxide nanofibers represent a new class of high-performance catalytic materials with potential applications in industrial chemistry. By providing excellent dispersion, order and access to the catalytic sites, La₂O₃-CeO₂ fabrics exhibited high OCM performance at significantly lower feed gas temperatures (T_f) than analogous

powder catalysts. These nanofiber fabrics also exhibited large voids, which should enhance diffusivity and decrease sintering.

Chapter 6. OCM Using La₂O₃-CeO₂ Fabrics: Reaction Engineering Aspects.

The nanofiber fabric catalysts of Chapter 5 are further analyzed in a reaction engineering study. A wide range of process parameters are investigated to determine their influences on catalytic performance. The durability of the catalyst is also investigated via time on stream tests, imaging and temperature profile measurements. This chapter is based on a publication in the *Journal of Natural Gas Science & Engineering* [117].

6.1. Nanofiber Catalyst Synthesis by Electrospinning.

Nanofibers are prepared by electrospinning [37]. In a typical preparation, polyvinylpyrrolidone (PVP; 1.3 MDa) is mixed with a solvent containing water and ethanol (~1:2 weight ratio). To this solution, La(NO₃)₃·6H₂O and Ce(NO₃)₃·6H₂O are added. Water is necessary to allow for the mutual solubility of PVP and the metal salts while ethanol is used primarily to lower the surface tension of the solution, allowing it to be electrospun into fibers. The final solution is 6 wt% PVP with a metal-to-polymer weight ratio of 0.20.

The electrospinning setup is the same as that of Chapter 4, Figure 4.1, and features a syringe loaded with the spinning solution being pumped through a metal needle under 30 kV, causing streams to jet out towards the grounded collector, which has aluminum foil wrapped tightly around it. The syringe pump is programmed to then pump the fluid at a fixed rate of 1.0 mL/h. The material collected on the aluminum foil comprises nanofibers of PVP and the embedded La and Ce metal salts. After a sufficient amount of material is

collected, the foil is then placed inside an oven for air calcination at 625 °C. This temperature allows for the fiber sample to be calcined without melting the foil. The La/Ce weight ratio of the material studied in this part of the work is 3/1.

6.2. Catalytic Performance Evaluation and Temperature Profiling.

The nanofiber catalyst is packed in a 4 mm ID quartz tube, sandwiched between two quartz wool plugs and placed inside a temperature controlled tube furnace (Thermolyne® 21100). The reactor pressure is 1 atm. Inlet gas flow rates are regulated by electronic mass flow controllers (MKS, Burlington, MA). Flow rates of 80-320 standard cubic centimeters per minute (sccm), catalyst weights of 5-20 mg (0.94 void fraction) and feed temperatures of 300-620 °C are examined. The inlet is a binary gas of CH₄ and O₂ with 75-87.5 mol% CH₄. Reaction products are sampled by a 300 micron ID capillary tubing and analyzed by online gas chromatography (Varian 4900 Micro-GC), with Molecular sieve 5Å and PoraPLOT U columns).

In separate experiments, a 0.25 mm diameter thermocouple (K-type, Omega Engineering, CT) is placed inside the catalytic zone to measure the axial temperature profiles. The thermocouple is inserted tightly into a quartz capillary, the combination of which is placed on a micro-translation device that allows for precise incremental changes in the axial position of the thermocouple along the reactor [118]. In these experiments, 20 mg catalyst loading is used to form a bed depth of ~1.4-1.5 cm to improve the spatial resolution of the axial temperature profiles.

6.3. Nanofiber Fabric Imaging.

Shown in Figure 6.1 is an SEM image of the calcined $\text{La}_2\text{O}_3\text{-CeO}_2$ nanofiber fabric. First and foremost, the fibers show considerable uniformity in diameter (~ 70 nm) and dispersion. The BET area is about $25 \text{ m}^2/\text{g}$, suggesting the nanofibers are dense and do not possess internal porosity. Second, the fibers appear individually well exposed with little clustering, concomitant with the large and uniform interfiber spacing and a void fraction of 0.94. Although these features provide rapid access to and from active sites, which should be advantageous in improving the selectivity for labile products in partial oxidation reaction schemes, they also promote homogeneous gas phase reactions. In contrast, co-precipitated $\text{La}_2\text{O}_3\text{-CeO}_2$ particles exhibit a high degree of agglomeration in which a significant fraction of $\text{La}_2\text{O}_3\text{-CeO}_2$ remains inaccessible or are accessible only through pores, concomitant with pore diffusion limitations and associated problems. Previously, we demonstrated that $\text{La}_2\text{O}_3\text{-CeO}_2$ nanofiber fabric catalysts exhibit lower ignition temperatures and broader operating windows than the corresponding powder catalysts [111].

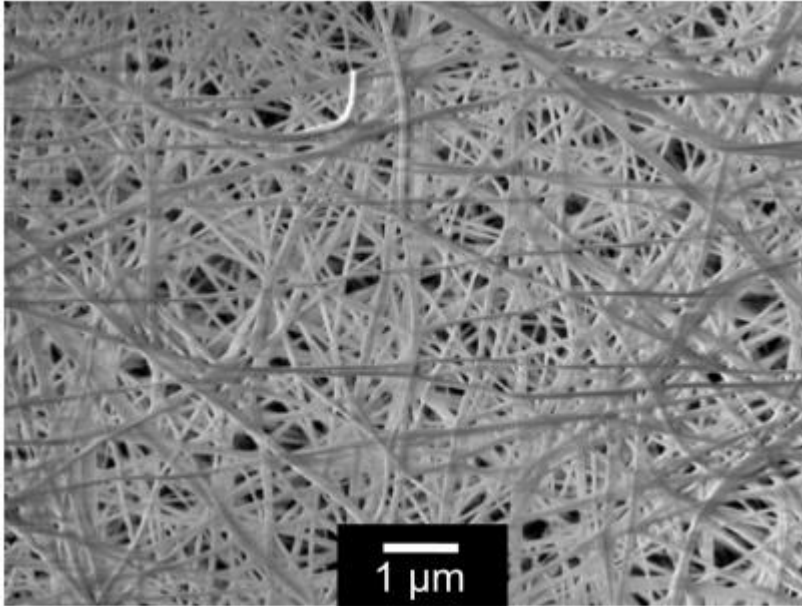


Figure 6.1. Representative calcined $\text{La}_2\text{O}_3\text{-CeO}_2$ nanofibers utilized in this portion of the work, with diameters of ~ 70 nm (secondary electron imaging; $\times 13,000$ magnification; 6.7 mm working distance; 4.0 kV).

6.4. Feed temperature hysteresis.

Before results are presented, it should be pointed out that the major C_2 products observed over $\text{La}_2\text{O}_3\text{-CeO}_2$ catalysts are C_2H_6 and C_2H_4 , with the $\text{C}_2\text{H}_6/\text{C}_2\text{H}_4$ ratio being in the 1-2 range. In addition, some C_3H_6 is also formed, constituting 5-8% of the C_{2+} products. Furthermore, some C_4 products were also consistently detected under OCM conditions, though in significantly lower amounts compared to other products. The major undesirable products were CO_2 and CO .

In Figure 6.2, the axial temperature profiles are presented for a CH_4/O_2 feed ratio of 5 and at a feed gas flow rate of $F = 160$ sccm with $m_{\text{cat}} = 20$ mg of catalyst packed into the bed at various feed gas temperatures T_f . Filled symbols represent the temperature

profiles measured when the furnace temperature was stepwise heated up, while empty symbols were obtained during the stepwise cooling process. The temperature profile measurements were acquired while the reactant gases were flowing. The embedded thermocouple was used to monitor the establishment of the steady-state bed temperature. Once the steady-state temperature was reached (~30 min during heating and ~60 min during cooling), the temperature profile was measured by axially moving the thermocouple. After data acquisition, the furnace temperature was readjusted to its new set point. As seen in Figure 6.2, the difference between the peak temperature in the catalytic zone and feed temperature T_f ranges between ~300 and 400 °C. This difference is at its largest at the lowest feed temperature $T_f = 390$ °C. However, the locations of the peaks were noted to shift downstream during the cooling trajectory, i.e. at values for T_f that are lower than the ignition temperature T_{ig} . This could also be due to insufficient cooling period (60 min) to attain steady-state during the cooling process.

In Figure 6.3, the accompanying reactor exit CH₄ conversions and C₂₊ selectivities are presented while Figure 6.4 shows the O₂ conversions and C₂H₆/C₂H₄ ratios, both as a function of feed gas temperature T_f . As seen in Figure 6.2 and Figure 6.3, the onset of catalyst ignition was at 450 °C when *increasing* T_f , with a C₂₊ selectivity of 55% at 28% CH₄ conversion. Oxygen was completely consumed and the C₂H₆/C₂H₄ ratio was about 1 at the ignition point. For $T_f > T_{ig}$, the catalyst performance is limited by the exhaustion of O₂, with no change in the location of the peak bed temperature. As evident from Figure 6.2 and Figure 6.3, a hysteresis window was noted. On the *decreasing* T_f path, the high C₂₊ selectivity of 52-59% extended down to about 300 °C. Both the CH₄ and O₂ conversions

steadily decreased and the C_2H_6/C_2H_4 ratio increased with decreasing T_f below the ignition temperature. These results are consistent with the lower catalyst peak temperature with decreasing T_f (Figure 6.2).

6.5. Effect of feed flow rate and CH_4/O_2 ratio.

In Figure 6.5, the effects of feed gas flow rate on the spatial temperature profiles are presented at a CH_4/O_2 ratio of 5 and feed gas temperature of 570 °C. As evident from this figure, increasing the feed gas flow rate dramatically increases the reactor temperature, while only slightly shifting the location of the maximum temperature. For example, at 80 sccm flow, the peak temperature is 825 °C at ~12 mm within the bed. In contrast, at 200 sccm, the peak temperature reached 960 °C at ~11 mm. These results indicate that the rate of the OCM process in the experiments was significantly under mass transfer limited conditions [119]. That is, the increased flow rates increased mass transfer coefficients and thus transport rates to the catalyst surface, thereby increasing the rates of the OCM reaction and thus heat generation rates. Increases in temperature results in the establishment of steeper temperature gradients which then lead to increased heat conduction both to upstream and downstream of the hot spot. On the other hand, increases in gas flow rates would decrease the residence times as well as convectively pushing the hot gases downstream. As a consequence of the complex combination of these conduction, convection and reaction processes, the peak temperatures can shift either upstream or

downstream. Clearly, performing a detailed modeling work involving both the chemical kinetics and transport phenomena of the OCM process is called for.

Another possible contributor to the observed shifts in peak temperature locations in the OCM reactors is heat conduction in along thermocouple wires placed into the bed. Due to their higher thermal conductivity, metal thermocouples can transfer heat more efficiently than gases and the solid catalysts. As a result, thermocouples only provide spatially averaged readings, averaged along a few bead or fiber diameters, especially when steep temperature gradients are present. Ideally, thermocouples should be placed perpendicular to gas flow in order to accurately determine axial temperature profiles. However, such an option is not readily available for most catalytic reactor studies, including this work. In our experiments, thermocouples were placed for the downstream side of the reactor.

In Figure 6.6, the effect of CH_4/O_2 ratio on reactor temperature is shown. As can be seen, decreasing the CH_4/O_2 ratio from 7 to 4 increases the peak reactor temperature from 850 °C to 980 °C, while also resulting in a shift of the peak location from 12 mm to 10.8 mm. The increase in reactor bed temperature is the expected consequence of decreased methane dilution in the feed gas based on the overall OCM and well as combustion reaction stoichiometries.

In Figure 6.7 and Figure 6.8, CH_4 and O_2 conversions, C_{2+} selectivities and $\text{C}_2\text{H}_6/\text{C}_2\text{H}_4$ ratios are presented as a function of feed gas flow rate and CH_4/O_2 ratio at a feed gas temperature of $T_f = 570$ °C. An inspection of Figure 6.7 reveals several interesting trends. First, increasing gas flow rates and decreasing CH_4/O_2 ratios have an adverse effect on C_{2+} selectivity, which reaches as high as 70% at a CH_4/O_2 feed ratio of 7 and feed flow

rate of $F = 160$ sccm. The only exception to this trend is seen at the CH_4/O_2 ratio of 7 at low gas flow rates, which can be attributed to greater mass transfer limitations. Additionally, the depth of the catalyst bed could be a significant factor increasing low C_{2+} selectivities for low and for the high CH_4/O_2 ratio. In a previous work, when using an 8 mg $\text{La}_2\text{O}_3\text{-CeO}_2$ bed, a T_f hysteresis plot similar to that of Figure 6.3 here was constructed [111]. It was found that for a CH_4/O_2 feed ratio of 4 that C_{2+} selectivities reached their highest at the quench temperature of $T_f = 230$ °C. In Figure 6.3 at the quench temperature, the C_{2+} selectivity is at one of its lowest observed values. A key difference between these two experiments is the bed depth, which clearly explains why C_{2+} selectivities are sacrificed at very low flow rates at $\text{CH}_4/\text{O}_2 = 7$. Over our OCM catalyst, we have previously shown that O_2 was completely consumed at about one-third of the 20 mg $\text{La}_2\text{O}_3\text{-CeO}_2$ bed [118]. This would not necessarily occur within a shallow 5 mg bed. That is, products of OCM with a deep bed are being exposed to the catalyst at *low temperatures* that could lead to the destruction of C_{2+} products.

Second, methane conversions consistently increase with decreasing CH_4/O_2 ratio as a consequence of increased bed temperature caused by decreased methane dilution, reaching as high as 33% at a CH_4/O_2 feed ratio of 4 and the lowest feed rate examined of $F = 80$ sccm. Third, the effect of gas flow rates on methane conversions is complex. Methane conversion decreases with increasing gas flow rate for CH_4/O_2 ratios of 4 and 5, but the reverse trend is observed for 7. For the CH_4/O_2 ratios of 4 and 5, decreases in CH_4 conversions with increases in gas flow rates can readily be accounted for by the decreases in contact/reaction times since under these conditions, the catalyst is at a sufficiently high

temperature. Also, CO_x selectivities tend to be higher at larger flow rates due to high temperatures. Since pathways that produce CO_x consume more O_2 , less CH_4 will be converted at the end. From Figure 6.8, the variation in oxygen conversion with respect to flow rate is less significant than for methane conversion, consistent with the argument that increasing CO_x selectivities with flow rates being the primary reason for the decreasing CH_4 conversions as opposed to reduced contact times. For the CH_4/O_2 ratio of 7 at 80 sccm, the catalyst temperature evidently is not hot enough, resulting in increases in methane conversion slightly with increases in the gas flow rate. This result is also in harmony with results noted above.

Third, O_2 conversions uniformly increase with increasing gas flow and leveled off at higher flow rates for all CH_4/O_2 ratios (Figure 6.8). Interestingly, O_2 conversions leveled off earlier and to a slightly lower level at the CH_4/O_2 ratio of 7. Fourth, $\text{C}_2\text{H}_6/\text{C}_2\text{H}_4$ ratios exhibited trends that consistently decreased with increasing gas flow rates and decreasing CH_4/O_2 ratios, an expected result based on increased reactor bed temperatures. The $\text{C}_2\text{H}_6/\text{C}_2\text{H}_4$ ratios were significantly higher (i.e. 1.3-1.6) at the CH_4/O_2 ratio of 7. For the CH_4/O_2 ratio of 4, the $\text{C}_2\text{H}_6/\text{C}_2\text{H}_4$ ratio decreased from 1.15 at 80 sccm to 0.95 at 320 sccm. Carbon dioxide, an abundant byproduct in OCM, has also been documented as a catalyst poison and has strong binding affinity for highly basic materials [120]. Consequently, under certain conditions, CO_2 could limit the rates of the OCM reaction.

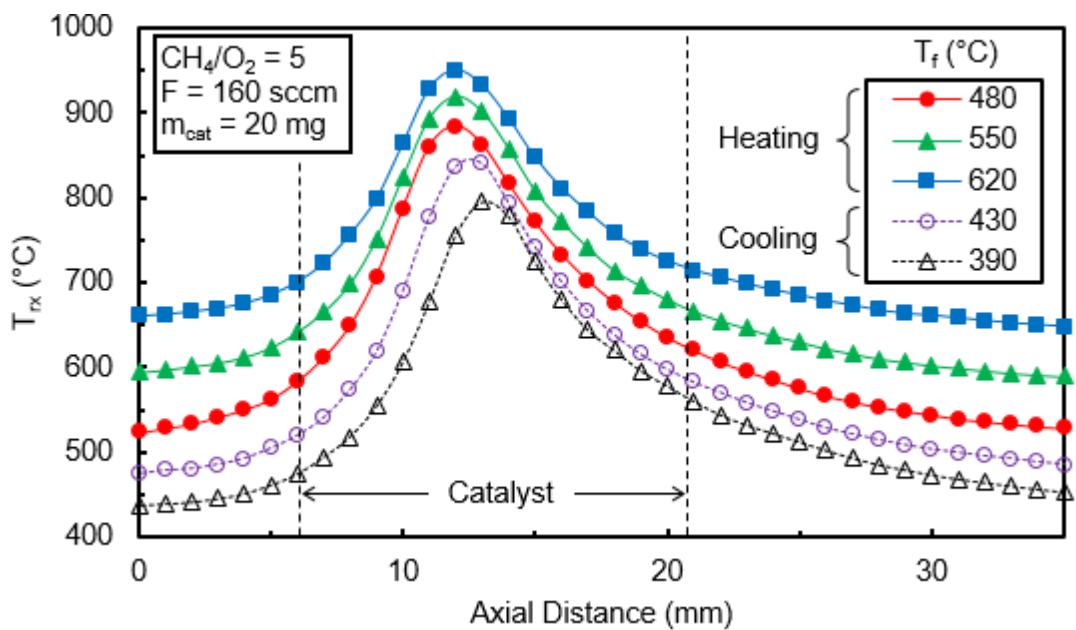


Figure 6.2. Reactor temperature T_{rx} as a function of axial distance in and near the catalytic zone.

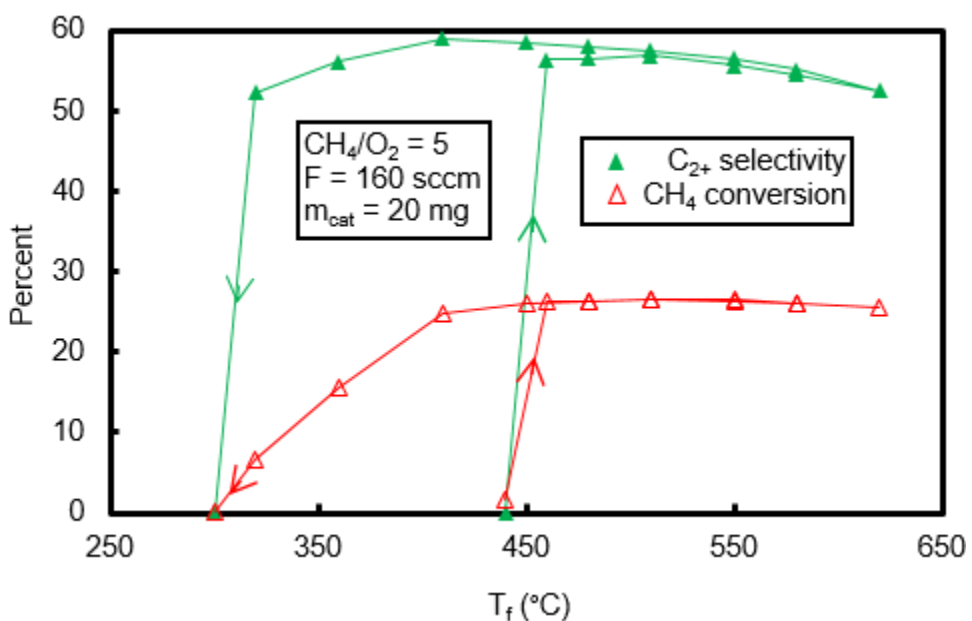


Figure 6.3. C_{2+} selectivity and CH_4 conversion as a function of feed temperature T_f , where the arrows indicate the increasing or decreasing path for T_f .

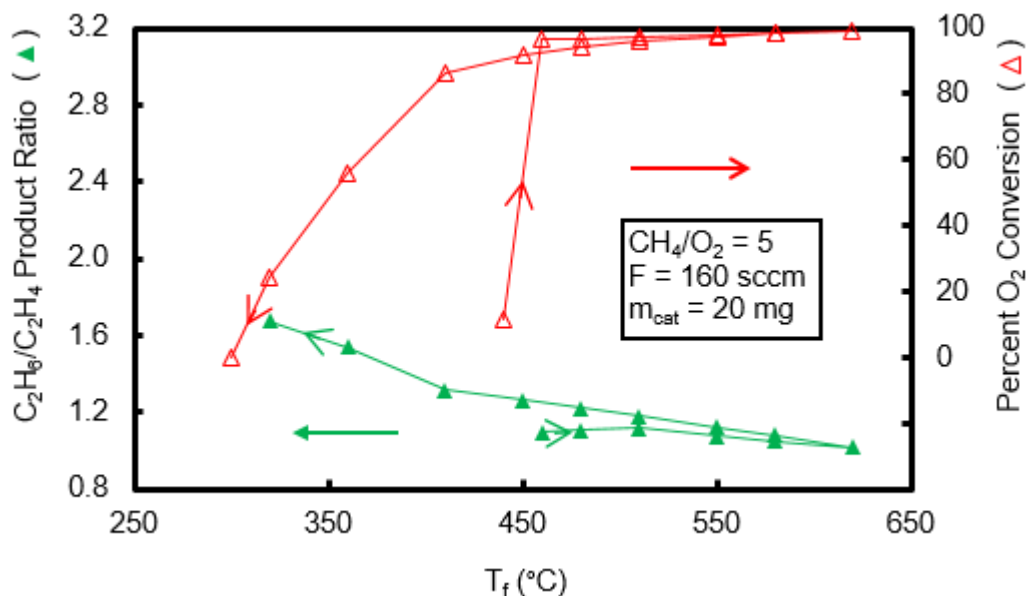


Figure 6.4. Ethane-to-ethylene product ratio (left ordinate) and percent O_2 conversion (right ordinate) as a function of feed temperature T_f , where the arrows indicate the increasing or decreasing path for T_f .

6.6. Effect of bed depth and space velocity.

In order to better assess the importance of transport limitations relative to surface reactions, the performances of three reactors having 5, 10 and 20 mg catalyst loadings were investigated as a function of space velocity (i.e. $F/m_{cat} = [\text{Feed gas flow rate (sccm)}]/[\text{Catalyst weight (mg)}]$). In Figure 6.9 and Figure 6.10, CH_4 and O_2 conversions, and C_{2+} selectivities and C_2H_6/C_2H_4 ratios are presented respectively, as a function of space velocity for each of these packed beds. The CH_4/O_2 ratio was kept at 5 and the feed gas temperature was 570 °C in all of this set of experiments. An inspection of Figure 6.9 reveals several trends. First, both the C_{2+} selectivities and methane conversions decreased with space velocity for all the three beds. Second, neither the methane conversion nor the C_{2+}

selectivity profiles overlapped, clearly indicating that mass transfer rates were the limiting process in the OCM reaction. As seen in Figure 6.9, C_{2+} selectivities were dramatically different, with the smaller packed bed reactor performing the best. For example, at the 15 sccm/mg space velocity, the C_{2+} selectivities were 64%, 55% and 45% for the 5, 10 and 20 mg catalyst bed reactors, respectively. These results indicate that deeper bed reactors are detrimental in OCM as they result in subsequent destruction of C_{2+} products once formed in the early part of the bed. Consequently, shallow bed reactors are desirable to maximize C_{2+} selectivities.

From Figure 6.10, it can be seen that O_2 conversions in the shorter 5 mg bed were consistently lower at 85-93% than the two others, both of which exhibited near complete oxygen consumption (>95%). Evidently, the 5 mg bed utilizes the reactants more efficiently towards OCM products while the other, i.e. deeper, beds lead to the subsequent combustion of C_{2+} products. These results are consistent with the higher C_{2+} selectivity of the 5 mg bed with its similar methane conversion (Figure 6.9) and the lower C_{2+} selectivities of the deeper beds.

The trends exhibited by the C_2H_6/C_2H_4 ratios were all similar, decreasing with increasing space velocity as a result of increasing reactor temperatures. However, unlike C_{2+} selectivities, the deeper bed reactors were more beneficial for ethylene production. For example, at a space velocity of 20 sccm/mg, the C_2H_6/C_2H_4 ratios were 1.3 and 1.05 for the 5 mg and 10 mg beds respectively. This appears to be due to increased rates of surface mediated ethane dehydrogenation through the deeper catalyst bed. If gas phase dehydrogenation processes were responsible, then the C_2H_6/C_2H_4 ratios would have been

expected to be similar. These results are also consistent with a previous work in which concentration profiles in a similar reactor showed a delayed production of C_2H_4 relative to C_2H_6 [118]. Such a lag is expected since C_2H_4 is understood to be produced by the *sequential* catalytic dehydrogenation of C_2H_6 .

6.7. Time on stream.

In Figure 6.11, the time on stream performance of the $La_2O_3-CeO_2$ nanofiber fabric catalyst is presented for over a 10 h continuous operation. The experimental conditions were: feed gas flow rate of 80 sccm, 20 mg catalyst, CH_4/O_2 ratio of 5 and feed temperature of 570 °C. As evident from Figure 6.11, the $La_2O_3-CeO_2$ fabric exhibits an excellent performance, showing negligible deterioration in activity and selectivity, rendering it a promising practical OCM catalyst. Confirmatory SEM images of representative nanofibers, taken before and after 10 h of performance testing, are also shown in Figure 6.12 and suggest no morphological changes (e.g. no sintering).

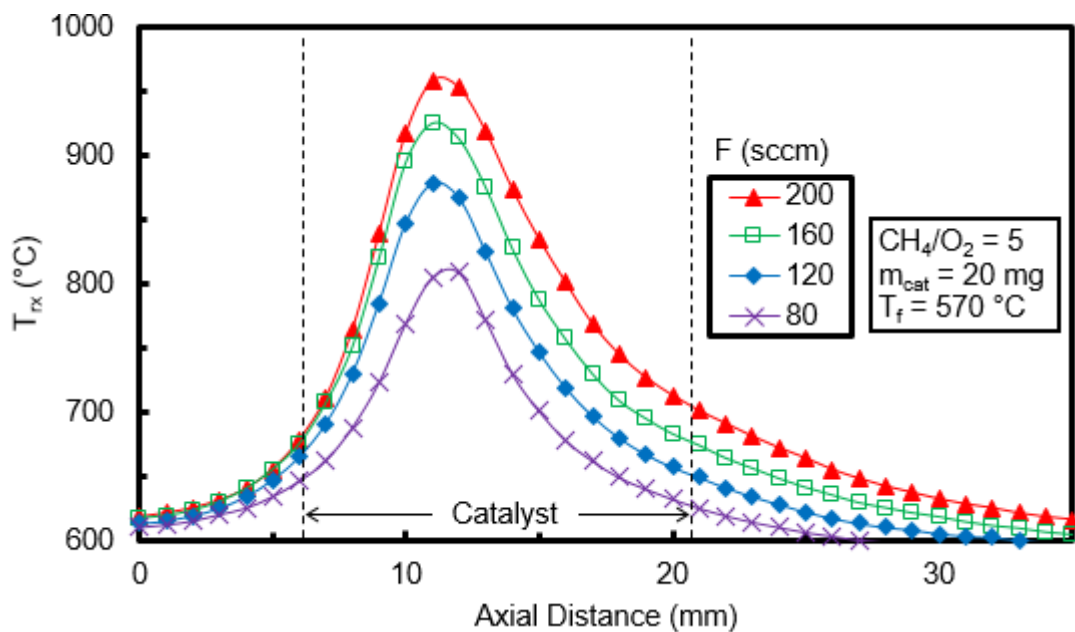


Figure 6.5. Reactor temperature T_{rx} as a function of axial distance in and near the catalytic zone for various feed flow rates F .

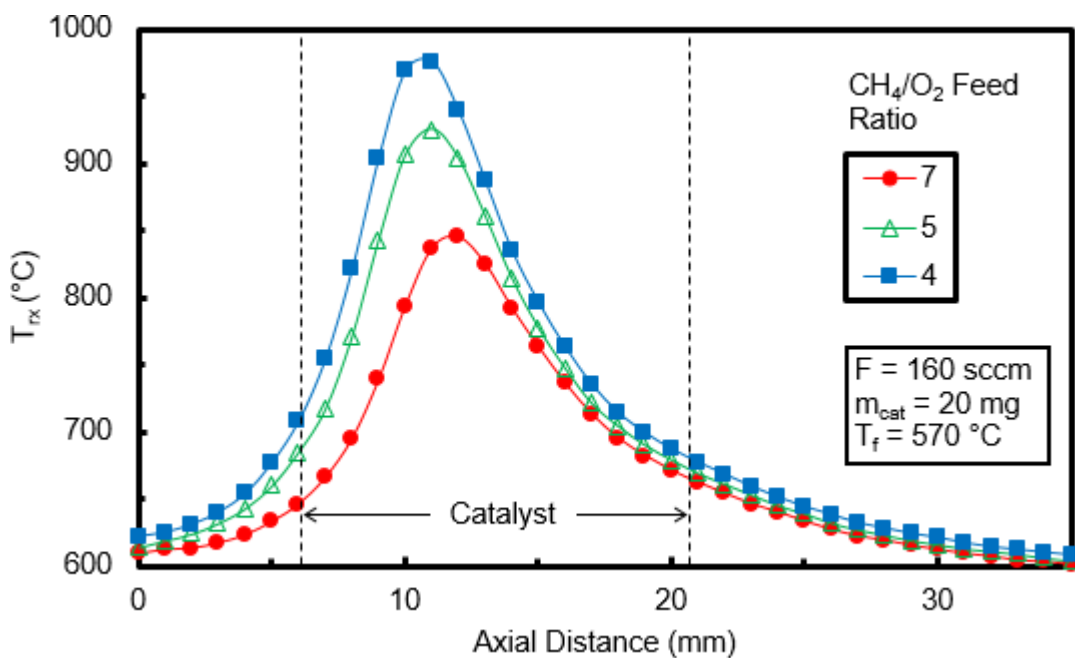


Figure 6.6. Reactor temperature T_{rx} as a function of axial distance in and near the catalytic zone for the various feed CH_4/O_2 ratios.

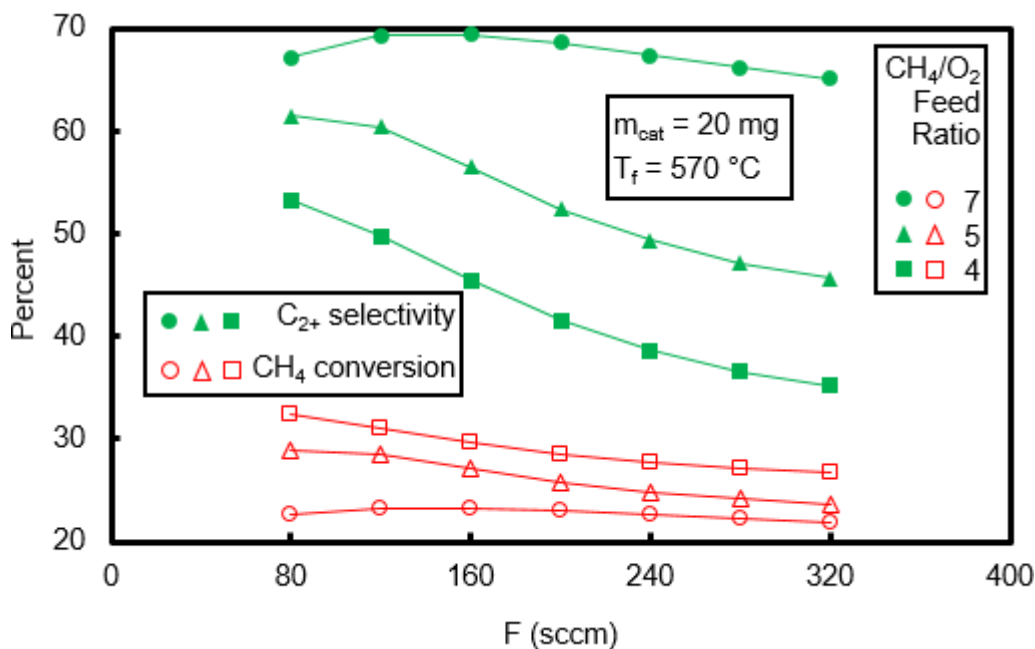


Figure 6.7. C₂₊ selectivity and CH₄ conversion as a function of flow rate and the CH₄/O₂ feed ratio.

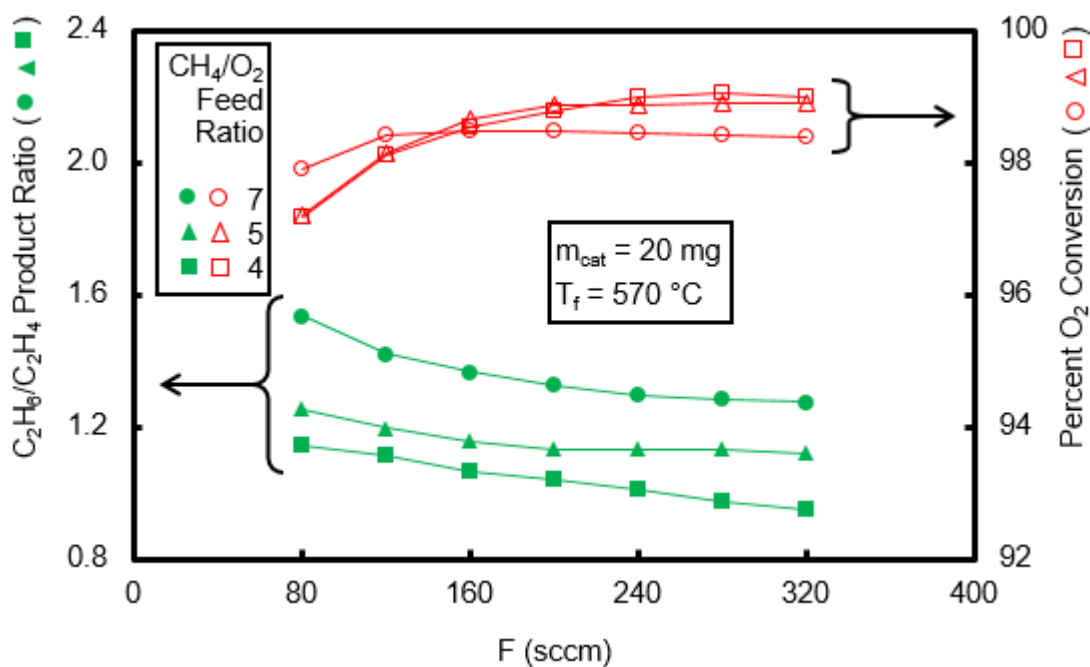


Figure 6.8. Ethane-to-ethylene product ratio (left ordinate) and percent O₂ conversion (right ordinate) as a function of feed flow rate and the CH₄/O₂ feed ratio.

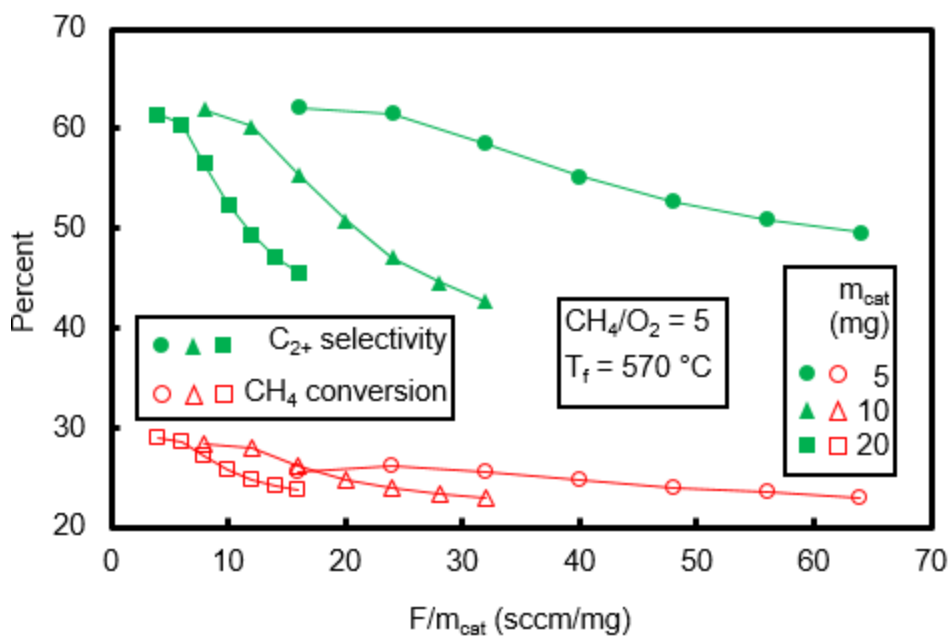


Figure 6.9. C_{2+} selectivity and CH_4 conversion as a function of space velocity F/m_{cat} and catalyst weight m_{cat} .

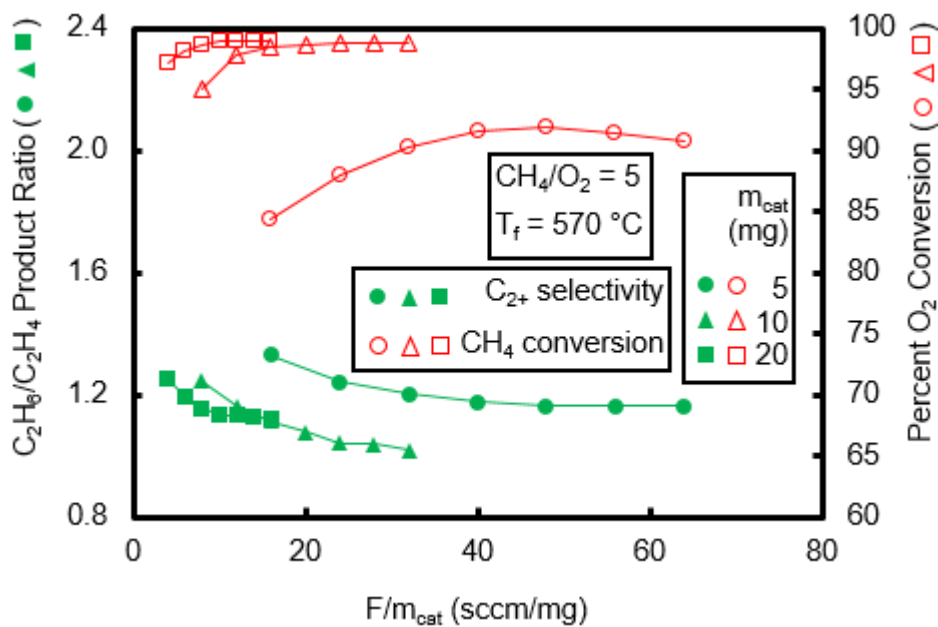


Figure 6.10. Ethane-to-ethylene product ratio (left ordinate) and percent O_2 conversion (right ordinate) as a function of space velocity F/m_{cat} and catalyst weight m_{cat} .

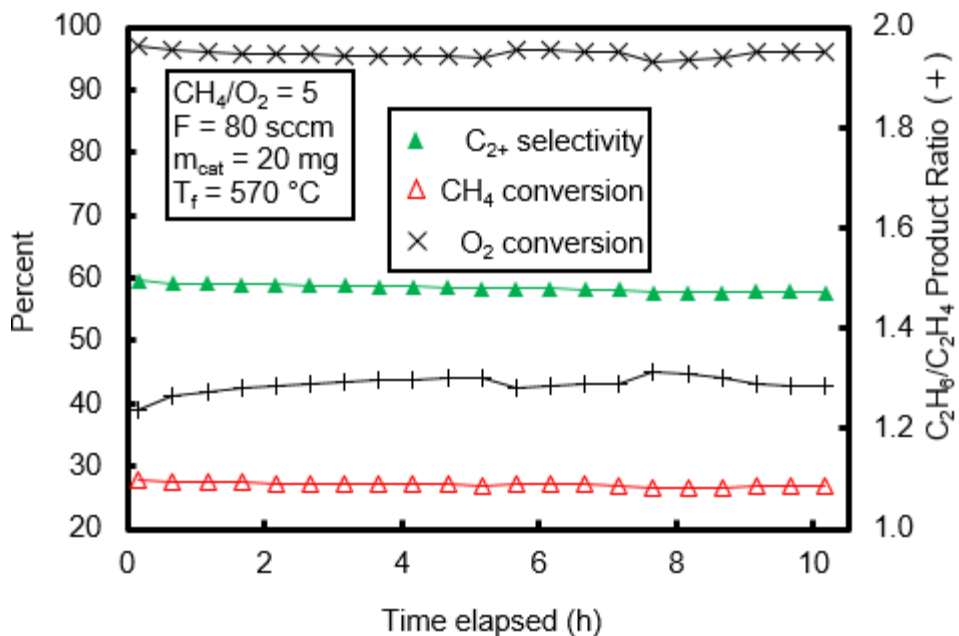


Figure 6.11. Time on stream showing C₂₊ selectivity, CH₄ conversion and O₂ conversion as a function of time.

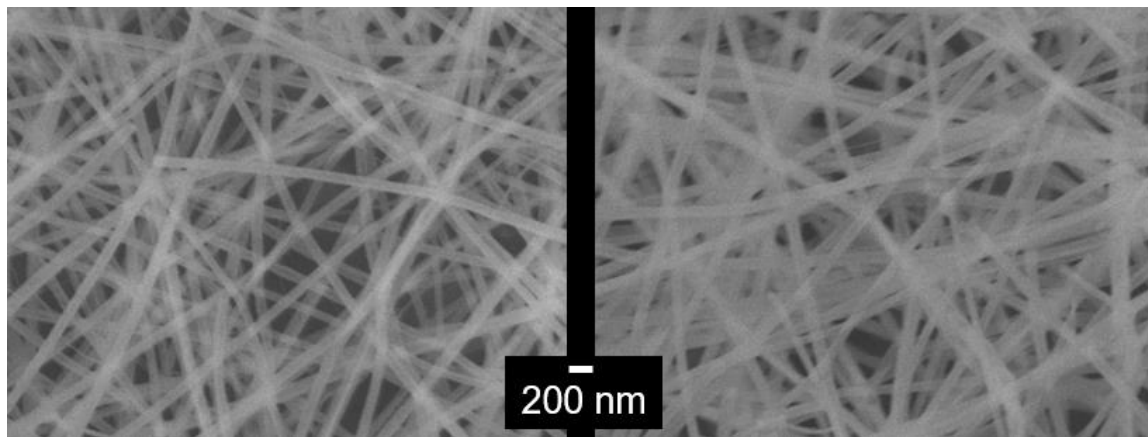


Figure 6.12. La₂O₃-CeO₂ nanofibers of ~100 nm diameter prior to (left) and after (right) ~10 hours of OCM performance evaluation, in experiments separate from but similar to that of Figure 6.11 (secondary electron imaging; 15 kV; 30,000× magnification; 8.7 mm working distance).

6.8. Summary.

In conclusion, the reaction engineering aspects of a $\text{La}_2\text{O}_3\text{-CeO}_2$ nanofiber fabric catalyst have been evaluated using packed bed reactors over a broad range of operating conditions. These studies indicated that the rates of the OCM reaction are largely dominated by mass transfer limitations, evidenced by the increases in the bed temperature with increasing feed flow rates. Our studies also revealed that short catalytic beds are preferred for increasing C_{2+} selectivities in OCM reactors. C_{2+} selectivities and yields of 70% and 18% respectively were also attained in this study.

Chapter 7. Direct In-Situ Spatial Concentration and Temperature Profiling and OCM Reactors of Multiple Fixed Beds.

In this portion of the work, the concept of in-situ spatial concentration and temperature profiling is developed as a means of ascertaining detailed data sets that may be used in refining detailed chemical kinetic mechanisms (DCKM) for oxidative coupling of methane (OCM). Transport and kinetic models of the process may be critical to developing catalytic materials and reactor designs that maximize C_{2+} yield. By obtaining spatial profiles of all stable chemical species within the reactor as well as the temperature, we are thus able to provide insightful data that can be compared to OCM models, allowing them to be improved. The profiling method developed here is easily applied to the nanofiber fabrics of Chapters 6 and 7. In this chapter, we also design OCM reactors of two fixed beds with interstage cooling and O_2 injection. By doing this, CH_4 effectively remains in plug flow while the concentration of O_2 is more evenly distributed spatially along the bed, which minimizes the combustion of CH_4 and C_{2+} hydrocarbons while still maintaining a high supply of O_2 overall to the reactor. This chapter is based on two *ChemCatChem* publications [118, 121].

7.1. Reactor Setup.

Experiments were performed by using a fixed-bed tubular reactor system, as shown in Figure 7.1. The reactor was packed with La_2O_3 - CeO_2 nanofiber fabric catalysts that were

prepared by electrospinning a viscous solution of polyvinylpyrrolidone (PVP; 1.3 MDa, 0.60 g), water/ethanol (\approx 1:1 wt ratio, 9.5 g) in which the metal precursors, as $\text{La}(\text{NO}_3)_3 \cdot 6\text{H}_2\text{O}$ and $\text{Ce}(\text{NO}_3)_3 \cdot 6\text{H}_2\text{O}$ (La/Ce weight ratio = 3, 0.35 g), were dissolved [111]. The electrospun material was calcined at 625 °C in a furnace to form metal oxide nanofiber fabrics. SEM images confirmed that the nanofibers had an average diameter of approximately 90 nm. The fabric also had a low BET area of approximately 20 m²/g, which suggested that the nanofibers were dense and did not possess internal porosity. This fabric (20 mg) was loosely packed into a 6 mm diameter quartz tube and sandwiched between quartz wool plugs (20 mg, Figure 7.1). The bulk density and void fraction of the bed were determined to be approximately 0.3 g/cm³ and 0.94 respectively. The reactor was placed inside a cylindrical tubular furnace, which preheated the feed gasses and the catalyst bed. The total flow of reactant gases was maintained at 160 cm³/min at standard temperature and pressure (STP) in all of the single-bed experiments by using electronic mass flow controllers (MFCs; MKS Billerica, MA). This flow rate corresponded to a nominal space time of approximately 60 ms. The experiments were performed at 101.3 kPa.

7.2. Acquisition of Spatial Profiles.

Gas sampling was accomplished by centrally inserting a conically tapered and closed-end quartz capillary tube (800 μm ; Friedrich and Dimock, Millville, NJ) into the packed bed followed by gas analysis by on-line gas chromatography (Varian 4900 Mini GC, with 5 Å molecular sieves and Poraplot U columns). The capillary had an 80 μm

diameter orifice laser drilled on its side [78, 122] to withdraw gases from within the bed (see inset in Figure 7.1). The location of the sampling orifice and the overall length of the probe were designed such that the capillary tip always remained outside of the packed bed at any sampling position to avoid gas bypass. The capillary probe withdrew gas samples at a rate less than 5 cm³/min at STP; thus, the flow within the reactor (160 cm³/min at STP) was minimally perturbed. This sampling rate corresponded to an average gas velocity of 50-100 cm/s within the capillary (depending on the temperature), which enabled the rapid removal of gas samples from within the reactor. Temperature measurements were performed by placing a thin (250 μm diameter) K-type thermocouple inside the capillary probe in the absence of gas withdrawal. The tip of the thermocouple was positioned at the sampling orifice. Capillary sampling lines as well as the GC injection system were heated to approximately 100 °C to prevent water condensation in the transfer lines. Water subsequently was condensed out by using an ice bath before GC analysis. The temperature and concentration profiles were obtained by moving the capillary (with and without the thermocouple) in the axial direction by using a micropositioning device (Velmex, Bloomfield, NY). Positional accuracy within the reactor was estimated to be ±0.25 mm. Similar uncertainty would be expected to exist between the temperature and concentration profiles as well.

Experiments involving dual fixed beds were performed similarly as shown in Figure 7.2. The reactor was sequentially packed with the same La₂O₃-CeO₂ nanofiber fabric catalysts such that two sections, each with 20 mg, were packed into the quartz tube with an interbed spacing of approximately 15 mm. The feed to the first reactor was fixed

at $120 \text{ cm}^3/\text{min}$. The interstage O_2 was introduced at the middle of the interspace, that is, approximately 27-28 mm downstream of the start of the first quartz wool plug at a rate of 12-15 mL/min. Acquisition of the spatial profiles was conducted in the same manner as with the single fixed bed reactor.

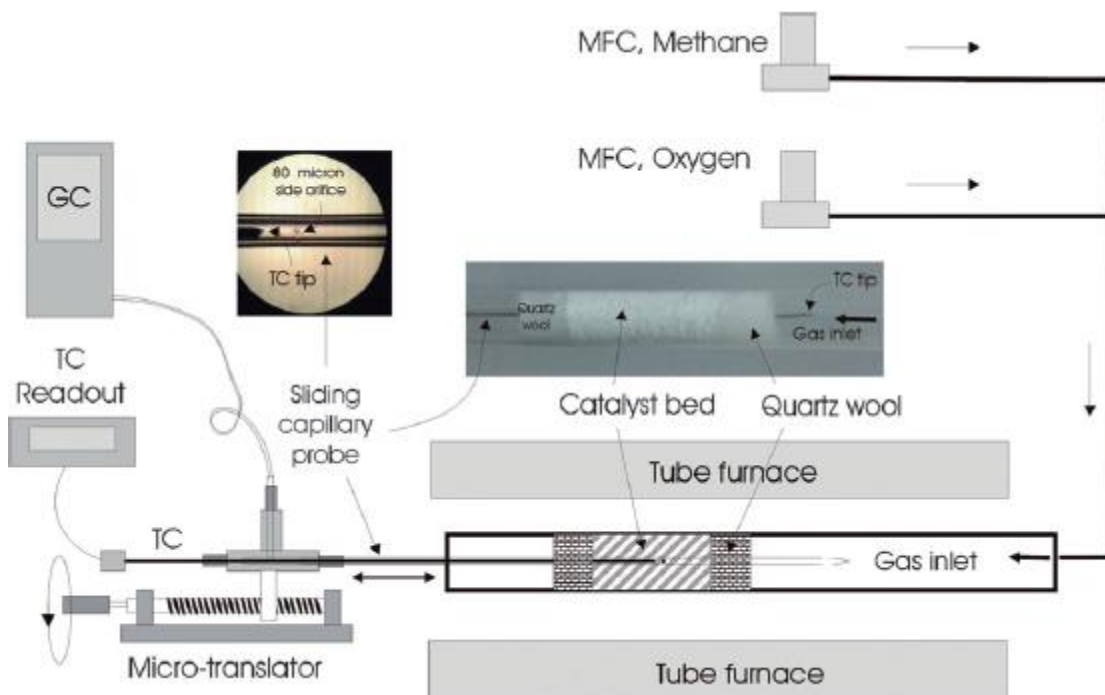


Figure 7.1. The reactor system used to acquire spatial temperature and concentration profiles. The reactor comprised a 6 mm diameter quartz tube packed with $\text{La}_2\text{O}_3\text{-CeO}_2$ nanofiber fabric catalyst (20 mg), which was sandwiched between quartz wool plugs (20 mg, right image). Gas samples were withdrawn from within the packed bed by using an 800 μm closed-end capillary with an approximately 80 μm side sampling orifice (left image) that was centrally inserted into the reactor. Gas analysis was accomplished by on-line gas chromatography (GC). Spatial profiles were generated by sliding the capillary within the packed bed by using a microtranslation device. Temperature profiles were measured by a 250 μm diameter K-type thermocouple (TC) that was inserted into the capillary after the concentration profile measurements. The tip of the thermocouple was placed at the same location of the sampling orifice.

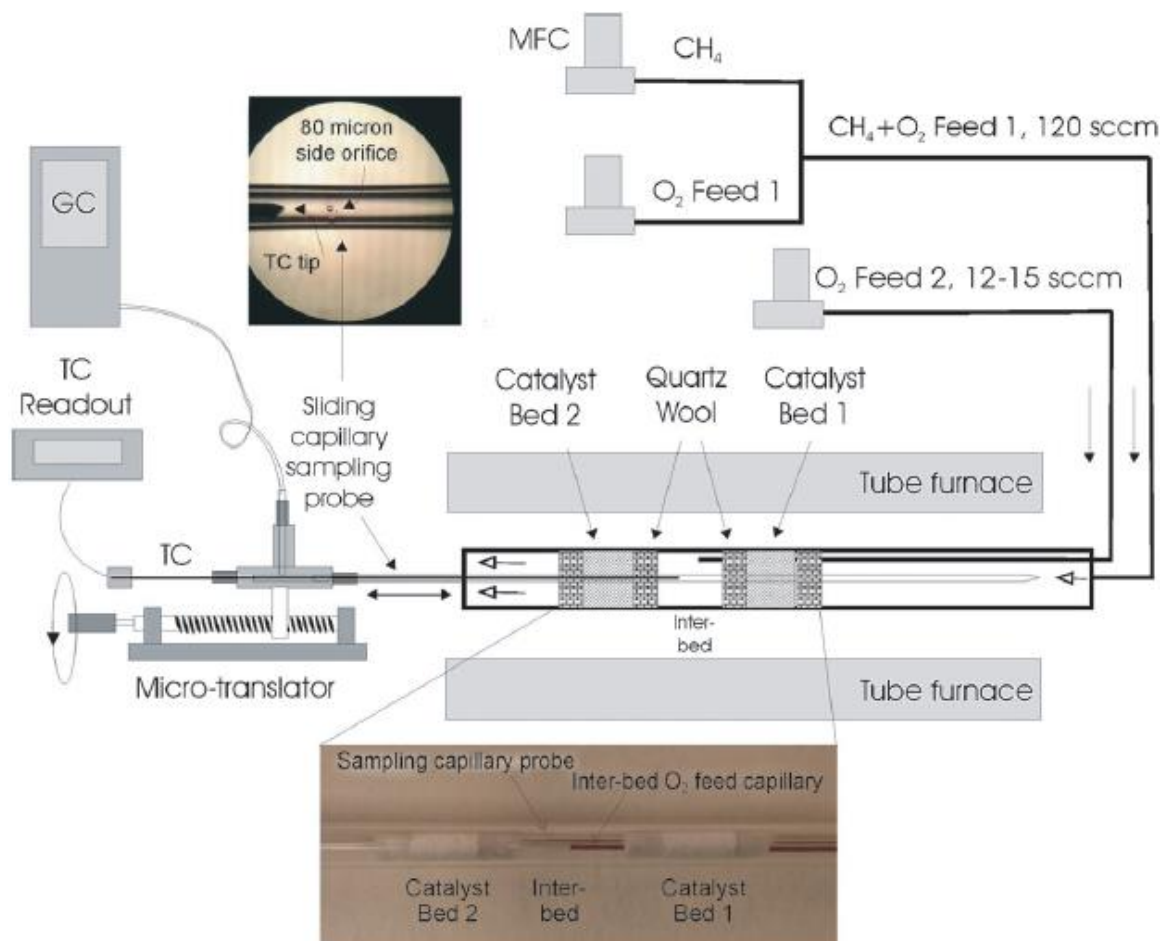


Figure 7.2. The reactor system used to acquire spatial temperature and concentration profiles in catalytic reactors comprising dual fixed beds with inter-stage O_2 injection and cooling. The sampling procedure was the same as described in Figure 7.1.

7.3. Spatial Profiles on a Single Fixed Bed Catalytic Reactor.

In Figure 7.3, Figure 7.4 and Figure 7.5 the spatially resolved temperature and species mole percent profiles are presented for $CH_4/O_2 = 7, 9$ and 11 respectively, without the use of a diluent gas. A total of nine species were quantified: CH_4 , O_2 , C_2H_6 , C_2H_4 , C_3H_8/C_3H_6 (C_3), H_2 , H_2O , CO and CO_2 . With the exception of the concentration of H_2O , which was calculated from oxygen atomic balances, all of the species were quantified

directly from GC measurements by using a multipoint GC calibration process performed before the OCM experiments. In Figure 7.6, the spatially resolved CH₄ conversions and C₂₊ (C₂H₆ + C₂H₄ + C₃) selectivities are also presented. As is evident from these figures, the spatial concentration and temperature profiles measured in the early parts of the catalytic bed provide information-rich data on the kinetics and mechanism of the OCM scheme. In contrast, the profiles are essentially featureless and contain very limited information towards the reactor exit.

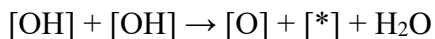
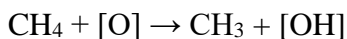
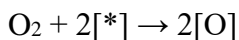
In all of the figures, the location of the catalyst bed is indicated by the vertical dashed lines; the catalyst packing starts at approximately 4 mm and ends at approximately 18 mm, which corresponds to a bed depth of 14 mm. The feed temperature used (furnace temperature) for each CH₄/O₂ ratio was different because of the different ignition temperatures that were exhibited. As expected, the feed temperature for ignition increased from 600 °C for CH₄/O₂ = 7 (Figure 7.3) to 640 °C for CH₄/O₂ = 9 (Figure 7.4) and to 730 °C for CH₄/O₂ = 11 (Figure 7.5). However, the peak reactor temperatures were relatively close to one another at 810, 790 and 840 °C for CH₄/O₂ = 7, 9 and 11 respectively. The temperature profiles as shown in these figures are direct thermocouple measurements. The possible presence of radial temperature gradients was also explored by simultaneously placing multiple thermocouples at the same axial position but at different radial positions during the reaction. These measurements indicated maximum radial temperature differences in the 10-20 °C range at peak reactor temperatures of approximately 800 °C. Consequently, the treatment of the reactor as quasi-1D appears to be a reasonable assumption.

At $\text{CH}_4/\text{O}_2 = 7$ (Figure 7.3), the temperature sharply increased to its maximum of approximately 800 °C at 6 mm into the catalyst bed (i.e., at 10 mm axial distance in the plot), which corresponds to a temperature increase of approximately 200 °C, and it then decreased towards the exit of the reactor. Given that the reactor was not adiabatic, this temperature profile was expected and could be used directly in reactor simulations to decouple the energy balance equation from mole balance equations [123, 124].

The species profiles in Figure 7.3 exhibit both confirmatory and new information. First, the integral OCM performance was 23% CH_4 conversion and 68% selectivity for C_2+ products (see also Figure 7.6), an expected result. However, close examination of the profiles at the upstream part of the catalyst reveals intriguing new information. Most importantly, significant levels of H_2 were produced very early in the catalytic zone, that is, prompt H_2 ; a peak level of approximately 2.5 mol% was reached within 5 mm inside the catalyst bed (9 mm axial distance). Within this zone, the reactor temperature was still relatively low at 625-675 °C; thus, H_2 formation is expected to be due to surface-catalyzed reactions. Hydrogen formation is closely followed up by CO_2 (peak at $\approx 5\%$) and CO ($\approx 1.8\%$) formation and then by C_2H_6 formation ($\approx 3.5\%$).

The measured concentration profiles for C_2H_6 and H_2O are consistent with the well-established elementary reactions leading to their formation. Surface oxygen species [O] are widely accepted to be responsible for CH_4 activation, which leads to the formation of CH_3 radicals and surface [OH] [125-127]. The CH_3 radicals then diffuse away from the catalyst surface and recombine in the gas phase to produce C_2H_6 . Regeneration of the active sites is also well accepted to occur through the formation and desorption of H_2O [125, 126]. The

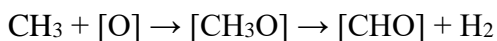
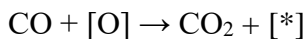
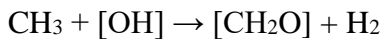
vacated active sites are then rapidly repopulated by O₂ chemisorption. These events are summarized by the following elementary reaction set:

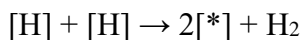
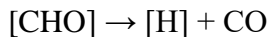
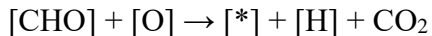


in which [*] represents a vacant catalytic surface site for oxygen chemisorption. It is likely that a dynamic equilibrium exists between gaseous O₂ and the various forms of surface oxygen, for example, chemisorbed and lattice oxygen. Undesired catalytic and gas phase reactions of CH₃ with O₂ and [O] can also lead to the formation of CO₂ and CO (CO_x) [125, 126]. C₂H₄ is then produced by the oxidative or catalytic dehydrogenation of C₂H₆. As a consequence, the formation of C₂H₄ exhibits significant lag relative to that of C₂H₆, which is clearly observed in Figure 7.3. Ethylene levels peak at 2.5% at 8 mm (12 mm axial distance) into the catalyst bed. Once formed, both C₂H₆ and C₂H₄ can also interact with [O] and create additional paths for the formation of CO_x [125, 126]. Figure 7.3 also shows the early formation and rapid rise in the concentration of H₂O concomitant with a decrease in the concentration of O₂. It is well recognized that the steady-state rate of the OCM reaction is controlled not by the activation of CH₄ and formation of C₂H₆ but by the reactions that lead to the formation of H₂O (e.g. reaction 4). This is because of the requirement to close the catalytic cycle [125, 126]. The data presented in Figure 7.3 are in harmony with this argument, for which sharp changes in species mole fraction profiles cease only after O₂ is largely consumed, that is, at an axial distance of approximately 10-

11 mm. Peak H₂O concentrations reached in this system (CH₄/O₂ = 7) were approximately 13%. Notably, in spite of the presence of an excess amount of CH₄, some O₂ slipped through the reactor. This is likely caused by a sharp decrease in the temperature, as seen in Figure 7.3.

Hydrogen could be produced by surface reactions similar to those reported in the catalytic partial oxidation (CPO) of methane to synthesis gas on Pt and Rh surfaces [75, 119]. However, in our experiments, the temperatures were lower and CO₂ was formed in larger amounts than CO. Alternately, the catalytic water gas shift (WGS) reaction, that is, H₂O + CO ↔ CO₂ + H₂, could be another potential route for hydrogen production. Analysis of the experimental data in Figure 7.3 indicates that the mol fraction ratio $Y_{CO_2}Y_{H_2}/(Y_{H_2O}Y_{CO})$ was in the 0.5-0.6 range within 5 mm into the catalyst bed. These values are significantly lower than the WGS equilibrium constant of 1.5-2 at the prevailing temperatures; this indicates that La₂O₃-CeO₂ is not a good WGS catalyst. These and other plausible surface reactions leading to H₂ formation should be incorporated into current DCKMs to broaden their range of applicability and to increase their utility to predict OCM performance over a wide range of operating conditions [124, 125, 127]. Since H₂ formation is also accompanied by CO₂ and CO, some examples of possible reactions accounting for this are:





In Figure 7.4, the spatial profiles are presented for $\text{CH}_4/\text{O}_2 = 9$. Prompt H_2 formation was also noted in this case, albeit at a slightly lower peak level of approximately 2.2%. The production of CO_2 decreased and reached only 3.5%, whereas C_2H_6 production increased to a peak level of approximately 3.5%. As before, C_2H_4 formation lagged behind C_2H_6 formation and increased to a peak level of approximately 2.1%. The integral CH_4 conversions and C_{2+} selectivities were approximately 19 and 72% respectively (Figure 7.6). Water formation leveled off at approximately 11-12%. Oxygen slippage was less in this system than in the system with $\text{CH}_4/\text{O}_2 = 7$.

The spatial profiles obtained at the highest ratio, $\text{CH}_4/\text{O}_2 = 11$, exhibited new trends, as shown in Figure 7.5. Most importantly, C_2H_6 was formed very early in the catalyst bed, and significantly, C_2H_6 production surpassed H_2 production, which is in stark contrast to the experiments for lower CH_4/O_2 ratios discussed above (i.e. Figure 7.3). Hydrogen levels peaked at approximately 1.9%. Ethane also became the most abundant product (peak at $\approx 4\%$), surpassing CO_2 (peak at $\approx 3\%$). However, ethylene levels remained surprisingly similar to those of previous experiments and exhibited a peak concentration of only 2.2%, although temperatures were significantly higher. As seen in Figure 7.5, C_2H_4 production abruptly ceased at 6 mm into the catalyst bed (10 mm axial distance), at which point O_2 was entirely consumed and the temperature peaked at 840 °C. This result is consistent with the generally accepted mechanism that oxidative dehydrogenation of C_2H_6 is the primary

path for C_2H_4 formation in OCM experiments. Similar observations were made in experiments in which lower CH_4/O_2 ratios were studied (Figure 7.3 and Figure 7.4). Maximum water concentrations of approximately 10% were also reached at 6 mm into the catalyst bed. Exit CH_4 conversions were lowest at approximately 17% whereas C_{2+} selectivities were the highest at 77% among the three CH_4/O_2 ratios investigated.

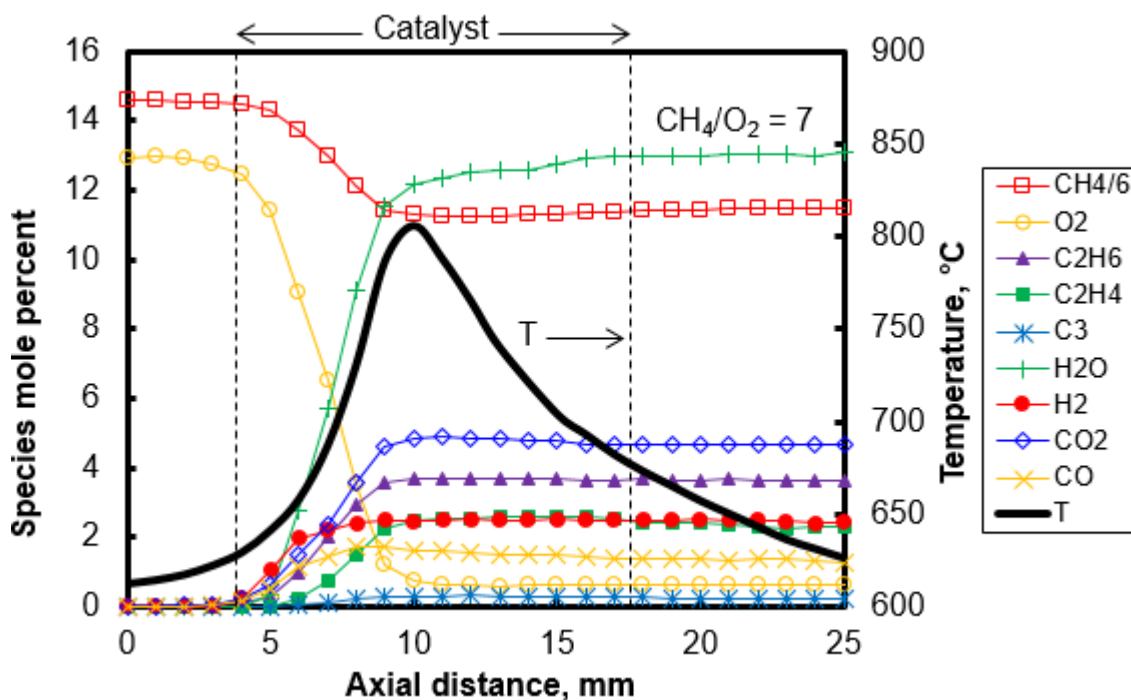


Figure 7.3. Spatial temperature and species mole percent profiles for: feed CH_4/O_2 ratio of 7, total gas flow rate of $160\text{ cm}^3/\text{min}$, nominal space time of $\sim 60\text{ ms}$, furnace temperature of $600\text{ }^\circ\text{C}$.

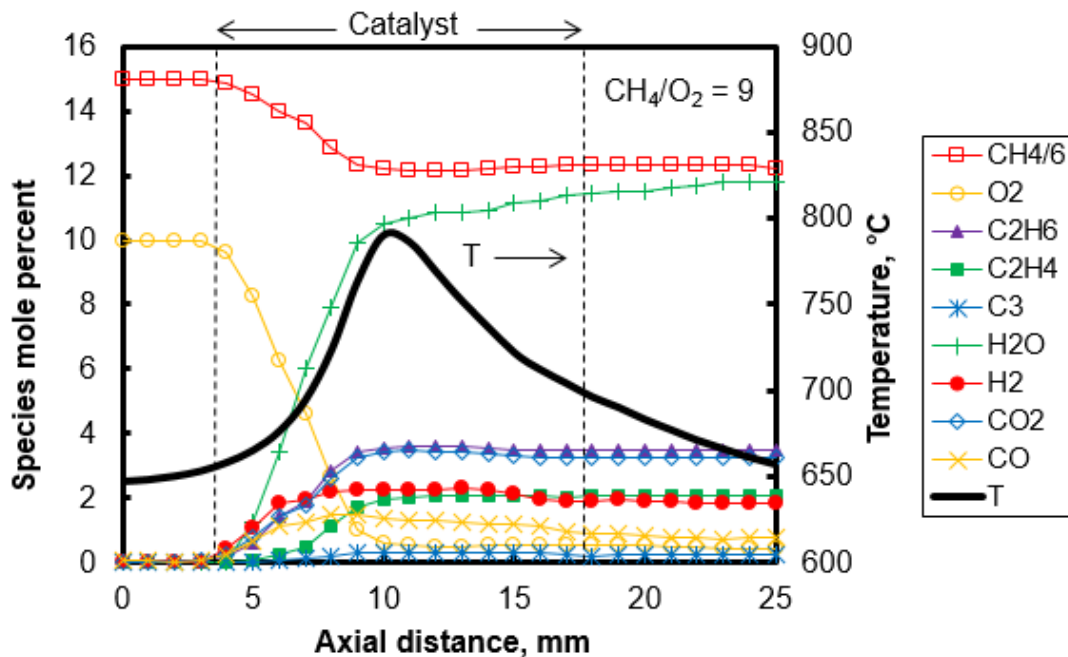


Figure 7.4. Spatial temperature and species mole percent profiles for: feed CH_4/O_2 ratio of 9, total gas flow rate of $160 \text{ cm}^3/\text{min}$, nominal space time of $\sim 60 \text{ ms}$, furnace temperature of $640 \text{ }^\circ\text{C}$.

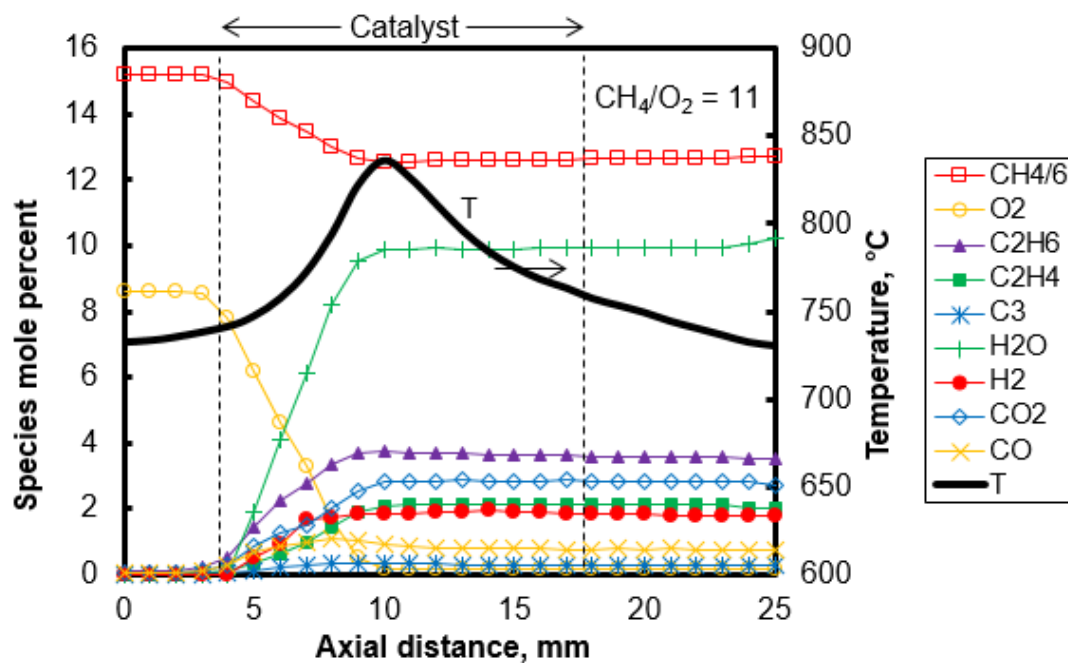


Figure 7.5. Spatial temperature and species mole percent profiles: feed CH_4/O_2 ratio of 11, total gas flow rate of $160 \text{ cm}^3/\text{min}$, a nominal space time of $\sim 60 \text{ ms}$, furnace temperature of $730 \text{ }^\circ\text{C}$.

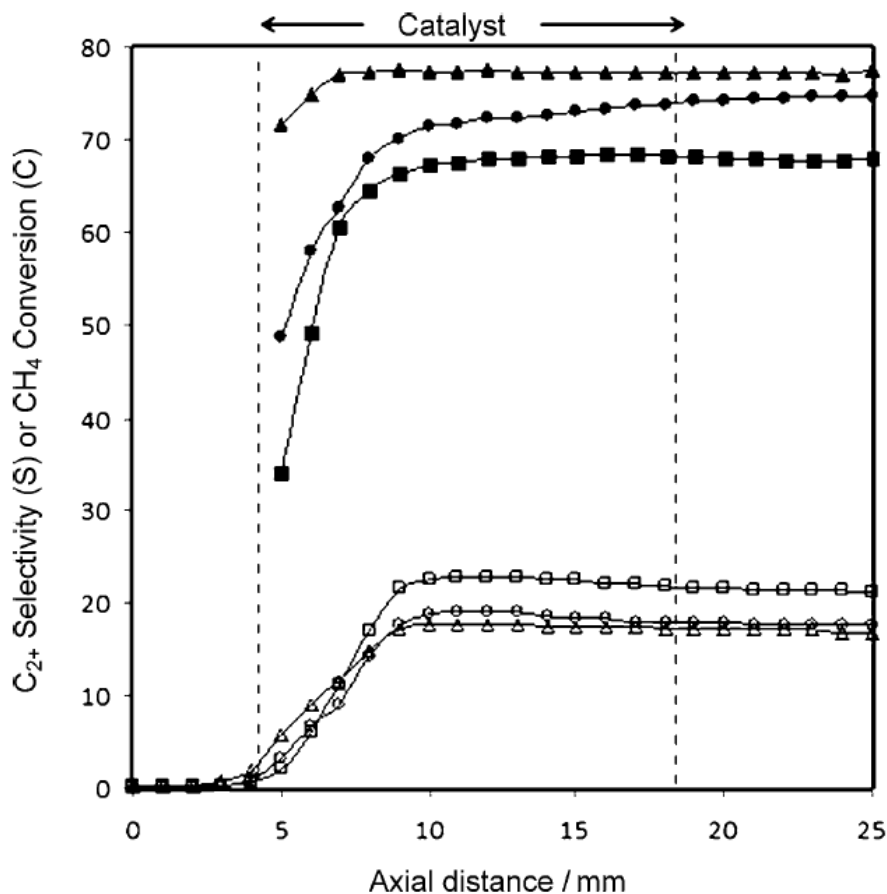


Figure 7.6. Spatial profiles for CH₄ conversions and C₂₊ selectivities for the different CH₄/O₂ ratio experiments. Total gas flow rate was 160 cm³/min, which corresponded to a nominal space time of approximately 60 ms.

7.4. Spatial Profiles on a Dual Fixed Bed Catalytic Reactor.

To demonstrate the improvements provided by the split introduction of O₂ on the yields of C₂₊ products, two sets of experiments were performed. First, a single-bed experiment (SB1) was performed in which methane and oxygen were fed at a CH₄/O₂ ratio of 4.0 at 120 mL/min (≈60 ms space time). In the first dual-bed experiment (DB1), the first

reactor feed was at 120 mL/min having a CH₄/O₂ ratio of 9.0, followed by 12 mL/min O₂ addition into the interstage zone, which thereby maintained the overall CH₄/O₂ ratio at 4.0.

An additional dual bed experiment was also performed at the overall CH₄/O₂ ratio of 4.4 (DB2 experiment) to assess the impact of the CH₄/O₂ ratio on the reactor performance. In this case, the feed flow rate to the first reactor was kept at 120 mL/min with a CH₄/O₂ ratio of 11.0, followed by the introduction of 15 mL/min O₂ to the interstage zone. Notably, in the dual bed experiments (DB1, DB2) both of the catalyst beds were kept inside one tubular furnace (Figure 7.2).

In Figure 7.7, the spatially resolved temperature and species mole percent profiles are presented for the single bed reactor experiments (SB1). In Figure 7.8 and Figure 7.9, the same profiles are presented for the dual bed reactor experiments DB1 and DB2 respectively. In Figure 7.10, the CH₄ conversion and C₂₊ selectivity profiles are presented for the SB1, DB1 and DB2 experiments.

In all the figures, the locations of the various sections of the reactor system are indicated by vertical dashed lines; the first La₂O₃-CeO₂ nanofiber fabric catalyst packing starts at approximately 5 mm and ends at approximately 15 mm, which corresponds to bed depth of approximately 10 mm. The first 5 mm in the graphs correspond to the quartz-wool packing. The first bed is followed by another 5 mm of quartz packing, followed by 15 mm of interspace (no packing). The quartz packing for the second bed starts at approximately 35 mm followed by approximately another 10 mm La₂O₃-CeO₂ nanofiber fabric catalyst and 5 mm of quartz-wool packing. The secondary O₂ injection point was approximately at 25 mm, as indicated by an arrow pointing down. Other than the interspace concentration

profiles, the location of the O₂ injection point had no discernible effect on the performance of the second reactor.

The spatial concentration and temperature profiles for the single-bed experiment (SB1) with a CH₄/O₂ ratio of 4 were acquired at a furnace temperature (T_f) of 600 °C, which was sufficient to achieve ignition. As seen in Figure 7.7, the maximum bed temperature reached approximately 1015 °C at approximately 10 mm (i.e. 5 mm within the catalytic zone), concomitant with the near-complete consumption of O₂ and approximately 30% CH₄ conversion and 55% C₂₊ selectivity (see also Figure 7.10). These values represent a C₂₊ yield of approximately 16%.

Close examination of the profiles at the upstream part of the catalyst bed reveals significant levels of H₂ production early in the catalytic zone, that is, prompt H₂; a peak level is reached at approximately 3.7 mol% within 3 mm inside the catalyst bed (8 mm axial distance). Within this zone, the reactor temperature is still relatively low at 650-725 °C; thus, H₂ formation is expected to be due to surface-catalyzed reactions. Hydrogen formation precedes H₂O formation (peak 19%) and is closely followed up by CO₂ (9.31%) and CO (\approx 3%) and then by C₂H₆ (3.6%). As expected, C₂H₄ formation exhibits significant lag relative to C₂H₆ formation, which is clearly observed in Figure 7.7. Ethylene levels peaked at 3.1% at 4 mm into the catalyst bed. Figure 7.7 also shows the early formation and rapid rise of H₂O concomitant with a decrease in the O₂ concentration.

The spatial concentration and temperature profiles for the dual-bed operation (DB1) for the OCM reaction at the overall CH₄/O₂ ratio of 4 as presented in Figure 7.8 reveal several important features. First, the feed CH₄/O₂ ratio of 9 used in the first catalyst bed

necessitated the use of a higher T_f of approximately 750 °C for ignition. As seen in Figure 7.8, the bed temperatures rapidly increased within the catalytic zones and reached maximum bed temperatures of 920 °C in the first bed and 866 °C in the second bed, both at approximately 5 mm within the catalyst zones, which corresponds to complete conversion of O₂. This trend of the temperature profile is similar to the SB1 experiment presented in Figure 7.8 and yet gives us additional insight into the effects of temperature on C₂₊ yield in OCM. For example, the peak temperatures in each bed for the dual-bed experiments are significantly lower than those in the single-bed experiment. This was the consequence of the split introduction of oxygen and heat removal realized within the interstage zone, which collectively decreased the maximum temperature attained in the OCM reactors, in spite of the higher ignition temperature. As seen in Figure 7.10, a C₂₊ selectivity of 70% and an ultimate C₂₊ yield of 21% was achieved in the DB1 experiment; the latter is a value significantly higher than the 16% yield observed in the single-bed experiment at the same overall CH₄/O₂ ratio of 4. This clearly demonstrates that distributing the oxygen feed with interstage cooling is a good strategy to increase CH₄ conversion, whereas adverse effects on the selectivity of C₂₊ products are minimized. These comparative results are also presented in Table 7.1.

Second, although the mixing of the secondary O₂ feed with the reactor gases was not instantaneous, as evidenced by the presence of a steep axial oxygen concentration profile, a uniform composition was achieved within the interbed zone lose to the upstream quartz-wool packing of the second reactor. Third, the concentrations of all the species decreased upon O₂ introduction (i.e. dilution), but remained virtually unchanged along the

interbed zone and within the quartz-wool packing. Furthermore, the temperature in the interbed zone remained at approximately 755 °C, close to the furnace temperature. These measurements clearly indicate both the absence of any gas phase reactions and the inert nature of the quartz wool. This is a surprising result, as packets of high O₂ concentrations would be expected to cause gas phase combustion at the indicated interbed temperatures, especially if H₂ is present. The OCM reaction commenced once the gases entered the second catalytic bed at approximately 40 mm.

As seen in Figure 7.8, CO exhibited peak concentrations of 1.2% at 9 mm in the first bed and of 2.2% at 43 mm in the second bed, which ultimately leveled off at 2.0% at the reactor exit. Hydrogen levels were 2.3 and 3.6% at the exits of beds 1 and 2 respectively. Carbon dioxide and water levels reached 3.4 and 11.5% in bed 1 respectively and became 7 and 25.5% at the exit of the dual bed reactor respectively.

Hydrocarbon products generally increased monotonically within the catalytic zones with increasing methane conversions and ceased to change if O₂ was consumed. At the exit of the first bed, the following levels were reached: C₂H₆ (3.7%), C₂H₄ (2.23%) and C₃ (0.25%) whereas CH₄ conversion was 17%. Under these conditions, C₂₊ selectivities corresponded to 76.6%, which represents a yield of 13%. However, at the exit of the second bed the species concentrations became: C₂H₆ (4.4%), C₂H₄ (4.1%) and C₃ (0.41%), whereas CH₄ conversion increased to approximately 30% with a small reduction in the C₂₊ selectivities and, hence, a 21% yield at the end of the dual bed reactor.

Temperature and species concentration profiles within the second catalytic zone were qualitatively similar to those within the first bed, and the reactions ceased

immediately after the exhaustion of O_2 . This is an interesting result because unlike the first reactor, the feed to the second catalyst bed possessed significant levels of H_2 , CO , CO_2 and H_2O , together with C_{2+} products. Considering the fact that with complete consumption of oxygen in the second bed, H_2 and H_2O production levels are consistent with our expectations from the OCM reaction scheme and there is no sign of H_2O consumption in the second bed. Therefore, as apparent from the species concentration profiles in the second bed, even in the presence of an excess amount of steam produced in the first bed, $La_2O_3-CeO_2$ does not promote the steam reforming of methane reaction. Moreover, the excess amounts of carbon dioxide and water fed to the second bed did not cause any apparent deactivation of the OCM catalyst.

The profiles for the DB2 experiment at the overall CH_4/O_2 ratio of 4.4 as presented in Figure 7.9 are in harmony with the DB1 experiment at $CH_4/O_2 = 4.0$ (Figure 7.8), which thereby gives us confidence regarding the validity of our measurements. In the DB2 experiment, the feed CH_4/O_2 ratio of 11 used in the first catalyst bed necessitated the use of a higher T_f of approximately 780 °C for ignition, and the maximum bed temperatures reached 930 and 910 °C in the first and second beds respectively. These values are significantly lower than the single bed temperature peak of 1015 °C (Figure 7.7). Again, the location of the maximum temperatures corresponds to the complete conversion of O_2 . Moreover, the interbed temperature remained relatively constant at approximately 800 °C.

From Figure 7.9, it can be seen that CO exhibited a peak concentration of 1.0% at 5 mm within the first bed, and ultimately reached 1.6% at the exit of the second catalyst bed. Hydrogen levels were 2.2 and 3.5% at the exits of beds 1 and 2 respectively. Carbon

dioxide and water levels reached 2.8 and 10% in bed 1 respectively and become 6 and 24.2% at the exit of the second bed respectively.

In the DB2 experiment, the hydrocarbon products also exhibited similar trends, which generally increased within the catalytic zones with increasing methane and oxygen conversions and which ceased to change after the complete conversion of O₂. At the exit of the first bed, the following levels were recorded: C₂H₆ (3.52%), C₂H₄ (2.1%) and C₃ (0.21%) whereas CH₄ conversion was 19%. Under these conditions, C₂₊ selectivities would be 74%, which represents a yield of 14%. At the second bed exit, the concentration levels became C₂H₆ (4.1%), C₂H₄ (3.8%) and C₃ (0.35%), with a maximum CH₄ conversion of approximately 28%. These results corresponded to a C₂₊ selectivity of 67% and represent a final yield of approximately 19%. This value is slightly lower than the 21% yield obtained in the DB1 experiment yet higher than the 16% yield of the single bed experiment (see Table 7.1).

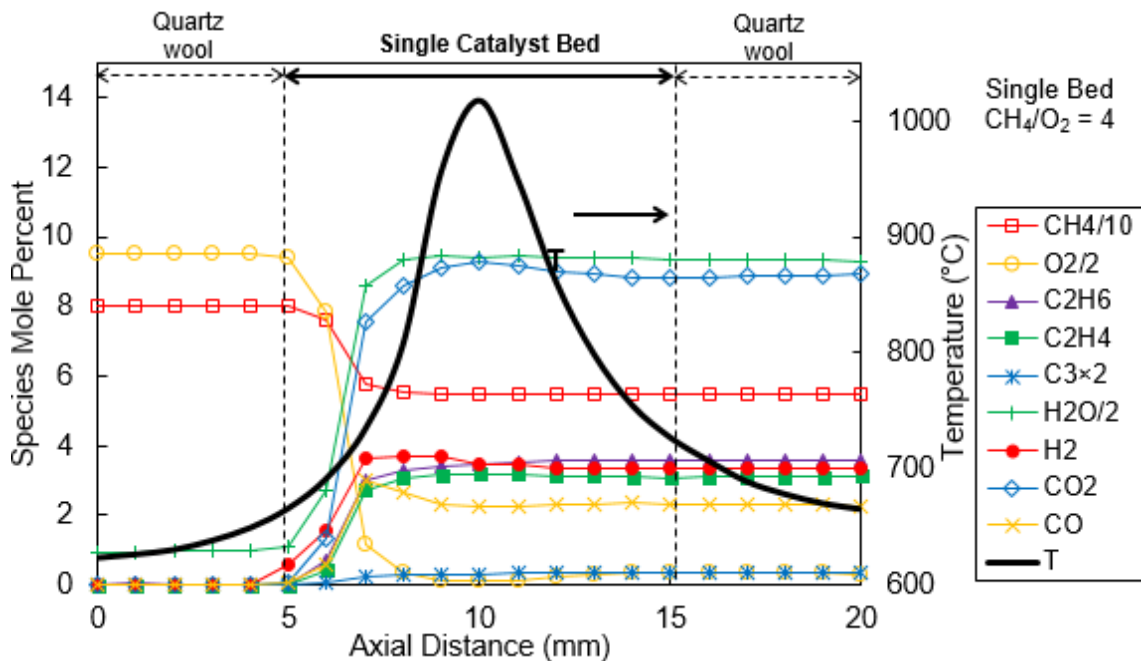


Figure 7.7. Spatial temperature and species mole percent profiles for a feed CH_4/O_2 ratio of 4. Total gas flow rate was $120 \text{ cm}^3/\text{min}$, which corresponds to a nominal space time of $\sim 70 \text{ s}$.

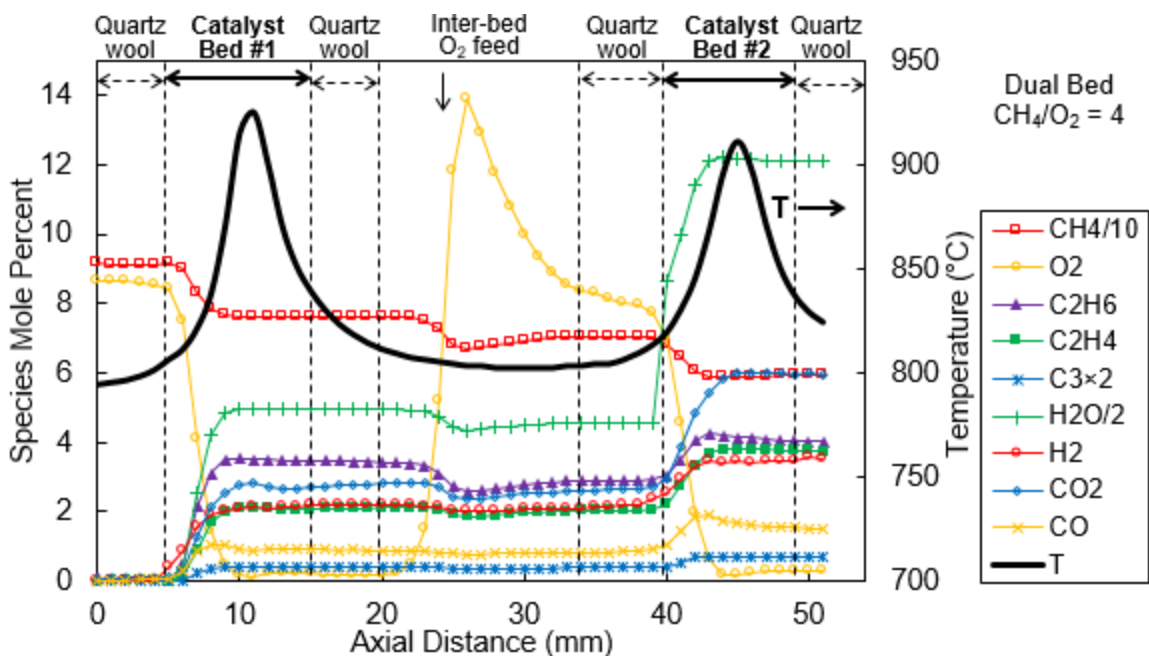


Figure 7.8. Spatial temperature and species mole percent profiles for the dual-bed reactor system (DB1). Feed to first reactor was $120 \text{ cm}^3/\text{min}$ STP at $\text{CH}_4/\text{O}_2 = 9$. Interbed O_2 flow rate was $12 \text{ cm}^3/\text{min}$ STP, which rendered an overall $\text{CH}_4/\text{O}_2 = 4.0$.

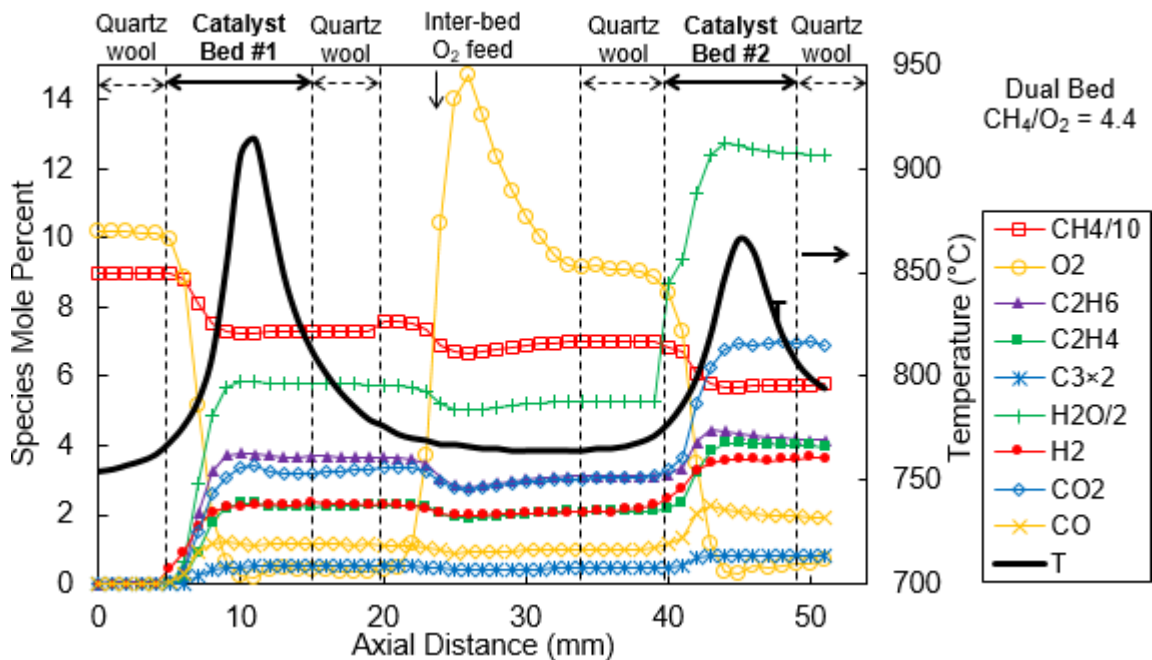


Figure 7.9. Spatial temperature and species mole percent profiles for the dual-bed reactor system (DB2). Feed to first reactor was 120 cm³/min STP at a CH₄/O₂ = 11. Interbed O₂ flow rate was 15 cm³/min STP, which rendered an overall CH₄/O₂ = 4.4.

Table 7.1. Reaction conditions and reactor exit values for conversions, selectivities and yields.^[a]

T_i	Overall CH ₄ /O ₂	T_{peak}	Feed 1 CH ₄ /O ₂	Exit 1 CH ₄ conv. [%]	Exit 1 C ₂₊ sel. [%]	Exit 1 C ₂₊ yield [%]	$T_{interbed}$	$T_{peak 2}$	Exit 2 CH ₄ conv. [%]	Exit 2 C ₂₊ sel. [%]	Exit 2 C ₂₊ yield [%]	
[°C]	ratio	[°C]	ratio				[°C]	[°C]				
SB1	600	4	1015	4	30	55	16	–	–	–	–	
DB1	750	4	920	9	17	77	13	755	866	30	70	21
DB2	780	4.4	930	11	19	74	14	800	910	28	67	19

[a] 1 and 2 refer to catalyst beds.

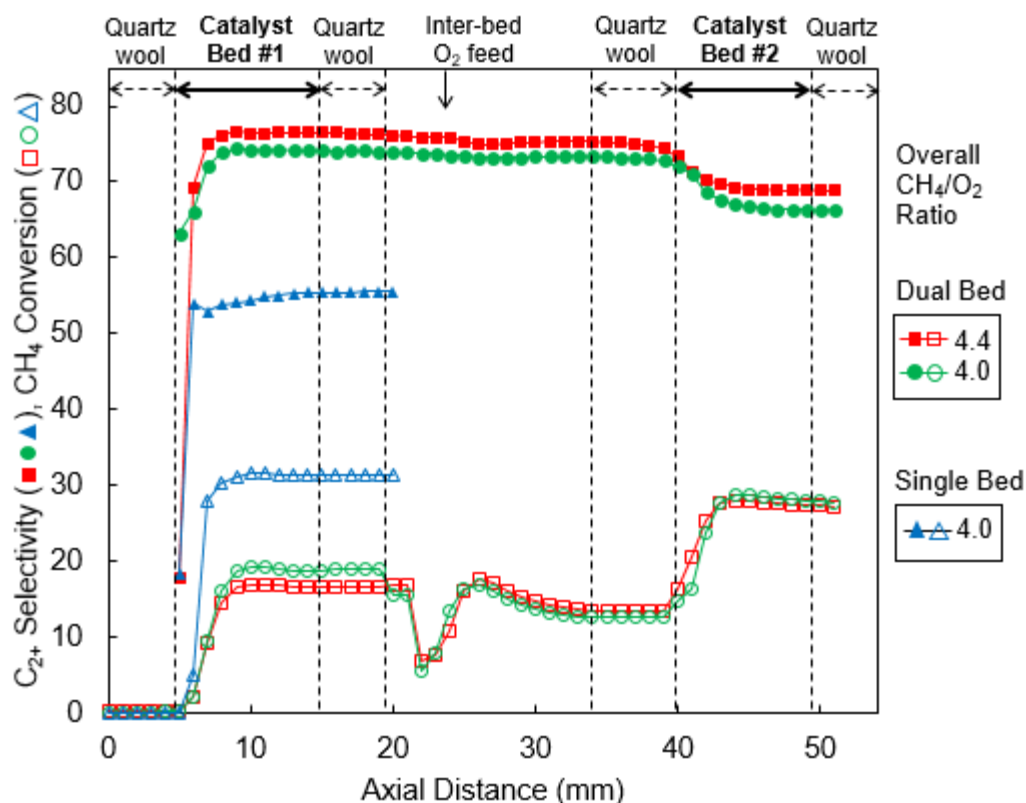


Figure 7.10. Spatial profiles for CH_4 conversions and C_{2+} selectivities for the single-bed (SB1) and dual-bed (DB1, DB2) experiments.

7.5. Summary.

Comprehensive spatial species and temperature profiles were reported for the first time in oxidative coupling of methane (OCM) fixed bed reactors. Profiles presented at different CH_4/O_2 ratios provided information-rich data necessary for the refinement and rigorous validation of detailed chemical kinetic mechanisms for this important process. The measurements revealed new insights into the kinetics and mechanism of the OCM reaction. In particular, the formation of significant levels of prompt H_2 deserve further investigation, as catalytic H_2 formation has not been fully addressed in the OCM literature.

Such reactions could be incorporated in future detailed chemical kinetic mechanisms to broaden their range of applicability and to increase their utility in predicting OCM performance over a wide range of operating conditions.

The microprobe sampling technique was then applied to dual-packed-bed catalytic reactors for OCM, demonstrating that distributing the O₂ feed can significantly increase C₂₊ product yields. By using La₂O₃-CeO₂ nanofiber fabric catalyst beds, the C₂₊ products were obtained in an ultimate yield of 21% in a double-bed OCM reactor with split O₂ introduction, which is significantly higher than the 16% yield observed in the single-bed experiment at the same overall CH₄/O₂ ratio of 4. The dual-bed configuration with interstage cooling increases the yield of the C₂₊ products primarily by increasing the CH₄ conversion and by maintaining the C₂₊ product selectivity levels.

Chapter 8. Examining the Transition from OCM to the Catalytic Partial Oxidation of Methane Using Spatial Profiles.

The catalytic partial oxidation (CPO) of methane shares the same reactants as the oxidative coupling of methane (OCM). Hence, ascertaining the spatial profiles of both reaction schemes may provide insight that allows for the improvement of both mechanisms in synergistic fashion. In particular, we acquire spatial profiles on catalytic reactors in which $\text{La}_2\text{O}_3\text{-CeO}_2$ nanofiber fabrics are incrementally doped with Ir, which shifts the reaction scheme from OCM to CPO. Hence, we are able to see both pure OCM and CPO as well as middle ground in which OCM and CPO occur in series and in parallel within the same reactor.

8.1. Electrospun Fabric Synthesis and Reactor Setup.

Experiments were performed using a fixed-bed tubular reactor system as shown in Figure 7.1 [118]. The reactor was packed with $\text{La}_2\text{O}_3\text{-CeO}_2$ nanofiber catalysts, both neat and doped with Ir, prepared by electrospinning a viscous solution of polyvinylpyrrolidone (PVP; 1.3 MDa, 0.60 g), water/ethanol (~1:1 wt ratio, 9.5 g) in which the metal precursors, as $\text{La}(\text{NO}_3)_3 \cdot 6\text{H}_2\text{O}$ and $\text{Ce}(\text{NO}_3)_3 \cdot 6\text{H}_2\text{O}$ (La/Ce wt ratio = 3, 0.35 g) were dissolved [111, 117]. The required amount of precursor IrCl_3 was also dissolved in co-spun samples. The electrospun material was calcined at 625 °C to form metal oxide nanofiber fabrics.

The fabric catalyst (20 mg) was loosely packed into a 6 mm diameter quartz tube and sandwiched between two quartz wool plugs (20 mg each, Figure 7.1) [118]. The bulk density and void fraction of the catalytic bed were approximately 0.3 g/cm^3 and 0.94 respectively. The reactor was placed inside a cylindrical tubular furnace, which preheated the feed gas and catalyst. Electronic mass flow controllers (MFCs; MKS Billerica, MA) were used to set the total reactant flow at 120 sccm, corresponding to a nominal space time of about 60 ms. The experiments were performed at atmospheric pressure with a furnace temperature of $750 \text{ }^\circ\text{C}$ and CH_4/O_2 ratio of 5.

8.2. Acquisition of Spatial Profiles.

Sampling was accomplished by withdrawing gases from within the bed using a closed-end quartz capillary tube (800 μm ; Friedrich and Dimock, Millville, NJ) with a 80 μm diameter sampling orifice laser drilled on its side (see insert Figure 7.1) [78, 118, 122]. Gas analysis was accomplished by on-line gas chromatography (Varian 4900 Mini GC, with 5 \AA molecular sieve and PoraPLOT U columns). The location of the sampling orifice and overall probe length were designed such that the capillary tip always remained outside the bed at any sampling position to avoid gas bypass. Samples were withdrawn through the capillary probe at a rate of about 5 sccm; thus, the flow within the reactor was minimally perturbed. Temperature measurements were performed by placing a 250 μm diameter K-type thermocouple inside the capillary probe in the absence of gas withdrawal. The tip of the thermocouple was positioned at the sampling orifice. The temperature and

concentration profiles were obtained by moving the capillary (with and without the thermocouple respectively) in the axial direction using a micropositioning device (Velmex, Bloomfield, NY). Positional accuracy associated with the placement of the capillary probe within the reactor was estimated to be ± 0.25 mm. Similar uncertainty would be expected to exist between the temperature and concentration profiles as well.

8.3. Characterization Studies.

In Figure 8.1, a SEM image of the 1 wt% Ir doped $\text{La}_2\text{O}_3\text{-CeO}_2$ fabric is shown, which is virtually identical to the undoped fabric. As evident from this image, the fibers are long, straight and uniform, possessing diameters of about 100 nm. BET surface area analyses were performed (Micromeritics ASAP 2020 at 77 K) on all fabrics tested in this work, and, consistent with SEM, were all found to have specific surface areas of about $10 \text{ m}^2/\text{g}$. This value is close to what would be expected for the specific surface areas of 100 nm diameter, straight, non-porous cylinders, suggesting the fibers do not have internal porosity regardless of the level of Ir doping.

In Figure 8.2 the XRD spectra of the undoped, [111] 0.05 wt% and 1 wt% Ir-doped $\text{La}_2\text{O}_3\text{-CeO}_2$ fabrics are presented (PANalytical X'Pert PRO, using $\text{CuK}\alpha$ radiation with 45 kV, 40 mA, fitted with Ni filter and Soller slit collimator). The XRD of the undoped fabric exhibits much taller peaks compared to the doped fabric but has an overall shape that is curiously similar to that with 0.05 wt% Ir. All three samples, including the 1% Ir, appear to have similar cubic crystal structures. Increasing the level of Ir doping apparently suppresses

the XRD peaks. However, the analysis using the Scherrer equation suggests that sizes of the crystals formed remained at approximately 5 nm, regardless of Ir doping.

It is possible that metal ions can segregate during the solvent evaporation in electrospinning and in the subsequent calcination steps, resulting in the establishment of radially non-uniform metal composition across the fiber. Consequently, we performed XPS studies to determine the surface composition of the 5 wt% Ir-doped $\text{La}_2\text{O}_3\text{-CeO}_2$ fabric (Al $K\alpha$ monochromatic radiation, $h\nu = 1,486.74$ eV with SPECS spectrometer). The relevant XP spectra are shown in Figure 8.3. The surface atomic metal composition was estimated by integrating the areas under the La3d, Ce3d and Ir4f curves and computing the fraction that each constitutes relative to the total area, yielding 84% La, 12% Ce and 3% Ir. Since the bulk overall (bulk) atomic composition of this sample is 72% La, 24% Ce and 4% Ir, the surface composition of the fresh Ir-doped fabrics exhibit La-Ce-Ir atom ratios seem reasonably consistent with the overall (bulk) composition, especially with respect to Ir. Therefore, surface enrichment or depletion of Ir relative to the fiber (bulk) can be considered unsubstantial.

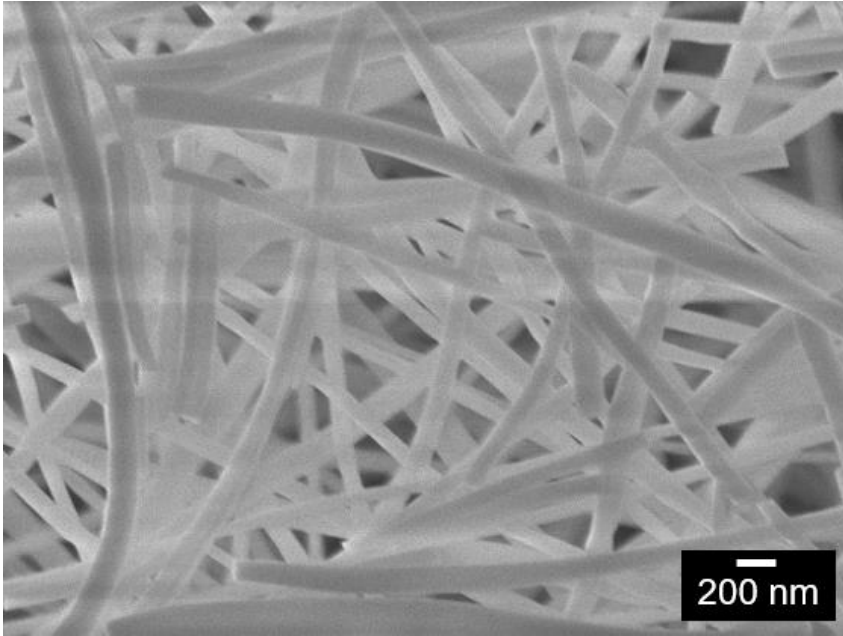


Figure 8.1. SEM image of $\text{La}_2\text{O}_3\text{-CeO}_2$ nanofiber doped with 1 wt% Ir, with negligibly different morphology than undoped fibers (secondary electron imaging, 7.6 mm working distance, $\times 30,000$ magnification, 5.0 kV).

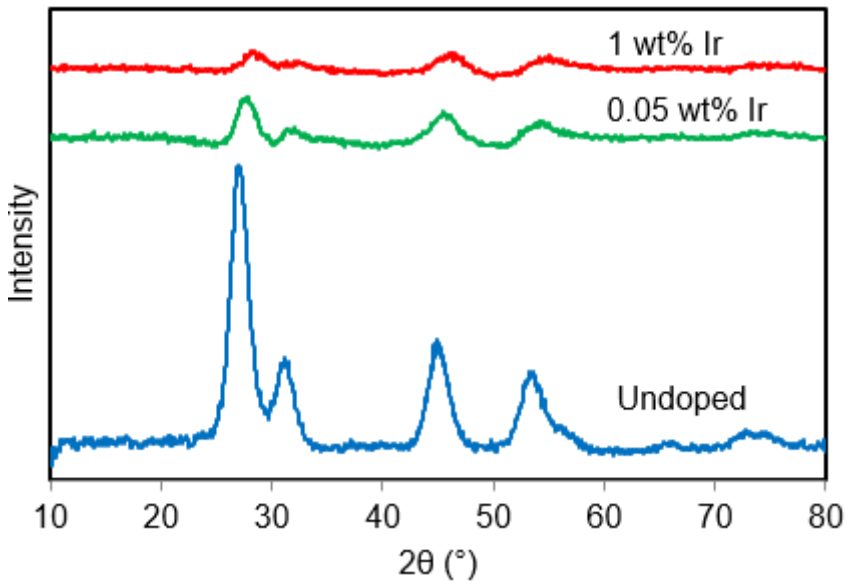


Figure 8.2. X-ray diffractograms of $\text{La}_2\text{O}_3\text{-CeO}_2$ nanofibers, undoped and with metal doping of 0.05 wt% and 1 wt% Ir. Based on Scherrer analysis, the crystal sizes were about 5 nm for all samples.

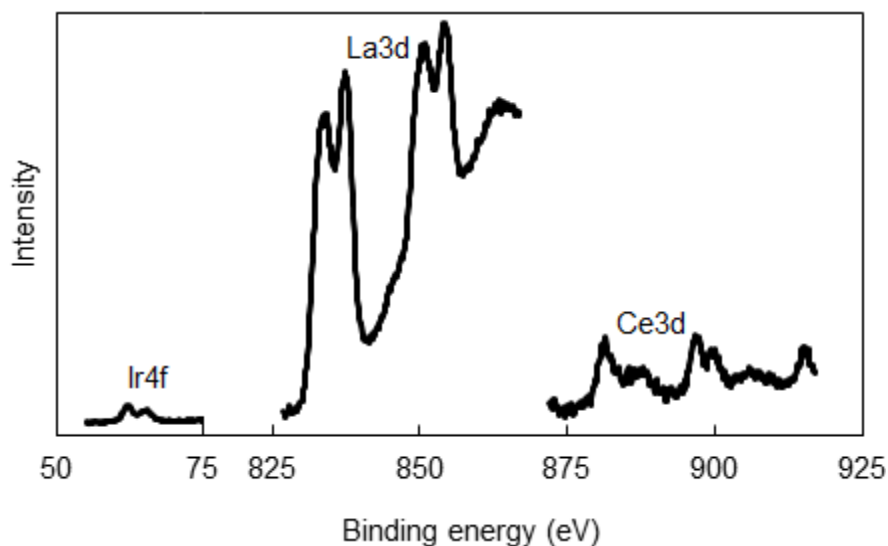


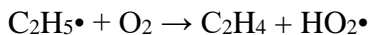
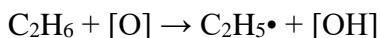
Figure 8.3. X-ray photoelectron spectra of the $\text{La}_2\text{O}_3\text{-CeO}_2$ nanofibers doped with 5 wt% Ir.

8.4. Reaction Studies.

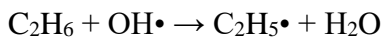
Shown in Figure 8.4 are the axial temperature and concentration profiles for the reactor packed with the undoped $\text{La}_2\text{O}_3\text{-CeO}_2$ fabric catalyst. These profiles exhibit behaviors similar to those reported in our previous OCM studies [111, 117, 118, 121]. The key similarity is that C_2+ hydrocarbons are the principal products. As evident from Figure 8.4, the peak temperature of 970 °C occurs 4 cm past the start of the catalytic zone. It is worth noting that C_2H_6 and C_2H_4 both peak at about same depth within the catalyst at 3 cm at values of 3.4 and 1.9% respectively. The level of H_2 peaks at 5.8%, 2 cm deep within the catalyst bed and levels off at about 5%, after 5 cm. The CO_2 concentration peaks and levels off at about 7.4%, 10 cm deep. The profile of CO peaks at 4.0%, earlier at 3 cm within the catalyst and stabilizes at 2.4%, 11 cm into the catalyst. The water concentration,

as calculated by O balance, peaks at 15.6%, 4 cm deep. Also, O₂ reaches nearly complete consumption within 2 cm and CH₄ stabilizes at about the same location at 62.1%.

Substantial lag time was previously observed for the formation of C₂H₄ relative C₂H₆ when the feed contained CH₄/O₂ at 7 or higher [118]. Here, with CH₄/O₂ = 5 and also at CH₄/O₂ = 4, comparatively insignificant lag is observed [121]. This is consistent with the notion that C₂H₄ is formed principally by oxidative dehydrogenation of C₂H₆ and is also indicative that C₂H₄ formation is sensitive to concentration of O₂ in the gas phase. It is widely accepted that OCM is induced by a surface oxygen atom, [O], activating CH₄, generating a CH₃ radical and [OH] [125-127]. Ethane is then created in the gas phase by combination of two CH₃ radicals. The catalyst is regenerated through the formation and desorption of H₂O and subsequently by the dissociative chemisorption of O₂. The generation of C₂H₄, however, may be initiated on the catalyst surface or in the gas phase, but either way is strongly influenced by the presence of O₂. In the catalytic route, [O] may abstract hydrogen from C₂H₆ in a manner similar to CH₄ activation. Ethane may then interact with other species to form C₂H₄. This is summarized by [128]:

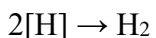
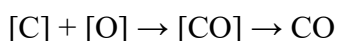
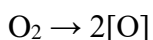


C₂H₆ dehydrogenation is also feasible in the gas phase by [128]:



Clearly, the rates of reactions 1, 2, 4 and 5 may all be directly or indirectly impacted by the concentration of O₂ in the feed gas, which is consistent with our observations of C₂H₄ lag diminishing at lower CH₄/O₂ ratios.

In Figure 8.5, the temperature and concentration profiles are presented for the catalyst doped with 0.05 wt% Ir. The addition of Ir clearly diminishes the ultimate importance of the OCM reactions as the reactor effluent concentrations of C₂H₆ and C₂H₄ fall to 1.80% and 0.02% respectively (from 3.4 and 1.9% with the undoped catalyst). However, the peak concentrations of C₂H₆ and C₂H₄ are higher at 2.3% and 1.1%, respectively and occur at about 3 cm into the catalyst. Hence, methane coupling clearly plays a substantial role early in the reactor, but C₂H₆ and C₂H₄ are oxidized upon prolonged contact with the Ir-doped catalyst. The partial oxidation of methane has been proposed to be initiated by the complete fragmentation of CH₄ onto the active catalyst site, which would likely be the Ir in our studies [75, 78, 79]. The chemisorption of O₂ would then lead to the formation of CO. The steps are summarized by [75, 78, 79]:



However, CH₄ and O₂ may also undergo both wet and dry complete combustion, such that CO₂ and H₂O serve as intermediates to synthesis gas.

Some additional features of Figure 8.5 are worth noting. First, the peak temperature of 950 °C is slightly lower than the undoped catalyst, suggesting a decrease in the overall

heat release. Water levels increase to 12.7% at 3 mm within the catalyst bed, then decreased substantially and leveled off at about 7%; which was not observed in the undoped experiments (see Figure 8.4). This finding indicates the presence steam reforming reactions, which is consistent with the literature where catalysts containing Ir have been reported in methane-steam reforming [129, 130]. Oxygen consumption is completed at a depth of 4 cm, which is slightly later than the undoped catalyst. Carbon monoxide and H₂ levels were 10% and 15%, respectively, both of which are significantly higher than the undoped experiments (Figure 8.4). Carbon dioxide peaks and levels off at 6.2%.

Figure 8.6 shows the temperature and concentration profiles for the catalyst doped with 1 wt% Ir. The results here are consistent with the trends observed in the previous two experiments. First, the peak temperature decreased further to about 890 °C, which is about 80 °C cooler than the undoped experiments. Second and most dramatically at 1% Ir doping, the reaction selectivity for OCM was completely switched off (i.e. no C₂₊ products observed) with CPO products (i.e. CO and H₂) dominating the product mix. Exit H₂ and CO levels were 42% and 20%, respectively, which are in harmony with the reactant CH₄ molecule. Some CO₂ and H₂O were also produced as shown in Figure 8.6.

A close inspection of Figure 8.6 indicates several new important features that were not present in the previous experiments. First, there appears to be no discernible region early in the catalyst bed where OCM occurs as seen in the 0.05% Ir doped case. In other words, at 1% Ir doping, the La₂O₃-CeO₂ nanofibers exhibit only CPO catalysis throughout the entire catalytic zone. Second, significant H₂ was detected in the upstream outside of the catalytic zone when reactant concentrations are still flat, i.e. no reaction. This observation

has to be attributed to the diffusion of H_2 due to the presence of its steep concentration gradient concomitant with a peak level of 42% and its high diffusivity.

The profiles for H_2O initially rise to 9% and then sharply decrease to levels of about 1%, again suggestive of methane-steam reforming reactions as the possible reason for this behavior. In this case, oxygen is fully consumed early at a depth of 3 cm. Carbon dioxide production is reduced in this CPO process reaching 1.7% at a depth of 3 cm. A summary of the peak temperatures and peak and exit product concentrations for the various cases investigated are provided in Table 8.1.

Shown in Figure 8.7 is the enthalpy change of the gas mixture as a function of position for the three catalysts examined in Figure 8.4, Figure 8.5 and Figure 8.6, using the enthalpy of formation for each component from the TRC Thermodynamic Tables and assuming ideal gas behavior. The reactor utilizing the 1 wt% Ir fabric has the shallowest enthalpy change from inlet to outlet (least exothermic) while the undoped has the deepest (most exothermic). Hence, higher doping levels reduce heat release, which is expected largely because CPO produces H_2 as co-product while OCM principally produces H_2O . The plots of Figure 8.7 are also consistent with the temperature profiles of Figure 8.4, Figure 8.5 and Figure 8.6, with the undoped catalyst having the highest peak temperature and the 1 wt% Ir catalyst the lowest. Lastly, the enthalpy change and temperature profiles for the 1 wt% Ir case both have kinks at 8 mm and 11 mm respectively. These both could be resulting from the apparent endothermic steam reforming, despite that the kinks occur at different locations. Heat conduction within the solid catalyst could cause the temperature profile to spread and advance downstream relative to the concentration profiles.

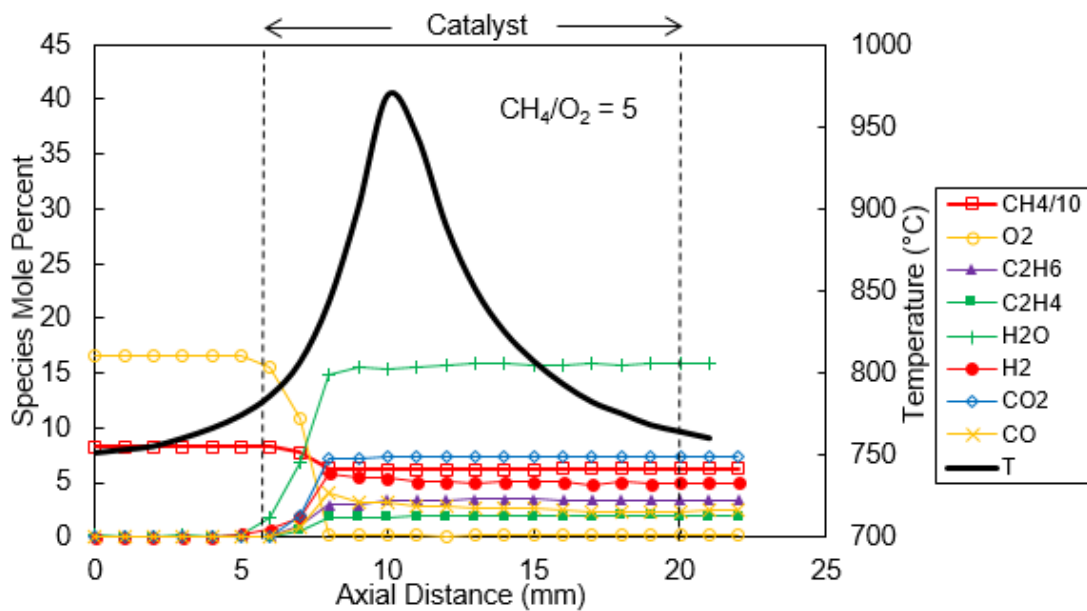


Figure 8.4. Spatial temperature and species mole percent profiles for the undoped $\text{La}_2\text{O}_3\text{-CeO}_2$ fabric catalyst.

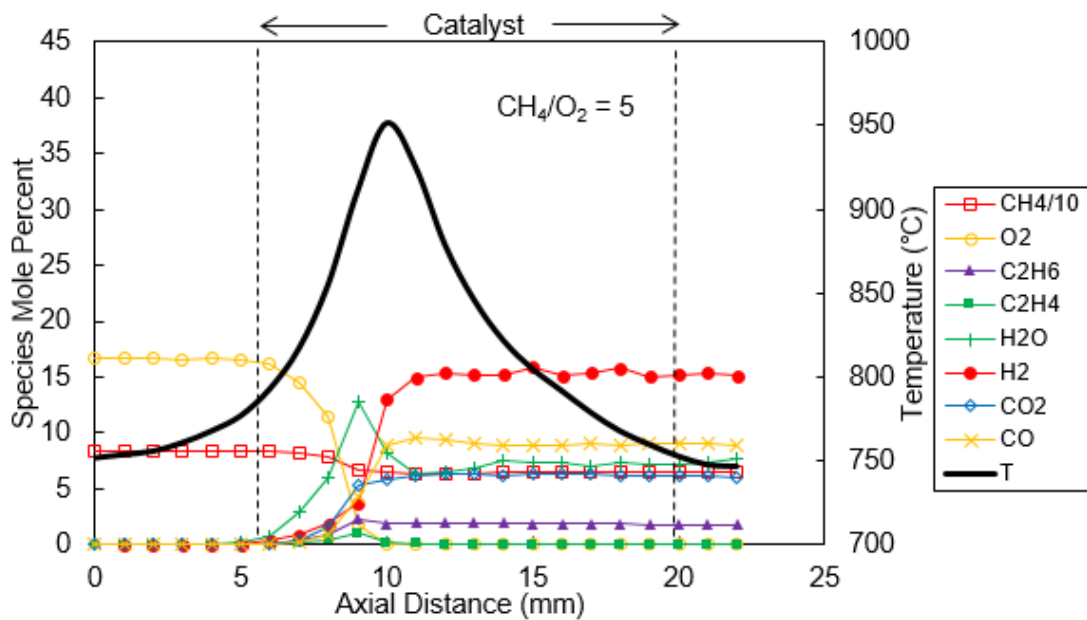


Figure 8.5. Spatial temperature and species mole percent profiles for the $\text{La}_2\text{O}_3\text{-CeO}_2$ fabric catalyst doped with 0.05 wt% Ir.

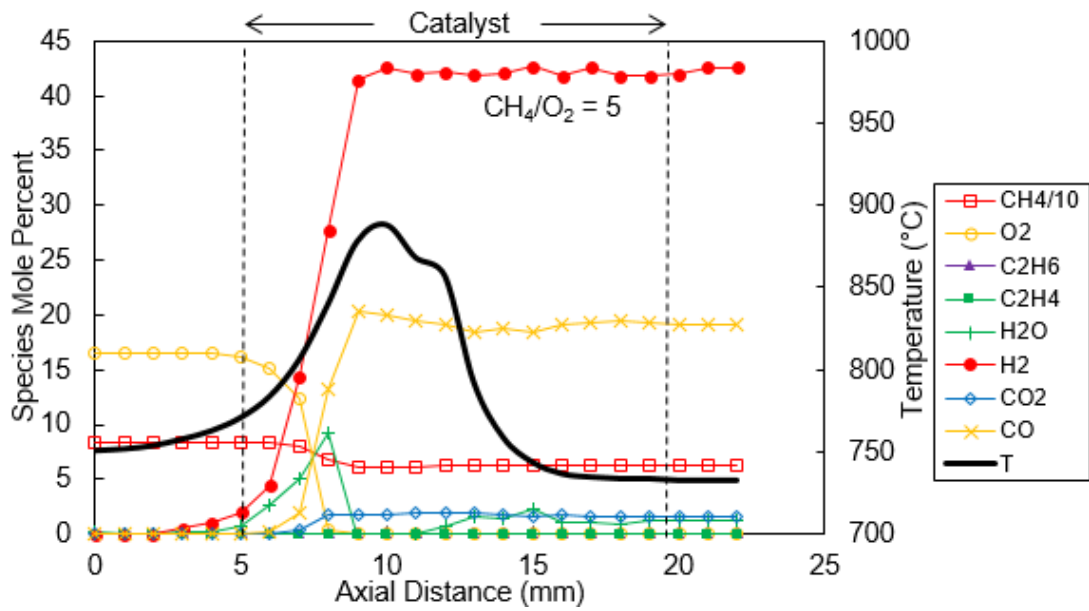


Figure 8.6. Spatial temperature and species mole percent profiles for the $\text{La}_2\text{O}_3\text{-CeO}_2$ fabric catalyst doped with 1.00 wt% Ir.

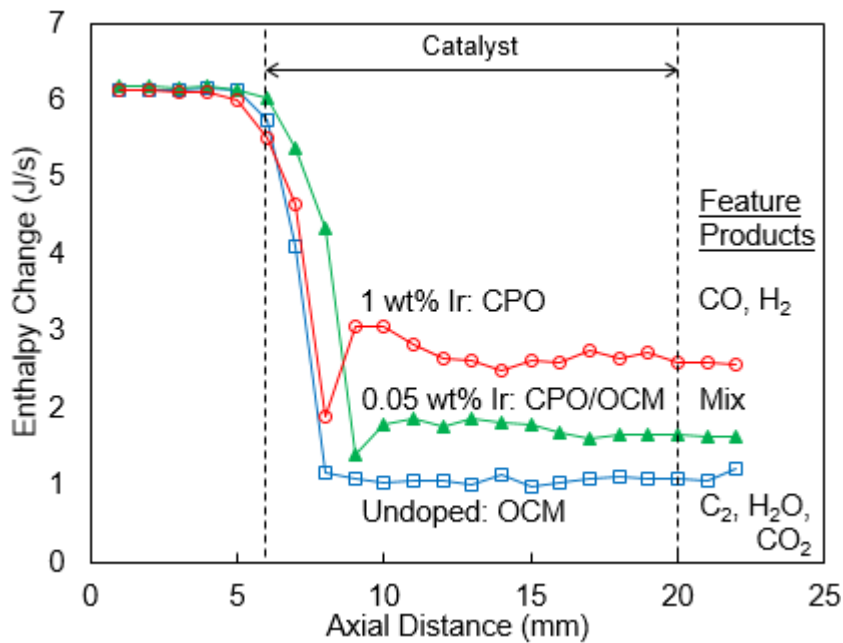


Figure 8.7. Spatial enthalpy change profiles, relative to feed conditions, for the undoped (Figure 8.4), 0.05 wt% Ir (Figure 8.5) and 1 wt% Ir (Figure 8.6) catalytic $\text{La}_2\text{O}_3\text{-CeO}_2$ -based fabrics.

Table 8.1. Peak temperature and peak exit and effluent species mole percents for the reaction products of Figure 8.4, Figure 8.5 and Figure 8.6. Locations of peaks are provided in parentheses in cm measured in catalytic zone.

		Figure 8.4 – undoped catalyst	Figure 8.5 – 0.05 wt% Ir	Figure 8.6 – 1 wt% Ir
Peak %, (location, cm)	Temperature, °C	970 (4)	950 (4)	890 (5)
	C₂H₆, mol%	3.4 (6)	2.3 (3)	0
	C₂H₄	1.9 (5)	1.1 (3)	0
	H₂O	15.8 (7)	12.7 (3)	9.2 (3)
	H₂	5.8 (2)	15.4 (6)	42 (4)
	CO₂	7.3 (5)	6.2 (8)	1.7 (3)
	CO	4.0 (3)	9.5 (5)	20.4 (4)
Exit	C₂H₆	3.4	1.8	0
	C₂H₄	1.9	0.02	0
	H₂O	15.8	7.2	1.2
	H₂	5.0	15.4	42
	CO₂	7.3	6.2	1.7
	CO	2.4	9.5	19.2

8.5. Summary.

Detailed species concentration and temperature profiles obtained over $\text{La}_2\text{O}_3\text{-CeO}_2$ nanofiber fabric catalysts at varying levels of Ir doping, in a fixed bed reactor fed by CH_4 and O_2 ($\text{CH}_4/\text{O}_2=5$) indicated a clear transition from the oxidative coupling of methane (OCM) to the catalytic partial oxidation (CPO) of methane reaction. With the undoped fabric catalyst, ethane and ethylene were the dominant products, with a total C_2 selectivity of 54%. The catalyst doped with 1 wt% Ir produced exclusively synthesis gas (CO/H_2) and virtually no C_2 products. At 0.05 wt% Ir doping, the spatial profiles indicated the presence of two distinct and sequential reaction zones: in the upstream there was substantial formation of C_2 hydrocarbons, characteristic of OCM, followed by the formation of CPO products CO/H_2 in the downstream. These results clearly demonstrate the interconnectivity of the mechanisms of the OCM and CPO processes.

Chapter 9. Spatial Profiles in RuO₂-CuO-NaCl/SiO₂ Packed-Bed Propylene Epoxidation Reactors.

In this chapter, spatial profiling is implemented on the direct epoxidation of propylene by molecular oxygen. This portion of the work shows that the profiling technique has both broad applicability to many different reaction schemes and may be used on powder based catalysts as opposed to just nanofiber fabrics. Powders pose the challenge of having much smaller void spaces than fabrics, creating operational difficulties in profiling. Nevertheless, we show here that this technique can still be used on traditional nanoparticle-based materials. This chapter is based on a publication in *Industrial & Engineering Chemistry Research* [131].

9.1. Reactor System and Powder Catalyst Used.

Experiments were performed using a fixed-bed tubular reactor system, as shown in Figure 9.1. The silica-supported multimetallic RuO₂-CuO-NaCl catalyst was prepared via the *co-impregnation* method described previously [86]. Briefly, predetermined weights of amorphous fumed silica powder (SiO₂, Alfa Aesar, surface area of 145 m²/g, bulk density of powder ≈ 0.2 g/cm³) were mixed with an aqueous solution of ruthenium [(NH₄)₂RuCl₆, Aldrich], copper [Cu(NO₃)₂, Alfa Aesar, ACD, 98.0-102.0%], and sodium [NaCl, Alfa Aesar, 99.99% (metals basis)]. The metal salt solution was then allowed to impregnate the support for 24 h in air. The resulting material was then heated at 165 °C until dried, and

calcined at 480 °C for 6 h in air. The catalyst used in the experiments had a Ru:Cu:Na metal ratio of 4:2:1 (weight ratio, or ~3:4:4 atomic ratio) at 12.5 wt% total metal loading, whose combination maximized the propylene oxide (PO) selectivity [89]. Fifty milligrams (50 mg) of this catalyst was packed into a 6-mm-diameter quartz tube and sandwiched between two quartz wool plugs, each weighing 10 mg (Figure 9.1). The bulk density and void fraction of the bed were determined to be about 0.27 g/cm³ and 0.90 respectively, assuming non-porous SiO₂ nanoparticles having a solid density of 2.65 g/cm³. The reactor was placed inside a cylindrical tubular furnace, which also preheated the feed gases. Using electronic mass flow controllers (MFC, MKS Billerica, MA), the total flow of reactant gases was maintained at 100 cm³/min at STP in all of the experiments.

9.2. Acquisition of Spatial Profiles.

Gas sampling was accomplished by centrally inserting a conically tapered and closed-end quartz capillary tube (800 μm, Friedrich and Dimock, Millville, NJ) into the packed bed, followed by gas analysis using online gas chromatography (Varian 4900 mini GC, with molecular sieve 5Å and PoraPLOT U columns). The capillary had several 80-μm-diameter orifices laser-drilled on its side to withdraw gases from within the bed (see inset in Figure 9.1). The location of the sampling orifice and the overall length of the probe were designed such that the capillary tip always remained well outside the packed bed at any sampling position to avoid channeling and gas bypass. That is, the probe body always remained inserted into the entire bed length, including the quartz wool plugs. If the probe

tip were moved into the bed during measurements, channeling would occur through the hole created. The capillary probe withdrew gas samples at a rate of $\sim 5 \text{ cm}^3/\text{min}$ at STP, thus minimally perturbing the gas flow within the reactor, which was flowing at a rate of $100 \text{ cm}^3/\text{min}$ at STP. At this sampling rate, the residence time of the gases in the capillary probe can be estimated to be in the range of 25-50 ms. Temperature measurements were performed by placing a thin (250- μm -diameter) K-type thermocouple inside the capillary probe in the absence of gas withdrawal. The tip of the thermocouple was positioned at the sampling orifice. Temperature and concentration profiles were obtained by moving the capillary (with and without the thermocouple) in the axial direction using a micropositioning device (Velmex, Bloomfield, NY). Positional accuracy associated with the placement of the capillary probe within the reactor is estimated to be $\pm 0.25 \text{ mm}$. Similar uncertainty would also be expected to exist between the temperature and concentration profiles.

The propylene conversions and product selectivities were calculated on the basis of carbon atom balances. GC calibrations for propylene, oxygen and CO_2 were performed using mass flow controllers (MKS) and He as a carrier gas. Calibrations for PO, acrolein (AC), acetone (AT) and propionaldehyde (propanal, PA) were performed by vaporizing known quantities of the liquid in a heated, evacuated $2,250 \text{ cm}^3$ stainless steel tank and using He as a carrier gas [86]. All calibrations yielded linear five-point curves with a correlation factor of at least $R^2 = 0.995$, using the peak area as the basis for GC calculations.

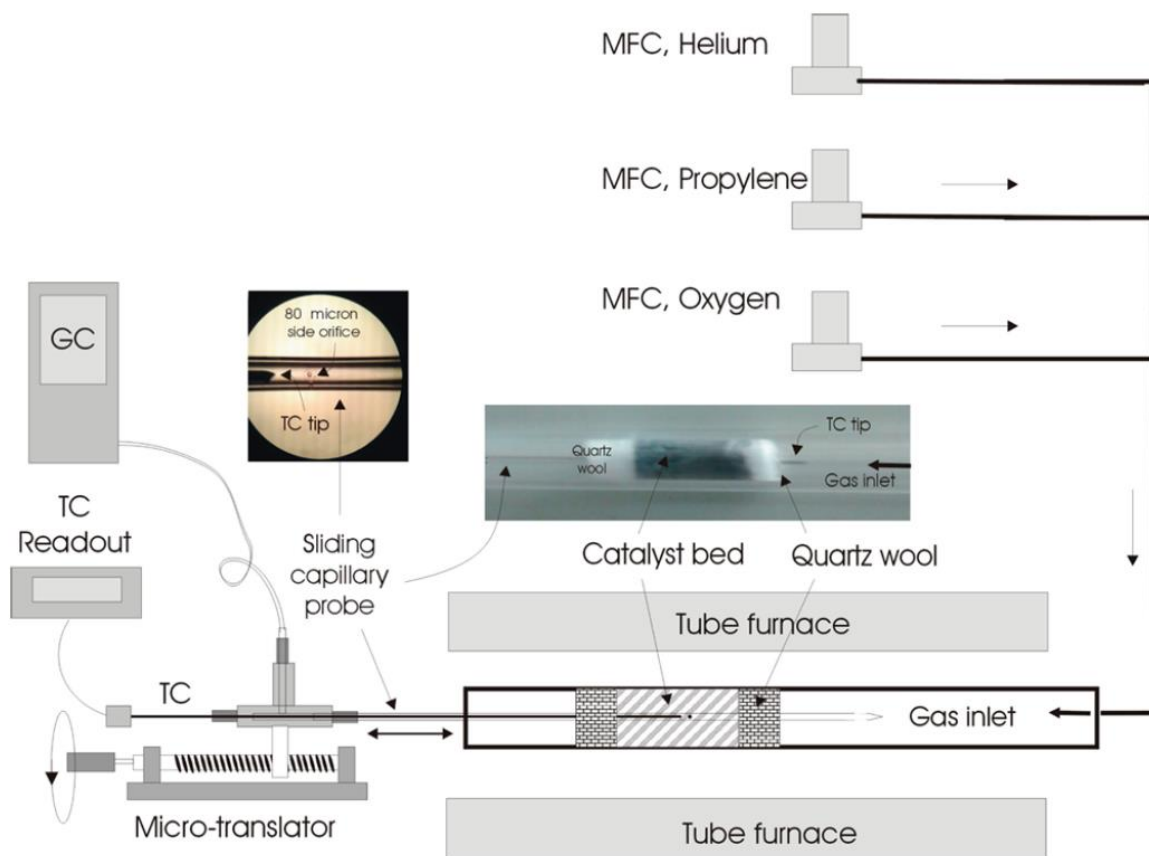


Figure 9.1. Schematic of the mass flow control system, heated quartz tube reactor setup, capillary sampling probe and gas chromatography and temperature measurement system. Photographic images of the packed-bed reactor, magnified capillary probe, 80 μm sampling orifice and inserted thermocouple are also shown.

9.3. Spatial Profiling Results in Nanoparticle-Based Propylene Epoxidation Catalytic Reactors.

Before presenting the results, several properties of the $\text{RuO}_2\text{-CuO-NaCl/SiO}_2$ catalyst should be noted. First, this catalyst is well-documented to require ~ 1 h of activation [86]; consequently, the results reported here were obtained after this period. Second, this catalyst is also known to exhibit deactivation after 6 h of continuous operation because of

the loss of chlorine [86]. Although co-feeding chlorinated hydrocarbons at a parts per million level remedies this problem [89], we did not implement this method. Instead, experiments were performed during this initial 2-5 h age period of the catalysts, after which the catalysts were replaced.

In Figure 9.2 and Figure 9.3, the spatially resolved temperature and species mole percent profiles are presented for the feed O_2/C_3H_6 ratio of 2 at furnace temperatures of 250 and 270 °C respectively. A total of seven species were quantified: O_2 , C_3H_6 , PO, AT, AC, H_2O and CO_2 . Concentrations of other likely products [e.g. PA and acetaldehyde (AA)] were too low for detection using the GC system with any appreciable accuracy. With the exception of the H_2O concentrations, which were calculated from oxygen atom balances, all the species were quantified directly from GC measurements, using a multipoint GC calibration process performed before the experiments. In Figure 9.4 and Figure 9.5, the corresponding spatial profiles for the PO and CO_2 selectivities and C_3H_6 conversions are presented.

In all of the figures, the positions of the catalyst bed and quartz wool packing are indicated by vertical dashed lines; the catalyst packing starts at ~1.5 cm and ends at ~3.0 cm, corresponding to a bed depth of 1.5 cm. As evident from Figure 9.2 and Figure 9.3, the spatial concentration and temperature profiles measured within the bed provide information-rich data on the kinetics and mechanism of the propylene and oxygen reaction. In contrast, the profiles at the catalyst exit were essentially featureless and contain very little information.

As seen in Figure 9.2, the temperature increased to a maximum of ~ 272 °C at 1.1 cm into the catalyst bed (i.e. at a distance of 2.6 cm along the reactor), corresponding to a temperature rise of ~ 22 °C, then decreased toward the exit of the reactor. Since the reactor was not adiabatic, this temperature profile is expected for an exothermic reaction. The possible presence of radial temperature gradients was also explored by placing multiple thermocouples at different radial positions at the same axial position. These studies indicated radial temperature differences that were within measurement errors of 2-5 °C, which suggests that the treatment of the reactor as being quasi one-dimensional appears to be a reasonable assumption. The temperature decreases observed in the later stages of the catalytic bed are indicative of the increased importance of product adsorption on the title reaction. As product concentrations increase in the gas phase, their desorption rates from the catalyst surface should decrease, thereby decreasing the overall rate of the reaction. Consequently, decreases in the heat generation rate can no longer exceed heat losses into the furnace (at 250 °C), resulting in a net decrease in reactor temperature at increased propylene conversions.

An important issue that must also be considered in the acquisition of accurate temperature profiles in reactors is the thermal conduction along the thermocouple wires. Conduction can result in temperature smoothing and profile shifts, especially when large temperature gradients (e.g. >100 s of °C/mm, as seen in flames) exist [132]. However, in the current experiments, such effects appear to be relatively insignificant.

The species profiles shown in Figure 9.2 at a feed temperature of 250 °C show both confirmatory and new features. First, the integral (i.e. exit) reactor performance was $\sim 10\%$

C_3H_6 conversion and 42% PO and 58% CO_2 selectivities, consistent with the O_2/C_3H_6 ratio of 2 (see also Figure 9.4) and previous experiments [86]. Second, the quartz wool packing had no catalytic activity, with respect to either propylene or the products, as all the concentration profiles remained flat prior to and after the catalyst bed. Third, reactions outside the catalyst bed can also be ruled out under the prevailing conditions. The fact that the measured concentration profiles remained flat (i.e. did not change with axial position within the quartz wool and reactor exit) supports the notion that reactions inside the sampling capillary were unimportant in our experiments. Fourth, the entire catalyst bed depth was actively utilized in creating the integral results (i.e. PO levels monotonically increased with distance along the reactor until the end of the catalyst bed). Finally, there was a sudden increase in the AT concentration at 3.4 mm (i.e. within the quartz wool packing), which can be attributed to the detection limits of the GC. Evidently, at the lower temperatures associated with the downstream quartz wool section and beyond, the increased gas density was sufficient to bring AT levels above the detection limits of the GC.

From Figure 9.2, it can be seen that PO formation started early in the catalytic bed and steadily increased with distance along the reactor, reaching a peak level of ~0.075%. On the other hand, CO_2 formation rate was faster, ultimately reaching a peak level of 0.25% at the exit, concomitant with the formation of H_2O (peaking at 0.38%). The higher CO_2 formation rate is not surprising, since 3 moles of CO_2 are produced per mole of C_3 species combusted. The profiles presented in Figure 9.4 reveal that PO selectivity also steadily increased and that for CO_2 decreased with increasing residence time in the reactor. These

results clearly present useful trends that can be exploited for the design and operation of packed-bed reactors to improve PO selectivities. For example, increasing residence time can be beneficial in improving PO selectivity under the prevailing conditions.

The corresponding spatial profiles along the reactor at 270 °C feed temperature are shown in Figure 9.3. In this case, the temperature peak of 301 °C occurred at a distance of 2.6 cm along the reactor (i.e. 1.1 cm within the catalyst bed). Under these conditions, propylene conversion expectedly increased to a value of ~17.5% as shown in Figure 9.5. This increase corresponds to an apparent activation energy of ~11 kcal/mol. However, the higher feed temperature of 270 °C had a significant detrimental impact on PO formation, both with respect to concentration (Figure 9.3) and selectivity (Figure 9.5). For example, the peak PO levels were only 0.06%, while CO₂ levels increased to 0.65%. The apparent activation energy for CO₂ formation corresponds to ~15 kcal/mol. Similarly, the PO selectivity only reached 20% (Figure 9.5), in contrast to 80% for CO₂. At 270 °C, the spatial profile for PO selectivity also exhibited a weak increasing trend, with respect to the distance along the reactor, in marked contrast with the results at 250 °C (Figure 9.4).

As noted earlier, trace levels of AC and AT were also produced in the current experiments, the profiles of which are shown in Figure 9.2 and Figure 9.3. AC clearly was more abundant than AT under the conditions investigated. The absence of any measurable PA in the product mix may suggest that C2OMMP is the major route for PO formation, which also produces AT. However, the subsequent destruction of PA cannot be ruled out without a detailed chemical kinetic analysis. At a feed temperature of 250 °C (Figure 9.2), the peak levels of AT and AC were $\sim 0.2 \times 10^{-3}\%$ and $\sim 0.1 \times 10^{-2}\%$ respectively. That is, AC

levels were a factor of ~5 higher. It is interesting to note an abrupt increase in AT levels at the exit of the catalyst bed in Figure 9.2. This is related to the insensitivity of the GC to the low concentrations of AT early in the reactor. That is, sampling probe artifacts can be ruled out, since at slightly higher concentrations (i.e. at 270 °C, Figure 9.3), AT profiles exhibit the expected trends. Unlike PO, increasing the feed temperature to 270 °C increased the AT and AC peak levels to $0.4 \times 10^{-3}\%$ and $0.5 \times 10^{-2}\%$ respectively (see Figure 9.3). Concentrations reported on Figure 9.2 and Figure 9.3 suggest apparent activation energies of ~11 and ~30 kcal/mol for AT and AC formation reactions respectively. The higher temperature sensitivity of AC formation is also consistent with the relatively weaker allylic C-H bonds.

In addition to their magnitudes, the shapes of the concentration profiles presented in Figure 9.3 also provide new insights on the kinetics and mechanisms of formation of AC, AT and PO. For example, AC formation can be seen to be prompt, exhibiting its highest rate at the entrance to the catalytic bed. In contrast, AT and PO exhibited a well-defined induction period. These results are consistent with two different mechanisms associated with the formation of AC and PO/AT respectively a discussed earlier.

In order to quantify the effects of feed gas composition on species concentration profiles, experiments were also performed at the O_2/C_3H_6 ratio of 4 and at a feed temperature of 250 °C, and these results are presented in Figure 9.6. The corresponding profiles for propylene conversion and PO and CO_2 selectivities are presented in Figure 9.7. The peak temperature was ~271 °C, a 21 °C temperature increase, where the peak is positioned at a distance of ~2.5 cm along the reactor (i.e. 1.0 cm within the catalyst bed).

From Figure 9.6, peak PO, CO₂ and H₂O levels were 0.09%, 0.50% and 0.63% respectively. A comparison of these results to Figure 9.2 indicate that increasing O₂ increases the degree of propylene total combustion to CO₂, relative to epoxidation, which is an expected result. As seen in Figure 9.7, although propylene conversions increased and exhibited a peak level of ~25%, the maximum PO selectivity decreased to 38%, with CO₂ selectivity increasing to 62%. The PO selectivity also increased modestly with increasing residence time in the catalytic bed, in sharp contrast to the experiments at the O₂/C₃H₆ ratio of 2 (Figure 9.4). Significantly higher levels of AT and AC were also produced at the O₂/C₃H₆ ratio of 4, with peak concentrations of $\sim 0.3 \times 10^{-3}\%$ and $\sim 0.2 \times 10^{-2}\%$ respectively. These levels are ~50% higher than those observed in Figure 9.2.

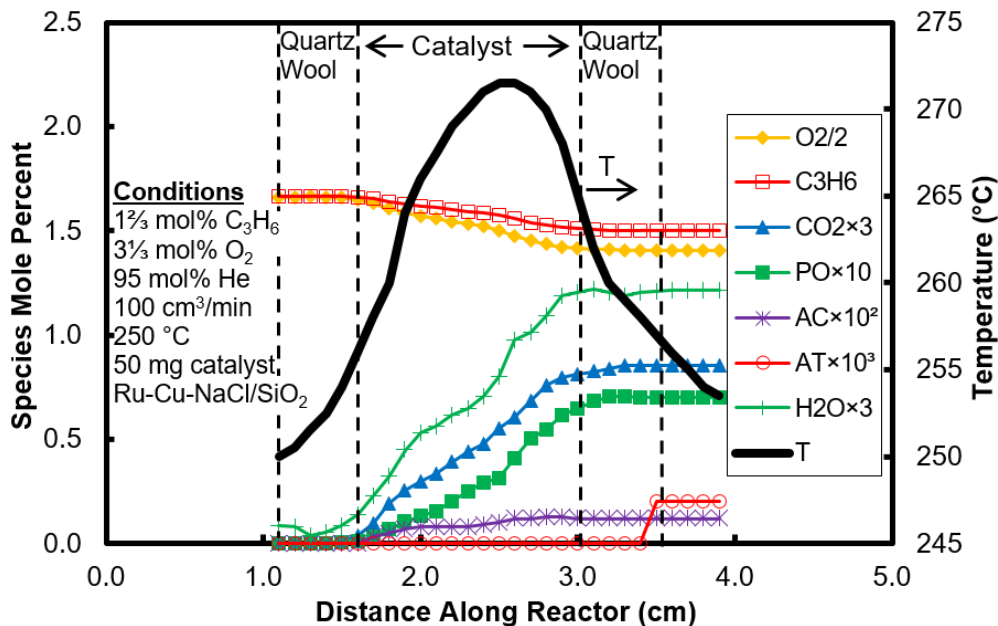


Figure 9.2. Species concentration profiles, including O₂, propylene (C₃H₆), CO₂, propylene oxide (PO), acrolein (AC), acetone (AT) and H₂O and temperature profile for a feed of $1\frac{2}{3}$ mol% C₃H₆, $3\frac{1}{3}$ mol% O₂ and 95 mol% He at 250 °C.

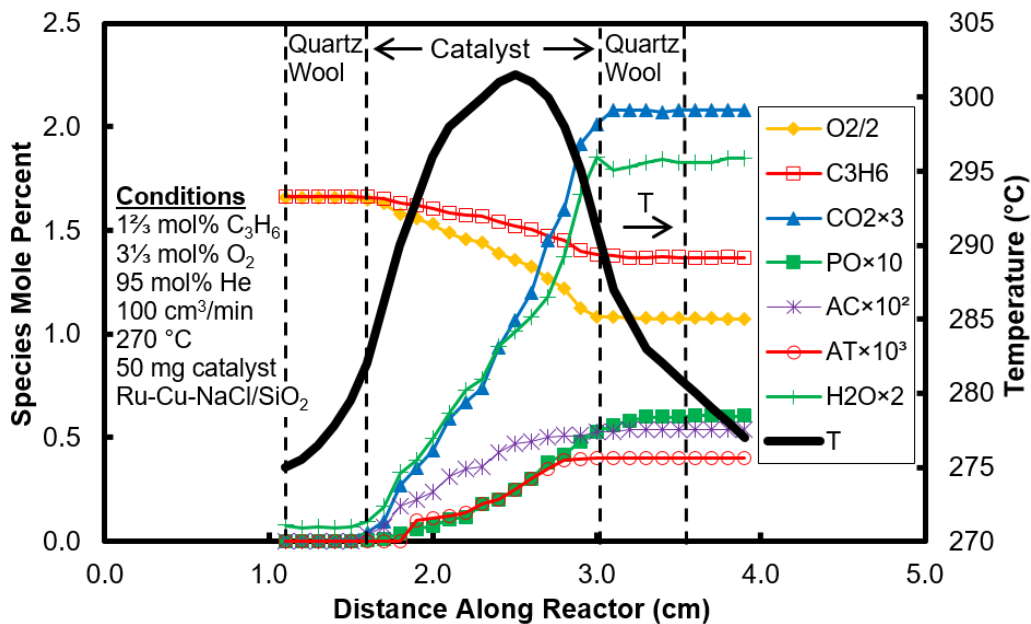


Figure 9.3. Species concentration profiles, including O₂, propylene (C₃H₆), CO₂, propylene oxide (PO), acrolein (AC), acetone (AT) and H₂O and temperature profile a feed of 1 ²/₃ mol% C₃H₆, 3 ¹/₃ O₂ and 95 mol% He at 270 °C.

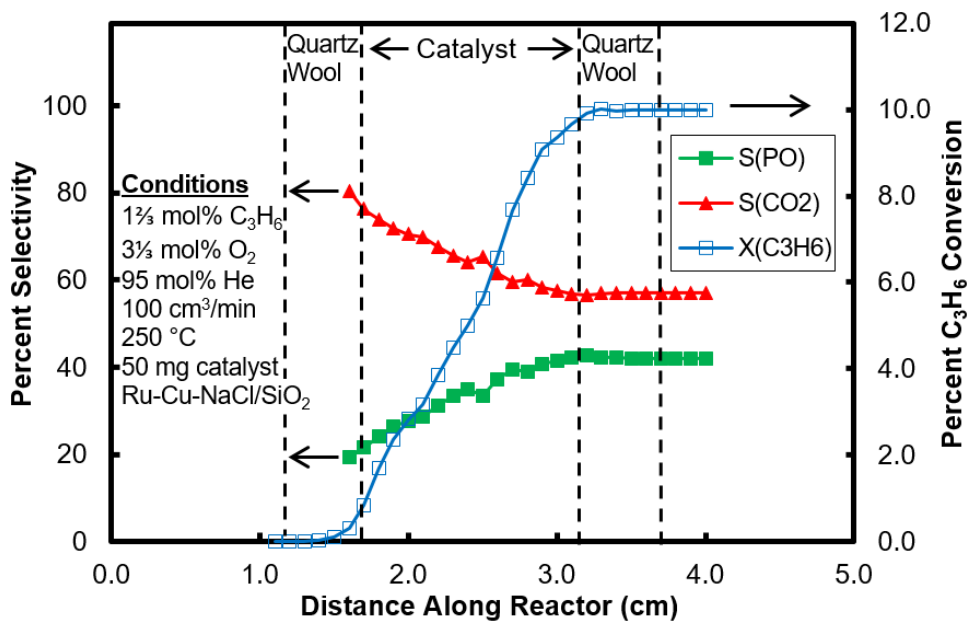


Figure 9.4. Propylene oxide (PO) selectivity, CO₂ selectivity and propylene (C₃H₆) conversion profiles corresponding to Figure 9.2.

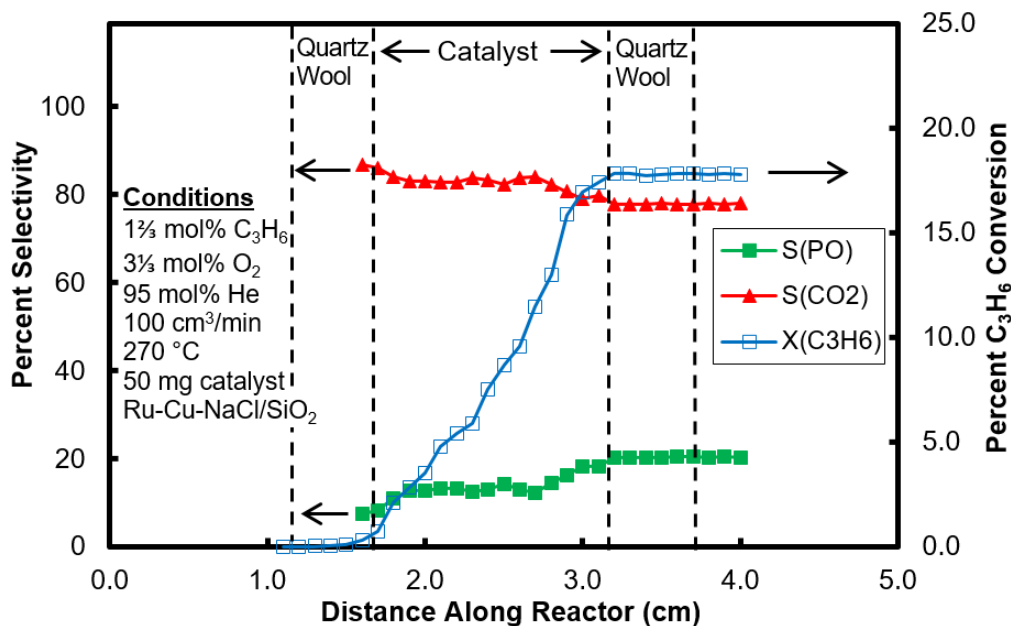


Figure 9.5. Propylene oxide (PO) selectivity, CO₂ selectivity and propylene (C₃H₆) conversion profiles corresponding to Figure 9.3.

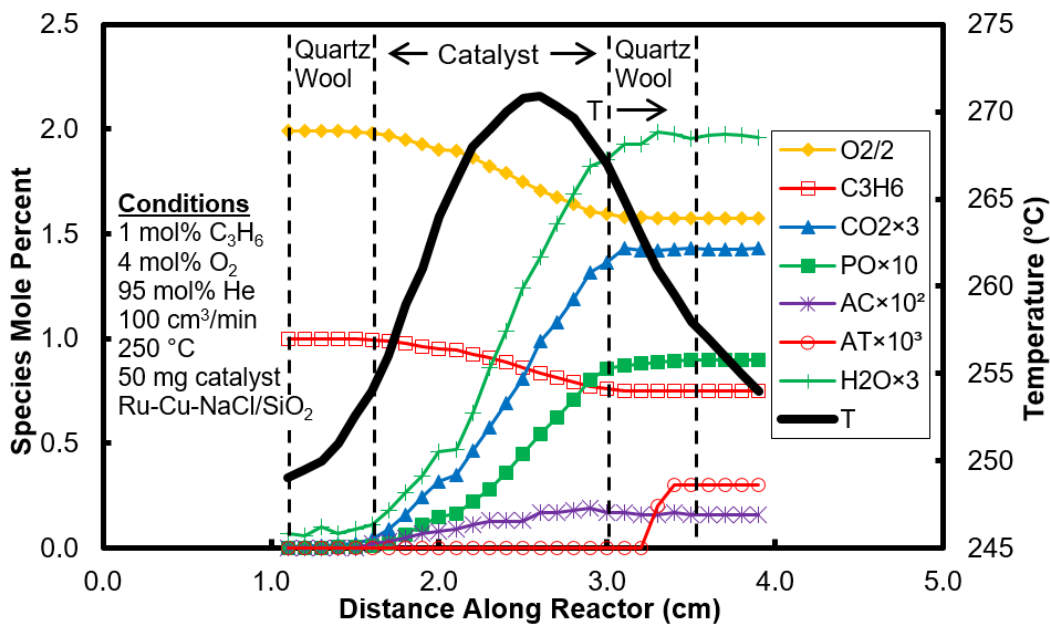


Figure 9.6. Species concentration profiles, including O₂, propylene (C₃H₆), CO₂, propylene oxide (PO), acrolein (AC), acetone (AT) and H₂O and temperature profile for a feed of 1 mol% C₃H₆, 4 O₂ and 95 mol% He at 250 °C.

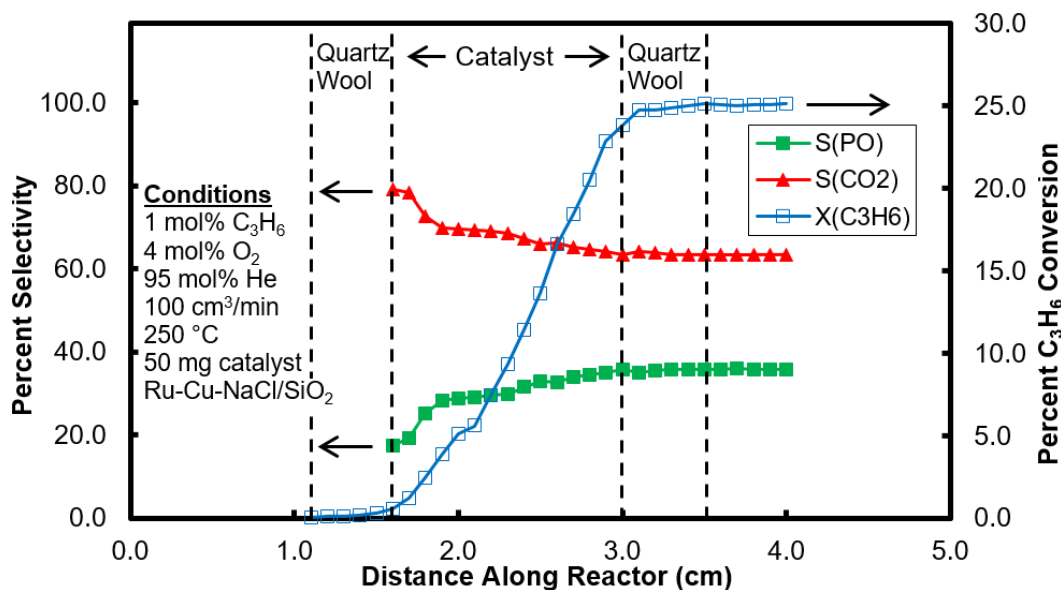


Figure 9.7. Propylene oxide (PO) selectivity, CO₂ selectivity and propylene (C₃H₆) conversion profiles corresponding to Figure 9.6.

9.4. Summary.

Detailed species concentration and temperature profiles have been obtained for the first time in a propylene epoxidation fixed bed reactor packed with RuO₂-CuO-NaCl/SiO₂ catalysts. These profiles reveal significant new insights on the catalytic kinetics and mechanism of propylene epoxidation. In particular, spatial profiles indicate that acrolein (AC) formation was prompt and occurred early in the catalyst bed. In contrast, both acetone (AT) and propylene oxide (PO) production exhibited well-defined induction periods. These findings point to two different mechanisms associated with the formation of AC and AT/PO respectively. The absence of any measurable propanal (PA) in the product mix also suggests that C2OMMP may be the preferred route for PO formation in this catalytic system. The spatial profiles reported represent information-rich data that are of significant

utility for the development and validation of detailed chemical kinetic mechanisms for propylene partial oxidation in general and epoxidation in particular.

Chapter 10. Simulation of Oxygen Vacancies on La₂O₃-based Surfaces Using Quantum Espresso.

This section covers density functional theory simulations of various lanthanum-oxide-based slabs doped with various materials using Quantum ESPRESSO. The forty atom slabs were simulated with all atoms intact and also with a lattice oxygen neighboring the dopant removed in order to ascertain the dopant's effect on the strengths of the local metal-oxygen bonds. All figures here depicting molecular structures were generated using CrystalMaker®: a crystal and molecular structures modeling program for Mac and Windows (CrystalMaker Software Ltd, Oxford, UK, www.crystallmaker.com).

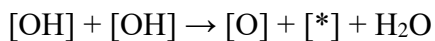
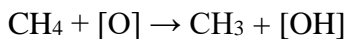
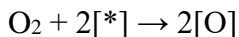
10.1. Motivation Behind Simulating Oxygen Vacancies.

The synthesis of a delicate chemical intermediate that can be further combusted into CO₂ is a challenge that requires the catalyst to have a finely tuned nanostructure allowing for the intermediate's stabilization at high yield. This has yet to be accomplished to the level of economic viability in the oxidative coupling of methane (OCM), although the emergence of novel nanofiber fabric catalysts and reactor designs that facilitate the spatial distribution of the oxygen offers promising leads for the future direct utilization of natural gas as a feedstock [111, 121]. Despite that both the theoretical and experimental literature suggests that the OCM yield is limited to 25-30% in a single packed bed due to *gas phase radical reactions*, most, if not all, stable catalysts in the literature are not able to

achieve even this figure. Hence, research into optimizing the structure of the solid catalyst is needed, in parallel with advancements in catalytic reactor designs.

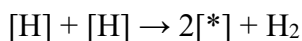
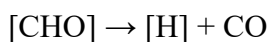
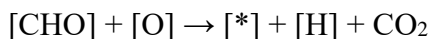
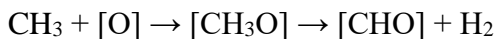
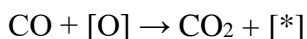
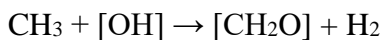
In this work, density functional theory (DFT) calculations are used to evaluate the metal-oxygen bond strengths on the surfaces of La₂O₃-based slabs, most of which are doped with a single metal atom other than La. The tendency for an oxygen atom to vacate the surface of the slab is thought to be correlated with trends in catalysis related to OCM reactors that utilize La₂O₃-based catalytic materials. This tendency thus may be key in tuning the OCM performance. Highly mobile surface oxygens would intuitively result in a highly active catalyst, but one that readily participates in combustion rather than coupling. Surface oxygen species [O] are widely accepted to be responsible for not only the activation of CH₄ but also, at least partly, for the synthesis of CO_x directly or indirectly.

The path that leads to ethane is summarized by:



in which [*] represents a vacant catalytic surface site for oxygen chemisorption. In this scheme, the activation of methane results in the generation of CH₃ radicals that diffuse into the gas phase and subsequently couple to form C₂H₆. The active exterior [O] species are understood to be regenerated through the formation and desorption of H₂O, followed by repopulation of the vacated sites by O₂ chemisorption. Ethylene is produced by either

oxidative or catalytic dehydrogenation of C₂H₆. Other catalytic reactions that may lead to CO_x include:



Gas phase reactions of CH₃ with O₂, O and OH can also lead to CO_x. Regardless, enhancing the mobility of surface oxygen atoms by doping the catalyst would plausibly enhance CO_x production either catalytically by reactions 5-11 or by causing the dynamic equilibrium between gaseous O₂ and surface oxygenates to favor the former, thus leading to gas phase combustion. Based on the previous mechanism, oxygen atoms that leave the catalyst's surface are replenished by gaseous O₂ supplied in the feed. High surface oxygen activity may also result in surface reduction. In the most extreme case, a dopant may cause surface oxygen atoms to permanently vacate, leaving a fully reduced surface behind, maximizing gas phase concentrations of O₂. The tendency for oxygen vacancies to form may be particularly critical for OCM since H₂O desorption is generally accepted to be the rate determining step kinetically and the water's O-atom originates from the catalyst's surface.

Simulations of this system have been accomplished in previous works using the Vienna Ab initio simulation package (VASP) [133, 134]. Here, we use Quantum ESPRESSO (QE), whose name arises from its status as an opEn-Source Package for Research in Electronic Structure, Simulation and Optimization and compare our simulation findings to catalytic performance screening results for powders tested in the literature and nanofiber fabrics examined in our own experiments. Specifically, the Plane-Wave Self-Consistent Field (PWscf) component of the package is utilized for DFT calculations.

10.2. Quantum ESPRESSO Simulation Procedure.

The simulations were accomplished using periodic, spin-polarized, density functional theory (DFT) calculations via the PWscf module of Quantum ESPRESSO. The La_2O_3 slab was a 2×2 surface cell with a vacuum region of 12.3 Å. The slab was trimmed to have 10 atomic layers and such that surface oxygen atoms were directly exposed to the vacuum. The slab itself also had a thickness of 12.3 Å. All atoms were relaxed during structural optimization. The Perdew-Burke-Ernzerhof (PBE) exchange correlation was used while the electron-ion interactions varied depending on the element. The La atoms were described by the projector augmented wave (PAW) method of Blochl while the O atoms were described by the PAW method of Kresse and Joubert. The dopant metal atoms utilized various methods depending on pseudopotential availability. Multiple simulations of the same doped structures were often explored with different pseudopotentials to assure consistency.

Ionic minimization was stopped when both the total energy change between two consecutive SCF steps was less than 10^{-3} - 10^{-4} atomic units and the force on the atoms was less than 10^{-2} - 10^{-3} atomic units, depending on the dopant used. The energy cutoff for wavefunctions was 30 Ry while that for the charge density and potential was 360 Ry. Gaussian smearing was implemented with a spreading of 10^{-3} Ry. Local-density-dependent Thomas-Fermi screening was implemented with a mixing factor of 0.7 and eight iterations used in the mixing scheme.

Initially, Monkhorst Pack k-point grids of increasing sizes were used in calculating the oxygen vacancy energy E_{vac} of the undoped La_2O_3 slab. A k-point grid of $2 \times 2 \times 1$ was found to be sufficient for this E_{vac} to reach an asymptotically converging value and was thus used for all structures investigated in this work.

10.3. Simulated Oxygen Vacancies and Structural Changes.

Shown in Figure 10.1 is E_{vac} as a function of the dopant's metal oxide formation enthalpy. A total of 20 dopants were investigated in addition to the undoped structure of the unimetallic La_2O_3 slab. The trend is relatively linear, with substantial scatter, and is relatively confirmatory of a previous investigation done on the system using VASP [133]. The alkali metals of Li, Na, Rb and Cs consistently have some of the lowest observed E_{vac} values and $|\Delta H_f^\circ|$ values of the library of materials tested. The slabs doped with the transition metals of Pt, Cu, Ni, Ir, Ru and Fe also tend to lie low on the trend. The only transition metal examined that did not follow this behavior was Mo. The alkaline earth

metals Mg, Ca and Sr all lie in the middle of the trend with $E_{\text{vac}} \sim 41.65$ Ry. The rare earth metals consistently lie on the higher side of the trend, with the undoped unimetallic La_2O_3 slab possessing the highest E_{vac} , indicating that it thermodynamically withholds surface oxygen atoms the strongest.

The results of Figure 10.1 are relatively consistent with catalytic performance results of the literature done on powder catalysts and in screening results of nanofiber fabrics examined in our work [64, 112]. The best OCM catalysts are those that comparably do not readily mobilize or surrender surface oxygen atoms (e.g. rare-earth metal oxides and alkaline earth metal oxides), which is reasonably consistent with the prevailing mechanistic understanding of OCM in that exposed oxygen atoms need to abstract H from CH_4 ; however, it does not appear that mobilizing lattice oxygens particularly benefits OCM performance despite likely facilitating the desorption of the H_2O byproduct. Additionally, the alkali metals are generally known as dopants for OCM that tend to enhance C_{2+} selectivity in some cases, despite that Figure 10.1 would predict that they would cause the catalytic system to tend towards combustion. Alkali metals, especially at high doping levels, are known to diminish overall catalytic activity in a wide range of partial oxidation reaction schemes and that selectivity and yield improvements towards the target pathways occur on the order of 1 wt% doping or less. This is due to alkali metals' tendency to create dipoles in the same direction that adsorbed methyl species would, thus raising the activation energy barrier for methane adsorption [135].

OCM catalytic materials based on $\text{La}_2\text{O}_3\text{-CeO}_2$ have been regarded as state of the art performers. Figure 10.1 does not appear to provide any measureable justification for

this as its E_{vac} is near that of the undoped system (~ 41.9 Ry). Additionally, unimetallic catalysts of CeO_2 tend to lead towards total combustion of CH_4 . The unexpected effects of Ce-doping may therefore be related to effects that the DFT simulations may not quite capture, such as the element's ability to easily change oxidation states, its oxides' tendency to form solid solutions with La_2O_3 as well as kinetic bond scission and formation effects. Clearly Figure 10.1 and thus the enthalpy of formation of the dopant's metal oxide may serve as a general guideline for dopant selection in OCM. It is certainly not a stand-alone predictor of performance.

Shown in Figure 10.2, Figure 10.3, Figure 10.4, Figure 10.5 and Figure 10.6 are bird's eye views of the relaxed La_2O_3 slabs prior to (left) and after (right) oxygen removal for the following respective cases: undoped, Cu-doped, Ce-doped, Na-doped and Mg-doped. These dopants represent a diverse set of materials from various parts of the periodic table. Accordingly, Table 10.2 shows bond lengths between the doping site and neighboring surface oxygens as well as the oxygen-metal-oxygen dihedral angle. Doping with Cu, Mg and Na caused the most significant structural shifts, all similar to each other, yet they all give substantially different catalysis experimentally. Doping the system with Ce offers unsubstantial changes structurally relative to the undoped slab.

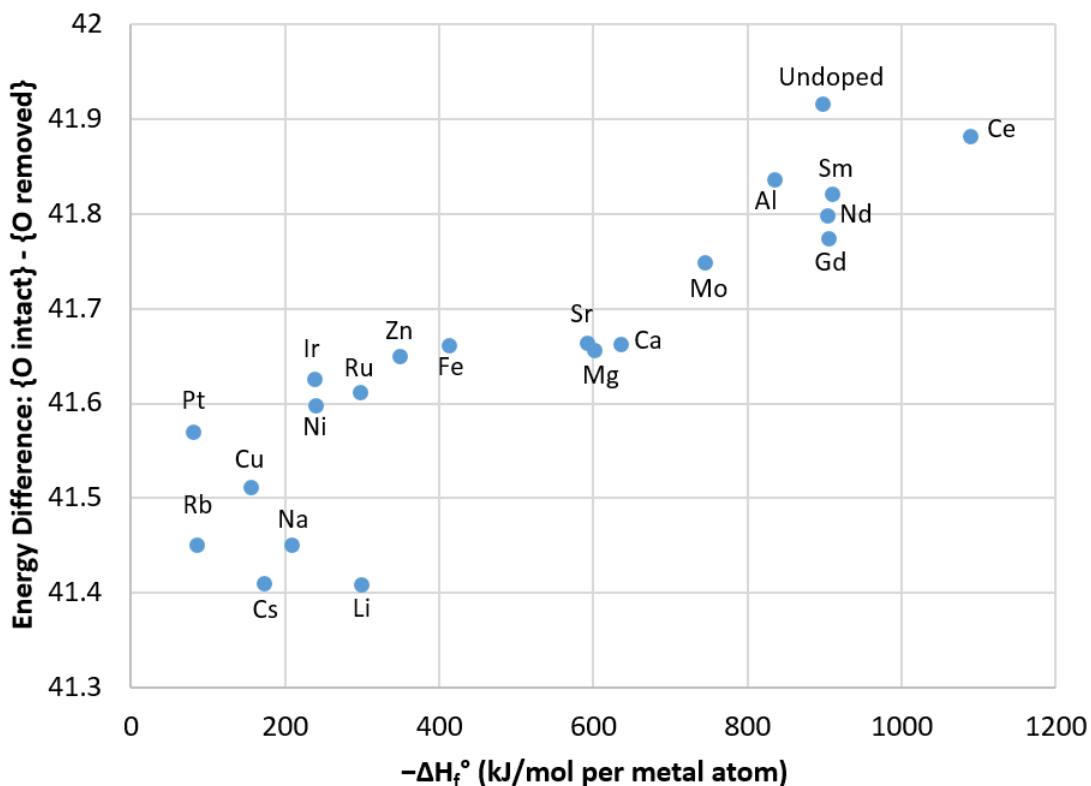


Figure 10.1. Energy differences between various La_2O_3 -based slabs with all atoms intact versus with an oxygen atom removed. Each label on the plot signifies a particular dopant used to replace a single La atom on the slab's exterior.

Table 10.1. Catalytic performance screening results of nanofiber fabric catalysts used on feed mixtures of CH_4 and O_2 in fixed bed reactors inside 6 mm diameter quartz tubes. Co-spun samples were synthesized with all precursor metal salts present in the electrospinning solution. Feed gas flow rates were 80-120 sccm.

Catalyst	Feed molar CH_4/O_2 ratio	Feed Temperature ($^\circ\text{C}$)	% Selectivity	% CH_4 Conversion
Co-spun La_2O_3 -CuO, 8 mg	4	550	10% C_{2+} , 90% CO_2	18

Co-spun La ₂ O ₃ -CeO ₂ -Ni	7	518	38% C ₂₊	19
Co-spun La ₂ O ₃ -CeO ₂ - Zn	7	539	66% C ₂₊	25
Co-spun La ₂ O ₃ -CeO ₂ - Nd	7	616	62% C ₂₊	24
La ₂ O ₃ -CeO ₂ - CsCl co-spun fabric	7	546	64% C ₂₊	18
La ₂ O ₃ -CeO ₂ - MgO co-spun fabric	7	605	70% C ₂₊	26
La ₂ O ₃ -CeO ₂ fabric impregnated with Pt	7	560	53% CO, 47% CO ₂	15
La ₂ O ₃ -CeO ₂ fabric impregnated with Sr	7	726	73% C ₂₊	14

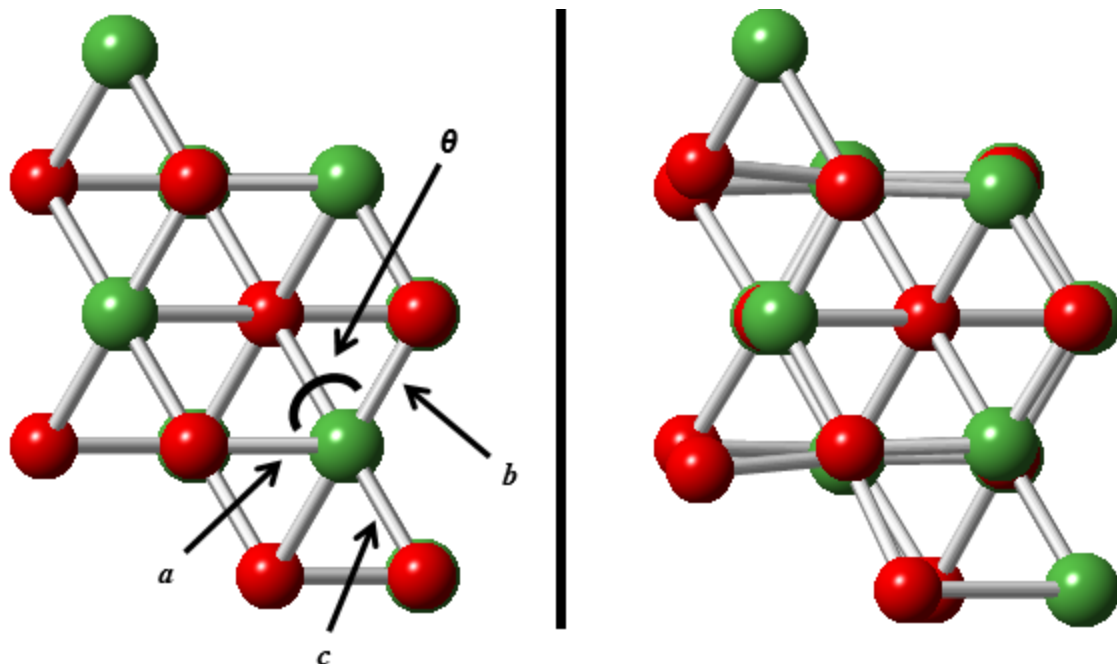


Figure 10.2. Undoped La_2O_3 slab with neighboring lattice oxygen intact (left) and removed (right).

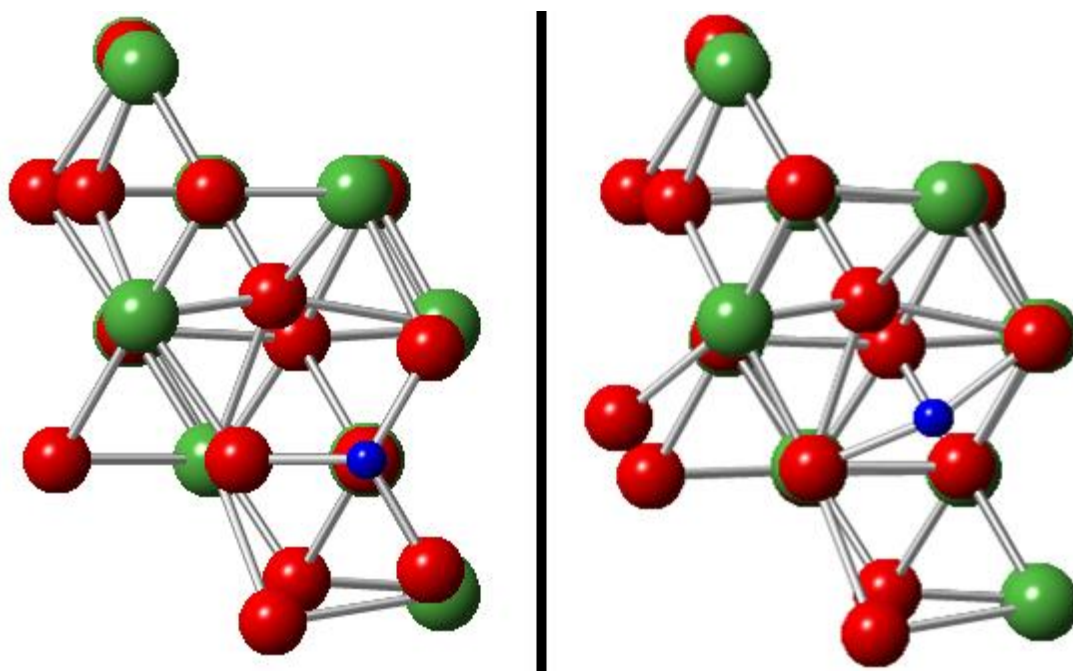


Figure 10.3. Cu-doped La_2O_3 slab with neighboring lattice oxygen intact (left) and removed (right).

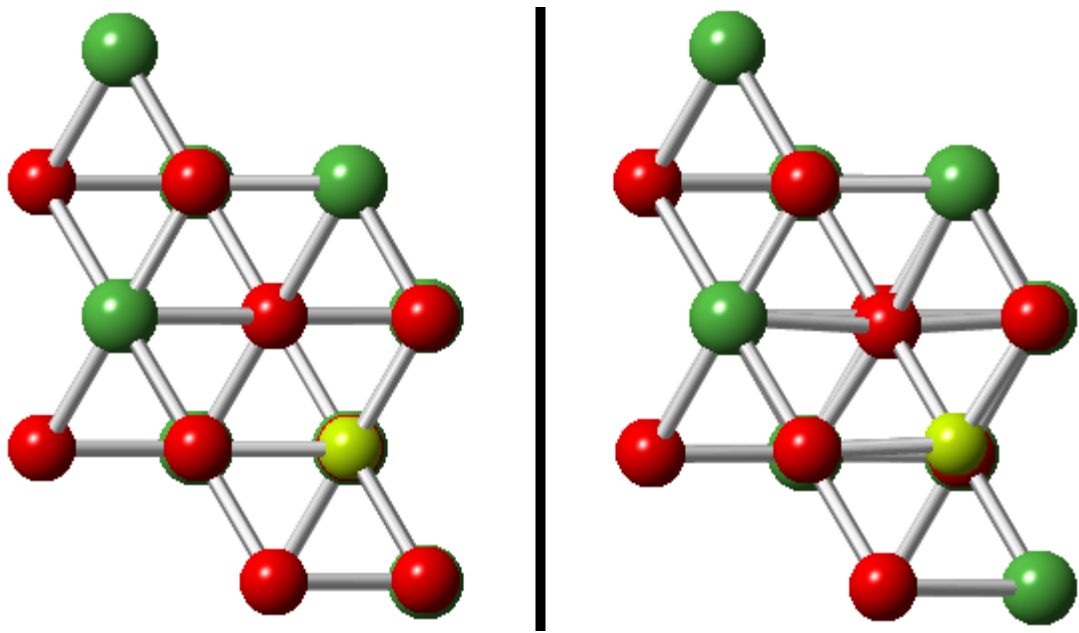


Figure 10.4. Ce-doped La_2O_3 slab with neighboring lattice oxygen intact (left) and removed (right).

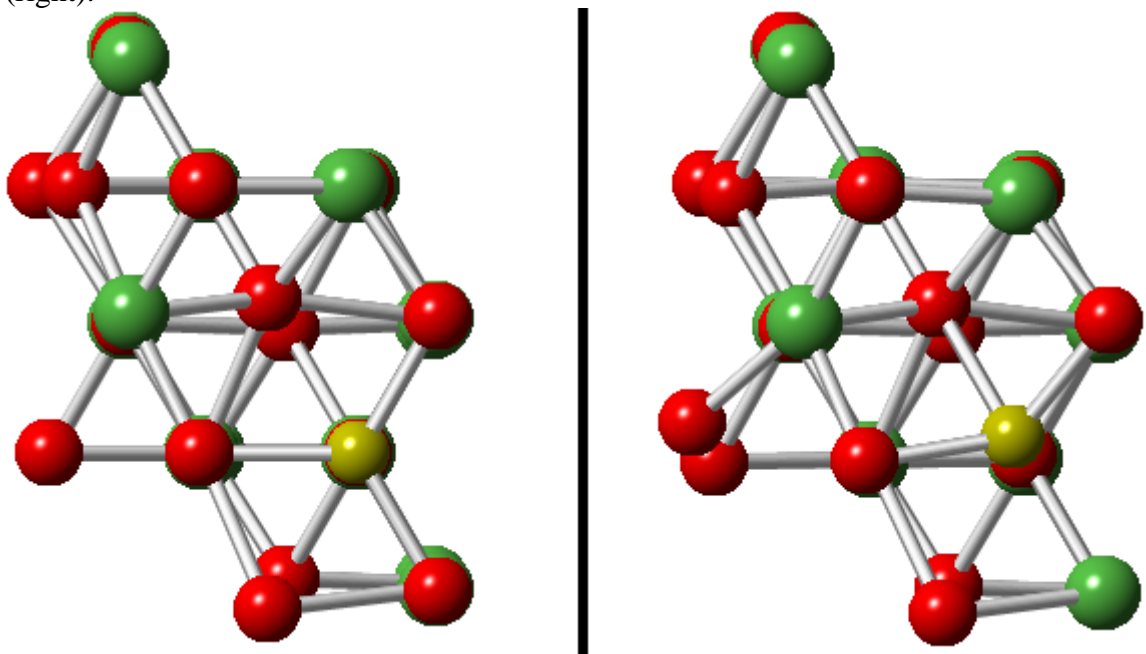


Figure 10.5. Na-doped La_2O_3 slab with neighboring lattice oxygen intact (left) and removed (right).

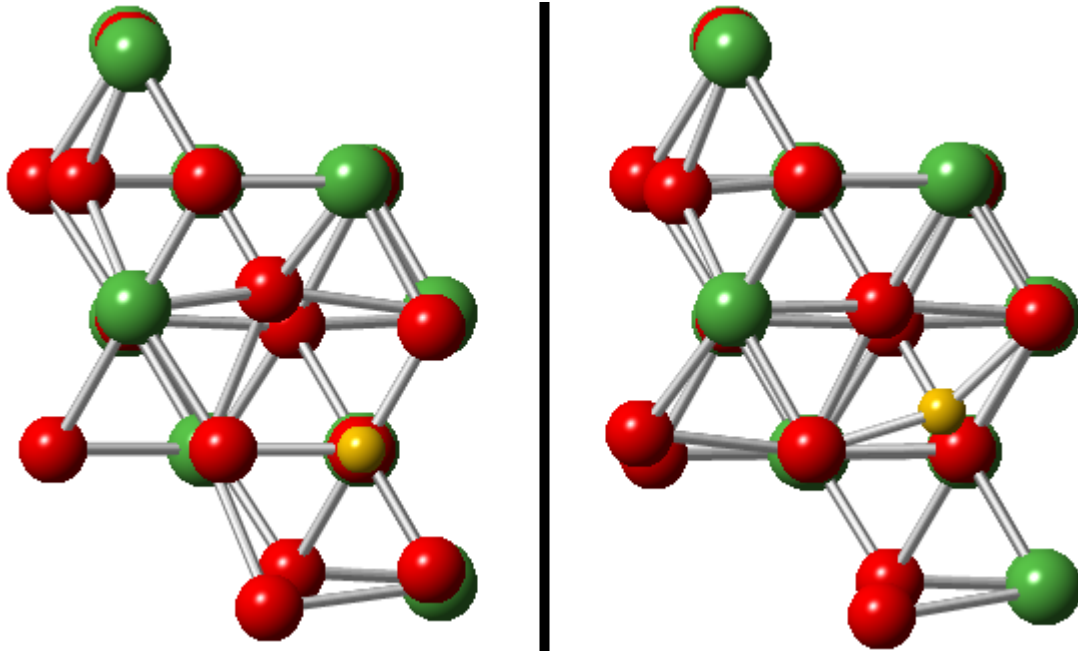


Figure 10.6. Mg-doped La_2O_3 slab with neighboring lattice oxygen intact (left) and removed (right).

Table 10.2. Bond lengths a , b and c and bond angle θ , defined in Figure 10.2, for various structures appearing in Figure 10.1.

Dopant	O-atom intact				O-atom removed		
	a (Å)	b (Å)	c (Å)	θ (°)	a (Å)	b (Å)	θ (°)
Undoped	2.37	2.37	2.37	112.3	2.27	2.27	113.1
Cu	1.88	1.88	1.88	120	1.90	1.90	162.4
Ce	2.33	2.33	2.33	112.9	2.30	2.30	114.5
Na	2.35	2.35	2.35	119.4	2.23	2.23	134.4
Mg	2.05	2.05	2.05	119.8	2.00	2.00	146.7

10.4. Summary.

Forty atom lanthanum-oxide based slabs were subjected to full geometric relaxation using Quantum ESPRESSO to ascertain the tendency for lattice oxygens to mobilize and vacate the surface. Structures doped with rare-earth metals tend to withhold surface oxygens relative to other materials. Transition metals and alkali metals do the opposite. The tendency for the oxygen to vacate was positively correlated with the enthalpy of formation of the dopant's metal oxide, consistent with previous works. The structures simulated with highly mobile surface oxygens tend to give experimental catalysis more towards methane combustion as opposed to oxidative coupling, though alkali metals did not follow this behavior.

Chapter 11. Conclusions.

The use of electrospun nanofiber fabrics as heterogeneous catalysts has the potential to create novel high-performing catalytic reactors where nanoparticle-based powder materials have failed. In general, the creation of solid materials of catalytic value such that their nanostructures can readily be finely tuned in scalable fashion arguably should be the focus of heterogeneous catalysis research, whether it be the creation of nanofibers, rods, cubes, etc. Electrospinning particularly offers a new route to the scalable synthesis of novel catalysts and can be used to create metal oxide based catalytic fabrics, both supported and unsupported. Although this work has shown electrospun fabrics based on RuO₂-CuO-NaCl/SiO₂ materials do not appear to be effective for the direct epoxidation of propylene by molecular oxygen, unsupported rare-earth metal oxide nanofibers are promising in the oxidative coupling of methane (OCM), which aims for the direct conversion of natural gas to products traditionally manufactured from crude oil.

Electrospun nanofiber fabrics of La₂O₃-CeO₂ were found to give comparable selectivity towards ethane, ethylene and higher order hydrocarbons to nanoparticle-based catalysts in the literature, except at several hundred degrees Celsius lower feed gas temperatures. Ethylene is an industrial chemical intermediate whose annual revenues are approximately \$150 billion and is produced mostly by naphtha cracking, as well as *indirectly* from natural gas using steam reforming. Creating a viable catalyst for OCM would allow for *direct* ethylene production from natural gas and bypass the energy demands of steam reforming. We enhanced the performance of the catalytic nanofiber

fabrics by implemented them in dual bed catalytic reactors. In between the two fixed beds was an inter-stage injection of molecular oxygen and gas phase cooling that allowed for the enhancement of process yields from 16% to 21% relative to a single bed run at the same total oxygen feed. The primary driving factor for this performance enhancement is the spatial distribution of oxygen and distribution of released energy, both of which lessen the extent of combustion reactions. Density functional theory studies using Quantum ESPRESSO and utilizing oxygen vacancies on lanthanum-oxide slabs doped with various metals showed reasonably expected behavior relative to experimental catalytic performance results and with similar literature simulations.

Further work on this project could be undertaken with the following recommendations. Since the spatial distribution of oxygen fed to an OCM catalytic reactor has shown to be beneficial, utilizing reactors with a larger number of fixed beds and oxygen injection points could, in turn, push yields even higher. Another option for a catalytic reactor of this nature would be to introduce the oxygen through a capillary tube within a single fixed bed via laser-drilled injection points. Here, localized spikes in the oxygen concentration close to the point of injection would need to be dealt with to avoid a runaway reaction; the use of a diluent (e.g. nitrogen). In both cases, distributing the oxygen requires higher feed temperatures. Lastly, the mechanistic and transport modeling that utilizes the data sets acquired from spatial profiling may be developed with intent of refining existing mechanisms for OCM and thus advancing the pace towards the discovery of a catalytic system of commercial value.

References

1. Linic, S. and P. Christopher, *Overcoming Limitation in the Design of Selective Solid Catalysts by Manipulating Shape and Size of Catalytic Particles: Epoxidation Reactions on Silver*. Chemcatchem, 2010. **2**(9): p. 1061-1063.
2. Bell, A.T., *The impact of nanoscience on heterogeneous catalysis*. Science, 2003. **299**(5613): p. 1688-1691.
3. Christopher, P. and S. Linic, *Engineering selectivity in heterogeneous catalysis: Ag nanowires as selective ethylene epoxidation catalysts*. Journal of the American Chemical Society, 2008. **130**(34): p. 11264-+.
4. Christopher, P. and S. Linic, *Shape- and Size-Specific Chemistry of Ag Nanostructures in Catalytic Ethylene Epoxidation*. Chemcatchem, 2010. **2**(1): p. 78-83.
5. Ma, Z. and F. Zaera, *Heterogeneous Catalysis by Metals*, in *Encyclopedia of Inorganic and Bioinorganic Chemistry*. 2014. p. 1-16.
6. NIST's Advanced Technology Program, C.a.B.T., *Leveraging Resources and Targeting Performance*. 1998.
7. National Research Council (U.S.). Panel on New Directions in Catalytic Science and Technology., *Catalysis looks to the future*. 1992, Washington, D.C.: National Academy Press. viii, 86 p.
8. Senkan, S., *Combinatorial heterogeneous catalysis - A new path in an old field*. Angewandte Chemie-International Edition, 2001. **40**(2): p. 312-329.
9. Anastas, P. and J. Warner, *Green Chemistry: Theory and Practice*. 1998, New York: Oxford University Press.
10. National Research Council (U.S.). Panel on Benchmarking the Research Competitiveness of the US in Chemical Engineering., *International benchmarking of U.S. chemical engineering research competitiveness*. 2007, Washington, D.C.: National Academies Press. x, 236 p.
11. Aiken, J.D. and R.G. Finke, *A review of modern transition-metal nanoclusters: their synthesis, characterization, and applications in catalysis*. Journal of Molecular Catalysis a-Chemical, 1999. **145**(1-2): p. 1-44.

12. Schmid, G., *Clusters and Colloids - Bridges between Molecular and Condensed Material*. Endeavour, 1990. **14**(4): p. 172-178.
13. Lei, Y., et al., *Increased Silver Activity for Direct Propylene Epoxidation via Subnanometer Size Effects*. Science, 2010. **328**(5975): p. 224-228.
14. Takahashi, A., et al., *Effects of added 3d transition-metals on Ag-based catalysts for direct epoxidation of propylene by oxygen*. Applied Catalysis a-General, 2005. **294**(1): p. 34-39.
15. Kalyoncu, S., et al., *Direct epoxidation of propylene to propylene oxide on various catalytic systems: A combinatorial micro-reactor study*. Catalysis Communications, 2015. **61**: p. 16-20.
16. Lu, J.Q., et al., *Epoxidation of propylene on NaCl-modified silver catalysts with air as the oxidant*. Applied Catalysis a-General, 2002. **237**(1-2): p. 11-19.
17. Li, D. and Y.N. Xia, *Electrospinning of nanofibers: Reinventing the wheel?* Advanced Materials, 2004. **16**(14): p. 1151-1170.
18. Kim, J.S. and D.H. Reneker, *Mechanical properties of composites using ultrafine electrospun fibers*. Polymer Composites, 1999. **20**(1): p. 124-131.
19. Bergshoef, M.M. and G.J. Vancso, *Transparent nanocomposites with ultrathin, electrospun nylon-4,6 fiber reinforcement*. Advanced Materials, 1999. **11**(16): p. 1362-1365.
20. Gibson, P., H. Schreuder-Gibson, and D. Rivin, *Transport properties of porous membranes based on electrospun nanofibers*. Colloids and Surfaces a-Physicochemical and Engineering Aspects, 2001. **187**: p. 469-481.
21. Kadler, K.E., et al., *Collagen fibril formation*. Biochemical Journal, 1996. **316**: p. 1-11.
22. Li, W.J., et al., *Electrospun nanofibrous structure: A novel scaffold for tissue engineering*. Journal of Biomedical Materials Research, 2002. **60**(4): p. 613-621.
23. Mo, X.M., et al., *Electrospun P(LLA-CL) nanofiber: a biomimetic extracellular matrix for smooth muscle cell and endothelial cell proliferation*. Biomaterials, 2004. **25**(10): p. 1883-1890.
24. Yoshimoto, H., et al., *A biodegradable nanofiber scaffold by electrospinning and its potential for bone tissue engineering*. Biomaterials, 2003. **24**(12): p. 2077-2082.

25. Jin, H.J., et al., *Human bone marrow stromal cell responses on electrospun silk fibroin mats*. *Biomaterials*, 2004. **25**(6): p. 1039-1047.
26. Luu, Y.K., et al., *Development of a nanostructured DNA delivery scaffold via electrospinning of PLGA and PLA-PEG block copolymers*. *Journal of Controlled Release*, 2003. **89**(2): p. 341-353.
27. Min, B.M., et al., *Electrospinning of silk fibroin nanofibers and its effect on the adhesion and spreading of normal human keratinocytes and fibroblasts in vitro*. *Biomaterials*, 2004. **25**(7-8): p. 1289-1297.
28. Jia, H.F., et al., *Enzyme-carrying polymeric nanofibers prepared via electrospinning for use as unique biocatalysts*. *Biotechnology Progress*, 2002. **18**(5): p. 1027-1032.
29. Xie, J.B. and Y.L. Hsieh, *Ultra-high surface fibrous membranes from electrospinning of natural proteins: casein and lipase enzyme*. *Journal of Materials Science*, 2003. **38**(10): p. 2125-2133.
30. Demir, M.M., et al., *Palladium nanoparticles by electrospinning from poly(acrylonitrile-co-acrylic acid)-PdCl₂ solutions. Relations between preparation conditions, particle size, and catalytic activity*. *Macromolecules*, 2004. **37**(5): p. 1787-1792.
31. Trimm, D.L. and C.W. Lam, *The Combustion of Methane on Platinum-Alumina Fiber Catalysts .1. Kinetics and Mechanism*. *Chemical Engineering Science*, 1980. **35**(6): p. 1405-1413.
32. Trimm, D.L. and C.W. Lam, *The Combustion of Methane on Platinum-Alumina Fiber Catalysts .2. Design and Testing of a Convective-Diffusive Type Catalytic Combustor*. *Chemical Engineering Science*, 1980. **35**(8): p. 1731-1739.
33. Lam, C.W., M.S. Stacey, and D.L. Trimm, *The Combustion of Methane on Platinum-Alumina Fiber Catalysts .3. The Kinetics of the Water Gas Shift Reaction*. *Chemical Engineering Science*, 1981. **36**(1): p. 224-226.
34. Somorjai, G.A. and R.M. Rioux, *High technology catalysts towards 100% selectivity fabrication, characterization and reaction studies*. *Catalysis Today*, 2005. **100**(3-4): p. 201-215.
35. Bhardwaj, N. and S.C. Kundu, *Electrospinning: A fascinating fiber fabrication technique*. *Biotechnology Advances*, 2010. **28**(3): p. 325-347.

36. Huang, Z.M., et al., *A review on polymer nanofibers by electrospinning and their applications in nanocomposites*. Composites Science and Technology, 2003. **63**(15): p. 2223-2253.
37. Tan, S., X. Huang, and B. Wu, *Some fascinating phenomena in electrospinning processes and applications of electrospun nanofibers*. Polymer International, 2007. **56**(11): p. 1330-1339.
38. Frenot, A. and I.S. Chronakis, *Polymer nanofibers assembled by electrospinning*. Current Opinion in Colloid & Interface Science, 2003. **8**(1): p. 64-75.
39. Lee, K.H., et al., *The change of bead morphology formed on electrospun polystyrene fibers*. Polymer, 2003. **44**(14): p. 4029-4034.
40. Wu, H., et al., *Electrospinning of Fe, Co, and Ni nanofibers: Synthesis, assembly, and magnetic properties*. Chemistry of Materials, 2007. **19**(14): p. 3506-3511.
41. Gouma, P., K. Kalyanasundaram, and A. Bishop, *Electrospun single-crystal MoO₃ nanowires for biochemistry sensing probes*. Journal of Materials Research, 2006. **21**(11): p. 2904-2910.
42. Kahlich, D., U. Wierchern, and J. Lindner, *Propylene Oxide*, in *Ullmann's Encyclopedia of Industrial Chemistry*. 2000. p. 313-335.
43. Cavani, F. and J.H. Teles, *Sustainability in Catalytic Oxidation: An Alternative Approach or a Structural Evolution?* Chemsuschem, 2009. **2**(6): p. 508-534.
44. Oyama, S.T., *Mechanisms in homogeneous and heterogeneous epoxidation catalysis*. 1st ed. 2008, Amsterdam ; Boston: Elsevier. xxi, 501 p.
45. Tullo, A., *BASF, Dow plan more propylene oxide units*. Chemical & Engineering News, 2005. **83**(44): p. 7-7.
46. Nijhuis, T.A., et al., *The production of propene oxide: Catalytic processes and recent developments*. Industrial & Engineering Chemistry Research, 2006. **45**(10): p. 3447-3459.
47. Serafin, J.G., A.C. Liu, and S.R. Seyedmonir, *Surface science and the silver-catalyzed epoxidation of ethylene: an industrial perspective*. Journal of Molecular Catalysis a-Chemical, 1998. **131**(1-3): p. 157-168.
48. Ozbek, M.O., I. Onal, and R.A. van Santen, *Why silver is the unique catalyst for ethylene epoxidation*. Journal of Catalysis, 2011. **284**(2): p. 230-235.
49. Ozbek, M.O. and R.A. van Santen, *The Mechanism of Ethylene Epoxidation Catalysis*. Catalysis Letters, 2013. **143**(2): p. 131-141.

50. Carter, E.A. and W.A. Goddard, *The Surface Atomic Oxyradical Mechanism for Ag-Catalyzed Olefin Epoxidation*. Journal of Catalysis, 1988. **112**(1): p. 80-92.
51. Hu, Z.M., H. Nakai, and H. Nakatsuji, *Oxidation mechanism of propylene on an Ag surface: dipped adcluster model study*. Surface Science, 1998. **401**(3): p. 371-391.
52. Lambert, R.M., et al., *Heterogeneous alkene epoxidation: past, present and future*. Journal of Molecular Catalysis a-Chemical, 2005. **228**(1-2): p. 27-33.
53. Jankowiak, J.T. and M.A. Barteau, *Ethylene epoxidation over silver and copper-silver bimetallic catalysts: I. Kinetics and selectivity*. Journal of Catalysis, 2005. **236**(2): p. 366-378.
54. Linic, S., et al., *Ethylene epoxidation on Ag: Identification of the crucial surface intermediate by experimental and theoretical investigation of its electronic structure*. Angewandte Chemie-International Edition, 2004. **43**(22): p. 2918-2921.
55. Torres, D., et al., *Low-basicity oxygen atoms: A key in the search for propylene epoxidation catalysts*. Angewandte Chemie-International Edition, 2007. **46**(12): p. 2055-2058.
56. Kulkarni, A., et al., *Reactions of Propylene Oxide on Supported Silver Catalysts: Insights into Pathways Limiting Epoxidation Selectivity*. Topics in Catalysis, 2012. **55**(1-2): p. 3-12.
57. Alvarez-Galvan, M.C., et al., *Direct methane conversion routes to chemicals and fuels*. Catalysis Today, 2011. **171**(1): p. 15-23.
58. Ren, T., M.K. Patel, and K. Blok, *Steam cracking and methane to olefins: Energy use, CO₂ emissions and production costs*. Energy, 2008. **33**(5): p. 817-833.
59. Urbancic, M.A., et al., *Maximize ethylene gain in acetylene removal units New-generation catalysts and proper operating strategies offer improved selectivity and cycle length*. Hydrocarbon Processing, 2009. **88**(6): p. 65-+.
60. Cahill, J., *Efficiently Cracking Hydrocarbons in Ethylene Furnaces*. Emerson Process Experts.
61. Rostrup-Nielsen, J.R., J. Sehested, and J.K. Norskov, *Hydrogen and synthesis gas by steam- and CO₂ reforming*. Advances in Catalysis, Vol 47, 2002. **47**: p. 65-139.

62. Mleczko, L. and M. Baerns, *Catalytic Oxidative Coupling of Methane - Reaction-Engineering Aspects and Process Schemes*. Fuel Processing Technology, 1995. **42**(2-3): p. 217-248.
63. Chase, M.W. and National Institute of Standards and Technology (U.S.), *NIST-JANAF thermochemical tables*. 4th ed. 1998, Washington, DC
New York: American Chemical Society ;
American Institute of Physics for the National Institute of Standards and Technology.
64. Zavyalova, U., et al., *Statistical Analysis of Past Catalytic Data on Oxidative Methane Coupling for New Insights into the Composition of High-Performance Catalysts*. Chemcatchem, 2011. **3**(12): p. 1935-1947.
65. Lunsford, J.H., *The Catalytic Oxidative Coupling of Methane*. Angewandte Chemie-International Edition in English, 1995. **34**(9): p. 970-980.
66. Conway, S.J., D.J. Wang, and J.H. Lunsford, *Selective Oxidation of Methane and Ethane over Li⁺-MgO-Cl⁻ Catalysts Promoted with Metal-Oxides*. Applied Catalysis, 1991. **79**(1): p. L1-L5.
67. Keller, G.E. and M.M. Bhasin, *Synthesis of Ethylene Via Oxidative Coupling of Methane .I. Determination of Active Catalysts*. Journal of Catalysis, 1982. **73**(1): p. 9-19.
68. Hinsén, W. and M. Baerns, *Oxidative Coupling of Methane to C₂-Hydrocarbons in the Presence of Different Catalysts*. Chemiker-Zeitung, 1983. **107**(7-8): p. 223-226.
69. Ito, T. and J.H. Lunsford, *Synthesis of Ethylene and Ethane by Partial Oxidation of Methane over Lithium-Doped Magnesium-Oxide*. Nature, 1985. **314**(6013): p. 721-722.
70. Nam, K.T., et al., *Virus-enabled synthesis and assembly of nanowires for lithium ion battery electrodes*. Science, 2006. **312**(5775): p. 885-888.
71. Lee, Y.J., et al., *Fabricating Genetically Engineered High-Power Lithium-Ion Batteries Using Multiple Virus Genes*. Science, 2009. **324**(5930): p. 1051-1055.
72. Mao, C.B., et al., *Virus-based toolkit for the directed synthesis of magnetic and semiconducting nanowires*. Science, 2004. **303**(5655): p. 213-217.
73. Nam, Y.S., et al., *Biologically templated photocatalytic nanostructures for sustained light-driven water oxidation*. Nature Nanotechnology, 2010. **5**(5): p. 340-344.

74. Wood, D.A., C. Nwaoha, and B.F. Towler, *Gas-to-liquids (GTL): A review of an industry offering several routes for monetizing natural gas*. Journal of Natural Gas Science and Engineering, 2012. **9**: p. 196-208.
75. Hickman, D.A. and L.D. Schmidt, *Production of Syngas by Direct Catalytic-Oxidation of Methane*. Science, 1993. **259**(5093): p. 343-346.
76. Enger, B.C., R. Lodeng, and A. Holmen, *A review of catalytic partial oxidation of methane to synthesis gas with emphasis on reaction mechanisms over transition metal catalysts*. Applied Catalysis a-General, 2008. **346**(1-2): p. 1-27.
77. Prettre, M., C. Eichner, and M. Perrin, *The Catalytic Oxidation of Methane to Carbon Monoxide and Hydrogen*. Transactions of the Faraday Society, 1946. **42**(3-4): p. 335-340.
78. Korup, O., et al., *Measurement and analysis of spatial reactor profiles in high temperature catalysis research*. Chemical Engineering and Processing, 2011. **50**(10): p. 998-1009.
79. Williams, K.A., R. Horn, and L.D. Schmidt, *Performance of mechanisms and reactor models for methane oxidation on Rh*. Aiche Journal, 2007. **53**(8): p. 2097-2113.
80. Senkan, S.M. and S. Ozturk, *Discovery and optimization of heterogeneous catalysts by using combinatorial chemistry*. Angewandte Chemie-International Edition, 1999. **38**(6): p. 791-795.
81. Senkan, S., et al., *High-throughput testing of heterogeneous catalyst libraries using array microreactors and mass spectrometry*. Angewandte Chemie-International Edition, 1999. **38**(18): p. 2794-2799.
82. Senkan, S., et al., *High-throughput metal nanoparticle catalysis by pulsed laser ablation*. Catalysis Today, 2006. **117**(1-3): p. 291-296.
83. Duan, S., M. Kahn, and S. Senkan, *High-throughput nanoparticle catalysis: Partial oxidation of propylene*. Combinatorial Chemistry & High Throughput Screening, 2007. **10**(2): p. 111-119.
84. Duan, S. and S. Senkan, *Catalytic conversion of ethanol to hydrogen using combinatorial methods*. Industrial & Engineering Chemistry Research, 2005. **44**(16): p. 6381-6386.
85. Miller, A., et al., *SnO₂-CuO-NaCl/SiO₂ Catalysts for Propylene Epoxidation*. Industrial & Engineering Chemistry Research, 2013. **52**(28): p. 9551-9555.

86. Seubsai, A., M. Kahn, and S. Senkan, *New Catalytic Materials for the Direct Epoxidation of Propylene by Molecular Oxygen*. Chemcatchem, 2011. **3**(1): p. 174-179.
87. Seubsai, A., et al., *Key Mechanistic Insight into the Direct Gas-Phase Epoxidation of Propylene by the RuO₂-CuO-NaCl/SiO₂ Catalyst*. Chemcatchem, 2014. **6**(5): p. 1215-1219.
88. Lu, J.Q., et al., *Direct propylene epoxidation over modified Ag/CaCO₃ catalysts*. Applied Catalysis a-General, 2006. **302**(2): p. 283-295.
89. Seubsai, A. and S. Senkan, *The Effects of Cofeeding Chlorinated Hydrocarbons in the Direct Epoxidation of Propylene by Molecular Oxygen*. Chemcatchem, 2011. **3**(11): p. 1751-1754.
90. Nanba, T., et al., *Characterization of Cu species on SiO₂ and ZSM-5 by temperature-programmed reduction by ammonia*. Journal of Thermal Analysis and Calorimetry, 2013. **113**(2): p. 793-802.
91. D'Ippolito, S.A., et al., *Propane oxidative dehydrogenation on V-Sb/ZrO₂ catalysts*. Catalysis Letters, 2008. **122**(3-4): p. 252-258.
92. Prins, R., *Hydrogen Spillover. Facts and Fiction*. Chemical Reviews, 2012. **112**(5): p. 2714-2738.
93. Mazzieri, V.A., et al., *Effect of Ge content on the metal and acid properties of Pt-Re-Ge/Al₂O₃-Cl catalysts for naphtha reforming*. Applied Catalysis a-General, 2009. **353**(1): p. 93-100.
94. Song, J.H., H.E. Kim, and H.W. Kim, *Production of electrospun gelatin nanofiber by water-based co-solvent approach*. Journal of Materials Science-Materials in Medicine, 2008. **19**(1): p. 95-102.
95. Sisson, K., et al., *Fiber diameters control osteoblastic cell migration and differentiation in electrospun gelatin*. Journal of Biomedical Materials Research Part A, 2010. **94a**(4): p. 1312-1320.
96. Strange, E.D., D.L. Vanhekken, and V.H. Holsinger, *Effect of Sodium-Chloride on the Solubility of Caseins*. Journal of Dairy Science, 1994. **77**(5): p. 1216-1222.
97. Yang, C.R., et al., *Comparisons of Fibers Properties between Vertical and Horizontal Type Electrospinning Systems*. Ceidp: 2009 Annual Report Conference on Electrical Insulation and Dielectric Phenomena, 2009: p. 514-517.

98. Kang, H.G., et al., *Preparation of silica-sustained electrospun polyvinylpyrrolidone fibers with uniform mesopores via oxidative removal of template molecules by H₂O₂ treatment*. *Materials Research Bulletin*, 2010. **45**(7): p. 830-837.
99. Kang, H.G., et al., *A novel catalyst based on electrospun silver-doped silica fibers with ribbon morphology*. *Journal of Colloid and Interface Science*, 2010. **341**(2): p. 303-310.
100. Zhao, Y.Y., et al., *Fabrication of refining mesoporous silica nanofibers via electrospinning*. *Materials Letters*, 2008. **62**(1): p. 143-146.
101. Brinker, C.J., *Hydrolysis and Condensation of Silicates - Effects on Structure*. *Journal of Non-Crystalline Solids*, 1988. **100**(1-3): p. 31-50.
102. Buckley, A.M. and M. Greenblatt, *The Sol-Gel Preparation of Silica-Gels*. *Journal of Chemical Education*, 1994. **71**(7): p. 599-602.
103. Klein, L.C., *Sol-Gel Processing of Silicates*. *Annual Review of Materials Science*, 1985. **15**: p. 227-248.
104. Hench, L.L. and J.K. West, *The Sol-Gel Process*. *Chemical Reviews*, 1990. **90**(1): p. 33-72.
105. Pan, H., et al., *Continuous aligned polymer fibers produced by a modified electrospinning method*. *Polymer*, 2006. **47**(14): p. 4901-4904.
106. Fennessey, S.F. and R.J. Farris, *Fabrication of aligned and molecularly oriented electrospun polyacrylonitrile nanofibers and the mechanical behavior of their twisted yarns*. *Polymer*, 2004. **45**(12): p. 4217-4225.
107. Dalton, P.D., D. Klee, and M. Moller, *Electrospinning with dual collection rings*. *Polymer*, 2005. **46**(3): p. 611-614.
108. Katta, P., et al., *Continuous electrospinning of aligned polymer nanofibers onto a wire drum collector*. *Nano Letters*, 2004. **4**(11): p. 2215-2218.
109. Broadbelt, L.J. and R.Q. Snurr, *Applications of molecular modeling in heterogeneous catalysis research*. *Applied Catalysis a-General*, 2000. **200**(1-2): p. 23-46.
110. Reneker, D.H. and A.L. Yarin, *Electrospinning jets and polymer nanofibers*. *Polymer*, 2008. **49**(10): p. 2387-2425.
111. Noon, D., A. Seubsai, and S. Senkan, *Oxidative Coupling of Methane by Nanofiber Catalysts*. *Chemcatchem*, 2013. **5**(1): p. 146-149.

112. Dedov, A.G., et al., *Oxidative coupling of methane catalyzed unexpected synergistic effect of the by rare earth oxides oxide mixtures*. Applied Catalysis a-General, 2003. **245**(2): p. 209-220.
113. Pak, S. and J.H. Lunsford, *Thermal effects during the oxidative coupling of methane over Mn/Na₂WO₄/SiO₂ and Mn/Na₂WO₄/MgO catalysts*. Applied Catalysis a-General, 1998. **168**(1): p. 131-137.
114. Imanaka, N., T. Masui, and Y. Kato, *Preparation of the cubic-type La₂O₃ phase by thermal decomposition of LaI₃*. Journal of Solid State Chemistry, 2005. **178**(1): p. 395-398.
115. Hu, C.G., et al., *Direct synthesis and structure characterization of ultrafine CeO₂ nanoparticles*. Nanotechnology, 2006. **17**(24): p. 5983-5987.
116. Cao, X.Q., et al., *Lanthanum-cerium oxide as a thermal barrier-coating material for high-temperature applications*. Advanced Materials, 2003. **15**(17): p. 1438-1442.
117. Noon, D., B. Zohour, and S. Senkan, *Oxidative coupling of methane with La₂O₃-CeO₂ nanofiber fabrics: A reaction engineering study*. Journal of Natural Gas Science and Engineering, 2014. **18**: p. 406-411.
118. Zohour, B., D. Noon, and S. Senkan, *New Insights into the Oxidative Coupling of Methane from Spatially Resolved Concentration and Temperature Profiles*. Chemcatchem, 2013. **5**(10): p. 2809-2812.
119. Nogare, D.D., et al., *Modeling spatially resolved data of methane catalytic partial oxidation on Rh foam catalyst at different inlet compositions and flowrates*. Journal of Catalysis, 2011. **277**(2): p. 134-148.
120. Papa, F., et al., *Acid-base properties of the active sites responsible for C-2(+) and CO₂ formation over MO-Sm₂O₃ (M = Zn, Mg, Ca and Sr) mixed oxides in OCM reaction*. Journal of Molecular Catalysis a-Chemical, 2011. **346**(1-2): p. 46-54.
121. Zohour, B., D. Noon, and S. Senkan, *Spatial Concentration and Temperature Profiles in Dual-Packed-Bed Catalytic Reactors: Oxidative Coupling of Methane*. Chemcatchem, 2014. **6**(10): p. 2815-2820.
122. Horn, R., et al., *Syngas by catalytic partial oxidation of methane on rhodium: Mechanistic conclusions from spatially resolved measurements and numerical simulations*. Journal of Catalysis, 2006. **242**(1): p. 92-102.
123. Thybaut, J.W., et al., *Catalyst design based on microkinetic models: Oxidative coupling of methane*. Catalysis Today, 2011. **159**(1): p. 29-36.

124. Hoebink, J.H.B.J., P.M. Couwenberg, and G.B. Marin, *Fixed bed reactor design for gas phase chain reactions catalysed by solids: The oxidative coupling of methane*. Chemical Engineering Science, 1994. **49**(24b): p. 5453-5463.
125. Sinev, M.Y., et al., *Kinetics of oxidative coupling of methane: Bridging the gap between comprehension and description*. Journal of Natural Gas Chemistry, 2009. **18**(3): p. 273-287.
126. Stansch, Z., L. Mleczko, and M. Baerns, *Comprehensive kinetics of oxidative coupling of methane over the La₂O₃/CaO catalyst*. Industrial & Engineering Chemistry Research, 1997. **36**(7): p. 2568-2579.
127. Senkan, S.M., *Detailed or micro chemical kinetic modelling*. 2000.
128. Sun, J., J.W. Thybaut, and G.B. Marin, *Microkinetics of methane oxidative coupling*. Catalysis Today, 2008. **137**(1): p. 90-102.
129. Rostrupnielsen, J.R. and J.H.B. Hansen, *Co₂-Reforming of Methane over Transition-Metals*. Journal of Catalysis, 1993. **144**(1): p. 38-49.
130. Postole, G., et al., *Catalytic Steam Methane Reforming Over Ir/Ce_{0.9}Gd_{0.1}O_{2-x}: Resistance to Coke Formation and Sulfur Poisoning*. Fuel Cells, 2012. **12**(2): p. 275-287.
131. Zohour, B., et al., *Spatial Profiles in RuO₂-CuO-NaCl/SiO₂ Packed-Bed Propylene Epoxidation Reactors*. Industrial & Engineering Chemistry Research, 2014. **53**(14): p. 6243-6248.
132. Fristrom, R.M. and A.A. Westenberg, *Flame structure*. McGraw-Hill series in advanced chemistry. 1965, New York,: McGraw-Hill. xiii, 424 p.
133. Li, B. and H. Metiu, *DFT Studies of Oxygen Vacancies on Undoped and Doped La₂O₃ Surfaces*. Journal of Physical Chemistry C, 2010. **114**(28): p. 12234-12244.
134. Derk, A.R., et al., *Methane Oxidation by Lanthanum Oxide Doped with Cu, Zn, Mg, Fe, Nb, Ti, Zr, or Ta: The Connection Between the Activation Energy and the Energy of Oxygen-Vacancy Formation*. Catalysis Letters, 2013. **143**(5): p. 406-410.
135. Chorkendorff, I. and J.W. Niemantsverdriet, *Concepts of modern catalysis and kinetics*. 2nd ed. 2007, Weinheim: Wiley-VCH. xvii, 457 p.